2020

Towards the development of benzobisoxazole and naphthodifuran based organic semiconductors for organic solar cells

BOSTON UNIVERSITY

GRADUATE SCHOOL OF ARTS AND SCIENCES

Dissertation

TOWARDS THE DEVELOPMENT OF BENZOBISOXAZOLE AND NAPHTHODIFURAN BASED ORGANIC SEMICONDUCTORS FOR ORGANIC SOLAR CELLS

by

ALFRED ALEXANDER BURNEY-ALLEN

B.S., University of Cincinnati, 2014
M.A., Boston University, 2019

Submitted in partial fulfillment of the

requirements for the degree of

Doctor of Philosophy

2020

Approved by

First Reader

Malika Jeffries-EL, Ph.D.
Associate Professor of Chemistry
Associate Professor of Materials Science and Engineering

Second Reader

Mark Grinstaff, Ph.D.
Distinguished Professor of Translational Research
Professor of Chemistry
Professor of Materials Science and Engineering
Professor of Biomedical Engineering
Professor of Medicine

"If we knew what we were doing, it would not be called research, would it?"

- Albert Einstein

DEDICATION

I would like to dedicate this work to my son Omari Zaire Burney-Allen, my mama Michelle Burney, my grandma Katherine Burney, the love of my life Tiffany Moody, my son's mother Tiffany Shanell Peterson, my brothers Twan, Billy, Tae, Carl, my dad, friends, and mentors, for all of their support and encouragement over the years.

ACKNOWLEDGMENTS

I would like to thank my research advisor, Dr. Malika Jeffries-EL for her mentorship, training, and support throughout my Ph.D. career. Dr. Jeffries-EL has been extremely supportive of my research interest and goals. She has also been supportive and understanding during the birth of my son allowing me to take periods time spend back home with him. Additionally, Dr. Jeffries-EL has created an environment that has allowed to grow.

I also would like to acknowledge the Jeffries-EL research group past and present for their support throughout my PhD process. All the times of encouragement and grilling in practice presentations that has pushed me to learn more in-depth about my craft. Specifically, past group members I would like to acknowledge, Monique Ewan, Achala Bhuwalka, Ramiro Chavez, and Jessica Shaw for their friendship and mentorship over the years.

Thirdly, I would like to acknowledge Boston University, Iowa State University, and the University of Cincinnati for assisting me with matters concerning personal or academic. Specifically, I want to acknowledge Lynette, and professors being really embracive and supportive faculty at Iowa State. I want to acknowledge Paul Ferrari, Kaitlin Valli, Dennis Bastista, and Norman Lee for all of their efforts in making things run smoothly around the lab and assisting with the identification of my compounds. Lastly, I would like to thank Dr. James Mack for assisting me during my times of need of advice as well creating a space for me in his group and at the University of Cincinnati when my son

was born. This made things easier allowing for me to simultaneously spend that quality time with Omari and still complete my research when he was born.

Last but not least, I would like to thank my mom and grandma for all their sacrifice in the past and present. Their sacrifice has allowed me to be here. Their support and love have been unconditional and I am greatly appreciative of that. I also would like to thank my brothers and dad for their continued encouragement over years. Lastly, I would to thank the love of my life Tiffany Moody for her unconditional and everlasting support, encouragement and understanding through this process. I am truly grateful for all of you. Thank you for believing in me.

TOWARDS THE DEVELOPMENT OF BENZOBISOXAZOLE AND NAPHTHODIFURAN BASED ORGANIC SEMICONDUCTORS FOR ORGANIC SOLAR CELLS

ALFRED ALEXANDER BURNEY-ALLEN

Boston University Graduate School of Arts and Sciences, 2020

Major Professor: Malika Jeffries-EL, Associate Professor of Chemistry

ABSTRACT

Currently, there is significant interest in the development of organic semiconductors for use in, for example, energy production. Integration of organic semiconductors into organic solar cells (OSCs) enables optimization of optical and electronic properties via chemical synthesis as well as solution processability. Due to reduced production costs, OSCs are being evaluated as potential alternatives to their inorganic counterparts. Although, there is already substantial work on OSCs, a detailed understanding of performance versus composition, film forming capability, and morphology are still lacking. Benzobisoxazoles (BBOs) are a unique class of organic semiconductors as the optical and electronic properties are tunable along two conjugation axis. This intrinsic characteristic of BBO presents an opportunity to develop an understanding of the structure - property relationships within BBO based materials and utilize them as potential donor material for OSCs.

Similarly, naphthodifuran (NDF) has a rigid coplanar structure that exhibit improved charge carrier mobilities and efficiencies in OSCs. These semiconducting materials are weak donors and when incorporated into weak donor – strong acceptor

molecular design motifs lead towards improved efficiencies in OSCs. Herein, the design, synthesis, and/or photovoltaic device optimization of BBO and NDF semiconducting based properties OSCs are discussed by the author of this dissertation.

TABLE OF CONTENTS

LIST OF TABLES

LIST OF FIGURES

LIST OF ACRONYMS AND DESCRIPTIONS

Acronym	Description
BBO	Benzobisoxazole
BHJ	Bulk Heterojunction
BPhen	4,7-Diphenyl-1,10-phenanthroline
CBP	4,4’-Bis(N-carbazolyl)-1,1’-biphenyl
CIE	Commission internationale de l'éclairage
CV	Cyclic Voltammetry
DP	Degree of Polymerization
DPV	Differential Pulse Voltammetry
DSC	Differential Scanning Calorimetry
EA	Electron Affinity
Eg^{opt}	Optical Band Gap Energy
EI	Electron Ionization
EL	Electroluminescence
EQE	External Quantum Efficiency
ESI	Electrospray Ionization
ETL	Electron Transport Layer
FRET	Förster Resonance Energy Transfer
FWHM	Full Width at Half Maximum
GPC	Gel Permeation Chromatography
HMW	High Molecular Weight
HOMO	Highest Occupied Molecular Orbital
HRMS	High Resolution Mass Spectrometry
HTL	Hole Transport Layer
HWE	Horner-Wadsworth-Emmons
IP	Ionization Potential
ITO	Indium Tin Oxide
LCD	Liquid Crystal Display
LED	Light-Emitting Diode
LMW	Low Molecular Weight
LUMO	Lowest Unoccupied Molecular Orbital
MCP	Microchannel Plate
MMW	Medium Molecular Weight
Mn	Number Averaged Molecular Weight
Mw	Weight Averaged Molecular Weight
NDF	Naphthodifuran
NMR	Nuclear Magnetic Resonance
NREL	National Renewable Laboratory

Acronym	Description
OLED	Organic Light-Emitting Diodes
OPV	Organic Photovoltaic
o-DCB	*o*-dichlorobenzene
OFET	Organic Field-Effect Transistor
OLED	Organic Light-Emitting Diodes
OPV	Organic Photovoltaic
PAV	Polyarylene vinylene
PBO	Polybenzobisoxazole
$PC_{61}BM$	[6,6]-Phenyl C61 butyric acid methyl ester
PCE	Power Conversion Efficiency
PDAF	Polydialkylfluorene
PDI	Poly Dispersity Index
PEDOT:PSS	Poly(3,4-ethylenedioxythiophene) poly(styrenesulfonate)
PL	Photoluminescence
PLED	Polymer Light-Emitting Diode
PPA	Polyphosphoric Acid
PPSE	poly(trimethylsilylphosphate)
PPV	Polyphenylene vinylene
PVK	Poly(N-vinylcarbazole)
SCE	Standard Calomel Electrode
TADF	Thermally Activated Delayed Fluorescence
TCSPC	Time Correlated Single Photon Counting
Td	Decomposition Temperature
Tg	Glass Transition Temperature
TGA	Thermal Gravimetric Analysis
THF	Tetrahydrofuran
UPS	Ultraviolet Photoelectron Spectroscopy
Wt%	Weight Percent
XRD	X-Ray Diffraction

CHAPTER ONE: REVIEW OF ORGANIC SEMICONDUCTORS AND ORGANIC PHOTOVOLTAIC APPLICATIONS

SECTION ONE - INTRODUCTION TO ORGANIC SEMICONDUCTORS

Today, the current ability of fossil fuel energy resources to supply all of societies needs is becoming an overwhelming concern. The necessity to meet the increasing energy demand has spurred the push for the development of renewable energy resources and energy conservation methods. Solar cells have arisen as a promising candidate to serve as a renewable energy alternative. The total global energy consumption is predicted to increase from 17 TW in 2010 to 27 TW by 2050.[1] The sun provides approximately 120,000 TW of energy annually, thus more energy strikes the earth in 1 hour than is consumed annually worldwide.[2] In theory covering an area of approximately 26,000 km^2 in Nevada with 15% power conversion efficient solar cells could supply power to the United States (**figure 1**).[3] Solar cells have surfaced as a promising candidates for renewable energy. Consequently, in an effort have surmounted to meet the increasing global demand for energy, there has been a large amount research and development on materials for solar cell applications. Currently, many commercial solar cell technologies are based on inorganic based semiconductor materials such as silicon, gallium arsenide, cadmium, indium, and other metalloids.[3,4] However, inorganic based semiconductor materials like silicon, suffer drawbacks such as high costs due to efforts to achieve extensively pure silicon; severe toxicity of cadmium, and scarcity of indium.[4]

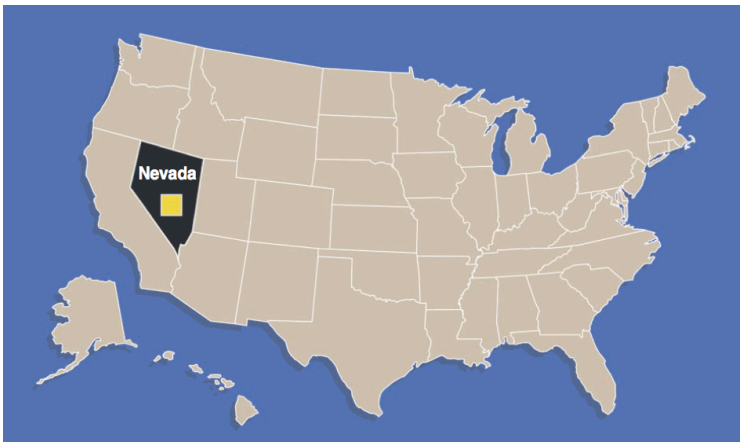

Figure 1. Area covered with 15% efficient solar cells can supply a years' worth of electricity to the United States.

Organic semiconductors offer solutions to the aforementioned problems. They are light weight and can be solution processed on to flexible substrates allowing for organic solar cells to be manufactured via inexpensive techniques such as spin coating and inkjet printing.[5,6,7] In addition, organic semiconductors provide unique opportunities to tune their optical and electronic properties via chemical synthesis. Thus organic semiconductors can be modified for specific applications such as organic light emitting diodes (OLED)s, organic field effect transistors (OFET)s, and organic solar cells (OSC)s.[8,9] Despite relatively low efficiencies of OSCs in comparison to their inorganic counterparts, organic based semiconductor materials have received a tremendous amount of attention in the past two decades and their performance is steadily improving.

Organic semiconducting materials to exhibit conductivity as a result of their conjugated backbone comprised of alternating single and double bonds.[9] A classic example of an organic semiconductor is polyacetylene (PA) (**figure 2**). Every atom in PA is sp^2 hybridized containing one electron in a π-bonding molecular orbital creating a network of

adjacent π-bonding molecular orbitals with electrons that are delocalized throughout the backbone of PA. As the degree of conjugation continues to increase the number of π-bonding molecular orbitals increases and overlap until they begin to resemble the band like structure observed in inorganic semiconductors. Consequently, as the conjugation increases, the highest occupied molecular orbital (HOMO) increases in energy whereas the lowest unoccupied molecular orbital (LUMO) decreases in energy, resulting in a reduction in the bandgap. However, due to difference between single and double bond length (1.35 Å and 1.45 Å) respectively, geometric distortion within PA backbone (Peirel's distortion) occurs giving rise to a splitting of energy levels resulting in the formation of a band gap. This band gap is what provide organic semiconductors their semiconducting like properties.[10]

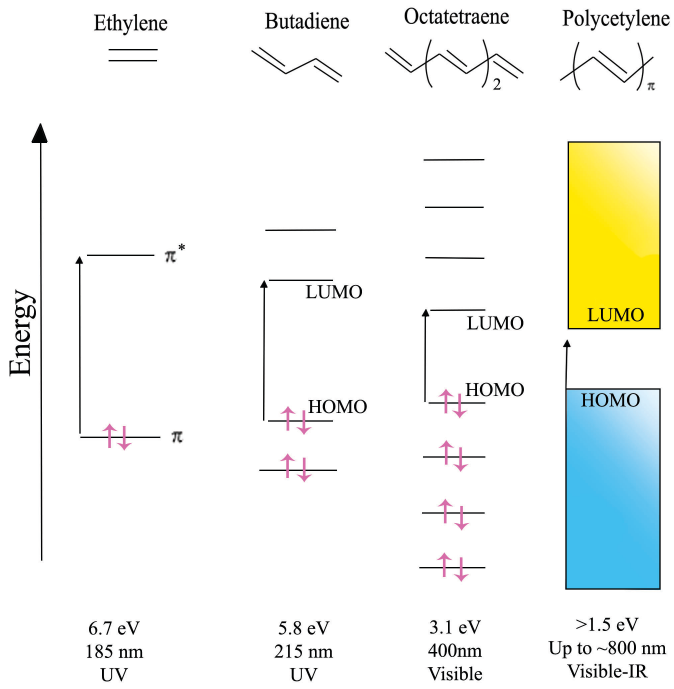

Figure 2. Impact of increasing the degree of conjugation on the energy levels of PA.

The optical and electronic properties is also known to be impacted by increase in conjugation. As depicted in **figure 3**, the as conjugation length increases with the increase in number of repeat units of oligofluorene and the absorption onset gradually red shifts towards lower energy. In addition, as the number of conjugated repeat units approaches approximately seven (OFV7) to eight (OFV8) repeat units the increase in conjugation does not impact the optical and electronic properties of the material.[11] This intrinsic property is known as the effective conjugation length. Additionally, the effective conjugation length of oligofluorene grows until it begins to twist within the backbone due to steric hinderance. The twisting in the backbone causes poor delocalization of π electrons along the entire oligofluorene backbone leading towards delocalization of π electrons over relative chain lengths.[12] Consequently, any increase in conjugation beyond the effective conjugation length does not impact the optical and electronic properties i.e., band gap and absorption, of oligofluorene. The effective conjugation length can vary between different materials and range from seven repeat units and beyond.[13] This presents the opportunity to tune the optical and electronic properties via substituent manipulation. Tuning these properties through modular synthesis and chemical modification provides a platform for molecular engineering towards desired semiconductor properties for organic electronic applications.

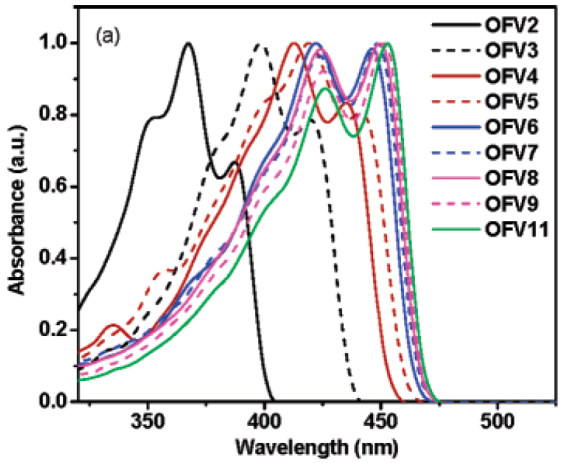

Figure 3. Impact of increasing the degree of conjugation on the optical properties of PA.

Taking advantage of systems that favor the quinoid state over the aromatic state is a strategy utilized for molecularly engineering desired semiconducting properties such as narrow band gaps.[14,15] Highly conjugated polymers e.g. polythiophene, polyphenylene, etc., are bound together through alternating single and double carbon-carbon bonds. This gives rise to two possible non-degenerate ground state resonance structures (**figure 4**). The aromatic state maintains aromaticity keeping π electrons localized within the ring system. As π electrons delocalize along the backbone, single bonds are converted to double bonds giving rise to a less stable, higher energy quinoidal state[16]. The quinoidal state is a not as stable energetically due increase in rigid backbone and loss in stabilization energy. This increase in planarization the polymer backbone decreases steric twisting leading to longer effective conjugation lengths. Introducing substituents that are less aromatic such as vinylene, thiophene, and furan can be utilized to achieve materials with relatively small band gaps. Take into consideration polyisothianapthene (PITN) which has a relatively narrow band gap of 1 eV (**figure 4**). The narrow band gap of PITN is due to the larger aromatic resonance energy of benzene in comparison to thiophene (1.56 and 1.26 eV,

respectively). As a result, it is more favorable for the quinoid to form along the main chain of PITN, and maintain the aromaticity of benzene affording PITN a relatively narrow band gap.

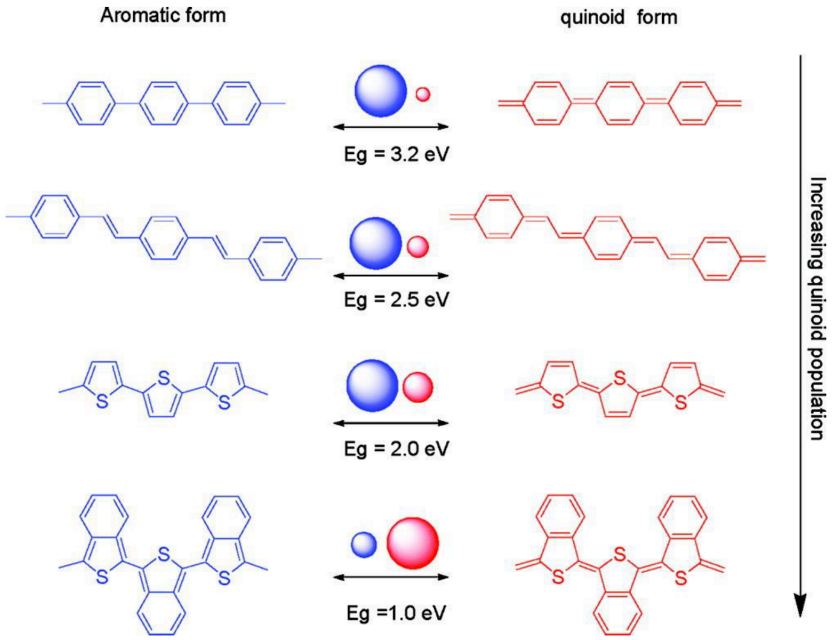

Figure 4. Incorporation of less aromatic substituents impact on narrowing of the band gap.

The properties of organic semiconductor i.e. polymer and small molecule properties can be additionally tuned via incorporation of various substituents such as fused ring systems[16]. Traditionally, introducing electron rich and electron deficient substituents has served as an effective strategy towards tuning the HOMO and LUMO levels, respectively. This tuning of the frontier molecular orbital (HOMO and LUMO) using different combinations of donor-acceptor systems to give rise to new energy levels (**figure 5**). In these the donor-acceptor systems, the LUMO level is lower in energy than that of donor or acceptor moiety, while the HOMO is higher in energy than either the donor or the acceptor leading to a narrowing of the band gap. HOMO of the donor influences the donor-acceptor

system (polymer) HOMO level whereas the LUMO of the acceptor primarily influences the LUMO of the donor-acceptor system. Thus, strategically selecting appropriate donor and acceptor moieties enables the manipulation of the polymers' energy levels for structure/property studies and their fine tuning for specific applications such as OLEDs, OFETs, and OSCs.

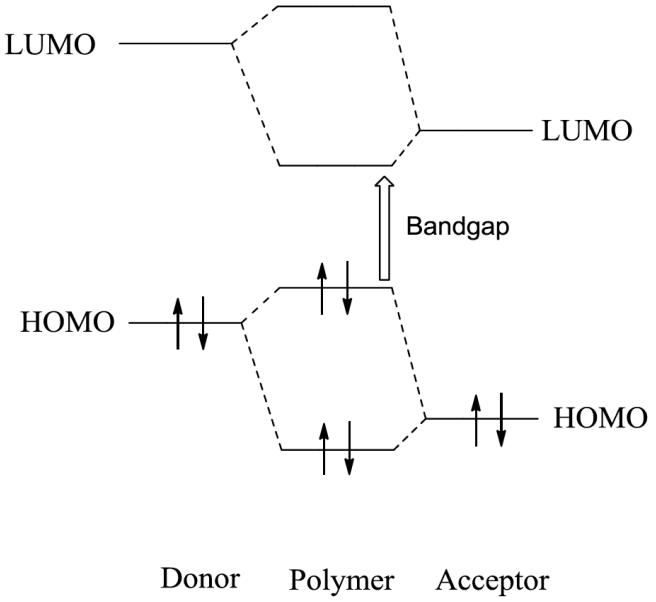

Figure 5. Donor and acceptor frontier molecular orbital mixing giving rise to a new set of energy levels.

Some of the more commonly used donors and acceptors are depicted in **figure 6**. Molecularly, donor moieties with deep HOMO levels are preferred as donors with high HOMO levels can readily react with oxygen. This leads to oxidative instability due removal of electron from the HOMO level. This has been observed in the case of poly(3-alkylthiophene) (**figure 5**).[17] Additionally, strategically selected acceptor moieties (**figure 6**) with LUMO levels -3.5 eV to -3.8 eV are preferred to have good energy level offset when paired with common n-type materials such as PCBM and ITIC.

The donor and acceptor moieties illustrated in figure 6 also possess "R" group that indicate generic (alkyl) side chains. The use of alkyl chains has traditionally been used to improve the solubility of π conjugated materials. More specifically, the use of alkyl side chains along the backbone of π-conjugated polymers improve intermolecular interactions with solvent molecules by disrupting π-π stacking between polymer chains. Thereby, improving the solubility and film forming ability of the polymers. They also have significant impacts on the solid state crystallinity of polymers.[18]

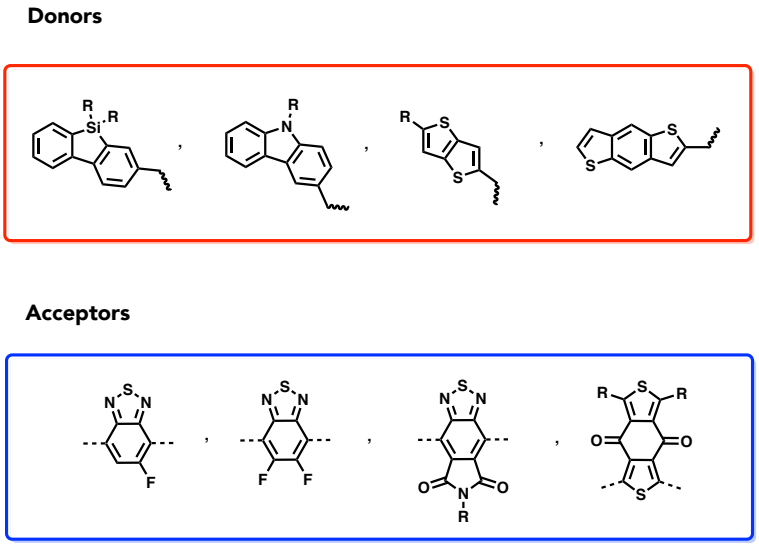

Figure 6. Example of commonly used donors and acceptors.

The influence of alkyl chains on the polymers' properties varies based on chain length, odd-even effects, and alkyl placement etc.[19,18] These effects can be significant to the molecular packing and charge transport properties of organic semiconductors in the solid state. Studies display that shorter alkyl chains tend to favor enhanced crystallinity and order in the solid state however, there are tradeoffs. Shorter chains do not impart solubility to polymeric conjugated materials in common organic solvents hindering solution

processing and producing poor morphological characteristics.[20,19] In contrast, longer alkyl chains increase the solubility but decrease crystallinity and ordering in the solid state.[18] Efforts to remedy this tradeoff has been to append short branched alkyl chains to strike the balance between good solubility in common organic solvents and the favorable π-π stacking between polymer chains needed for improved solid state packing. Odd-even effect have been shown to strongly correspond with solid state packing characteristics.[21] Even numbered *n*-alkanes have most favorable intermolecular interactions occurring at both ends of the alkane chain, albeit odd number n-alkane chains have only intermolecular interactions at one end with long distant interaction at the opposite end (**figure 7**).[21,22] Consequently, this leads towards less efficient solid-state packing and potentially poorer charge transport. Strategic placement of the alkyl chains on the donor and acceptor along the polymer backbone can reduce side chain impedance on the π-π stacking characteristics of the semiconducting material. Specifically, one method to circumvent steric hinderance has been through molecular docking.[23] This strategy has been utilized by moving alkyl chains from smaller sized units (red units, **figure 7**) and appending them to larger units (blue units). As a result, smaller sized aromatic units will dock into larger aromatic moieties allowing for more induced molecular ordering and decrease in reorganization energy resulting in higher mobilities (**figure 7**).[23,22]

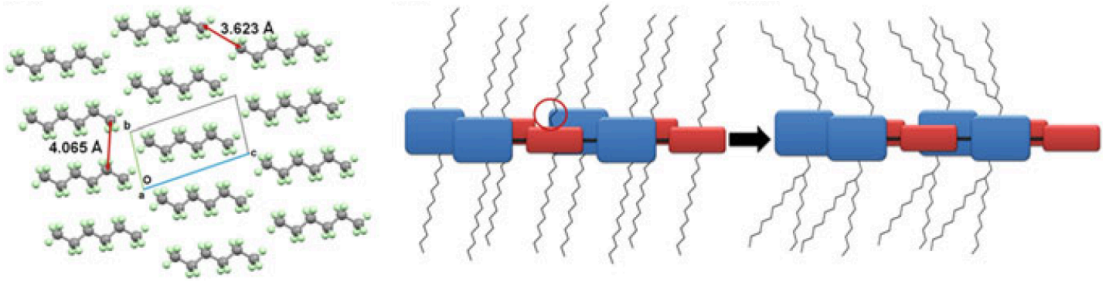

Figure 7. Adapted from ref. 14.

SECTION TWO – DEVELOPMENT OF MATERIALS FOR ORGANIC PHOTOVOLTAIC CELLS

1.2.1 – BENZOBISAZOLES: BENZOBISOXAZOLE AND BENZOBISTHIAZOLE

Organic semiconductor materials have represented a new frontier for organic photovoltaic technologies. In particular, benzobisazoles are a unique class of semiconducting materials that exhibit good electron transport and photoluminescne properties. In the 1980s, benzobisazoles were investigated for use as high performance materials for the United States Air Force.[24,19] The planar, rigid structure of the benzobisazoles ring system produces materials with high thermal, mechanical, oxidative stability. In addition, they exhibit good electron transport and photoluminescence properties. These desirable physical properties of polybenzobisazoles enable the creation of high-performance materials such as Zylon® and Kevlar® suitable material for several industrial applications.[25,26] However, harsh reaction conditions required for polybenzobisazoles (PBA) synthesis limited their application and utility. Historically, benzobisazole based materials were synthesized via acid catalyzed condensation of with 2,5-diamino-1,4-benzenedithiol or 2,4-diaminoresorcinol with a dicarboxylic acid functionalized moiety in acidic media at high reaction temperatures. (**scheme 1**).

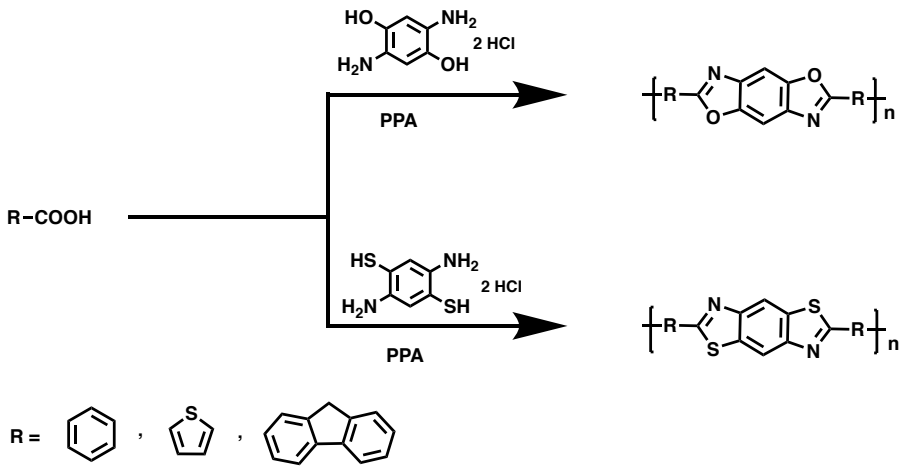

Scheme 1. Generic synthesis of polybenzobisazoles.

The harsh reaction conditions performed by Wolfe et al. restricted functional tolerance, thus limiting substrate scope and design. In order to take advantage of the physical properties PBAs possess, efforts to remedy the synthetic limitations have been explored by several groups. Substituting carboxylic acids with acid chlorides affords slightly milder reaction conditions and lower reaction temperature (>200°C) (**scheme 2**)[27,28] allowed for the incorporation of more functional groups. In addition, the use of functionalized aldehydes as a reaction handle was explored by Jenekhe and coworkers in efforts to synthesize polybenzobithiazoles.[25,26,29,30] They utilized one-pot acid-catalyzed imine formation from aromatic aldehydes followed by cyclo-condensation to yield the benzobisthiazole. Unfortunately, these reactions conditions lead to mediocre yields.[30]

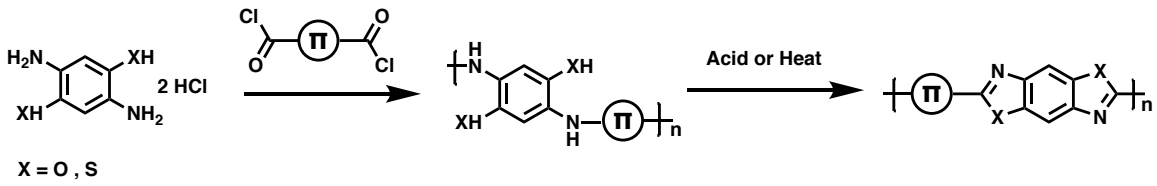

Scheme 2. Generic synthesis for milder reaction condition of Wolfe BBA condensation.

In recent years, progress has been made by the Jeffries-EL group to develop more versatile methods for the synthesis of PBAs. Dr. Jared Mike established a mild synthesis of benzobisoxazole and benzobisthiazole via a Lewis acid catalyzed condensation of diaminohydroquinone precursors (**scheme 3**). Instead of carboxylic acid or acid chloride functional groups as condensation handles, this synthetic route utilizes orthoester functional groups. This condensation methodology requires lower reaction temperatures (50 °C - 60 °C) and provides an opportunity for greater functional group tolerance toward greater synthetic practicality.[31,32]

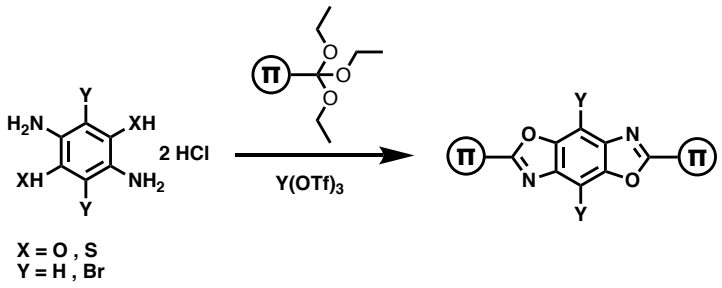

Scheme 3. Lewis acid catalyzed condensation of benzobisazole based organic semiconductors.

Using the Jeffries-EL – Mike orthoester condensation as a synthetic utility our group has been able to develop new functionalized benzobisazole semiconductor materials for organic electronic applications. This approach has enabled the synthesis of functionalized BBA building blocks based on vinylene linked its isomeric (*cis* and *trans*) BBO and the isoelectronic BBZT.[32] However, when employing these vinylene linked BBO materials as donor materials in BHJ OPVs they exhibited low photovoltaic performances.

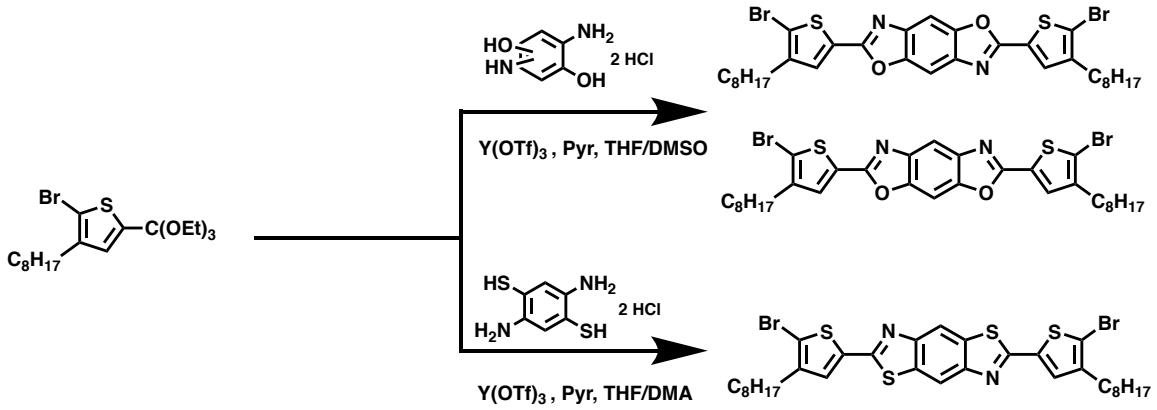

Scheme 4. Synthesis of 2,6-diarylbenzobisazole based monomers via Jeffries-EL – Mike orthoester condensation.

Moving away from vinylene linked BBO based materials, halogenated 2,6-diarylbenzobiazoles were synthesized via Jeffries-EL – Mike orthoester condensation (**Scheme 4**).[32] The use of 2,6-diarylbenzobisazoles allow for the synthetic availability for polymerization through the 2,6 axis by forming single bonds. The inclusion of alkyl chains made these benzobisazole based polymers solution processable, as needed for organic electronic applications. In addition, an alteration of the Jeffries-EL – Mike orthoester condensation was investigated by Dr. Tlach. 4,8-dibromoBBO were synthesized in efforts to expand the synthetic utility and scope of BBO based organic semiconducting materials (**figure 8**). Incorporating a halogenated handle at the 4,8 position of the BBO core allows for the creation of two dimensional cross-conjugated "cruciform" small molecules and polymers.[33,34,35,36,37] As a result, the cruciform motif allowed for our group to take advantage of cross-conjugated functionalization through the 2,6-axis and 4,8-axis providing more opportunity for tuning of opto-electronic and solubilizing properties. This enables for the development of a deeper understanding of the structure property

relationship of BBO as a potential organic semiconducting material for organic electronic applications.

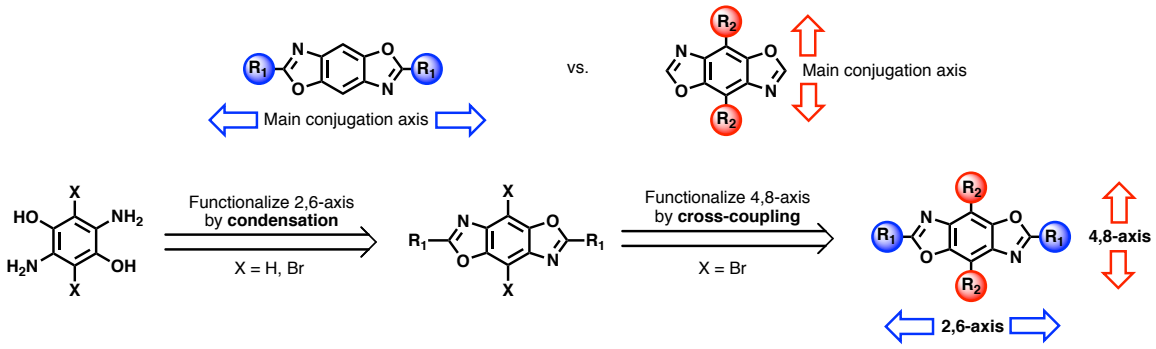

Figure 8. Functionalization of cross-conjugated BBOs via 2,6 and 4,8-axis.

In general, cruciforms are cross-conjugated small molecules consisting of spatially separated arms connected through a central aromatic core.[38,39,40,41] These spatially separated conjugation pathways give rise of two spatial separated frontier molecular orbitals (FMOs) that can be tuned independently. Dr. Tlach and co-workers investigated the influence of conjugation axis on the opto-electronic properties of 2,6-axis and 4,8-axis substituted BBO cruciforms.[34] Our group found that localization of the LUMO and HOMO occurs when relatively electron deficient substituents and electron rich substituents are placed on the 2,6-axis and 4,8-axis, respectively. As a result, through strategically manipulating substituents via 2,6-axis and 4,8-axis it is feasible to independently tune the HOMO and LUMO energy levels towards desired band gaps for effective absorption. The author of this dissertation also investigated this unique property of BBOs through the design and synthesis of 2,4,6,8-tetrarylBBO cruciform in efforts to tune the opto-electronic properties for organic photovoltaic applications.

1.2.2 – SELECT DONOR MATERIALS FOR OPVs: NAPHTHODIFURAN

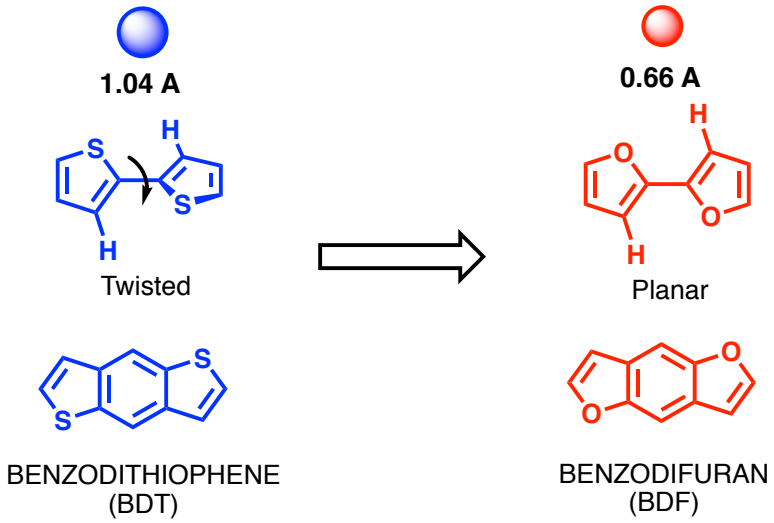

Figure 9. Fused heterocyclic ring systems containing thiophene and furan based analogs.

Several groups have investigated narrow band gap donor and acceptor copolymers with benzodithiophene (BDT) moiety as a donor due to these copolymers superior power conversion efficiencies when incorporating BDT.[42,43,44] In efforts to further improve the properties and performance of BDT based polymers, groups have assessed the influence of the heteroatom effect via substituting sulfur for oxygen to create benzodifuran (BDF) analogs (**figure 9**).[45,46,47] These BDF analogs are less twisted due to the smaller atomic radius of oxygen in comparison to sulfur. While furan based systems are isoelectronic to thiophene based systems, the smaller atomic radius of oxygen helps to lower Dewar resonance energy promoting the formation of the quinoidal state. Additionally, the use of furan based analogs have been shown to have deeper HOMO and LUMO levels in contrast to its thiophene counterparts which is advantageous for photovoltaic parameters.[48]

Attempts to improve upon these furan-based structures has been through the examination of tetracyclic naphthodifurans (NDF). NDF moieties are rigid coplanar

structures known to improve π-electron delocalization leading to better charger carrier mobilities with in a polymer system.[49,50] The enhanced co-planar structure of NDF based materials have resulted in high mobilities of 5.31 cm^2 V^{-1} s^{-1}.[51] These characteristics NDF based materials exhibit make them desirable candidates for organic photovoltaic applications. The incorporation of NDF based materials into OSCs is later discussed by the author of this dissertation.

SECTION THREE - ORGANIC PHOTOVOLTAIC CELLS

1.3.1 OPERATING PRINCIPLES – EXCITON GENERATION, DIFFUSION AND DISSOCIATION

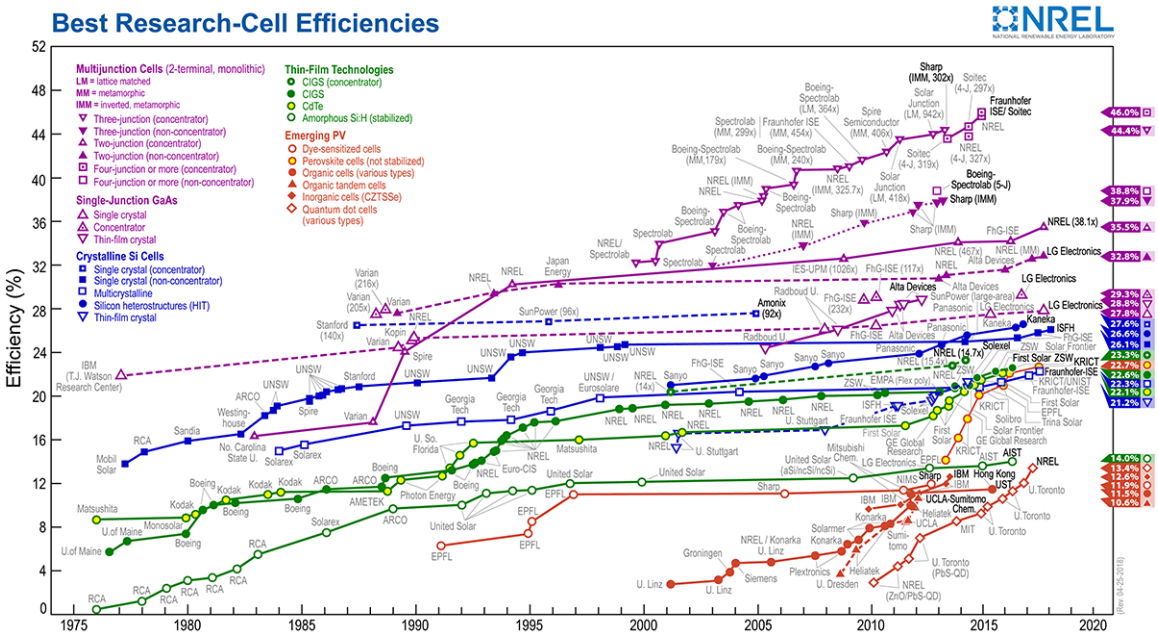

Figure 10. Certified best power conversion efficiency for a various number of photovoltaics.

Currently, the most efficient solar cells are silicon based (**figure 10**).[52] However, silicon rather high cost and elaborate fabrication conditions hold back their wide spread adoption. Organic solar cells represent a relatively low-cost alternative to silicon with projected cost of \$50/m^2 in contrast to \$350/m^2 for inorganic solar cells. Based on these

upsides and advantages organic solar cells have to offer, there has been a spur in research and development with OSC PCEs achieving 12-15%.[43,53,54] Investigations into new material horizons and device engineering can lead towards further improvement on organic solar cell performance and commercialization.

Upon exposure of a solar cell to light, a photon is absorbed initiating the exciton dissociation process. Within the absorbing layer (active layer) of the solar cell, an electron is excited from the electron donor (p-type) material HOMO to its LUMO (**figure 11**). This excitation forms a coulombically bound electron-hole pair called an exciton (step 1, **figure 11**).[55] The excitons then drift to the donor-acceptor interface to form charge transfer state complex (step 2-3, **figure 11**). Upon exciton migration to the donor-acceptor heterojunction, the exciton separates with electron transfer from the LUMO of the donor to the LUMO of the acceptor (n-type) and the hole remain on the HOMO of the donor. The exciton binding energy for organic semiconductors is much higher than its silicon counterparts with exciton binding energy of 0.1-1.4 eV and 0.1 eV or less for organic semiconductors and silicon, respectively.[56,57] As a result, the charge transfer state must be energetically more favorable in order to overcome this binding energy.[58]

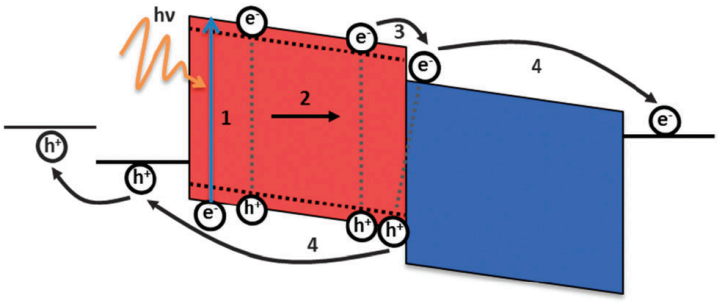

Figure 11. Exciton dissociation process within and organic solar cell (adapted from ref 1).

The dielectric constant for organic based semiconductor materials is lower than their silicon and inorganic counterparts.[1] Consequently, the extraction of electron and holes for current collection is more tenuous in comparison to inorganic based materials. The charge transfer process is a relatively fast process ~45 fs.[59] Electron-hole recombination is competing pathway occurring at a ~1 ns timescale preventing charge collection and extraction. With charge transfer occurring at a faster time scale than recombination it is possible for charge collection to occur efficiently in organic based materials. When excitons efficiently dissociate into free charge carriers, the distance required for free charge carriers to travel through the active layer heterojunction to their respective electrodes before recombination has been determined to be 10-20 nm (exciton diffusion length).[58,57] This eludes to the importance of having optimal morphology and phase separation between the donor and acceptor material to achieve optimal charge transport. The influence of morphology will be discussed later in more detail.

1.3.2. CHARGE COLLECTION – DRIFT AND DIFFUSION CURRENT

Free charge carriers that contribute to the current within a solar cell are electron and holes present in the conduction and valence band, respectively. Drift and diffusion currents are of the many driving forces for charge collection in solar cells. Upon generation of free charge carriers, electron and holes will be collected at different points in the active layer via selective metal contacts (electrodes). This selectivity is a property of the contact that will only allow electrons to be collected while blocking other types of charge carriers i.e. holes, and vise versa.

Among the charge transport driving forces, drift current arises from a built-up potential gradient within the solar cell allowing for charge carriers to move to their respective electrodes for charge collection. The choice of contacts heavily influences this charge transport mechanism. Traditionally, high work function anode (-4.7 eV) such as indium tin oxide (ITO), and a low work function cathode (-4.2 eV) such as aluminum are chosen as contacts for OSCs. As a result, this difference between the high and low work function creates a buildup of an internal electric field with the solar cell. Exposure of the solar cell to outside bias induces a change in the internal electric field of the solar causing a rise in drift current with electrons and holes drifting towards their respective electrodes (**figure 12**).[58] When this internal electric field is large, drift current is dominant.

Additionally, the accumulation of charge carrier concentration leads to diffusion current. Within the active layer of a solar cell at the donor-acceptor interface (heterojunction) excitons are generated. This leads to an increase in electron and hole concentration at the heterojunction. Therefore, when the internal electric field is approximately zero via an externally applied bias, electrons and holes will diffuse away from the heterojunction to regions of lower concentration giving rise to diffusion current (**figure 12**).[58] The efficiency of this process is in a delicate balance and is still not well understood in literature.

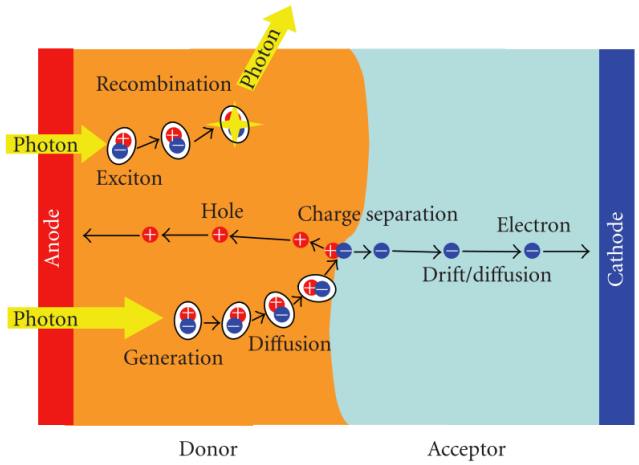

Figure 12. General charge generation and separation in solar cells (adapted from ref. 54).

1.3.3 ANODE AND CATHODE INTERLAYERS – OHMIC CONTACT AND SCHOTTKY-BARRIER

The efficiency of charge collection inside a solar cell has been shown to be influenced by efficient alignment of the anode and cathode work function with the p-type and n-type material, respectively.[58,60] Hwang et al. and Ishii et al. have illustrated metal-organic semiconductor interfaces and it has been shown to introduce complexities complicating charge extraction process in organic solar cells.[61,62] Upon depositing an organic molecule on the metal surface (in this case anode or electrode), interfacial disorder and reorganization of the metal surface electronic structure (pillow effect) occurs. These drawbacks contribute to the energetic barrier at the metal-organic interface leading to increased resistance and ultimately poor charge extraction. The introduction of interlayers has played an important role in decreasing the energetic barrier (Schottky barrier) between electrode contacts and the organic semiconductor active layer.[63] The role of interlayers has led towards better energetic alignment and lower resistance for efficient charge collection

(ohmic contact).[63,64] Frequently, hole (anode interlayer) and electron (cathode interlayer) transport interlayers have been used for this purpose.

Hole transport layers (HTLs) have been incorporated between the ITO anode and the organic active layer in efforts to remedy the aforementioned issues that have arisen. Historically, poly(3,4-ethylenedioxythiophene) - polystyrene (PEDOT: PSS) has been used as a HTL in organic solar cells. PEDOT:PSS has displayed beneficial properties for improving ohmic contact, open circuit voltage, and surface defects at the ITO surface.[65,63,66,67] Despite these benefits PEDOT:PSS has to offer, its acidic nature is known to corrode the ITO surface leading to chemical instability at the ITO anode PEDOT:PSS interface.[68] Efforts to resolve this issue have been examined through investigating the immersion of PEDOT:PSS films processed by spin coating various mixtures of water and solvents of different polarities.[69] Other HTLs have also been considered to improve ohmic contact. These HTLs include but not limited to vanadium oxide (V_2O_5), molybdenum oxide (MoO_3), polyaniline-poly(styrene sulfonate) (PANI-PSS), poly[(9,9-bis(3'-(N,N-dimethylamino)propyl)-2,7-fluorene)-alt-2,7-(9,9-dioctylfluorene)] (PFN).[70,71]

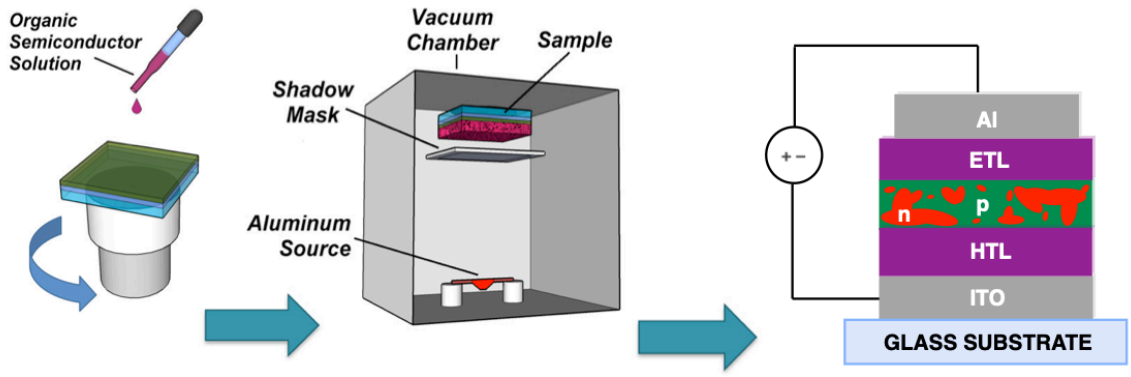

Figure 13. General device fabrication of organic solar cells.

Electron transport layers (ETLs) are incorporated into between the organic active layer and the aluminum cathode. Traditionally, the deposition of aluminum requires thermal evaporation (**figure 13**). The direction deposition of Al onto organic active layer leads to Al diffusing through the active layer causing surface defects and inefficient charge collection across the metal-organic semiconductor interface. Additionally, the thermal evaporation creates hot Al that is vacuum deposit potentially creating unwanted chemical binding and reactions to occur at the Al-organic semiconductor interface. Incorporation of ETL such as lithium fluoride (LiF), calcium, zinc oxide (ZnO), titanium oxide (TiO_x), and other transparent metal oxides has improved ohmic contact in OCSs leading towards improved efficiencies.[63,72] Water soluble polymers like PFN have been explored as well.

1.3.4 ABSORBING LAYER – P-TYPE AND N-TYPE MATERIALS

The absorbing layer (active layer) of OSC traditionally consist of p-type and n-type materials. When exposed to light, the active layer absorbs much of the visible spectrum converting incident photons to charge carriers for charge collection. Inside this active layer includes a delicate balance of p-type and n-type materials. To date, an insurmountable amount of research and development has gone into tailoring the properties of these materials for the improvement of OSC performance and stability.

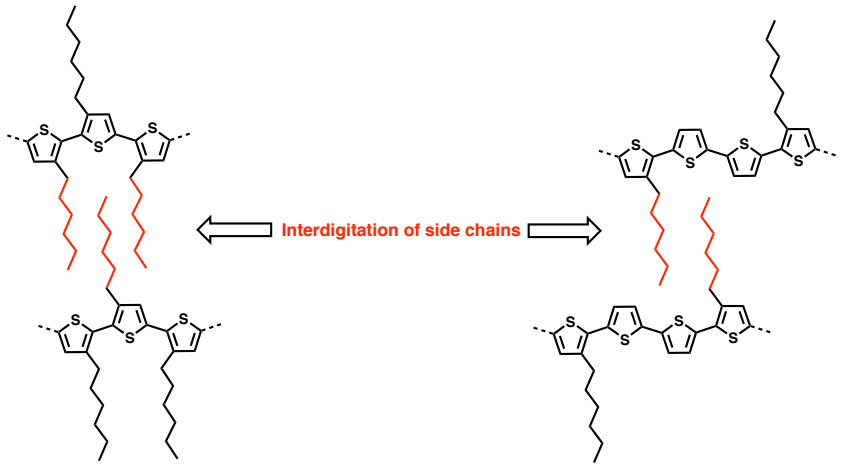

Figure 14. Examples of interdigitated side chains towards molecularly ordered polymer semiconductors.

P-type materials are the electron donors within OSCs and assist in the transport of holes to the HTL for further charge collection. There have been three main classes (generations) of p-type material development. From the early studies of first generation polyacetylene semiconducting materials, solution processable semiconductors have garnered attention. The emergence of second generation alkyl chain substituted poly(3-alkylthiophene) and alkylated poly(phenylene vinylene) allowed for improved solution processability and manipulation of molecular orientation which lead to the third generation of organic semiconductors.[73] The investigation of "head-to-head" and "head-to-tail" alkyl polythiophenes ushered in the investigation of regioselectivity impacts of polythiophene performance in organic electronic devices.[74] Strategic placement of alkyl chains along the polythiophene backbone allows for interdigitation of side chain alkyl group allowing for increased molecular ordering between polymer chains (**figure 14**).[75,76] This strategy led to a boost in charge carrier mobilities and performance in organic electronic devices, i.e. OSCs. Despite these developments, presence of paracrystalline disorder among alkyl polythiophene based semiconductors led to limited performance.[76] The desire for better

material performance sparked the second sub group of among the third generation of organic semiconductors towards the creation of donor-acceptor (D-A) copolymers and small molecules.[77] This combination of D-A moieties enabled better tuning of opto-electronic and macromolecular properties though modular synthesis for improved material performance in OSCs.[78,79,80] Some examples include polythieno[3,4-*b*]-thiophene-*co*-benzothiophene (PTB7), 5,5-bis((4-(7-hexylthiophen-2-yl)thiophen-2-yl)-[1,2,5]thiadiazolo[3,4-c]pyridine)-3-3-di-2-ethylhexylsilylene-2,2-bithiophene (DTS($PTTh_2$)$_2$ and poly[(2,6-4,8-bis(5-(2-ethylhexyl)thiophen-2-yl)-benzo[1,2-b:4,5-b']dithiophene))-alt-(5,5-(1',3'-di-2-thienyl-5',7'-bis(2-ethylhexy)benzo[1',2'-c:4',5'-c']dithiophene-4,8-dione)] (PBDB-T, PCE-12) (**figure 15**). The development of these three generations of organic semiconductors have led to a better understanding of the role p-type materials have played in OSC and has informed the design of n-type materials for OSC applications.

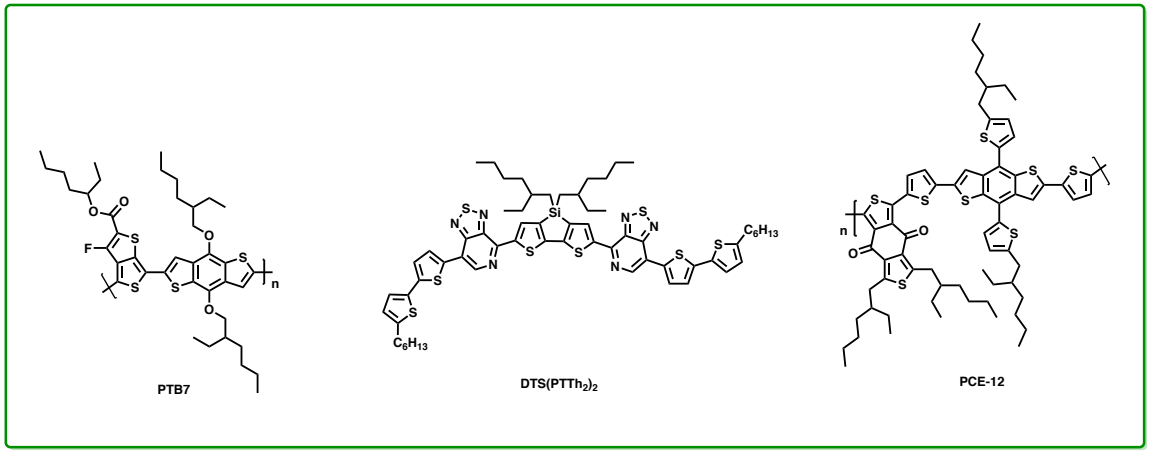

Figure 15. Molecular structures of current benchmark p-type materials.

Of late, N-type materials have garnered just as much attention and importance as p-type materials. To have efficient charge separation towards the generation of free charge

carriers n-type materials have to possess a low-lying LUMO in relation to p-type material LUMO (**figure 16**).[81] Conventionally, fullerene-based n-type materials were used in combination with p-type materials to undergo photoinduced electron transfer towards charge generation. In particular [6,6]-phenyl- C_{61}-butyric acid methyl ester ($PC_{61}BM$) and [6,6]-phenyl- C_{71}-butyric acid methyl ester ($PC_{71}BM$) when blended with select donors have displayed excellent OSC performance with PCEs at 10%-12%.[82–84] The delocalization of LUMO along the fullerene allow the creation of potential charge generation and extraction pathways due to its 3-deminstional nature. In addition, fullerene exhibit high electron mobilities and energy levels suitable for many p-type materials.[85]

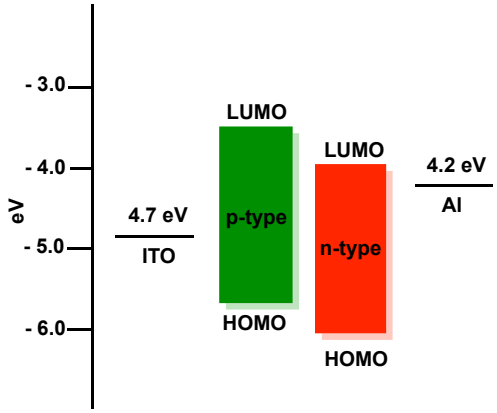

Figure 16. Generic energy level offset diagram for p-type and n-type materials for OSCs.

Despite these successes, fullerene-based n-type materials have presented some drawbacks. Fullerene illustrated limited synthetic utility (elaborate purification and synthetic processes) and tunability; thermal and photo instability; and poor UV-VIS/NIR absorption profile ultimately limiting OSC short-circuit current (Jsc).[86] As a result, the rise of non-fullerene alternatives (NFAs) gained interest in efforts to remedy fullerene drawbacks. Generally, organic NFAs present more facile chemical modification allowing

better tuning of opto-electronic properties and improved UV-VIS/NIR absorptivity. One of the most commonly used NFAs is 3,9-bis(2-methylene-(3-(1,1-dicyanomethylene)-indanone))-5,5,11,11-tetrakis(5-hexylthienyl)-dithieno[2,3-d:2',3'-d']-s-indaceno[1,2-b:5,6-b']dithiophene (ITIC-Th) and perylene diimide (PDI) (**figure 17**).

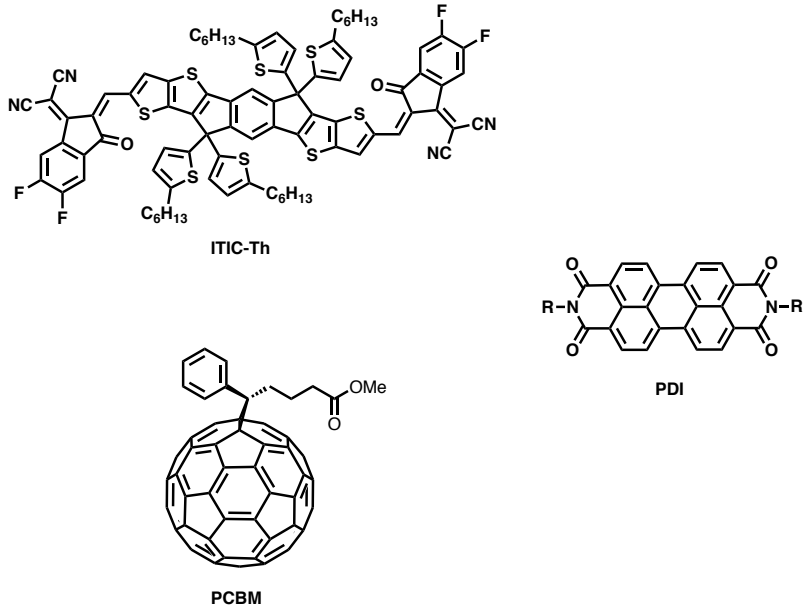

Figure 17. Molecular structures of commonly used n-type materials, ITIC-Th, PDI, and PCBM.

1.3.5. ORGANIC SOLAR CELLS – PLANAR VS. BULK HETEROJUNCTION ARCHITECTURE

Organic semiconductors were initially evaluated in a bilayer configuration in 1986 by Tang and coworkers. This bilayer configuration is also known as planar heterojunction architecture (PHJ), consisting of two layers of organic semiconductor materials (p-type and n-type) with good energy level alignment (**figure 18**).[87,88] In order for favorable absorption of the solar spectrum the active layer of p-type and n-type materials need to be adequately thick enough. However, the thick layers needed to achieve sufficient absorption for PHJ architecture lead to inefficient charge generation due to organic semiconductors

intrinsically lower dielectric constants, lower charge mobilities, and short exciton diffusion lengths.[89] Due to PHJ shortcomings, PHJ based solar cells faced limited charge generation and PCEs.

Efforts to solve this drawback, nearly a decade later Heeger and coworkers developed the bulk heterojunction architecture (BHJ, **figure 18**).[90] BHJ architecture enhanced efficiencies via introducing a bicontinuous network of intermixed p-type and n-type heterojunction active layer. Consequently, the presence of efficient phase separation and domain sizes within the exciton diffusion length of organic semiconductors improved the likelihood for enhanced charge separation and extraction towards improved PCEs.[91] The fabrication of the BHJ architecture requires spin-casting p-type and n-type blends. To date BHJ is the conventional architecture of choice for many OSCs.

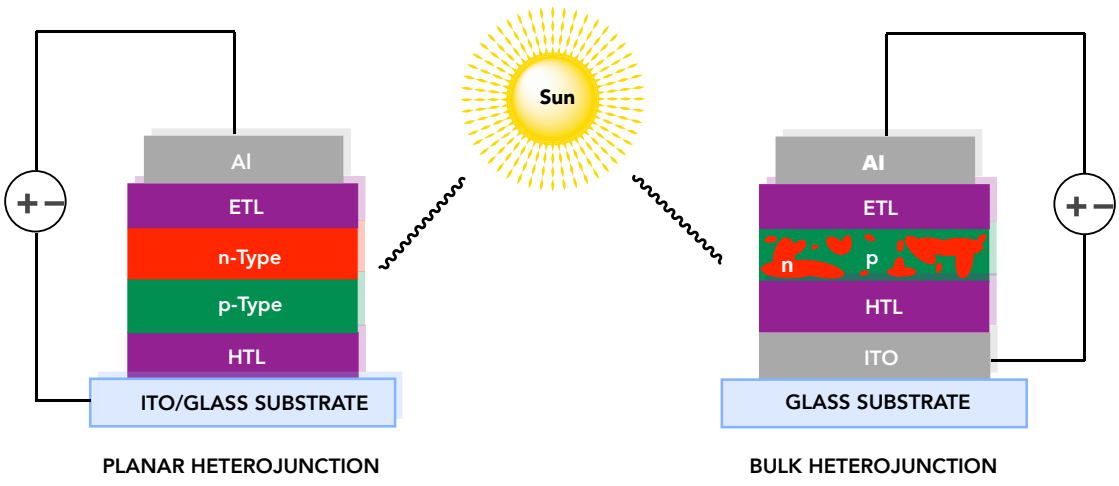

Figure 18. Device architecture for PHJ (left) and BHJ (right).

1.3.6. CHARACTERIZATION OF SOLAR CELLS – PCE, VOC, JSC, FF

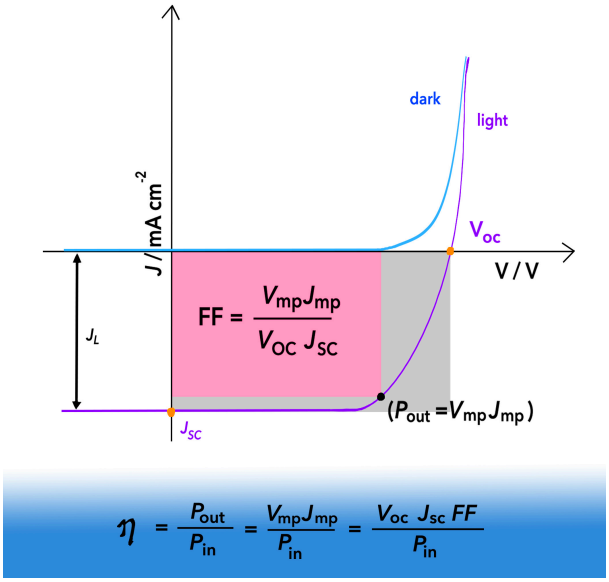

Figure 19. Voltage vs. current density (j vs. V) for a solar cell.

The photovoltaic performance of a solar cell has been characterized by the power conversion efficiency (PCE). Three important components influence the PCE (η) such as, open circuit voltage (V_{oc}), short circuit density (J_{sc}), and fill factor (FF). These characteristics are utilized to evaluate the PCE via the following equation.[92]

$$\eta = \frac{JscVocJsc}{Pin}$$

The PCE is also represented and illustrated by current density vs voltage curve (**figure 19**) for solar cell architectures represented in **figure 18**. More specifically, the V_{oc} has been shown to be determined by the difference in work function of the contacts when the current is zero. This represents the maximum voltage provided by a solar cell.[92,93] In addition under ohmic contact, V_{oc} has also shown to be influenced and partially determined by the difference between the HOMO and LUMO of the donor and acceptor, respectively. Of late, with V_{oc} being one of the prominent limitations preventing superior performance for OSCs, rigorous research has gone into gaining a deeper understanding of the origins of

V_{oc} in OSCs. In addition to the aforementioned, many factors have been shown to directly or indirectly influence the V_{oc} i.e. defect states and crystallinity, charge transfer states, donor-acceptor interface area, density of states morphology, and recombination. (**figure 20**).[93]

Figure 20. Parameters impacting open circuit voltage (V_{oc}) in OSCs (Adapted from ref. 89).

In the absence of no external field applied (voltage is zero) there is a presence of charges drifting or short circuit current density (J_{sc}) due to a presence of an internal field. The J_{sc} constitutes the collective amount of charge carriers produced and accumulated by the electrode within the solar cell. J_{sc} has also been shown to be influenced by the charge transport pathways within the solar cell, absorption coefficient of p-type and n-type materials, high charge carrier mobilities, and optimal nanoscale phase separation of p-type and n-type active layer blends.

The fill factor (FF) of a solar cell is represented by the pink and gray area in **figure 19** and illustrates the "squareness" of the J-V curve. The FF is defined by the following equation

$$FF = \frac{Jmp \times Vmp}{Jsc \times Voc}$$

where J_{mp} is the current density at maximum power point and V_{mp} is the voltage at maximum power point. As displayed, the FF is determined by the competition of the collection of photogenerated charge carriers and recombination of the photogenerated charge carriers back to the ground state.[1,92]

The external quantum efficiency (EQE) is a technique invaluable in understanding and evaluating the J-V characteristic of a solar cell. The EQE provides the ratio of the amount of photogenerated charge carriers collected by a solar cell versus the number of incident photons of a particular wavelength. This provides insight into the probability that upon the absorption of a single photon one electron will be photogenerated for charge collection towards an external circuit. The EQE outlines the efficiency of four major photovoltaic processes in OSCs such as charge separation, absorption, exciton diffusion, and charge collection, as defined by the following equation

$$EQE\ (\lambda) = \eta abs(\lambda) \times \eta diff(\lambda) \times \eta ct(\lambda) \times \eta coll(\lambda)$$

where ηabs is the photo-absorption coefficient, $\eta diff$ is the exciton diffusion efficiency of the p-type and n-type interface, ηct is the efficiency of charge transfer, $\eta coll$ is efficiency of charge collection, at λ wavelength respectively. EQE values close to 1 represent efficient charge generation and current collection at a particular wavelength. The increase in recombination leads to lower EQE less than 1 providing insight into inefficiency

in one of the four aforementioned photovoltaic processes. Other methods have been explored to further quantify and characterize OSC performance such as utilizing incident photon to electron conversion efficiency (ICPE) technique. The overall trends for EQE and ICPE should be comparative to the J_{sc}.

1.3.7. OPTIMIZATION OF ORGANIC SOLAR CELLS

The optimization of organic solar cell performance (PCE) consists of a various number of techniques and strategies towards improving photovoltaic parameters i.e. V_{oc}, J_{sc}, and FF. A delicate balance exists between these photovoltaic parameters and often present tradeoff in efforts to improve them. As mentioned above, the PCE represents the comprehensive parameter in evaluating OSC performance and is directly influenced by the V_{oc}, J_{sc}, and FF.

The V_{oc} is associated with the p-type/n-type energy gap, morphology, microstructure, defect states and crystallinity, and many other factors.[93,94] The choice of n-type material (acceptor) has been utilized as a strategy to improve V_{oc}. Research has illustrated that for OSCs, V_{oc} is directly related to the difference between the HOMO of p-type material (donor) and LUMO of n-type material (**figure 21**).[95] The rise of NFAs has presented opportunities for tuning energy levels NFAs through chemical modifications. This provides the ability to potentially tune and improve V_{oc} through choice of different acceptors. ITIC based NFAs are recent examples of NFAs through careful selection and can lead to maximum achievable V_{oc}. ITIC, ITIC-Th, and ITIC-2F, have LUMO of -3.83 eV, -3.93 eV, and -4.14 eV, respectively. Other methods such as improving defect states and crystallinity within the morphology of the active layer have been investigated towards

optimizing V_{oc}. The use of additives, annealing, and other active layer treatments have been essential in improving film formation and reducing defect states in order to reduce potential energy loss.

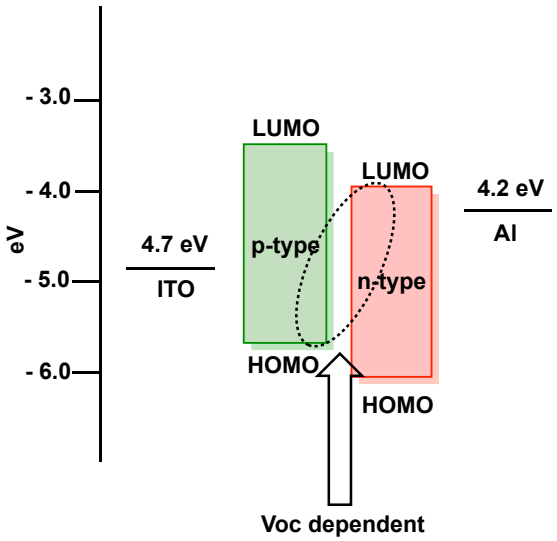

Figure 21. Open circuit voltage (V_{oc}) dependence on HOMO of p-type and LUMO of n-type energy gap in OSCs.

The J_{sc} has been shown to be dominated by the complete photovoltaic process i.e. generation of excitons, exciton diffusion and dissociation, free charge carrier transport and collection. These processes are found to be strongly dependent on active layer morphology.[94,96] There are a number of optimization strategies for improving the morphology towards highest possible J_{sc}. The use of solvent additives are an effective technique and strategy towards optimizing active layer blends solutions for better charge generation and collection. The role of solvent additives influences the kinetics of film formation leading towards reorganization of the active layer during film formation (**figure 22**).[94,97] Solvent additives preferentially prolong film drying leading towards more crystalline domains within the active layer. Consequently, this leads towards an improved

interpenetrating network of p-type and n-type materials for better mixing of active layer blends.

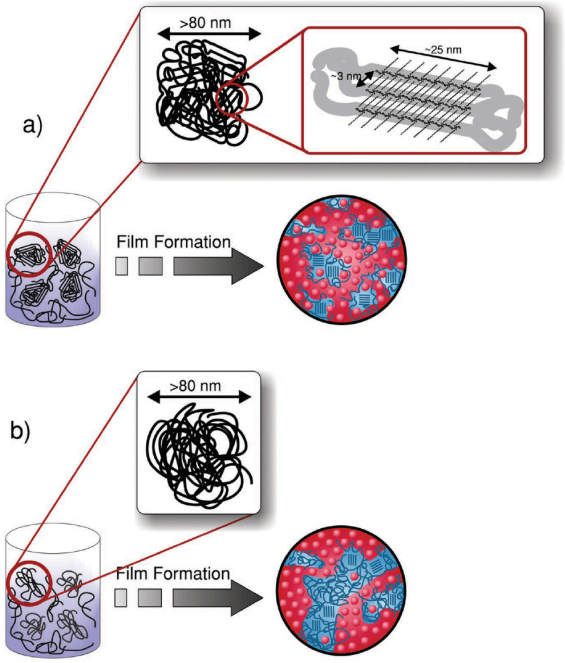

Figure 22. Illustration of polymer confirmation in solution towards film formation a) with additives b) without additives (adapted from ref. 90).

Heeger and co-workers presented the first class of effective solvent additives using alkane dithiols.[98] After extensive investigation into various alkane dithiols, 1,8-diiodooctane (DIO) proved to have the greatest impact on improving J_{sc} and ultimately PCEs.[99] Other commonly used additives reported as effective are 1,8-octanedithiol (ODT) and 1-chloronaphthalene (CN).[100–102] Following these findings, criteria arose for optimal additives for use in OSCs: higher boiling point than host processing solvent and selectively solvation of fullerene acceptors. To date, these criteria has influenced the use of numerous classes solvent additives i.e. halogenous and nonhalogenous additives, in enhancing J_{sc} and has informed the impact of morphological characteristics on more notably PCEs.

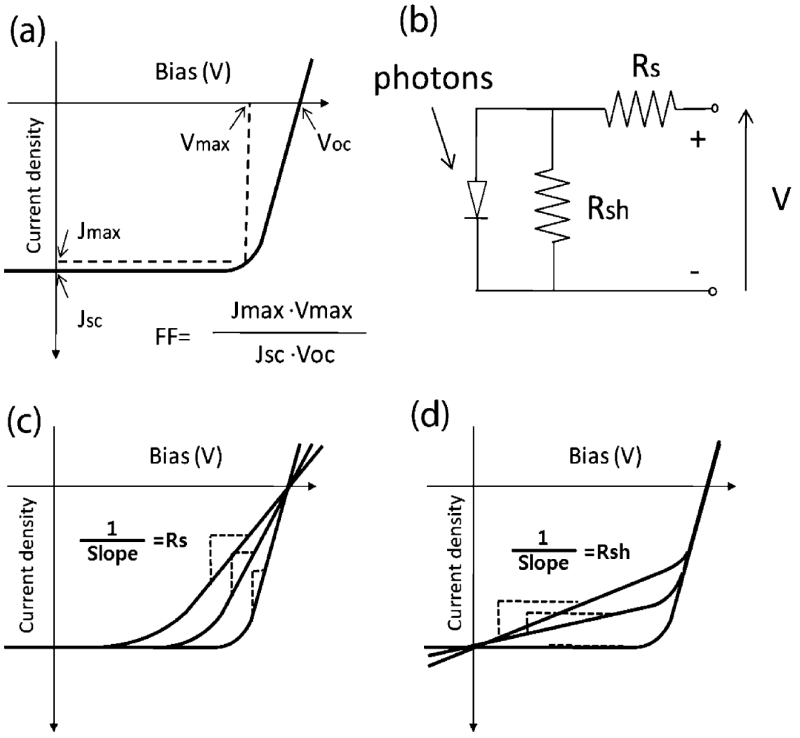

Figure 23. A) standard J-V curve defining FF. B) Conventional circuit model for a photovoltaic device. C) Influence of series resistance (R_s) on J-V cure. D) Influence of shunt resistance (R_{sh}) on J-V curve (adapted from ref. 101).

The FF represents the efficiency of how well photogenerated carrier are extracted from the OSC as well as indicates the squareness of the J-V curve (**figure 23**).[103] There are a number of factors that influence FF overall impacting the device performance of OSCs. Series resistance (R_s), shunt resistance (R_{sh}), and diode characteristics primarily influence FF. These three factors are in a delicate balance and influence each other in complex ways. R_s is impacted by the active layer thickness, intrinsic resistivity, morphology, and interface resistances between layers and contacts.[1,103] The lower the R_s leads towards less voltage and improved FF. R_{sh} specifies current leakage and losses present in the solar cell due to grain defects, trap states, impurities, and pinholes. The higher the R_{sh} the less amount of current leakage due to aforementioned drawbacks. In an ideal scenario, R_{sh} would approach

infinity with zero current loss. In other words, there is no current flow or loss through trap states, pin holes, etc.[103] The impacts of these defects can have a substantial impact on FF.

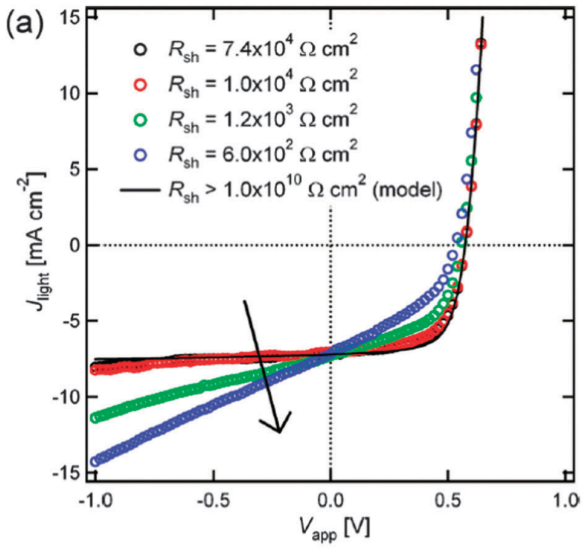

Figure 24. J-V curve of P3HT:PCBM. Various levels of R_{sh} illustrate influence on photovoltaic characteristics. Arrow pointing towards decreasing R_{sh}. (adapted from ref. 99).

Tumbleston and co-workers developed a model to assess the impact of R_{sh} on OSC device parameters.[103,104] They illustrated that when varying the R_{sh} from 0 Ω to 1 x 10^4 Ω, the slope of J_{sc} was altered leading to a lower FF (**figure 24**). Other research groups such as Kim *et al*. also found the thickness of the active layer have profound effect on fill factor as well. In evaluating, P3HT:PCBM OSCs they found increasing the thickness of active layer films can lead to improved J_{sc} due to more light absorption however, R_{sh} was found to decrease due higher presence of recombination and leakage current (**figure 25**).[105] Increasing the film thickness also increases the distance charge carries have to travel towards their respective electrodes. As a result, this also increases the probability for the aforementioned charge recombination and leakage current. This result displays the often-delicate balance and trade-offs present in optimizing FF towards higher PCEs.

Consequently, carefully tuning the active layer thickness, active layer annealing, and choice of interlayers i.e. ETL and HTL, can prove to be a viable strategy in increasing FF and overall PCE.

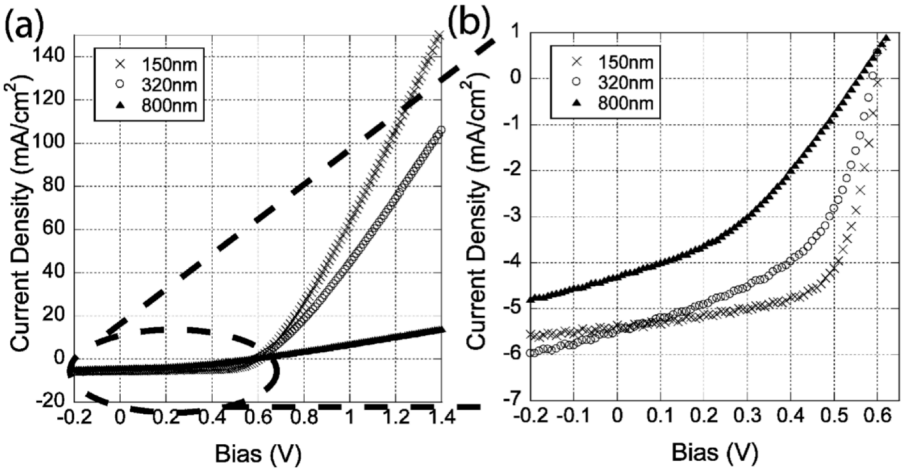

Figure 25. J-V curve of P3HT:PCBM OSCs. Impact of film thickness on R_{sh} and FF. Increasing film thickness lead to decrease in FF. (adapted from ref. 101).

SECTION FOUR – CONCLUSIONS

Overall, the utility of organic semiconductors for OSC applications has spurred interest into their research and development. However, there is much to be understood in terms of improving synthesis and large-scale fabrication in order to make organic semiconductor commercially viable and realizable in the photovoltaic market. Below are some key points discussed by the author of this dissertation aims to address and explore throughout this body of work.

- Section one - Organic semiconductors
    - Organic semiconductor present cheaper alternatives in comparison to their inorganic counterparts

- Through substituent manipulation organic semiconductors can independently tune the HOMO, LUMO, band gap, and opto-electronic properties via donor and acceptor moieties.

- Section two – Organic semiconductor material development
  - High performance material such as Benzobisazoles exhibit excellent oxidative stability, good electron transport, thermal, mechanical properties.
  - Jeffries-EL – Mike orthoester condensation created more assessable synthetic routes towards the functionalization of benzobisazole based materials.
  - 2,6 vs 4,8 axis of benzobisazole materials allows for the development of cross-conjugated cruciforms creating spatially separated frontier molecular orbitals. This creates opportunities for independent tuning of energy levels.
  - Naphthodifuran moieties rigid coplanar structure allows for improved π-electron delocalization leading to better charger carrier mobilities with in a polymer system.
- Section Three – Organic Photovoltaic Cells
  - Silicon high cost and elaborate fabrication conditions hold back their wide spread adoption. Organic solar cells represent a relatively low-cost alternative to silicon.
  - Organic semiconductors display some challenges due to their dielectric constants for organic based semiconductor materials is lower than their silicon and inorganic counterparts.

- Bulk-heterojunction solar cell architecture allow for the presence of efficient phase separation and domain sizes within the exciton diffusion length of organic semiconductors improving the likelihood for enhanced charge separation and extraction towards improved PCEs.
- There are many optimization strategies towards improving photovoltaic parameters; open circuit voltage (V_{oc}), short circuit density (J_{sc}), and fill factor (FF).

CHAPTER TWO: BENZOBISOXAZOLE CRUCIFORMS A TUNABLE, CROSS-CONJUGATED PLATFORM FOR THE GENERATION OF DONOR MATERIALS FOR ORGANIC SOLAR CELLS

SECTION ONE: ABSTRACT

A series of cross-conjugated small molecules based on a central benzo[1,2-d:4,5-d0]bisoxazole exhibiting tunable HOMO and LUMO levels were synthesized and the properties of these materials were investigated. The cruciforms exhibit absorption profiles ranging from 407 – 469 nm. In addition, the cruciforms exhibit thermal stability with 5% weight loss occurring well above 150 ^{o}C. Opto-electronic properties were analyzed providing insight into the synthetically tuning the band gap for effective absorption via substituent manipulation along the 4,8 and 2,6 axis of the benzobisoxazole core. Extending the conjugation through the 2,6 axis with relatively electron deficient moieties yield bathochromically shift absorption profiles and stabilization of the LUMO. Reduced electron density along the 2,6 axis also prolonged photoluminescent lifetimes due to

improved intramolecular charge transfer states between 4,8 and 2,6 axis. Evalution of the opto-electonic data suggest potential application for organic photovoltaic applications.

SECTION TWO - INTRODUCTION

Organic semiconducting materials have garnered a large amount of interest both academically and industrially due to their potential for use in a number of technologically important applications.[106–108] Some of the favorable attributes of these materials include their potential for large-area fabrication, reduced manufacturing costs, and ability to tune key properties such as the position of highest occupied molecular orbital (HOMO), the lowest unoccupied molecular orbital (LUMO) and the band gap via chemical synthesis. Although the pioneering research in the field focused on the design of polymeric materials, in recent years there has been an increased interest in molecular species. This is particularly important for the development of donor materials for use in bulk heterojunction organic solar cells (OSC)s since the material's overall performance depends largely upon variables such as the molecular weight, dispersity, defects and purity, all of which are difficult to control within polymeric species.[109,110] Over the past few years there has been a substantial improvement in the performance of these devices as photocurrent efficiencies (PCE)s have now exceeded 9%.[111,112] The rapid improvement in the performance of small molecule OSCs is a result of their well-defined molecular structures, and the optimization of the band gap, which determines the amount of solar energy harvested; the HOMO, which controls the open circuit voltage (V_{oc}); the LUMO, which drives charge separation while minimizing energy loss, and the charge carrier mobility, which facilitates efficient charge

transport.[113–116] These days, such optimization is usually accomplished through the synthesis of molecules with alternating electron-donating and electron-accepting units.[117–119] In theory, any combination of HOMO level, LUMO level and bandgap should be attainable through selection of the appropriate molecular components. However, in reality concurrent optimization of these parameters is challenging as the delocalized electrons within these systems prevent independent tuning of the HOMO and LUMO levels.

For this reason, X-shaped, cross-conjugated molecules are a promising motif for the development of tunable organic semiconductors. These "cruciforms" are based on a central aromatic core that participates in two different conjugation pathways.[39,120,121] As a result of this arrangement such molecules have spatially segregated frontier molecular orbitals (FMO)s enabling semi-selective tuning of either the LUMO or the HOMO level.[35,39,122–125] Benzo[1,2-*d*:4,5-*d*′]bisoxazole (BBO)-based cruciforms are especially interesting as these molecules have two different conjugation axes: the 2,6-axis which includes the two oxazole rings and the 4,8-axis which is perpendicular to it (**figure 26**).[34–36,120,126–129] Previously, it has been shown in donor-acceptor systems based on cross-conjugated BBOs the LUMO level is primarily localized along horizontal axis (2,6-), while the HOMO level is mainly localized along perpendicular axis (4,8-).[127,130,131] As a result it is possible to significantly alter the position of ones of these frontier molecular orbitals (FMO)s through strategic selection and placement of the substituents. While the literature on cross-conjugated systems is substantial, their utility for the development of tunable organic semiconductors is fairly limited.[35] Herein we demonstrate, that BBO cruciforms can be used as a tunable platform for the development of narrow band gap materials for potential use in OSCs.[131]

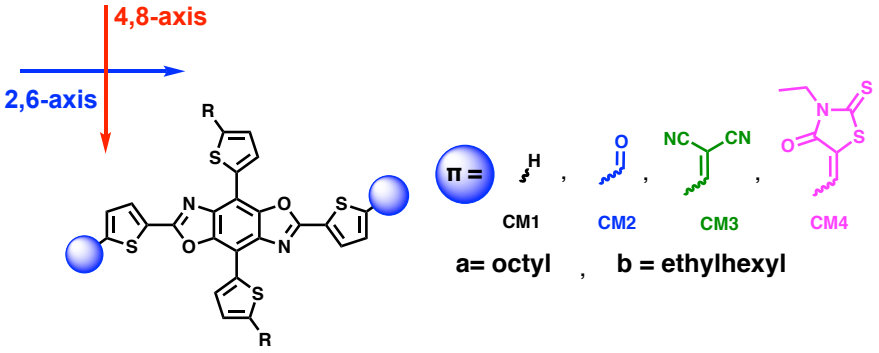

Figure 26. Structure of molecules synthesized.

SECTION THREE - RESULTS AND DISCUSSION

2.3.1 SYNTHESIS AND CHARACTERIZATION

The structures for the targeted molecules in shown in Chart 1. Based on our calculations, the thiophene substituted BBO **CM 1** was identified as a good starting material, since the electron donating groups along the 4- and 8- positions would serve to stabilize the HOMO level. Furthermore, subsequent functionalization of the thiophenes along the 2,6-axis could to increase the electron withdrawing nature of those arenes, reducing the bandgap by lowering the LUMO level. The synthetic routes and chemical structures are depicted in Scheme 1. We synthesized two versions of each cruciform, one with linear side chains and one with branched side chains in order to evaluate the impact of these side chains on the materials properties and performance. The condensation reaction of 3,6-diamino-2,5-dibromo-hydroquionone and 2-(triethoxymethyl)thiophene **1** afforded 4,8-dibromo-2,6-di(thiophen-2-yl)benzo[1,2-*d*:4,5-*d'*]bis(oxazole) **2** in 60% yield. The subsequent Stille cross-coupling reaction of **2** with either trimethyl(5-octylthiophen-2-

yl)stannane or (5-(2-ethylhexyl)thiophen-2-yl)trimethylstannane produced cruciforms **CM 1a** and **CM 1b** in yields of 63% and 65% respectively. Lithiation of **CM 1a** and **CM 1b** followed by quenching with N,N-dimethylforamide at 0 ˚C yielded **CM 2a** and **CM 2b** in yields of 57% and 47% respectively. The Knoveneagel condensation of **CM 2a** and **CM 2b** with malonitrile gave **CM 3a** and **CM 3b** in yields of 46% and 43% respectively. Whereas the Knoveneagel condensation of **CM 2a** and **CM 2b** with 3-ethylrhodanine gave **CM 4a** and **CM 4b** in yields of 46% and 43% respectively. All compounds were readily purified by column chromatography. All small molecules were readily soluble in chlorinated solvents and characterized by NMR spectroscopy and high-resolution mass spectroscopy. The thermal properties of the materials were studied using thermogravimetric analysis (TGA) and were heated to 110^{o}C at 10^{o}C/min, held at 110^{o}C for 20 minutes, heated 600^{o}C at 10^{o}C/min, and held at 600^{o}C for 10 minutes in nitrogen atmosphere. All the BBOs showed excellent thermal stability under nitrogen conditions with 5% weight loss temperatures all above 150 °C (Fig. S2,). These thermal characteristics are indicative of good stability above the typical operational temperature of OSC devices

2.3.2 OPTICAL AND ELECTROCHEMICAL PROPERTIES

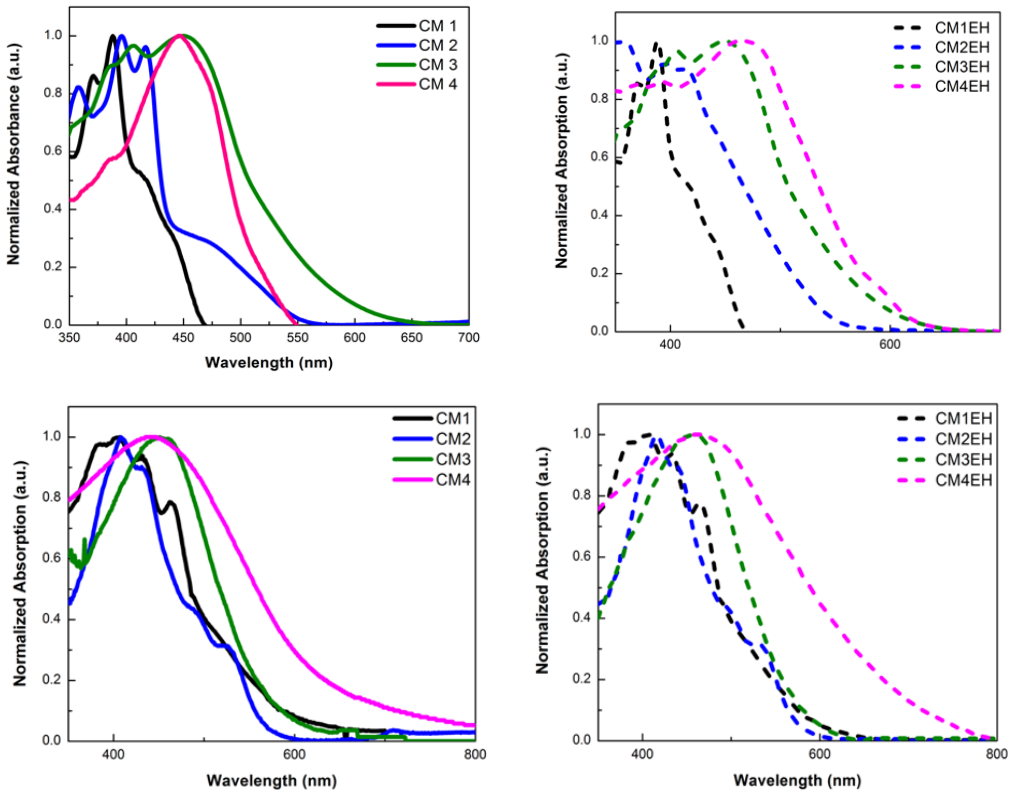

Figure 27. UV-vis absorption of the BBO cruciform in: a) solution chloroform (top) and b) thin film spin coated from chloroform (bottom).

The electrochemical properties of the cruciforms, was measured by cyclic voltammetry (CV) utilizing a platinum working electrode in acetonitrile, with 0.1 M Bu_4NPF_6 as the electrolyte and Ag/Ag^+ reference electrode. All cruciforms displayed reproducible and measurable reductions and oxidations. The HOMO and LUMO levels were estimated from the onset of oxidation and reduction using the absolute energy level of ferrocene/ferrocenium (Fc/Fc^+) as 5.1 eV under vacuum and are summarized in Table 2. The optical bandgaps were calculated from the absorption edge. All data is summarized

in Table 1. The electrochemical band gaps were all estimated to be slightly larger than the optical band gaps as expected due to energy barrier associated with the interface of the polymer film and the electrode surface. Cruciform **CM 1** with thiophenes along both axis, has a deep HOMO of -5.8 eV and high lying LUMO of -3.3 eV resulting in the widest band gap of 2.5 eV. The LUMO of **CM2**, **CM3**, and **CM4**, are relatively similar varying from -3.7 eV to -3.8 eV. These values are statistically similar enough to suggest that the LUMO are approximately the same. In addition CV results also indicate the HOMO level of this cruciform series appeared to be influenced by the strength of the acceptor ranging from -5.6 eV to -5.9 eV. Ultraviolet Photoelectron Spectroscopy (UPS) was also used to probe into the HOMO level as it provides an absolute determination of the HOMO level. The UPS data depicts a different outlook on the energy level trends in comparison to the electrochemical values. As conjugation is increased through the 2,6-axis of the BBO core the HOMO level is not as deep ranging from -5.33 eV to -5.63 eV as you move from **CM1-CM4** and **CM1EH-CM4EH**, respectively. The difference in the energy level values obtained between UPS and cyclic voltammetry eludes to an interesting point of discussion. Generally, the method for determining energy level values has been accomplished via solution cyclic voltammetry. However, this method has been shown to not accurately account for contributing factors such as solvent effects, energetic disorder, etc., that can influence the measurement of the HOMO or LUMO levels obtained.[93] Though the LUMOs of **CM1-CM4** and **CM1EH-CM4EH** show an ideal trend we expect via increasing the conjugation with relatively deficient substituents through the 2,6-axis, the HOMOs obtained via CV do not follow the same pattern (table 1). UPS has presented a more precise

an ideal trend of the HOMOs for **CM1-CM4** and can be corroborated with theory calculations. Notably, due to this difference in result in obtaining energy levels of **CM1-CM4** and **CM1EH-CM4EH**, it is important to note to compare energy levels of materials that have been derived from the same technique in efforts to fabricate devices. The UV-vis absorption spectra of the BBO cruciforms in solution and film are displayed in figure 27. The data is summarized in Table 1. The film spectra for all cruciforms displays a bathochromic shift in their absorption maximum relative to the solution spectra. Within each series of cruciforms, the introduction of electron donating carbonyl groups results in a red-shift in the absorbance spectra relative to unsubstituted **CM 1a/b**. The inclusion of the strongly withdrawing cyano vinylene and rhodamine groups resulted in a further red-shift relative to **CM 2a/b**. All small molecules exhibited strong absorption in the blue region of the visible spectrum with **CM1a/b** and **CM2a/b** having relatively narrow peaks in comparison to **CM3a/b** and **CM4a/b**. As conjugation is extended out with relatively electron deficient units along the 2,6 axis, **CM3** and **CM4EH** develop broader featureless peak in the film state. Interestingly, changing the side chain from linear to branched of **CM3**, **CM3EH**, **CM4** and **CM4EH** displays a broader and red shifted absorption profile in the film and solution state. Linear alkyl side chains are known to occupy less space in comparison to their branched chain counterparts ultimately resulting in differences in the π-π stacking interactions in the film state.[19,83] Changing the side chain from linear to branched could influence the degree to which π-π interactions

is occurring in this set of BBO cruciform series leading to broader and red shifted absorption observed in **CM3EH** and **CM4EH**.

BBO	λ_{max}^{soln} (nm)	λ_{max}^{film} (nm)	Φ (%)	τ_D[a] (ns)	Film Abs. Coe.	Film Thickness (nm)	E_g^{opta} (eV)	HOMO[a]	LUMO[a]	HOMO[b] (eV)	LUMO[b] (eV)	E_g^{ECd} (eV)
CM 1a	388	407	18	1.99	85.89	91	2.4	-5.7	-3.3	-5.33	-2.93	2.5
CM 1b	389	408	23	2.42	90.40	96	2.4	--	--	-5.35	-2.95	--
CM 2a	396	409	5	1.67	46.42	89	2.3	5.7	-3.8	-5.30	-3.00	1.9
CM 2b	397	415	3	1.51	46.40	80	2.3	--	--	-5.33	-3.03	--
CM 3a	451	451	5	1.99	34.82	74	2.0	-5.6	-3.7	-5.53	-3.53	1.8
CM 3b	452	455	5	2.09	35.22	68	2.0	--	--	-5.58	-3.58	--
CM 4a	443	448	2	2.16	42.78	85	1.8	-5.8	-3.7	-5.63	-3.83	2.1
CM 4b	446	469	2	3.54	50.10	94	1.8	--	--	-5.40	-3.60	--

Table 1. Opto-electronic properties of CM1-CM4 series. [a]HOMO and LUMO levels obtained via cyclic voltametry. [b]HOMO level determined by UPS. [c]LUMO level determined - HOMO + Eg^{OPT}.

These differences in side chain interactions can also affect **ITIC-2F** interactions with **CM**3, **CM3EH**, **CM4**, and **CM4EH** possibly leading differences in film forming ability and morphology. Figure 28 shows the absorption of **CM3/ITIC-2F**, **CM3EH/ITIC-2F**, **CM4/ITIC-2F**, and **CM4EH/ITIC-2F** blended films mixed in a 1:1 weight ratio spin coated from CB implemented in device preparations. The blended films illustrate complimentary broad absorption from 350 to 800 nm. In comparison to the neat absorption of **ITIC-2F**, the absorption band from approximately 350 to 600 nm is primarily due to **CM3**, **CM3EH**, **CM4**, and **CM4EH**. Photo-luminescent quenching experiments displayed a decrease in fluorescence intensity for **CM3/ITIC-2F**, **CM3EH/ITIC-2F**, **CM4/ITIC-2F**, and **CM4EH/ITIC-2F** blended films, respectively.

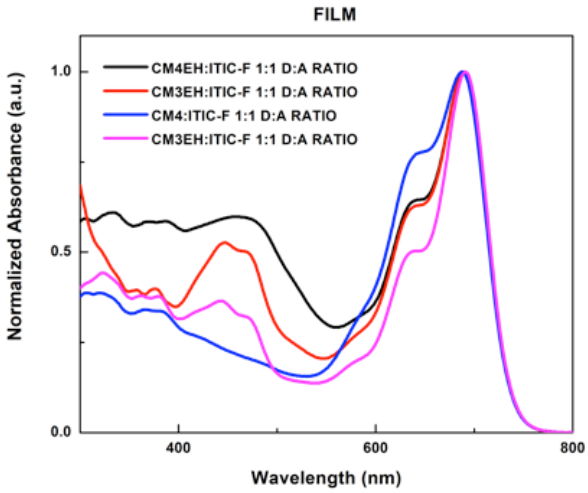

Figure 28. Film state active layer absorption profile spin coated from CB, 1:1 CM: ITIC-F D:A ratio.

2.3.3. PHOTOLUMINESCENCE LIFETIME AND QUANTUM YIELD PROPERTIES

Cruciform	τ_1 (NS) [REL.]	β_1	τ_2 (NS) [REL.]	β_2	τ_D^A (NS)	Φ (%)
CM1a	1.5 [41%]	5438.34	2.57 [59%]	4587.75	1.99	18
CM1b	2.42 [100%]	11421.79	--	--	2.42	23
CM2a	1.29 [66%]	8658.05	4.01 [34%]	1406.67	1.67	5

CM2b	1.1 [60%]	8429.35	3.43 [40%]	1796	1.51	3
CM3a	1.62 [65%]	8338.90	3.52 [35%]	2001.40	1.99	5
CM3b	1.75 [69%]	8140.25	3.75 [31%]	1708.03	2.09	5
CM4a	1.61 [57%]	7217	4.26 [41%]	1924.65	2.16	2
CM4b	1.44 [25%]	4417.67	3.45 [72%]	5374.61	3.54	2

Table 2. Photoluminescent lifetimes and quantum yield. [a]Average PL decay lifetime. Time correlated single photon counting technique with horizontal pulse ns 405 nm laser.

Time correlated single photon counting measurements (TCSPC) were performed to evaluate the photoluminescence lifetime of the exciton formation upon excitation of the small molecule cruciforms. All cruciforms were excited by a horizontal pulse nanosecond 405 nm laser beam to 10,000 counts. The lifetimes (τ_1 and τ_2) are given in table 1 on the order of nanoseconds (ns). **CM3a**-**CM4a** and **CM3b**-**CM4b** displayed longer lifetimes relative to that of **CM1a**-**CM2a** and **CM1b**-**CM2b**. In addition, cruciforms with branched side chains display longer lifetimes relative to cruciforms with linear side chains. This further suggest that there is an influence of branched ethyl hexyl chain on the opto-electronic properties of the cruciform. Extending conjugation through the 2,6-axis with relatively electron deficient units also has an influence on the lifetimes of the benzobisoxazole cruciforms. An increase in photoluminescent lifetime as conjugation increases through the 2,6-axis with electron deficient units suggest the hypothesis that **CM3** and **CM4** have a longer exciton lifetime compared to **CM1** and **CM2** analogs. This may be due to increasing the electron deficiency through the 2,6-axis with deficient dicyanovinylene and 2-ethylrhodanine moieties indicating to the affinity for exciton

dissociation competing efficiently with radiative recombination to charge transfer with a n-type acceptor material such as ITIC-F. The fluorescence quantum yields of the **CM3a-CM4a** and **CM3b-CM4b** were the lowest in comparison to **CM1a-CM2a** and **CM1b-CM2b** (Table 3). The presence of branched ethyl hexyl in comparison to linear octyl chain showed to have no influence on the fluorescence quantum yield.[34,132] Interestingly, extending the conjugation through the 2,6-axis with dicyanovinylene and 2-ethylrhodanine moieties decreases the fluorescence quantum yield impacting the cruciform excitation and radiative decay rates of the excited state. It is well known that high quantum yields can be detrimental to photovoltaic performance due to increased radiative decay pathways of the exciton, while low quantum yields are shown to enhance non-radiative decay pathways.[133] This decrease in quantum yield and increase in radiative lifetimes imply the BBO cruciforms are strongly affected by increased access to non-radiative quenching pathways such as intramolecular photoinduced electron transfer (PET) as conjugation is increased through the 2,6-axis with electron deficient units.[134,135]

SECTION FOUR – ORGANIC SOLAR CELLS

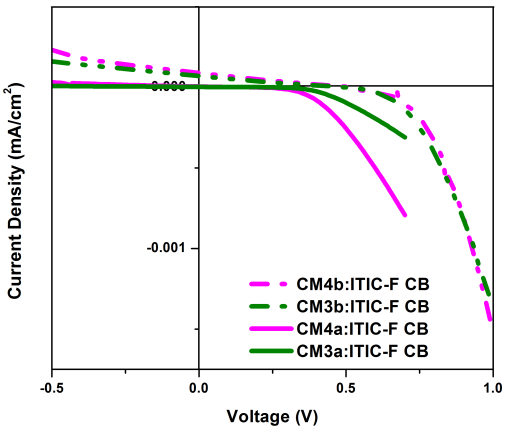

Figure 29. J-V curve of CM3-CM4: ITIC-F series devices.

The performance of **CM3-CM4** series in OSCs were assessed in BHJ architecture utilizing $PC_{71}BM$ as the electron acceptor with a device configuration of ITO/PEDOT:PSS/CM3-CM4: ITIC-F/Ca/Al. Active layers spin coated at different speeds are summarized in **figure 29** and **table 3**. All devices were fabricated under inert nitrogen atmosphere. The small molecules all exhibit relatively low performances when processed from chloroform (CF). The best performing devices were **CM3b** and **CM4b**. To optimize the photovoltaic parameters of the devices **CM3-CM4** were subject to various spin coating speeds and post-thermal annealing conditions. Spin coating of the **CM3a**: **ITIC-F** active layer from CF let to an active layer thickness of 29 nm and displayed a PCE of 0.02%. To optimize film thickness CF films were spun cast at lower speeds resulting in a film thickness of 31 nm and a PCE of 0.05%. Chlorobenzene (CB) evaluated as a processing solvent yielded a PCE of 0.007%. The **CM3**: **ITIC-F** active layer processed from CB showed no improvement on device performance in spite of lower spin speed to improve film thickness. Post-thermal annealing at 100^{o}C for 10 minutes led to no improvement on PCE. **CM3b**: **ITIC-F** active layer processed from CF led to a PCE of 0.01%. When processing from CB resulted in a film thickness of 34 nm and improved PCE of 0.11% upon post-thermal annealing. **CM4a** and **CM4b** analogs were taken through the same optimization parameters. **CM4a**: **ITIC-F** and **CM4b**: **ITIC-F** active layer processed from CF provided a PCE of 0.005% and 0.02%, respectively. Upon post-thermal annealing treatment, when processing **CM4a**: **ITIC-F** and **CM4b**: **ITIC-F** from CB led to an

efficiency of 0.01% and 0.17%, respectively. The improvement in OPV parameters within the CM3-CM4 series suggest that the difference in side chain has a potential impact on morphology leading to better J_{sc}, V_{oc}, FF, and overall PCE.

Cruciform	Solution	Active layer thickness [nm]	D/A	V_{oc} [V]	J_{sc} [mA/cm^2]	FF	PCE [%]
CM3a	CF	36	1:1	0.45	0.05	27.78	0.01
	CB	31	1:1	0.43	0.06	28.49	0.007
CM3b	CF	37	1:1	0.55	0.05	27.82	0.01
	CB	34	1:1	0.47	1.10	21.85	0.11
CM4a	CF	25	1:1	0.44	0.12	19.86	0.01
	CB	27	1:1	0.36	0.13	21.19	0.01
CM4b	CF	33	1:1	0.44	0.2	19.18	0.01
	CB	25	1:1	0.67	1.48	17.23	0.17

Table 3. Photovoltaic performances for CM1-CM4 series.

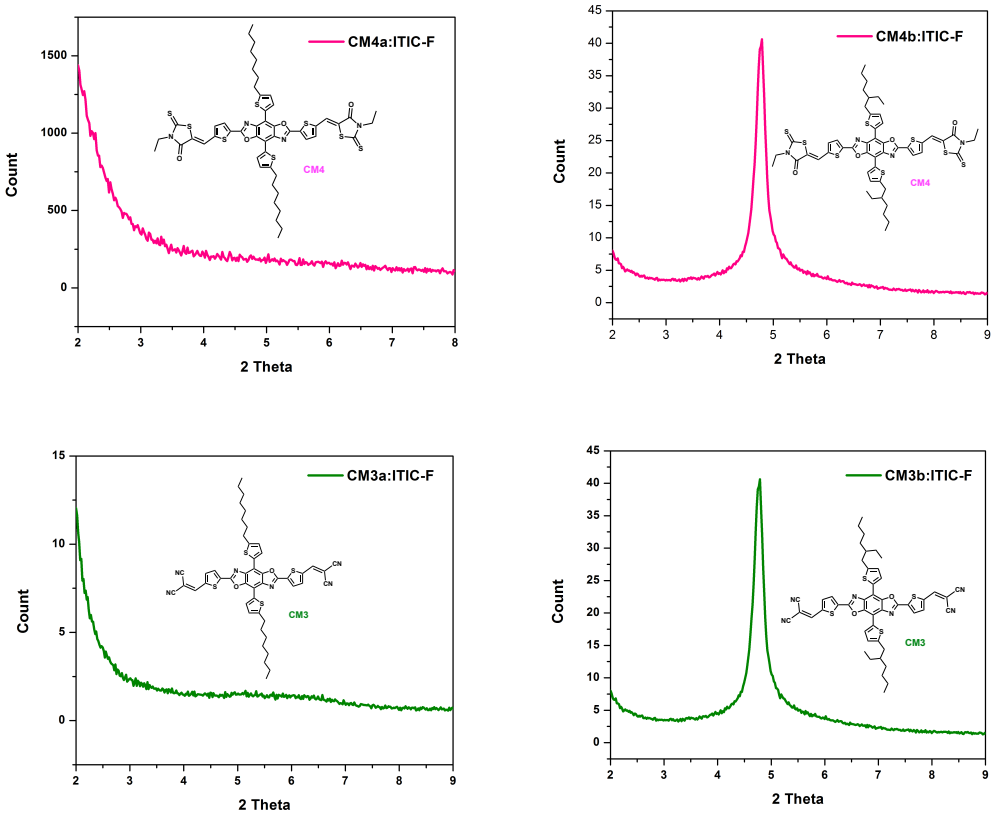

Figure 30. XRD films prepared via dropcasting from CB on glass substrate.

The degree of the order of the active layer films was primarily investigated via X-Ray Diffraction (XRD) to determined how the influence of side chains has an impact on device performance and active-layer morphology. The XRD diffraction patterns are exhibited in **figure 29**. A notable trend is observed in diffraction characteristics of active layer films. CM3a: ITIC-F and CM4a: ITIC-F displayed no diffraction peak indicating mostly amorphous film. Interestingly, CM3b: ITIC-F and CM4b: ITIC-F displayed similar diffraction patterns indicating some degree of order present in the within the active layer films, respectively. The broadness of the peaks also suggests possible defects in crystalline structure within the active layer. In addition, noteworthy difference between the active

layers is use of alkyl side chains. Further probing into influence of linear octyl versus branched ethylhexyl side chains on ITIC-F ordering via GIWAXS can provide insight into lamellar distance and crystal coherence length for these series of BBO cruciform based materials.

COMPUTATIONAL STUDIES

Our goal was to design OSC donor materials compatible with the widely used acceptor, [6,6]-phenyl C_{71} butyric acid methyl ester ($PC_{71}BM$). Since $PC_{71}BM$ has a LUMO of 4.2 eV, and requires an energetic offset of ~0.3 eV for favorable charge dissociation, the ideal donor material should have an approximate LUMO level of 3.9 eV. Additionally, the donor material should have a band gap between 1.2 – 1.9 eV to overlap the maximum solar spectrum flux. As a result the ideal HOMO level will be between 5.1 and 5.8 eV.[136] Based on these criteria we screened several BBO aryl group combinations using our previously benchmarked functional/basis set of mPW1PBE/SV on these cruciforms. Both **CM3** and **CM4** were predicted to possess HOMO levels and band gap within the target range and were therefore synthesized along with their precursors **CM1** and **CM2**. Once we had experimental values in hand, it was decided that further validation of the benchmarks was necessary. We then found that B3LYP/Midix and B972/SHC were the best pairings for the thin film and solution studies, respectively.[137] It was predicted that **CM1** which bears thiophene rings in all four positions had the widest band gap and highest lying HOMO level.[131] As the electron-withdrawing nature of the substituents along the 2,6-axis was increased the calculated HOMO levels in the gas phase were slightly lowered with **CM3** < **CM4** ≈ **CM2** < **CM1**.[138] The UPS data mirrored these results with the exception of **CM4a**.

This discrepancy is likely a result of the differences in film morphology, which are known to impact the work function of a material. In solution the calculated HOMO levels for **CM2**, **CM3** and **CM4** were all within 0.1 eV of each other, which was in agreement with the experimental data. The predicted band gaps showed a significant lowering upon substitution with **CM1 > CM2 > CM4 > CM3** which was consistent with the trend seen in the experimental data. However, since DFT methods are known to underestimate band gaps the predicted values were smaller than those determined experimentally. The calculated LUMO values showed a significant lowering upon substitution with **CM3 > CM4 >> CM2 >>> CM1**. Unfortunately, this trend was not mirrored experimentally. This discrepancy is likely an combination of the error associated with DFT predictions and the indirect determination of LUMO energies via cyclic voltammetry (CV).[139] To further our investigations an electron density population study was performed, Figure 1. The resulting FMOs and percent electronic distribution along each axis for the HOMO and LUMO are shown in Figure 2. All four molecules were planar in both the gas and solution phases indicating that the substituents had no impact on the geometry. In all cases the HOMO was localized along the 4,8-axis with only a 5.4% difference between the two extremes **CM4** and **CM2**. The electron density of the LUMO was delocalized throughout **CM 1**, indicative of a more localized excitation. Conversely, the electron density is localized along the 2,6-axis for all the other cruciforms, indicative of a charge-transfer type excitation. All together these findings validate our supposition that changes along the 2,6-axis primarily impact the LUMO level.

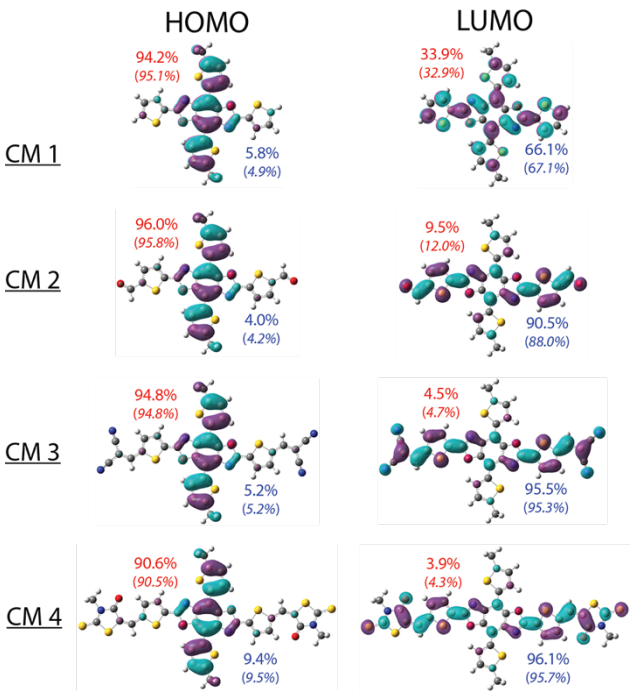

Figure 31. Frontier molecular orbitals (FMOs) of CM1 – CM4.

SECTION FIVE – FABRICATION OF ORGANIC SOLAR CELLS

Fabrication of all devices were evaluated under inert atmosphere and conditions via solution based spin-casting techniques. Organic solar cells were fabricated with a conventional bulk heterojunction architecture indium tin oxide (ITO)/ Poly(3,4-ethylenedioxythiophene): poly(styrene sulfonate) (PEDOT:PSS)/donor:[6,6]-phenyl-C_{71}-butyric acid methyl ester ($PC_{71}BM$)CA/Al). ITO glass substrates were cleaned via (i) sonication with Mucasol, (ii) deionized water, (iii) acetone, and (iv) isopropanol for 10 minutes each respectively. Slides were dried in oven followed by UV-ozone treatment for 15 minutes. PEDOT: PSS layers (Clevios P VP Al 4083) were filtered (0.45 um) and spin-coated onto ITO substrates at 3500 rpm for 2 minutes then annealed at 150^{o}C for 30 min

in air. After cooling, the substrates were transferred into nitrogen filled glove box. Small molecule: $PC_{71}BM$ solutions were prepared in a blend ratio of 1:1 20mg/ml **CM3a**, **CM3b**, **CM4a**, and **CM4b** in chloroform (CF) and chlorobenzene (CB). Solutions were then allowed to stir for 24 hours at 55^{o}C prior to spin coating (1200-2000 rpm, for 2 min). Substrates were then transferred into thermal evaporator to undergo successful deposition of Ca (15 nm) and Al (100 nm) electrodes. Keithley 2400 source meter and simulated AM1.5G illumination (100 mW/cm^2, Newport 91160) calibrated using a KG-5 filter Si reference cell were utilized to measure current density (J-V) data.

SECTION SIX – CONCLUSIONS

We have illustrated a series of cross-conjugated donor-acceptor materials based on benzo[1,2-*d*:4,5-*d*′]bisoxazole. The opto-electronic properties of these materials were tuned via substituent manipulation towards relatively narrow band gaps. Results exemplify spatial separation of the frontier molecular orbitals (FMOs) along the 2,6 and 4,8-axis have an impact on energy levels and bandgaps of benzo[1,2-*d*:4,5-*d*′]bisoxazole cruciforms. Consequently, as conjugation is increased through the 2,6-axis with relatively electron deficient units the film state absorption decreases. This intrinsic factor provides insight into material photovoltaic performance. Collectively, design requirements indicate BBO cruciform are a promising design motif towards readily tunable materials of organic photovoltaic cells. Preliminary organic photovoltaic cell performance for CM3-CM4 series warrant further investigation into improving photovoltaic parameters. Future work is underway in regards to OPV optimization and material design.

SECTION SEVEN – EXPERIMENTAL METHODS

Materials, Measurements, and Synthesis

3,6-diamino-2,5-dibromo-hydroquionone, isopropylmagnesium chloride were made in accordance to literature procedure. All other chemical reagents were purchased from commercial sources and used without further purification unless otherwise noted. Nuclear magnetic resonance experiments were performed in $CDCl_3$ at 500 MHz and 600 MHz for both ^{1}H and ^{13}C. Chemical shifts are provided in δ relative to tetramethylsilane. Coupling constants are reported in Hz. Unless stated otherwise, all UV-vis spectroscopy were acquired in CF.

2-(triethoxymethyl)thiophene (2).

In a dry 2N-flask equipped with an additional funnel and reflux condenser was filled with 0.73 g of Mg turnings and heated under vacuum at 90 ^{o}C for 1 hr. The flask was backfilled with Argon to sublime for 20 minutes after addition of a few I_2 crystals. The flask was then cooled to RT and filled up with 20 ml anhydrous diethyl ether. Then approximately 5 ml of 2-chloropropane in diethyl ether was added dropwise with gentle reflux for 1 hr until all Mg turnings were dissolved. Solution of 2-bromothiophene was added dropwise and allowed to reflux for 24 hours. The solution was cooled to room temperature and $C(OEt)_4$ was added dropwise and heated to reflux for 12hrs. The reaction was then cooled to room temperature and poured into a cold saturated aqueous NH_4Cl solution. The layers were separated and the aqueous layer was extracted with Et_2O. The combined organic layers were washed with brine and dried over Na_2SO_4. The solution was filtered and solvent removed under vacuum. Lower boiling impurities were removed via Kugelrohr distillation to yield pale yellow oil used without further purification (1.49 g, 65%). $^{1}HNMR$ (500 MHz

$CDCl_3$) δ 7.27 (dd, J = 5.0, 1.3 Hz, 1H), 7.17 (dd, J = 3.5, 1.3 Hz, 1H), 6.97 (dd, J = 5.0, 3.6 Hz, 1H), 3.57 (q, J = 7.1 Hz, 4H), 3.44 (q, J = 7.1 Hz, 6H), 1.19 (dt, J = 14.2, 7.1 Hz, 15H). ^{13}CNMR (600 MHz $CDCl_3$) 141.97, 126.69, 126.37, 126.02, 58.22, 14.84.

4,8-dibromo-2,6-di(thiophen-2-yl)benzo[1,2-*d*:4,5-*d'*]bis(oxazole) (3).

0.604 g of Br-DAHQ was placed under Argon in a dry round bottom flask. Approximately 3 ml of anhydrous DMSO were added to the flask under Argon. In another dry flask containing 1.41 g of 2-(triethoxymethyl)thiophene and 0.081 g of $Y(OTf)_3$ in 5 ml of THF was prepared. Both flask were deoxygenated under Argon for 30 minutes. After 30 minutes the flask containing 2-(triethoxymethyl)thiophene and $Y(OTf)_3$ in THF was warmed to 55^{o}C. Following, addition of dissolved *Br-DAHQ* in DMSO was added dropwise to the solution and allowed to stir overnight. The reaction cooled to room temperature and 1:1 mixture of cold methanol and water was poured into reaction. Cold mixture was then precipitated into 400 ml of -78^{o}C chilled methanol to yield off white powder upon vacuum filtration (1.76 g, 60%). Due to insolubility of product in common solvents product no ^{13}C NMR was not obtained and was used subsequently in further steps without further purification. 1H NMR (500 MHz, Chloroform-d) δ 7.27 (dd, J = 5.0, 1.3 Hz, 1H), 7.17 (dd, J = 3.5, 1.3 Hz, 1H), 6.97 (dd, J = 5.0, 3.6 Hz, 1H), 3.57 (q, J = 7.1 Hz, 4H), 3.44 (q, J = 7.1 Hz, 6H), 1.19 (dt, J = 14.2, 7.1 Hz, 15H). HRMS *m/z*: M^+ calcd for $C_{16}H_6Br_2N_2O_2S_2$ 479.82; found, 480.8135, error 0.415 ppm.

4,8-bis(5-octylthiophen-2-yl)-2,6-di(thiophen-2-yl)benzo[1,2-*d*:4,5-*d'*]bis(oxazole) (CM1a).

A solution of 1.316 g of 2-trimethyltinthiophene and 0.842 g of 4,8-dibromo-2,6-di(thiophen-2-yl)benzo[1,2-*d*:4,5-*d′*]bis(oxazole) in toluene was degassed with Argon for 45 min. Then $Pd(PPh_3)_4$ was added with gradually heated to reflux and stirring for 24 hours under Argon. The reaction was cooled to room temperature. Reaction mixture was diluted with water and extracted 3x with $HCCl_3$. Following extraction solution was rotovap to concentrate. Solid was purified via column chromatography gradient hexanes to 60/40 v/v hexanes/DCM gradient. Desired eluents were rotovap to concentrate and dissolved in 2 ml of $HCCl_3$ and precipitated into MeOH at -78°C. Precipitate was filtered to yield a bright yellow solid (0.783 g, 63%). ^{1}HNMR (600 MHz $CDCl_3$) δ 8.29 (d, *J* = 3.7 Hz, 1H), 8.07 (d, *J* = 3.7 Hz, 1H), 7.61 (d, *J* = 6.1 Hz, 1H), 7.24 (d, *J* = 4.9 Hz, 2H), 6.97 (d, *J* = 3.7 Hz, 1H), 2.96 (t, *J* = 7.5 Hz, 3H), 1.55 (s, 20H), 1.26 (s, 73H), 0.86 (dd, *J* = 15.0, 8.7 Hz, 46H).^{13}CNMR (600 MHz $CDCl_3$) 157.58, 148.38, 147.28, 143.78, 142.96, 137.94, 136.25, 130.78, 130.75, 128.78, 128.24, 107.47. HRMS *m/z*: M^+ calcd for $C_{40}H_{44}N_2O_2S_4$ 713.2358; found, 713.2342, error 2.3 ppm.

4,8-bis(5-ethylhexylthiophen-2-yl)-2,6-di(thiophen-2-yl)benzo[1,2-*d*:4,5-*d′*]bis(oxazole) (CM1b).

^{1}H NMR (500 MHz, Chloroform-d) δ 8.30 (d, J = 3.7 Hz, 2H), 8.05 (d, J = 3.7 Hz, 2H), 7.60 (d, J = 6.1 Hz, 3H), 7.24 (dd, J = 4.9, 3.7 Hz, 3H), 6.95 (d, J = 3.7 Hz, 2H), 3.44 – 3.37 (m, 3H), 2.90 (d, J = 6.7 Hz, 7H), 2.05 (d, J = 6.1 Hz, 7H), 1.74 (s, 6H), 1.68 (s, 6H), 1.51 – 1.28 (m, 44H), 0.95 (dt, J = 12.2, 6.5 Hz, 37H). ^{13}CNMR (500 MHz $CDCl_3$) 158.97, 146.63, 144.04, 136.34, 131.77, 130.23, 130.07, 129.01, 128.88, 128.18, 125.74, 107.63,

41.43, 34.16, 32.46, 28.92, 25.60, 23.11, 14.23, 10.88. HRMS *m/z*: M^+ calcd for $C_{40}H_{44}N_2O_2S_4$ 713.2364; found, 713.2358, error 0.8412 ppm.

5,5'-(4,8-bis(5-octylthiophen-2-yl)benzo[1,2-*d*:4,5-*d'*]bis(oxazole)-2,6-diyl)bis(thiophene-2-carbaldehyde) (CM2a).

In an oven dried flask, a solution of anhydrous THF containing 0.390 g of CM1 was cooled to 0°C. n-Butyl lithium (2.5 M) was added dropwise to the reaction mixture. The reaction was allowed to stir at 0°C for 15 minutes then was cooled to -78°C. Reaction was quenched with anhydrous DMF and warmed to room temperature to stir overnight. The reaction was diluted with distilled H_2O and brine. The organic layer was extracted with ethyl acetate and rotovap to concentrate. The residual solid was purified via column chromatography gradient hexanes to 75/25 v/v hexanes/ethyl acetate gradient. Desired eluents were rotovap to concentrate and dissolved in 2 ml of $HCCl_3$ and precipitated into MeOH at -78°C. Precipitate was filtered to yield a dark red solid (0.189 g, 45%). ^{1}H NMR (500 MHz $CDCl_3$) δ 9.99 (s, 1H), 8.00 (d, *J* = 3.6 Hz, 1H), 7.91 (d, *J* = 3.8 Hz, 1H), 7.79 (d, *J* = 3.8 Hz, 1H), 6.79 (d, *J* = 3.5 Hz, 1H), 2.85 (t, *J* = 7.7 Hz, 2H), 1.75 (p, *J* = 7.6 Hz, 3H), 1.44 (d, *J* = 7.5 Hz, 3H), 1.41 – 1.29 (m, 11H), 1.25 (s, 2H), 0.90 (t, *J* = 6.9 Hz, 5H). ^{13}C NMR (500 MHz $CDCl_3$) 182.74, 157.47, 148.66, 146.26, 143.26, 137.26, 136.49, 135.97, 130.64, 129.96, 129.18, 124.54, 109.98, 107.85, 31.91, 31.63, 30.18, 29.44, 29.36, 22.70, 14.13. HRMS *m/z*: M^+ calcd for $C_{42}H_{44}N_2O_4S_4$ 769.2262; found, 769.2269, error 0.9100 ppm.

5,5'-(4,8-bis(5-ethylhexylthiophen-2-yl)benzo[1,2-*d*:4,5-*d'*]bis(oxazole)-2,6-diyl)bis(thiophene-2-carbaldehyde) (CM2b).

^{1}H NMR (500 MHz, Chloroform-d) δ 9.98 (s, 1H), 8.09 (d, J = 3.6 Hz, 2H), 7.94 (d, J = 3.9 Hz, 2H), 7.78 (d, J = 3.9 Hz, 2H), 6.84 (d, J = 3.7 Hz, 2H), 3.12 (d, J = 1.2 Hz, 1H), 2.93 – 2.76 (m, 10H), 2.04 (s, 2H), 1.70 (tt, J = 15.8, 6.8 Hz, 7H), 1.51 – 1.19 (m, 47H), 1.08 – 0.81 (m, 35H). ^{13}C NMR (500 MHz $CDCl_3$) 182.79, 157.70, 147.43, 146.34, 144.20, 137.25, 136.69, 136.02, 130.96, 130.05, 129.30, 125.84, 108.07, 41.39, 34.18, 32.42, 28.86, 25.56, 23.13, 14.23, 10.84. HRMS *m/z*: M^+ calcd for $C_{42}H_{44}N_2O_4S_4$ 769.2262; found, 769.2300 error 4.9400 ppm.

2,2'-(((4,8-bis(5-octylthiophen-2-yl)benzo[1,2-*d*:4,5-*d'*]bis(oxazole)-2,6-diyl)bis(thiophene-5,2 diyl))bis(methaneylylidene))dimalononitrile (CM3a).

1ml of Pyridine was added to malonitrile in 80 ml of $HCCl_3$ and allowed to stir for 1 minute. Pale yellow color was observed and a solution of CM2 in $HCCl_3$ was added dropwise. After 2 hrs another equivalent of malonitrile and pyridine was added and was further monitored by TLC. The reaction was allowed to stir at room temperature under argon for 24 hrs. The reaction was quenched with water and worked up with distilled H_2O, brine, $HCCl_3$. Extracted organic layer was dried over anhydrous magnesium sulfate and rotovap to concentrate. The residual solid was dissolved in 2 ml of $HCCl_3$ and precipitated into was in cold methanol and vacuum filtered to provide a black solid. The black solid was further purified via column chromatography gradient 97/3 v/v hexanes/chloroform respectively to 50/50 v/v hexanes/chloroform to 100 chloroform gradient. Desired eluents were rotovap to concentrate to yield a black solid (0.182 g, 43%). ^{1}H NMR (500 MHz, Chloroform-d) δ 7.82 (s, 1H), 7.65 (s, 1H), 7.62 (s, 1H), 7.58 (s, 1H), 6.72 (s, 1H), 3.00 – 2.68 (m, 7H), 1.72

(p, J = 7.7 Hz, 4H), 1.32 (s, 23H), 1.26 (s, 15H), 0.89 (dq, J = 19.1, 12.4, 9.3 Hz, 14H). HRMS *m/z*: M^+ calcd for $C_{48}H_{44}N_6O_2S_4$ 865.2487; found, 865.2481 error 0.6934 ppm. Attempts to obtain ^{13}C NMR (500 MHz $CDCl_3$) were unobtainable due to the limited solubility of the material.

2,2'-(((4,8-bis(5-ethylhexylthiophen-2-yl)benzo[1,2-*d*:4,5-*d'*]bis(oxazole)-2,6-diyl)bis(thiophene-5,2 diyl))bis(methaneylylidene))dimalononitrile (CM3b).

1H NMR (500 MHz, Chloroform-d) δ 8.13 (d, J = 3.6 Hz, 2H), 7.92 (d, J = 4.0 Hz, 2H), 7.77 (d, J = 5.7 Hz, 4H), 6.89 (d, J = 3.6 Hz, 2H), 2.87 (d, J = 6.8 Hz, 8H), 1.73 (dd, J = 12.0, 6.1 Hz, 4H), 1.56 (s, 4H), 1.49 – 1.20 (m, 29H), 0.93 (ddd, J = 24.1, 15.9, 7.1 Hz, 23H). HRMS *m/z*: M^+ calcd for $C_{48}H_{44}N_6O_2S_4$ 865.2487; found, 865.2494 error 0.8090 ppm. Attempts to obtain ^{13}C NMR (500 MHz $CDCl_3$) were unobtainable due to the limited solubility of the material.

(5*Z*,5'*Z*)-5,5'-(((4,8-bis(5-octylthiophen-2-yl)benzo[1,2-*d*:4,5-*d'*]bis(oxazole)-2,6-diyl)bis(thiophene-5,2-diyl))bis(methaneylylidene))bis(3-ethylthiazolidine-2,4-dione) (CM4a).

In an oven dried flask, 0.360 g of CM2 was added to 50 ml of $HCCl_3$ following addition of 0.158 g of 3-ethylrhodanine. Solution was stirred and deoxygenated for 15 minutes to ensure all contents were dissolved and degassed. After 15 minutes, piperidine was added dropwise at room temperature. The reaction was heated to reflux for 3 days. Reaction was cooled to room temperature and worked up with H_2O. Organic layer was extracted and

dried over anhydrous magnesium sulfate for 1 hour. After 1 hour, organic layer was rotavap to concentrate. The residual solid was dissolved in 2 ml of chloroform and precipitated into cold methanol and vacuum filtered. The dark solid was further purified via column chromatography gradient chloroform. Desired eluent were rotovap to concentrate to yield a dark red solid (0.198 g, 51%). ^{1}H NMR (500 MHz, Chloroform-*d*) δ 7.86 – 7.82 (m, 2H), 7.66 (d, *J* = 9.1 Hz, 4H), 7.61 (s, 2H), 6.75 – 6.71 (m, 2H), 2.84 – 2.77 (m, 5H), 1.42 (s, 7H), 1.32 (s, 16H), 1.25 (s, 16H), 0.93 – 0.86 (m, 16H). HRMS *m/z*: M^+ calcd for $C_{52}H_{54}N_4O_4S_8$ 1054.2567; found, 1054.2745 error 0.6070 ppm. Attempts to obtain ^{13}C NMR (500 MHz $CDCl_3$) were unobtainable due to the limited solubility of the material.

(5*Z*,5'*Z*)-5,5'-(((4,8-bis(5-ethylhexylhiophen-2-yl)benzo[1,2-*d*:4,5-*d'*]bis(oxazole)-2,6-diyl)bis(thiophene-5,2-diyl))bis(methaneylylidene))bis(3-ethylthiazolidine-2,4-dione) (CM4b).

In an oven dried flask, 0.460 g of CM2 was added to 60 ml of $HCCl_3$ following addition of 0.258 g of 3-ethylrhodanine. Solution was stirred and deoxygenated for 15 minutes to ensure all contents were dissolved and degassed. After 15 minutes, piperidine was added dropwise at room temperature. The reaction was heated to reflux for 3 days. Reaction was cooled to room temperature and worked up with H_2O. Organic layer was extracted and dried over anhydrous magnesium sulfate. Organic layer was rotavap to concentrate. The residual solid was dissolved in 2 ml of chloroform and precipitated into cold methanol and vacuum filtered. The dark solid was further purified via column chromatography gradient chloroform. Desired eluent were rotovap to concentrate and was dissolved in 2 ml of chloroform and precipitated into cold methanol and vacuum filtered to yield a dark red

solid (0.298 g, 47%). ^{1}H NMR (500 MHz, Chloroform-*d*) δ 8.15 – 8.08 (m, 2H), 7.90 – 7.84 (m, 1H), 7.71 (s, 4H), 6.92 – 6.86 (m, 2H), 2.86 (s, 7H), 1.67 – 1.15 (m, 35H), 1.15 – 0.71 (m, 22H). HRMS *m/z*: M^+ calcd for $C_{52}H_{54}N_4O_4S_8$ 1054.2567; found, 1054.3276 error 2.6090 ppm. Attempts to obtain ^{13}C NMR (500 MHz $CDCl_3$) were unobtainable due to the limited solubility of the material.

Characterization

Nuclear magnetic resonance (NMR) spectra were carried out in $CDCl_3$ and recorded on Varian VXR (300 MHz), Varian MR (400 MHz) or a Bruker Avance III (600 MHz) as noted. ^{1}H NMR spectra were internally referenced to the residual protonated solvent peak. In all spectra, chemical shifts are given in ppm (δ) relative to the solvent. Cyclic voltammetry was performed using a e-DAQ e-corder 410 potentiostat with a scanning rate of 100 mV/s.

SECTION EIGHT – SUPPORTING INFORMATION

Device Fabrication and Characterization

All organic photovoltaic devices were performed under inert atmosphere and solution based spun cast via spin coater. Conventional architecture were used to fabricated organic photovoltaic devices via (ITO)/ POLY(3,4-ethylenedioxythiophene): poly(styrene sulfonate) (PEDOT:PSS)/small molecule:[6,6]-phenyl-C_{71}-butyric acid methyl ester ($PC_{71}BM$)/CA/Al). ITO glass substrates were cleaned via (1) sonication (Mucasol), (2) deionized water, (3) acetone, and (4) isopropanol for 10 minutes each respectively. Slides

were dried in oven followed by UV-ozone treatment for 15 minutes. PEDOT: PSS layers (Clevios P VP Al 4083) were filtered (0.45 um) and spin-coated onto ITO substrates at 3500 rpm for 2 minutes and annealed for 150^{o}C for 30 min in air. After cooling substrates were transferred into nitrogen filled glove box. All small molecule: ITIC-F solutions were prepared in 1:1 blend ratio (20 mg/ml) with CF or CB as processing solvent. The prepared solutions were allowed to stir for 24 hrs at 55 ^{o}C (CF) or 80^{o}C (CB) prior to spin coating 1200-2000 rpm for 2 minutes. Following spin coating, Ca (15 nm) and Al (100 nm) electrodes underwent successful deposition via thermal evaporation. Films were also evaluated under post-thermal annealing conditions at 100 ^{o}C for 10 minutes. Current-density (J-V) data were obtained via Keithley 2400 source meter and simulated AM1.5G illumination (100 mW/cm^2, Newport 91160) calibrated using a KG-5 filter Si reference cell.

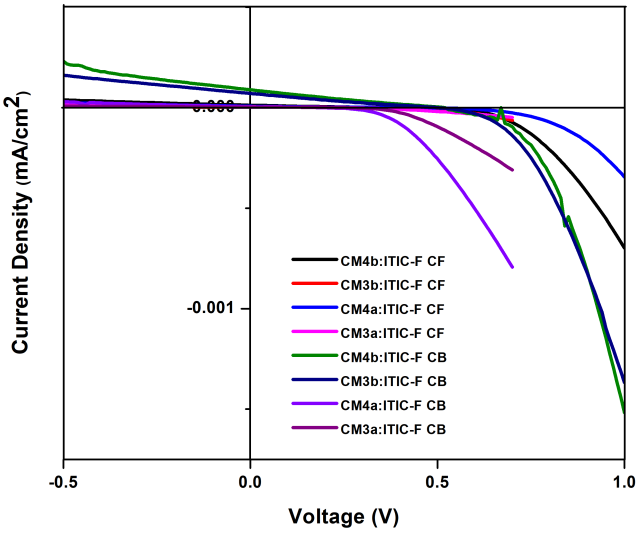

SI Figure 1. J-V curve of CM3-CM4 series.

UPS Measurements

Ultraviolet photoelectron spectroscopy (UPS) was used to acquire the ionization potentials and approximate the HOMO values for each material. All substrates (positively doped silicon; 10×10 mm^2) had 40 nm of silver deposited via thermal evaporation. Samples were prepared by dissolution in chloroform at a concentration of 5 mg/mL and stirred for a minimum of 4 h. Each solution was filtered to remove potential aggregates and sequentially spin-coated under a nitrogen atmosphere at 4000 RPM. Spectra were then acquired under ultrahigh vacuum. The presented HOMO energies and corresponding standard deviations are determined by using all values obtained at random positions on the formed film.

Thermal Gravimetric Analysis

TGA measurements were obtained using a TA Instruments TGA Q50. All measurements were performed under a flow of nitrogen. 1) Heat to 110 °C at 10 °C/min. 2) Hold at 110 °C for 20 min. 3) Heat to 600 °C at 10 °C/min. 3) Hold at 600 °C for 10 min.

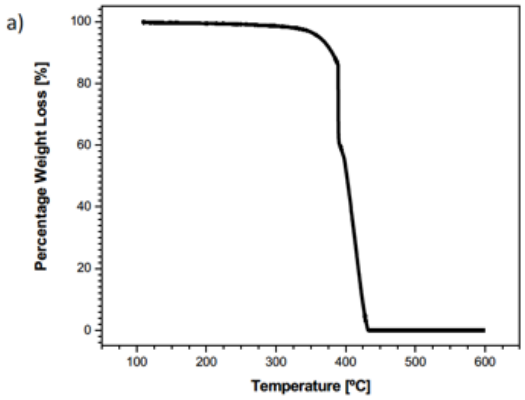

a) CM1a 5% Weight loss temperature measured by TGA T_d^a 362 °C.

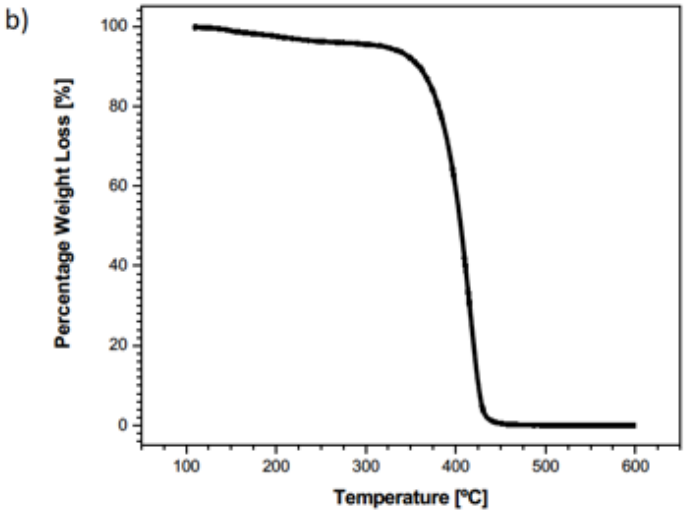

b) CM1b 5% Weight loss temperature measured by TGA T_d^a 319 °C.

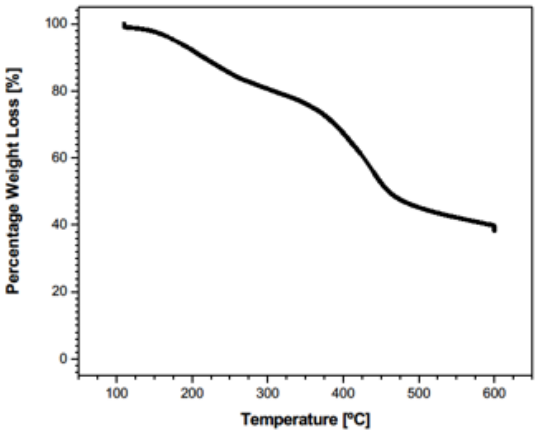

c) CM2b 5% Weight loss temperature measured by TGA T_d^a 177 ºC.

d)

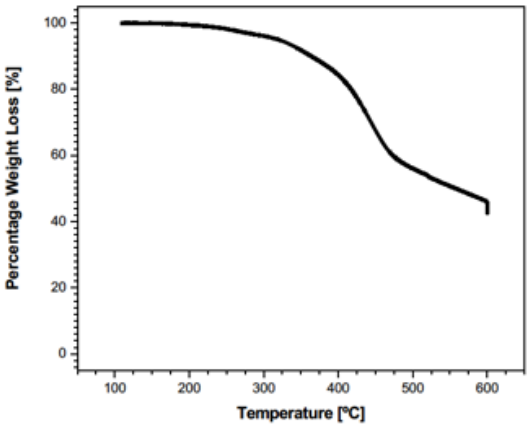

d) CM2b 5% Weight loss temperature measured by TGA T_d^a 177 ºC.

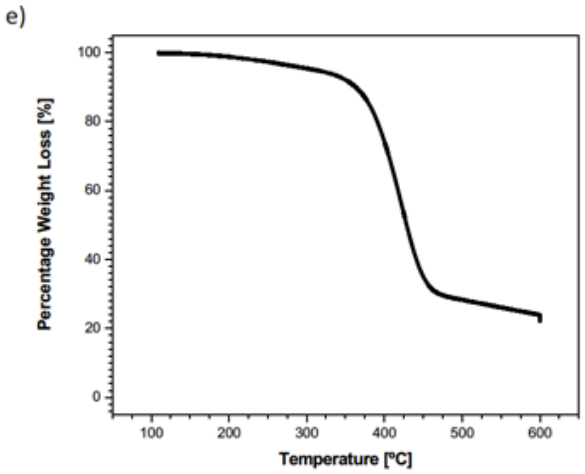

e) CM3a 5% Weight loss temperature measured by TGA T_d^a 319 ºC.

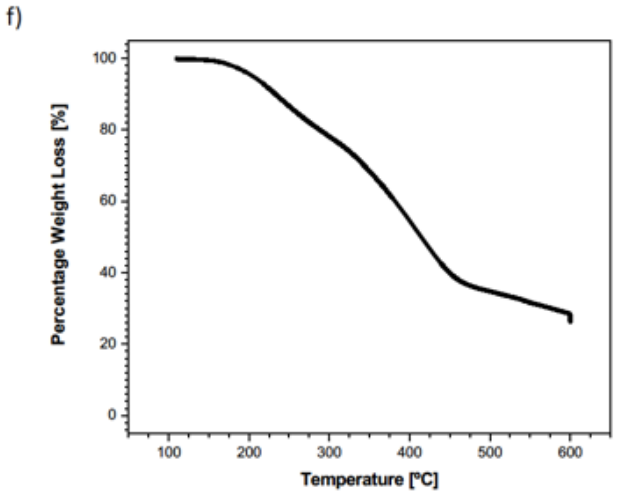

f) CM3b 5% Weight loss temperature measured by TGA T_d^a 310 ºC.

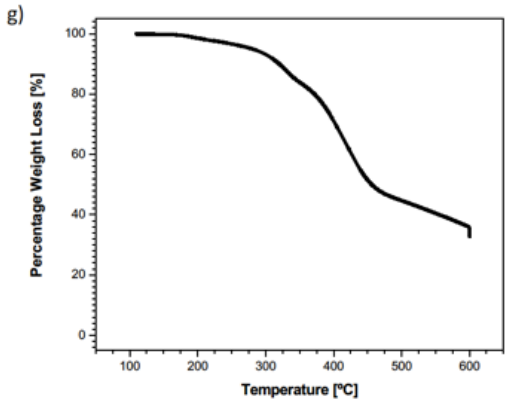

g) CM4b 5% Weight loss temperature measured by TGA T_d^a 280 °C.

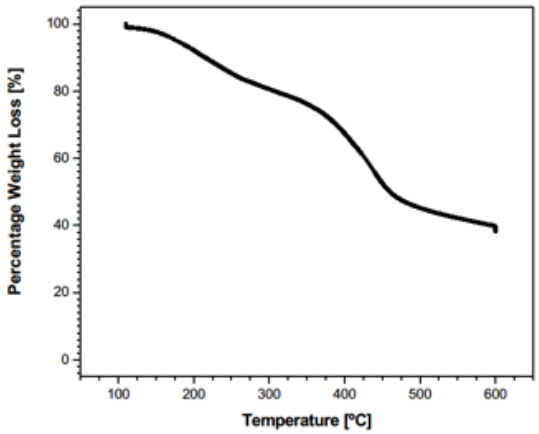

h) CM4a 5% Weight loss temperature measured by TGA T_d^a 205 °C.

SI Figure 2. a-h CM1a-CM4b respectively.

Photoluminescence Lifetime

Cruciform	τ_1 (NS) [REL.]	β_1	τ_2 (NS) [REL.]	β_2	$\tau_D{}^A$ (NS)	Φ (%)
CM1a	1.5 [41%]	5438.34	2.57 [59%]	4587.75	1.99	18
CM1b	2.42 [100%]	11421.79	--	--	2.42	23
CM2a	1.29 [66%]	8658.05	4.01 [34%]	1406.67	1.67	5
CM2b	1.1 [60%]	8429.35	3.43 [40%]	1796	1.51	3
CM3a	1.62 [65%]	8338.90	3.52 [35%]	2001.40	1.99	5
CM3b	1.75 [69%]	8140.25	3.75 [31%]	1708.03	2.09	5
CM4a	1.61 [57%]	7217	4.26 [41%]	1924.65	2.16	2
CM4b	1.44 [25%]	4417.67	3.45 [72%]	5374.61	3.54	2

SI Table 1. B1, B2 represents the weighting parameters of each lifetime.

The data was obtained as an exponential decay function, except the cases of SM 2-F and SM 3-F were obtained as biexponential decay functions by the following equations.

$$I(t)=B1e^{-t\tau 1}+B2e^{-t\tau 2}$$

$$\tau_{avg}=(B_1\tau_1 + B_2\tau_2)/(B_1+B_2)$$

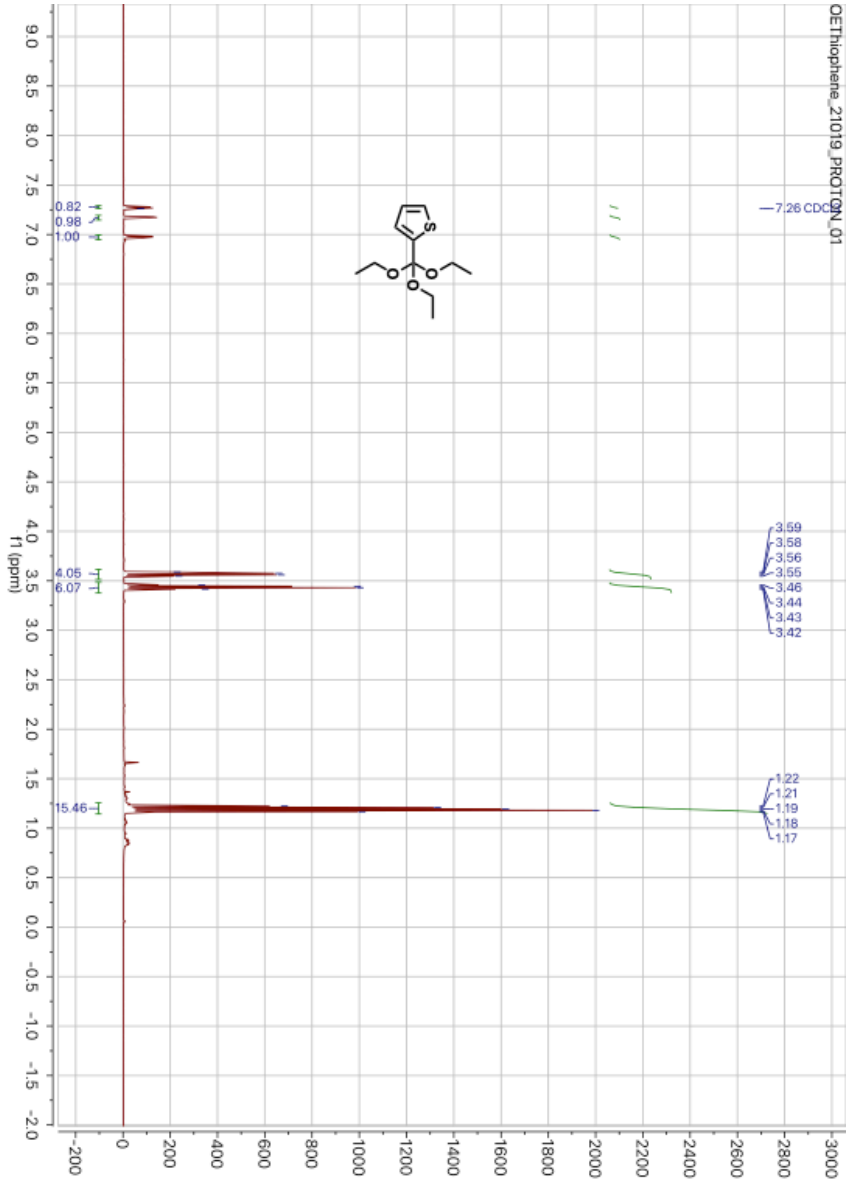

SI Figure 3. H NMR of 2-(triethoxymethyl)thiophene.

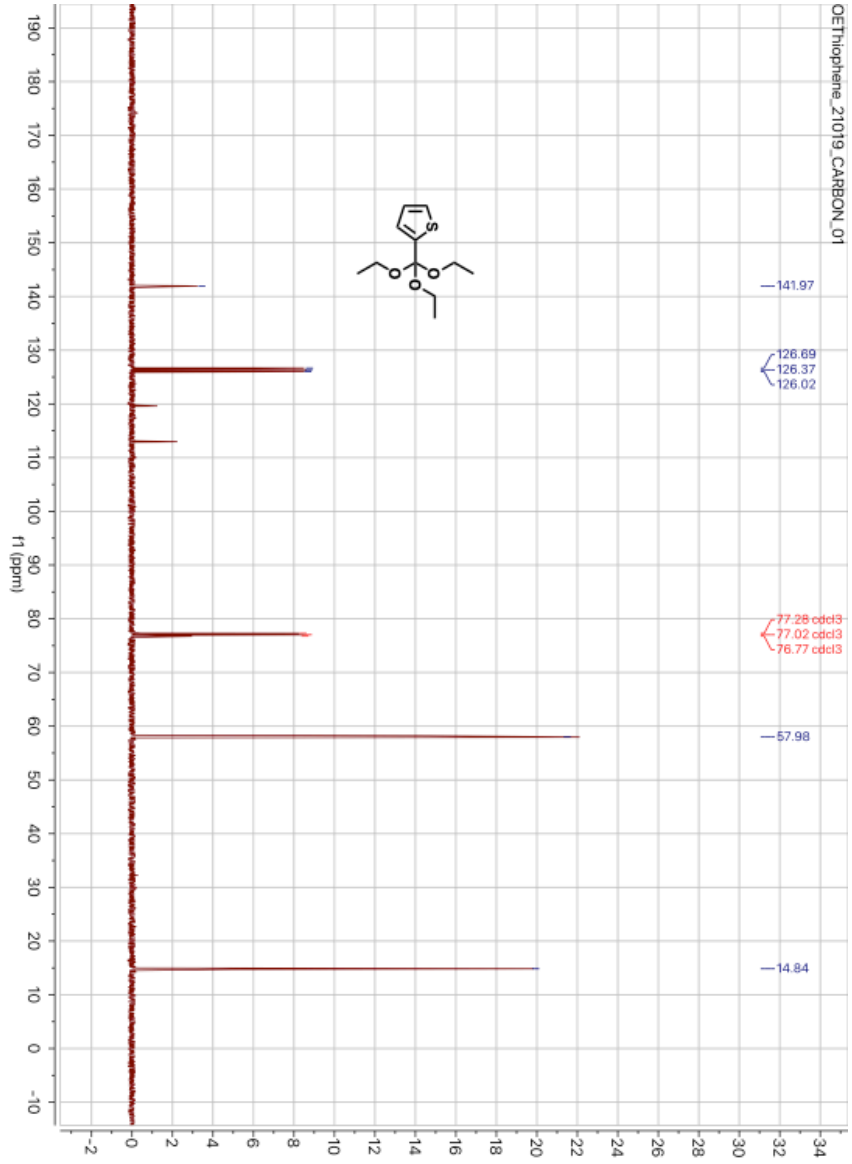

SI Figure 4. C NMR of 2-(triethoxymethyl)thiophene.

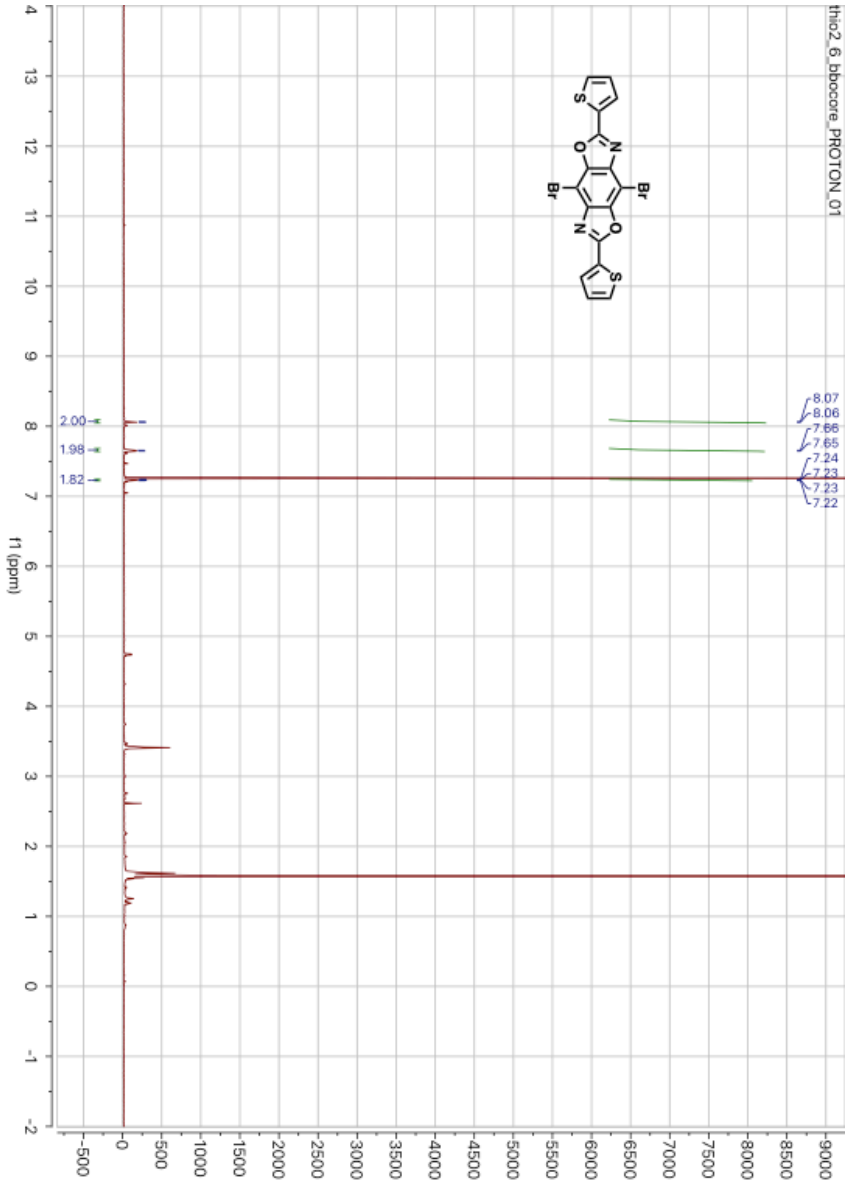

SI Figure 5. 4,8-dibromo-2,6-di(thiophen-2-yl)benzo[1,2-*d*:4,5-*d'*]bis(oxazole) (3).

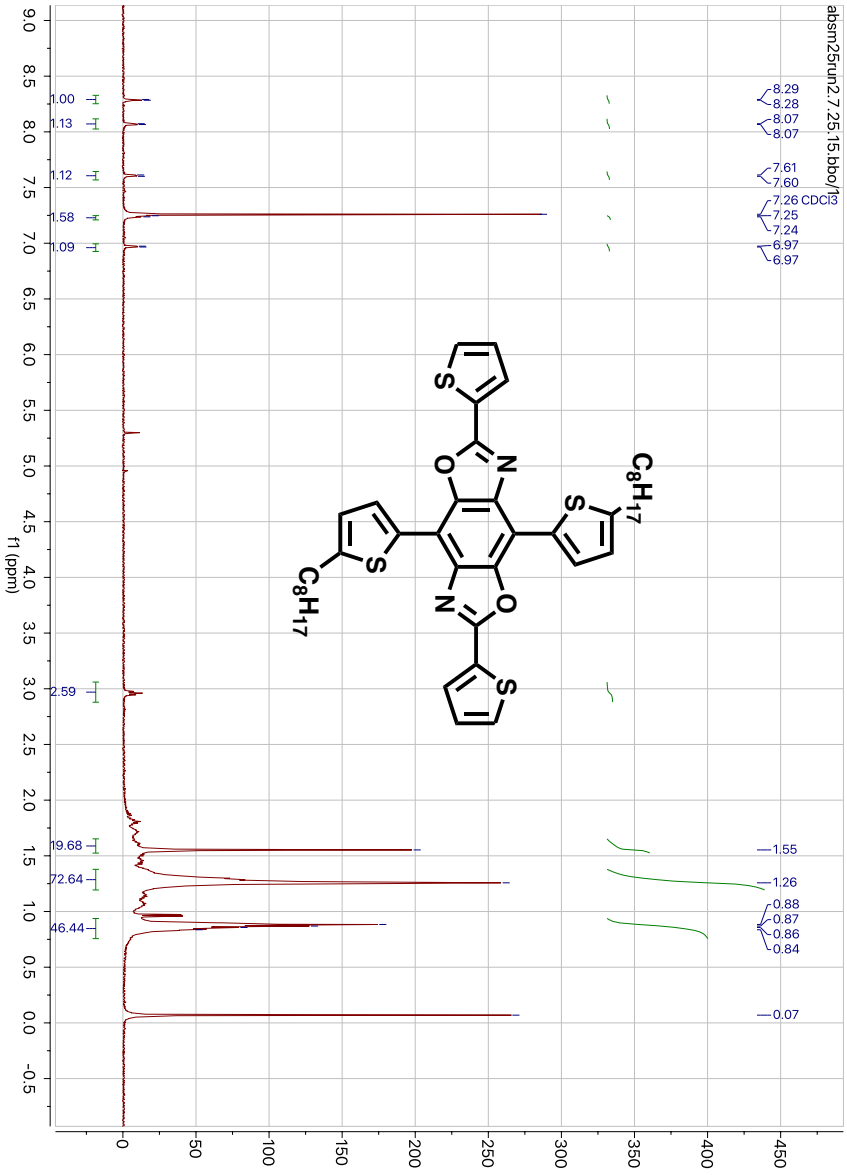

SI Figure 6. H NMR of CM1a

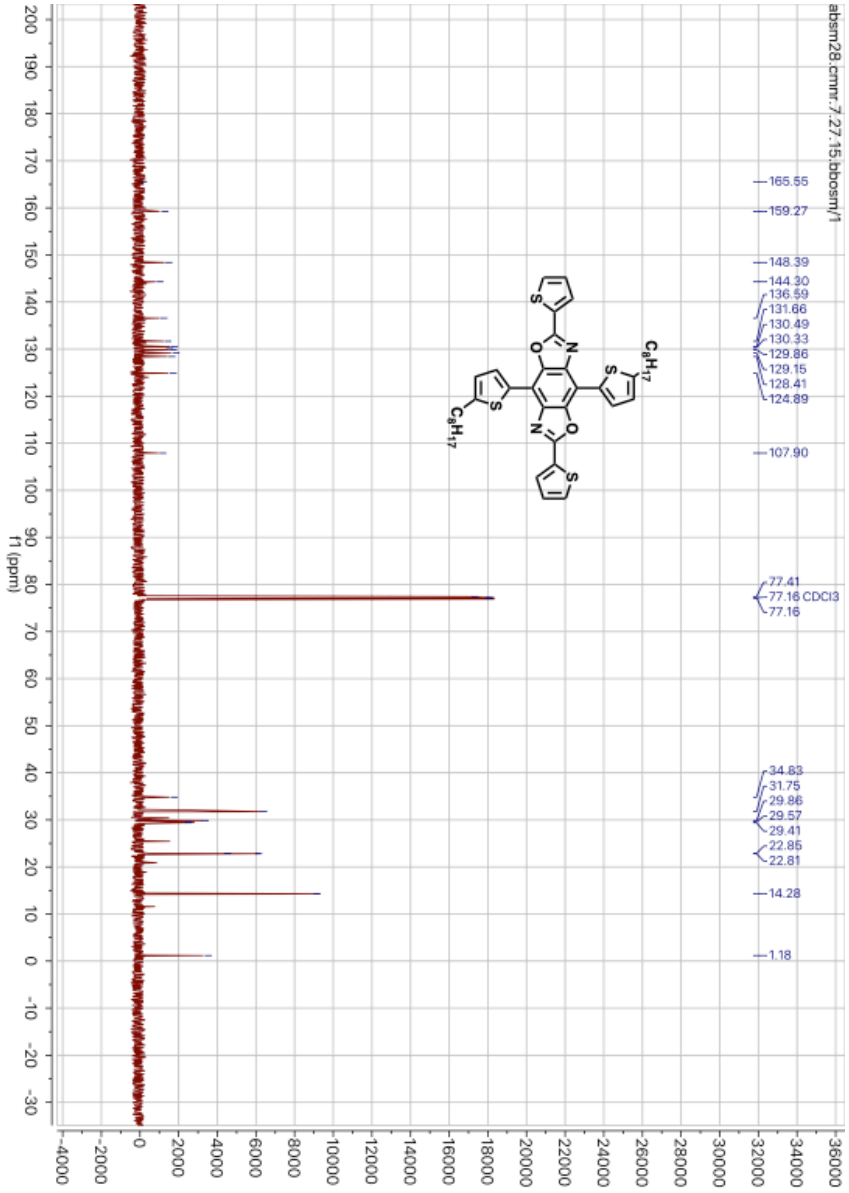

SI Figure 7. C NMR of CM1a

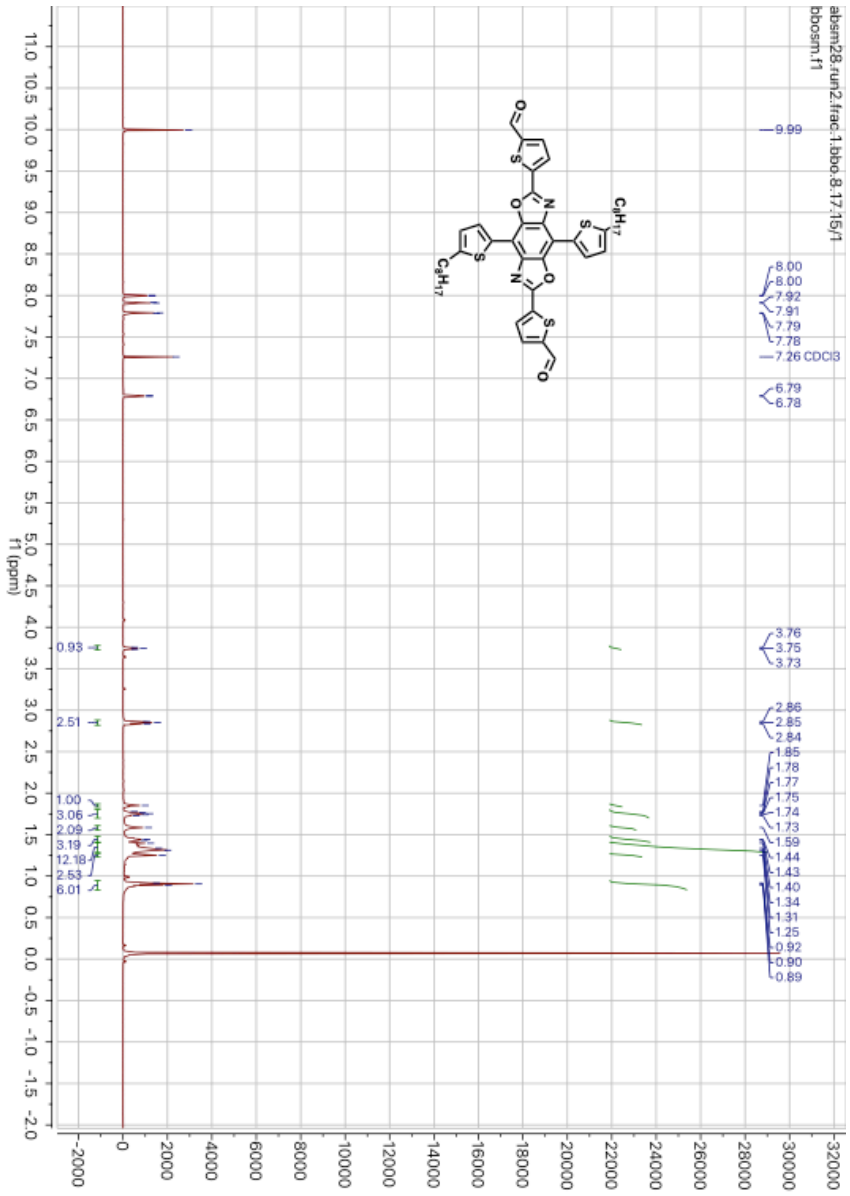

SI Figure 8. C NMR of CM2a

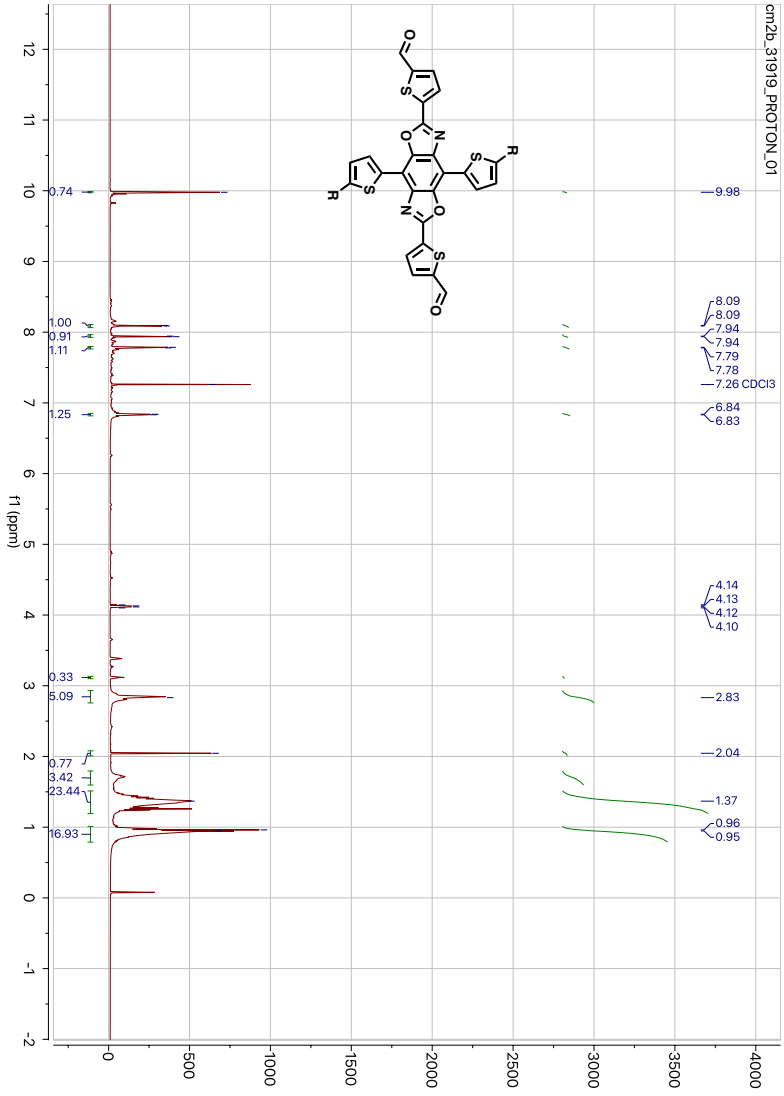

SI Figure 9. H NMR of CM2b

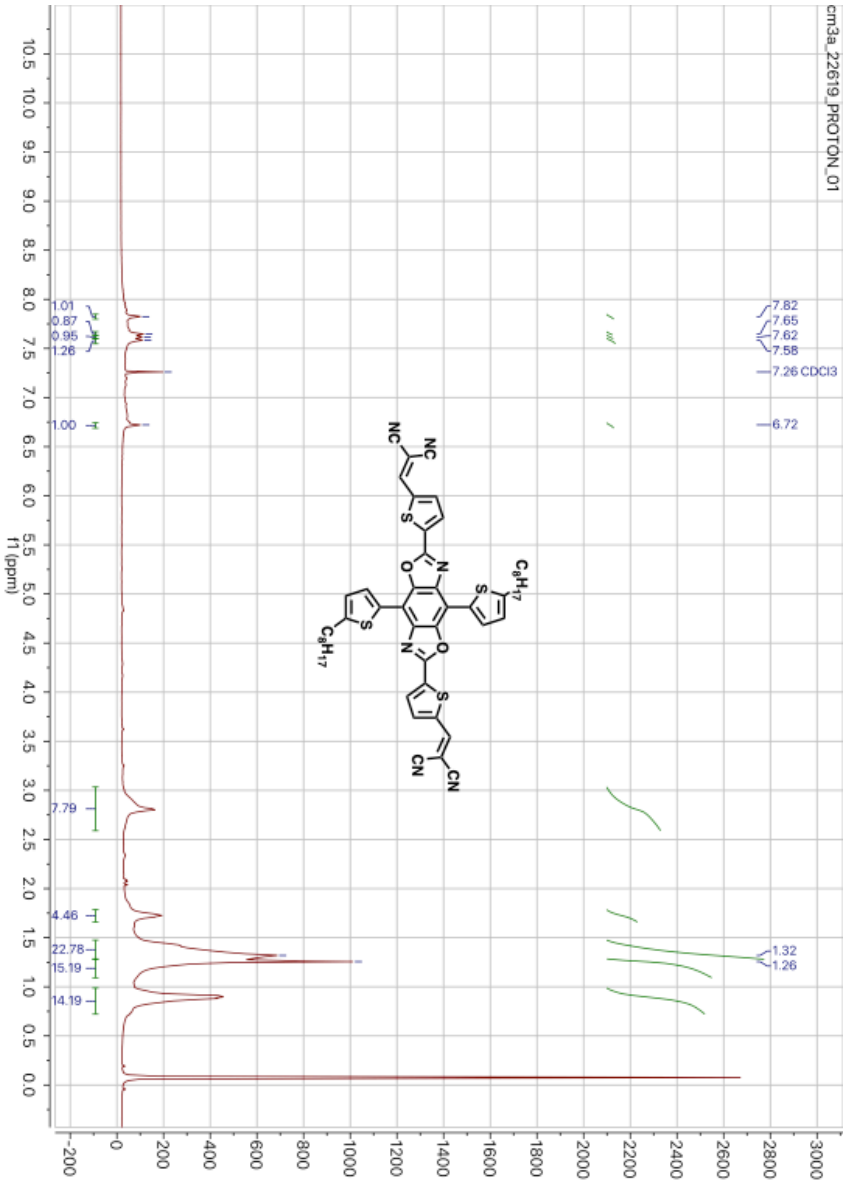

SI Figure 10. H NMR of CM3a

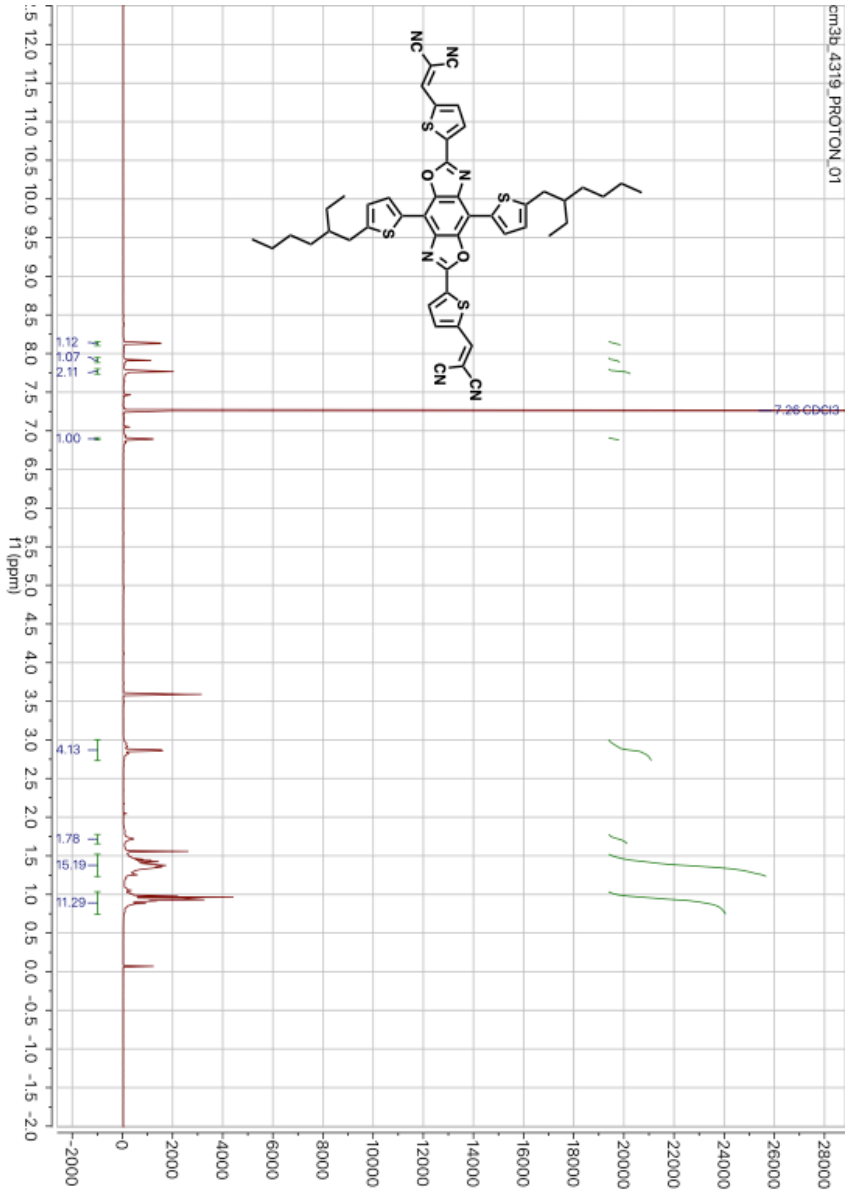

SI Figure 10. H NMR of CM3b

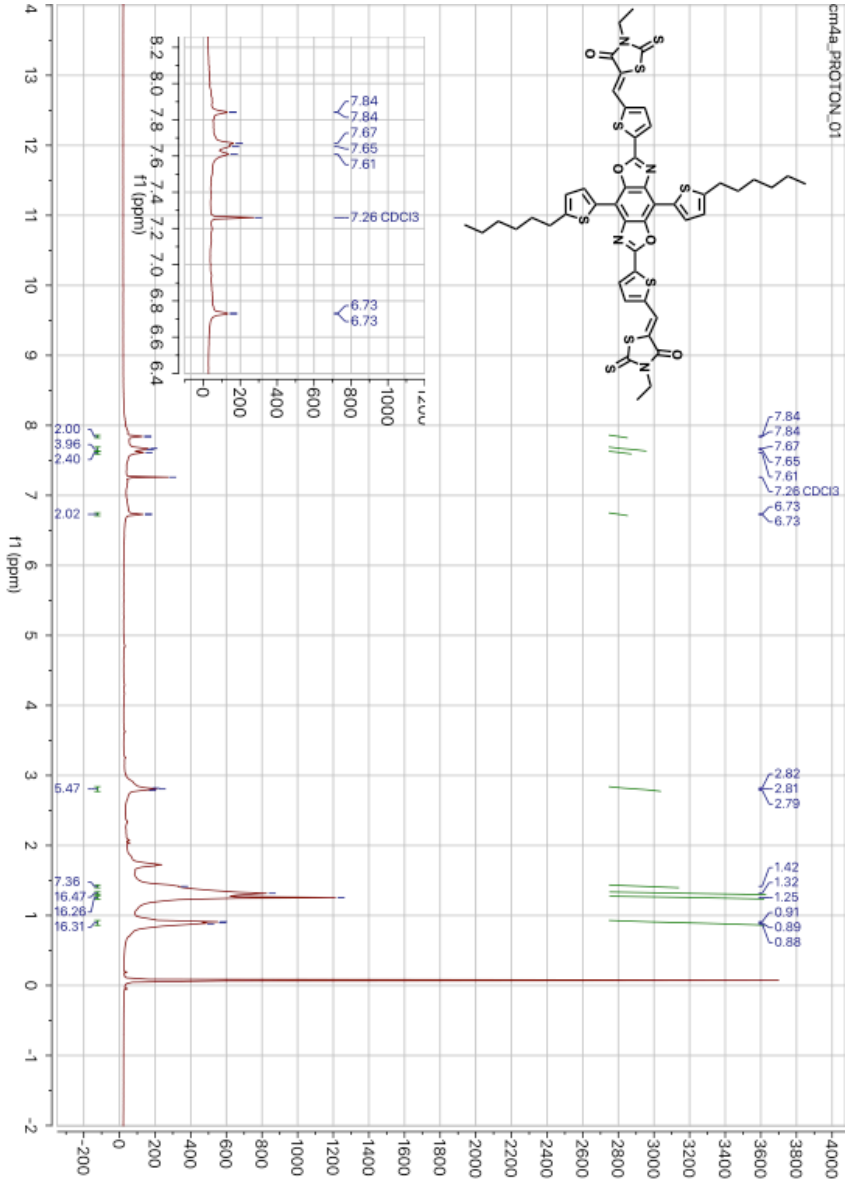

SI Figure 11. H NMR of CM4a

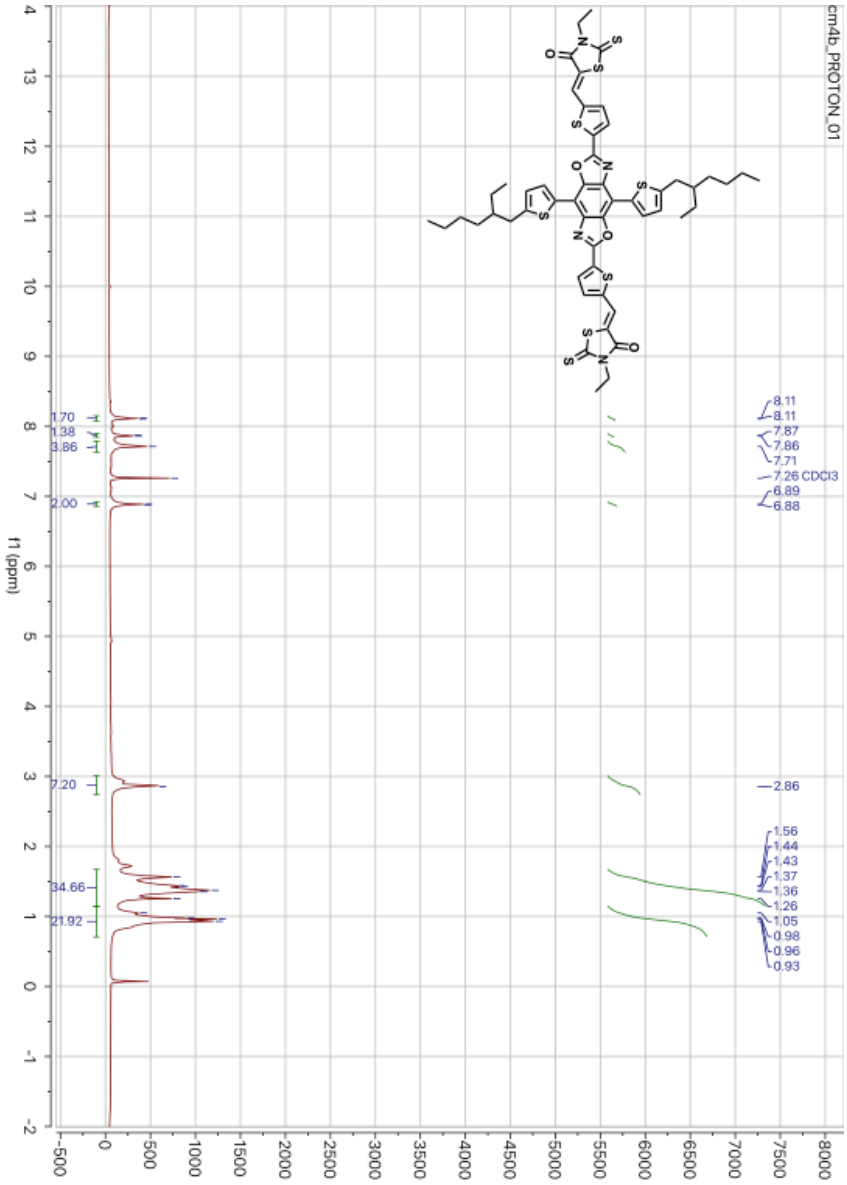

SI Figure 12. H NMR of CM4b

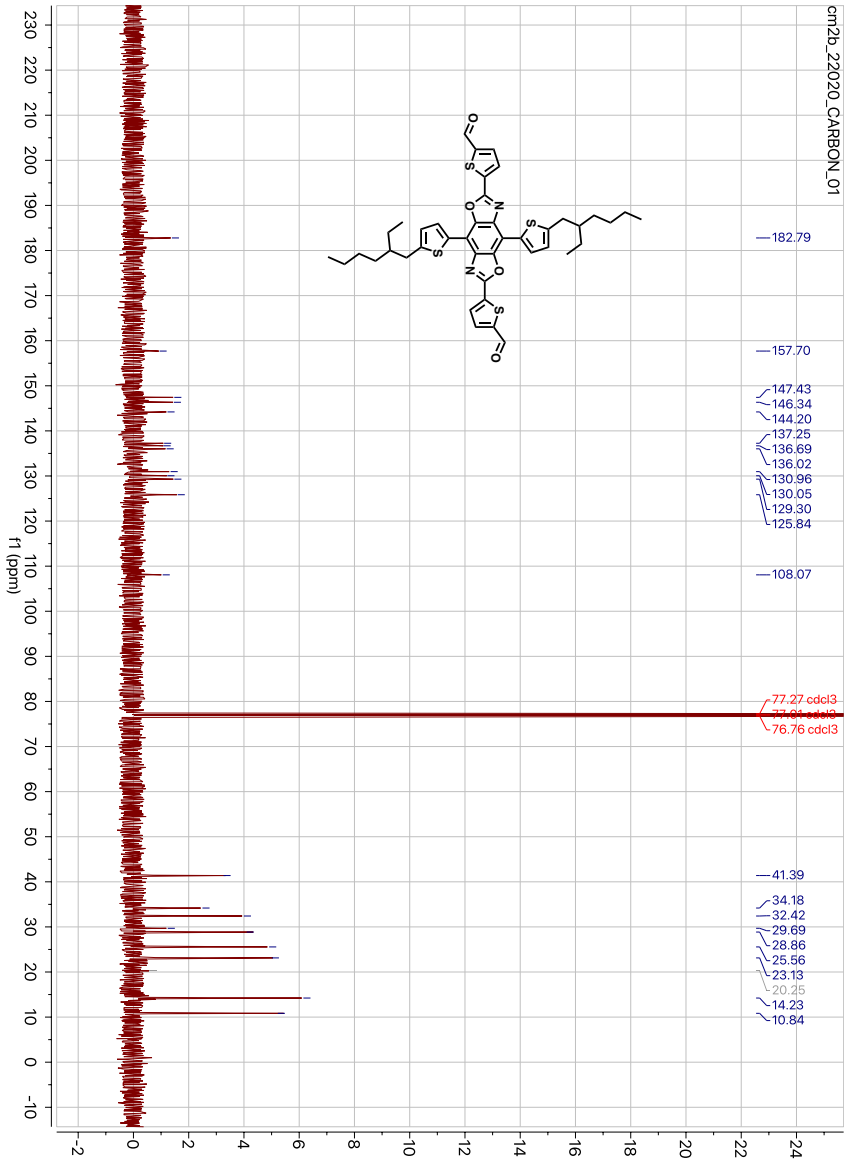

SI Figure 13. H NMR of CM2b

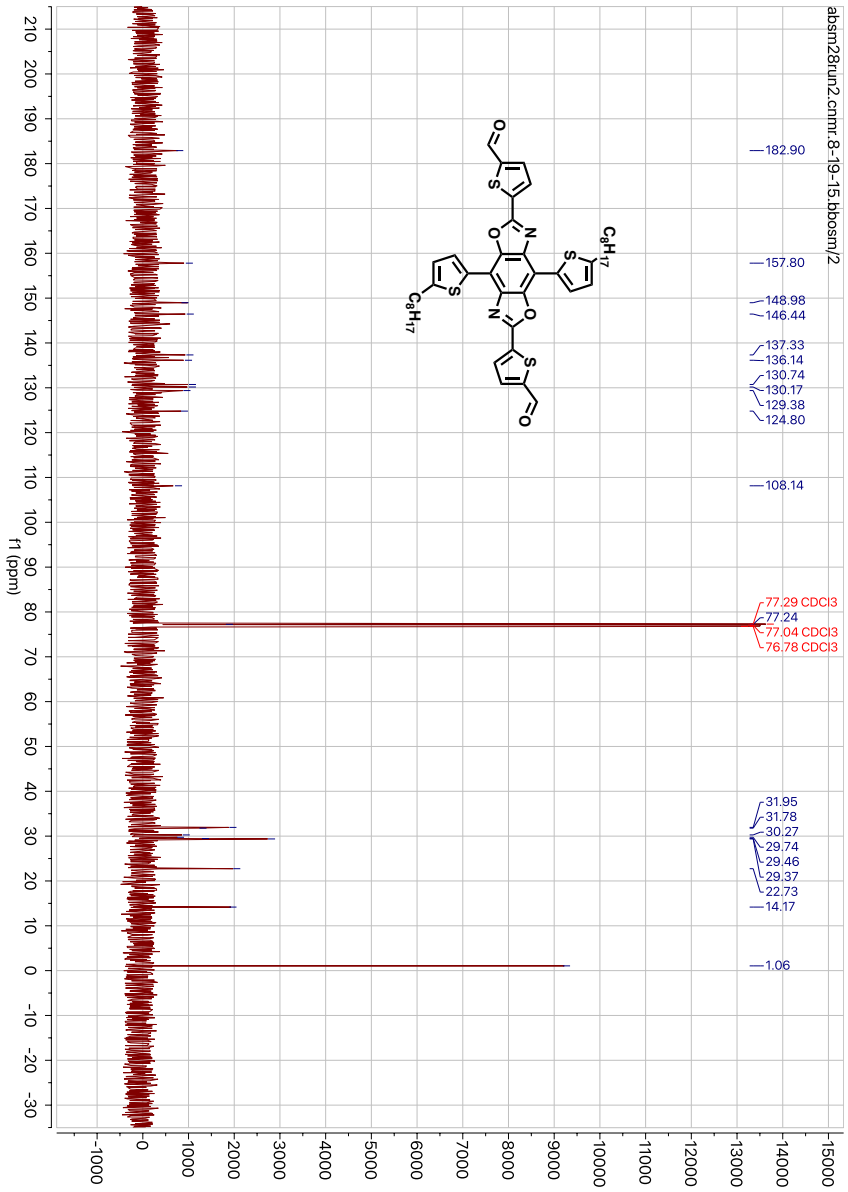

SI Figure 14. H NMR of CM2b

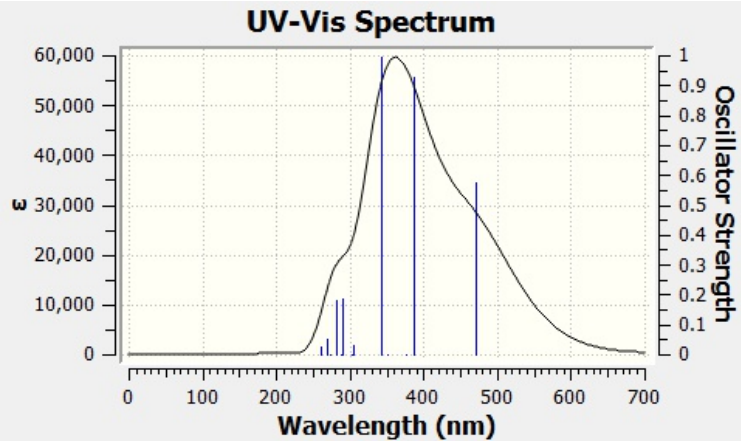

Excited state	Energy (eV)	Wavelength (nm)	Oscillator Strength
1	2.64	469.32	0.57
2	3.28	377.62	1.03
3	3.32	373.09	0.00
4	3.55	349.16	0.00
5	3.69	336.13	1.08
6	4.16	298.00	0.00
7	4.24	292.71	0.00
8	4.24	292.13	0.03
9	4.37	289.56	0.00
10	4.38	282.87	0.18
11	4.41	281.03	0.20
12	4.65	266.36	0.00
13	4.74	261.79	0.06
14	4.76	260.38	0.00
15	4.81	257.73	0.00

SI Figure 15. CM1 Simulated UV-Vis (the lines are indicative of the 15 excited states) excited states

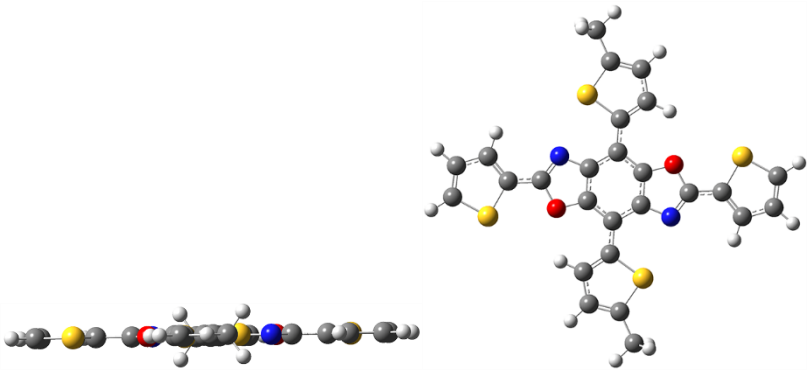

CM1 Geometric images gas phase

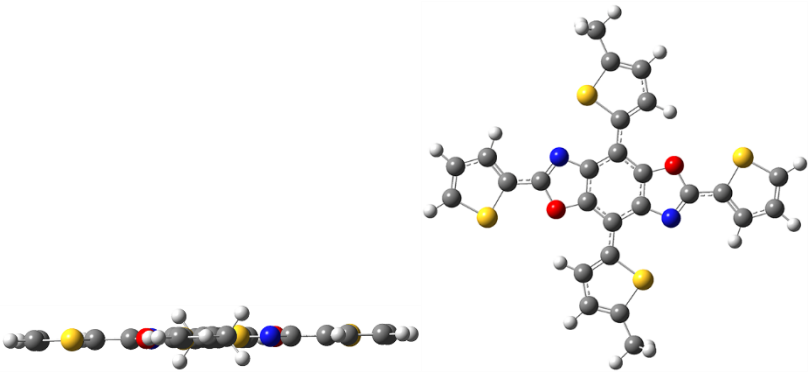

CM1 Geometric images chloroform phase

SI Figure 16. DFT geometries gas versus chloroform phase.

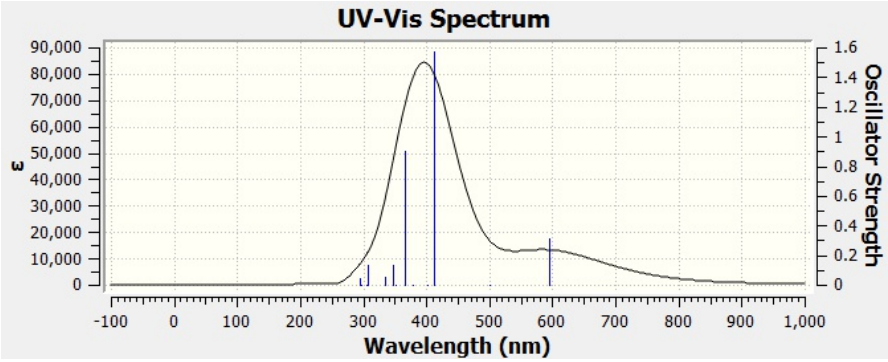

Excited state	Energy (eV)	Wavelength (nm)	Oscillator Strength
1	2.09	593.93	0.31
2	2.48	500.32	0.00
3	3.00	413.07	1.57
4	3.08	402.02	0.00
5	3.28	378.38	0.00
6	3.28	378.38	0.00
7	3.38	366.70	0.90
8	3.53	351.03	0.00
9	3.56	347.43	0.14
10	3.70	334.68	0.00
11	3.71	333.77	0.05
12	4.03	307.82	0.13
13	4.05	305.91	0.00
14	4.18	296.55	0.00
15	4.20	295.06	0.05

SI Figure 17. CM2 Simulated UV-Vis (the lines are indicative of the 15 excited states) excited states and CM 2 Lowest Excited States.

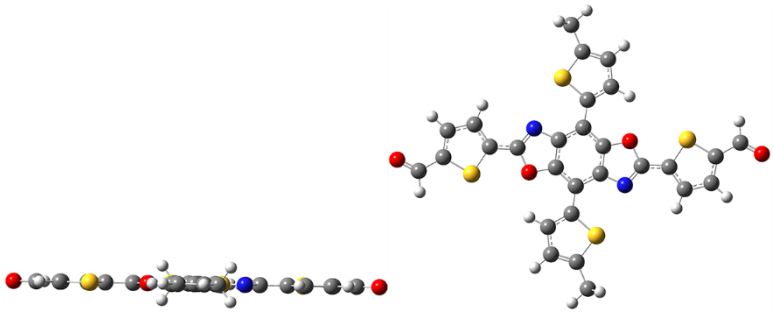

CM2 Geometric images gas phase

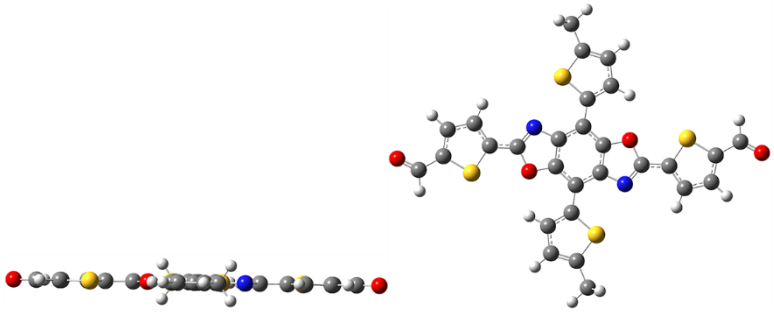

CM2 Geometric images chloroform phase

SI Figure 18. DFT geometries gas versus chloroform phase.

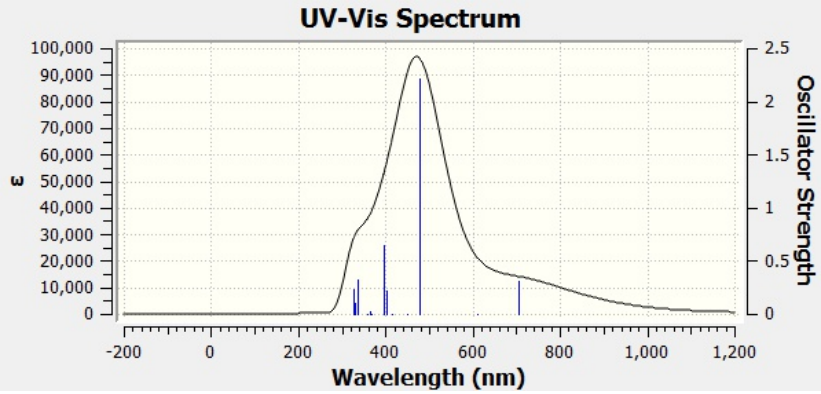

Excited state	Energy (eV)	Wavelength (nm)	Oscillator Strength
1	1.76	705.13	0.31
2	2.03	609.99	0.00
3	2.59	479.22	2.21
4	2.75	451.05	0.00
5	3.00	413.89	0.00
6	3.08	401.95	0.22
7	3.13	396.06	0.64
8	3.37	367.95	0.00
9	3.40	364.28	0.03
10	3.46	358.41	0.00
11	3.68	336.60	0.32
12	3.75	330.40	0.00
13	3.77	329.04	0.11
14	3.78	327.84	0.00
15	3.79	327.24	0.23

SI Figure 19. CM3 Simulated UV-Vis (the lines are indicative of the 15 excited states) excited states and CM 3 Lowest Excited States.

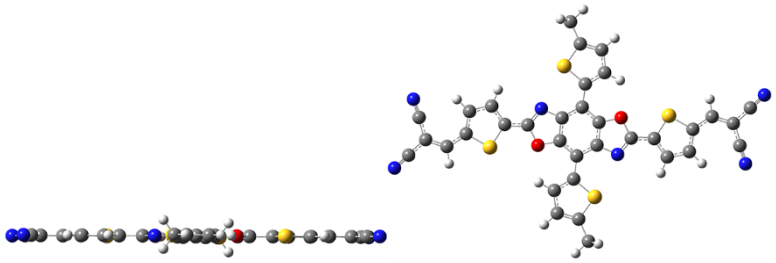

CM3 Geometric images gas phase

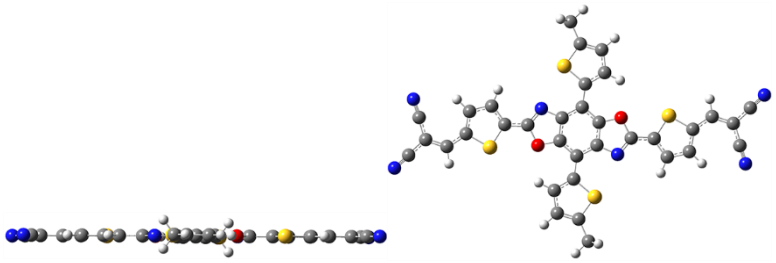

CM3 Geometric images chloroform phase

SI Figure 20. DFT geometries gas versus chloroform phase.

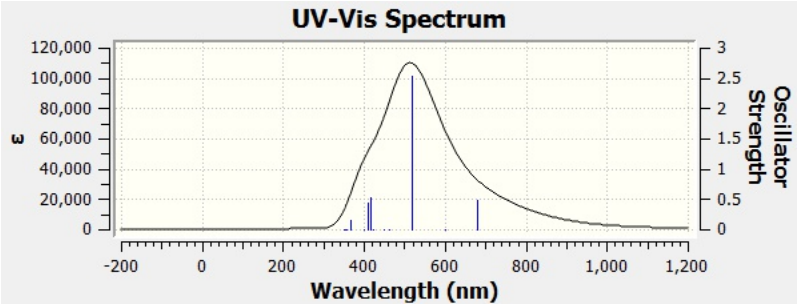

Excited state	Energy (eV)	Wavelength (nm)	Oscillator Strength
1	1.82	681.16	0.48
2	2.06	601.19	0.00
3	2.40	517.16	2.54
4	2.68	462.34	0.00
5	2.77	448.04	0.00
6	2.94	421.42	0.00
7	2.94	421.41	0.00
8	2.97	417.61	0.53
9	3.04	408.10	0.45
10	3.11	398.94	0.00
11	3.37	367.85	0.15
12	3.46	358.28	0.01
13	3.50	354.61	0.00
14	3.51	354.14	0.01
15	3.55	348.88	0.00

SI Figure 21. CM4 Simulated UV-Vis (the lines are indicative of the 15 excited states) excited states and CM4 Lowest Excited States.

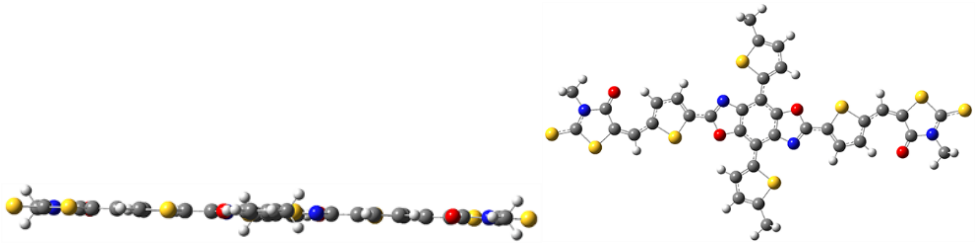

CM4 Geometric images gas phase

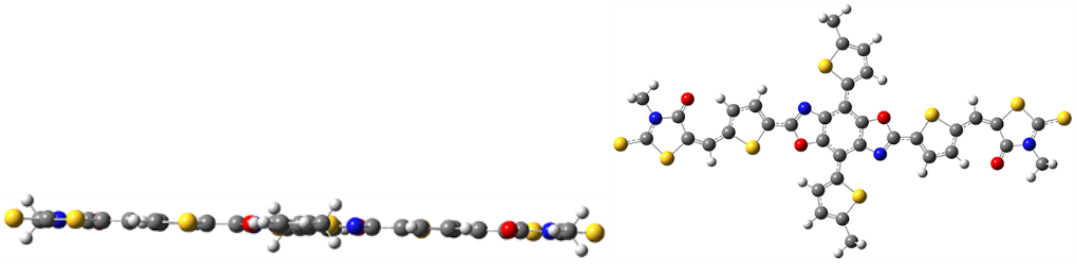

CM4 Geometric images chloroform phase

SI Figure 21. DFT geometries gas versus chloroform phase.

CHAPTER THREE: CROSS-CONJUGATED BENZOBISAZOLE COPOLYMERS FOR ORGANIC SOLAR CELLS

SECTION ONE - ABSTRACT

A new conjugated polymer were synthesized taking of the cruciform-like Benzobisoxazole (BBO) donor moiety with 1,3-bis(2-ethylhexyl)-4*H*,8*H*-benzo[1,2-*c*:4,5-*c'*]dithiophene-4,8-dione (BDD) as the acceptor moiety. The BBO-BDD polymer exhibit absorption max of 492 nm. BBO-BDD polymer also displayed thermal stability well above device operating temperature with 5% decomposition above 300ºC. Optical band gap of approximately 1.8 eV and highest occupied molecular orbital level of -5.3 eV and lowest occupied molecular level of -3.5 eV. Based on these opto-electronic properties indicate incorporating BBO cruciform into donor acceptor copolymer backbone serves as a promising molecular design motif for conjugated polymers for use in OPVs.

SECTION TWO - INTRODUCTION

Conjugated polymers have been incorporated into organic electronic applications such as organic photovoltaics (OPVs), organic field effect transistors (OFETs), and organic light emitting diodes (OLEDs).[29,96,140–142] Due to the relatively light weight and flexible characteristics of conjugated polymers this allows for them to be fabricated into device via low cost thin film techniques such as slot die coating and inkjet printing.[143,144] In addition, the recent development of conjugated polymers have allowed for the tuning of opto-electronic properties through careful selection of donor-acceptor moieties leading towards better energy level alignment for better charge transfer. Various strategies have also been developed to improve absorptivity of materials for optimal capture of the solar spectrum

and increased photocurrent generation. However, many materials that have been developed suffer from poor charge transport and oxidative stability. For reasons as such, benzobisoxazoles (BBOs) serves as promising building block for conjugated polymers for enhanced charge transport due its rigid-rod nature and high oxidative and thermal stability when incorporated into polymer backbone.[25,29,145] Traditionally, the synthesis of BBO based polymers required harsh reaction conditions utilizing sulfuric and polyphosphoric acid as solvent at 300°C. In efforts to establish more milder reaction conditions the Jeffries-EL group employed the use of acid chloride condensation in the presence of polyphosphoric acid trimethylsilyl ester (PPSE) at 90°C and ortho-ester condensation in THF at 50-60°C.

Previously, our group has synthesized a series of BBO copolymers with qaurterthiophene, 4,8-bis(5-(2-ethylhexyl)-thien-2-yl)-benzo[1,2-*b*:4,5-*b*′]dithiophene (BDT), and dithienylsilole (DTS) achieving moderate PCE of 1.14%, 2.78%, and 3.51%, respectively.[17,146,147] These materials exhibited moderate molecular weights ranging from 3,000-12,000 kDa and have absorption profile in the 300-600 nm region of the solar spectrum. BBO based systems have also been explored via a cruciform molecular design motif. Taking advantage to the 2,6- and 4,8- conjugation pathway of the BBO core allow for appropriate tuning of band gap for effective absorption.[34] Utilizing this strategy would potentially provide a better understanding of the structural activity relationship of BBO as a donor material. In efforts to improve upon the tuning of the optoelectronic properties and overall photovoltaic properties of BBO based polymers, a new BBO benzodithienodione (BDD) copolymer was synthesized.

SECTION THREE: RESULTS AND DISCUSSION

SYNTHESIS AND CHARACTERIZATION

The structure and synthetic route of target polymers are shown in **scheme 1**. The tetrathiophenebenezobisoxazole (**2**) precursor was synthesized according to literature procedure in moderate yields.[34] The use of branched ethylhexyl alkyl side chain was selected to improve solubility for solar cell fabrication. Furthermore, subsequent dilithiation of **2** at 0^{o}C in the presence of trimethyl tin chloride yielded **3**. Monomer **4** was synthesized according to literature procedure via Friedel-Crafts like ring closure to form 4 in low yields of 15%. **3** and **4** was subsequently used without further purification to undergo stille polymerization utilizing catalytic Pd_2dba_3 and P(*o*-tolyl)$_3$ to synthesize BBOBDD polymer in moderate yield of 51%. Resulting polymer was end capped with phenyl. BBOBDD polymer were readily soluble in chlorinated solvents, purified via Soxhlet extraction, and characterized via NMR spectroscopy and gel permeation chromatography. Purification of BBOBDD polymer consisted of precipitation in cold methanol with gentle stirring. The polymer precipitate was then filtered into cellulose thimble to undergo Soxhlet extraction in efforts to remove low molecular weight materials. Following Soxhlet extraction, BBOBDD were rotavap to concentrated and dissolved in approximately 4-5 ml of chloroform and passed through short silica gel column in efforts to remove any residual catalyst, salts, and impurities. BBOBDD were then precipitated again into cold methanol with gentle stirring. BBOBDD were dried under high vacuum for at least 48 hours. H NMR spectroscopy of was characterized at 50 ^{o}C and gel permeation chromatography (GPC) in

chloroform to identify chemical structure and molecular weights of target polymer. The thermal properties of the materials were studies utilizing differential scanning calorimetry (DSC) and thermogravimetric analysis (TGA) under nitrogen. BBOBDD polymer showed good thermal stability with 5% weight loss all above XXX ^{o}C. DSC traces did not show any transitions in regards to crystallization or melting before decomposition.

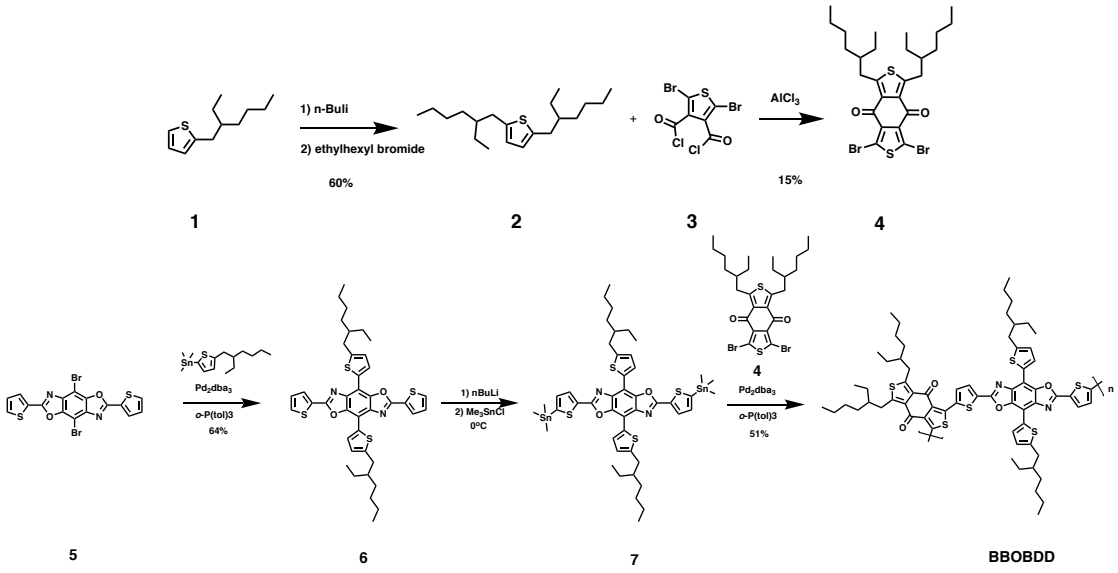

Scheme 5. Synthesis of Benzobisoxazole monomers and polymers.

OPTICAL AND ELECTRONIC PROPERTIES

The optical properties of the BBOBDD polymer was investigated via UV-Vis and fluorescence spectroscopy as illustrated in figure 29 summarized in **table 4**. BBOBDD polymer exhibited a solution and film maximum of 461 and 492 nm, respectively. Overall, the film state displays a pronounced bathochromic shift in comparison to solution phase absorption. In addition, the enhanced shoulder at approximately 575 indicate a more

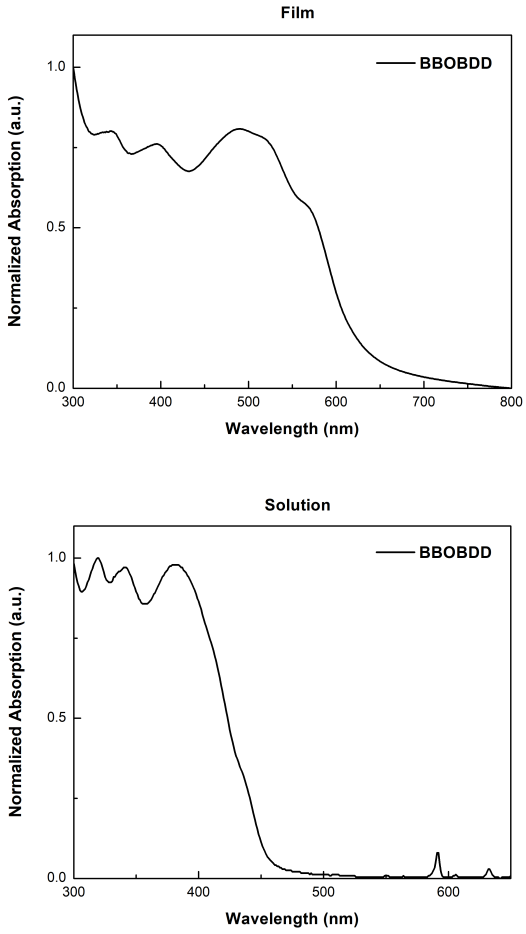

Figure 32. UV-Vis absorption profile of BBOBDD polymer film (top) and solution (bottom).

enhanced solid state π-π stacking interactions in the film. The fluorescence properties of the BBOBDD polymer was investigated via photoluminescent spectroscopy as illustrated in figure x. In solution, BBOBDD displayed a broad emission with a maximum of 601 nm and a weak shoulder at approximately 700 nm. The presence of the weak shoulder suggesting the vibronic transition from a low energy ground state mode to a higher ground state energy mode.[148] No detectable emission was observed in the polymer film state. This could be due to quenching of any emission via solid state π-π stacking interactions or aggregation present in the film state due planarization of the polymer backbone through the 2,6-axis of the benzobisoxazole core and benzodithiophenedione. The electrochemical properties of BBOBDD was evaluated via cyclic voltammetry (cv) and ultraviolet photoelectron spectroscopy (UPS). CV measurements were obtained using a platinum working electrode and an Ag/Ag^+ reference electrode. The onsets were references to Fc/Fc^+ and summarized in **table x**. BBOBDD displayed reproducible redox processes. BBOBDD HOMO and LUMO values obtained were -5.5 eV and -3.7 eV, respectively. Conversely, UPS measurements obtained a shallower lying HOMO level of -5.3 eV. LUMO level was obtained from - HOMO + Eg^{OPT} to yield a -3.5 eV LUMO.

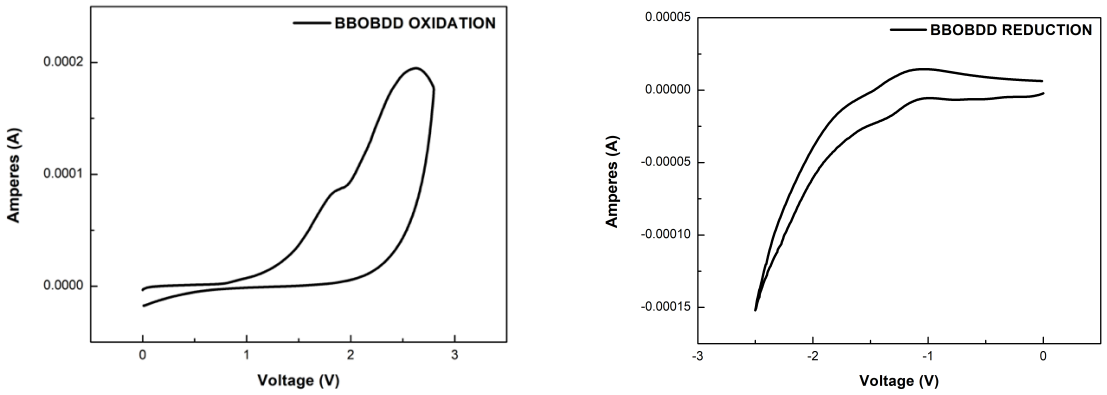

Figure 33. BBOBDD oxidation and reduction plots.

	HOMO	LUMO[a]	HOMO[b]	LUMO[b]	EgOPT	Mn	Mw	PDI	Abs
BBOBDD	**-5.3**	**-3.5**	**-5.5**	**-3.7**	**1.8**	**27909**	**30381**	**1.09**	**492**

Table 4. Summary of HOMO, LUMO, and molecular weight properties of BBOBDD polymer. [a]LUMO calculated from - HOMO + Eg^{OPT}. [b]HOMO and LUMO levels obtained from redox onset.

ORGANIC PHOTOVOTAIC DEVICES

The performance of BBOBDD in OSCs were preliminarily examined in a BHJ architecture with PC71BM as the electron acceptor. The BHJ architecture utilized conventional device fabrication of ITO/PEDOT:PSS/BBOBDD:PC71BM/Ca/Al. Active layers were spun cast from different processing solvents (CB and CF) and optimized spin coating speeds. All devices were prepared and characterized under inert atmosphere and conditions. Active layer solutions were prepared at a 1:2 (polymer: PC71BM) weight ratio. BBOBDD displayed the best device when processed from CB. Spin coating BBOBDD active layer from CB provided a film thickness of 45 nm and displayed a PCE of 0.90%.

Efforts to improve film thickness via optimizing spin coating speed lead to a marginally improved film thickness of 52 nm and PCE of 0.95%. In efforts to improve solution processability, BBOBDD: PC71BM active layer films processed from CF at 1200 rpm had a detrimental impact on active layer film thickness (58 nm) and device performance displaying a PCE of 0.67%. Optimizing active layer film thickness (1000 rpm) lead to an increasing in active layer thickness (73 nm) and an overall PCE of 0.94%. Evaluating the use of solvent additives in future device optimization could prove to be beneficial in obtaining higher Jsc and ultimately improved PCE. Atomic force microscopy (AFM) images of the best performing devices were examined to evaluate active layer surface morphologies and surface roughness. The height images of the active layer blends are illustrated in **figure 36**. When processed from CF and CB the active layer surface roughness was found to be 13.47 and 12.60, respectively. Interestingly BBOBDD active layer film displayed similar surface morphological characteristics. Further investigating the morphological characteristics of BBOBDD based polymers could offer insights into crystallinity, coherence length, and lamellar distances. The rather large surface domains (75 nm) indicated by AFM can lead inefficient charge extraction due to enhance recombination. Future exploration of optimization techniques via donor-acceptor ratio and additives could lead to improvement of morphological characteristics and overall PCE. Investigating increasing active layer solution concentration and further lowering spin coating speed of BBOBDD: PCBM can lead also lead towards optimal active thickness of 100 nm potential improving active layer absorptivity and current density.

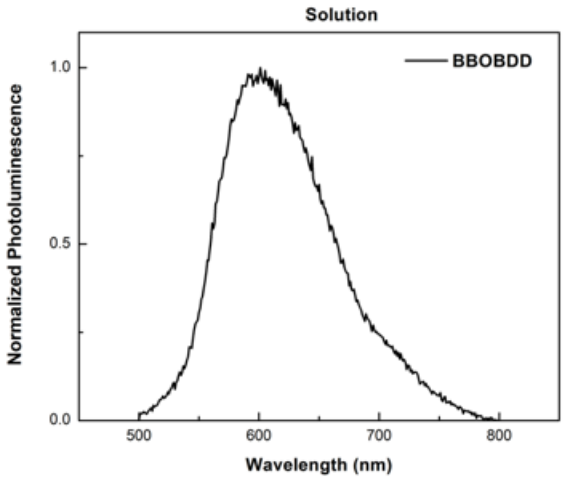

Figure 34. Photoluminescence emission profile of BBOBDD polymer solution.

	Film Abs max λ (nm)	Soln Abs max λ (nm)	Soln Em max λ (nm)	Eg^{OPTa}
BBOBDD	**492**	**451**	**601**	**1.8**

Table 5. Summary of UV-Vis and emission properties. [a]Optical bandgap determined from absorption onset.

FABRICATION OF PHOTOVOLTAIC DEVICES

All devices were evaluated under inert atmosphere via solution-based spin-casting fabrication techniques. Organic photovoltaic devices were fabricated in conventional architecture indium tin oxide (ITO)/ Poly(3,4-ethylenedioxythiophene): poly(styrene sulfonate) (PEDOT:PSS)/polymer:[6,6]-phenyl-C_{71}-butyric acid methyl ester ($PC_{71}BM$)/CA/Al). ITO glass substrates were cleaned via (i) sonication (Mucasol), (ii) deionized water, (iii) acetone, and (iv) isopropanol for 10 minutes each respectively. Slides

were dried in oven followed by UV-ozone treatment for 15 minutes. PEDOT: PSS layers (Clevios P VP Al 4083) were filtered (0.45 um) and spin-coated onto ITO substrates at 3500 rpm for 2 minutes then annealed at 150°C for 30 min in air. After cooling, the substrates were transferred into nitrogen filled glove box. Polymer: $PC_{71}BM$ solution were prepared in a blend ratio of 1:2 (25 mg/ml **BBOBDD**) with different solvents (CB or CF). The prepared solutions were then allowed to stir for 48 hours at 55°C (CF) or 85 °C (*o*-DCB) prior to spin coating (1000 – 1200 rpm, for 2 min). Ca (15 nm) and Al (100 nm) electrodes were successfully deposited via thermal evaporation. Current density (J-V) data were measured utilizing a Keithley 2400 source meter and simulated AM1.5G illumination (100 mW/cm^2, ABET Solar simulator) calibrated using a KG-5 filter Si reference cell.

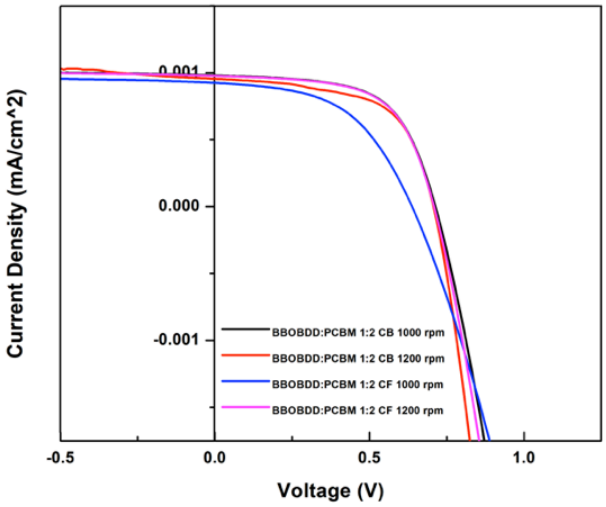

Figure 35. J-V Curve of best performing device for BBOBDD:PC71BM devices.

Polymer	*Solution*	*Acceptor*	*Spin coating speed [rpm]*	*Active layer thickness [nm]*	*D/A*	V_{oc} *[V]*	J_{sc} *[mA/cm²]*	*FF*	*PCE [%]*
BBOBDD	CB	C71	1200	45	1:2	0.68	2.12	40.30	0.87
						0.73	**2.02**	**43.52**	**0.90**
						0.78	2.27	43.02	0.83
			1000	52		**0.72**	**2.18**	**41.86**	**0.95**
						0.71	2.10	40.31	0.90
						0.70	1.85	40.93	0.80
						0.61	1.83	41.55	0.80
	CF	C71	1200	58	1:2	**0.65**	**2.05**	**40.96**	**0.67**
						0.61	1.96	49.63	0.63
						0.66	1.90	40.43	0.64
						0.62	1.83	48.11	0.55
			1000	73		0.61	2.18	49.92	0.93
						0.69	1.81	49.87	0.76
						0.50	1.54	27.69	0.06
						0.69	**2.17**	**41.43**	**0.94**

Table 6. Summary of BBOBDD device processing conditions. Best performing conditions.

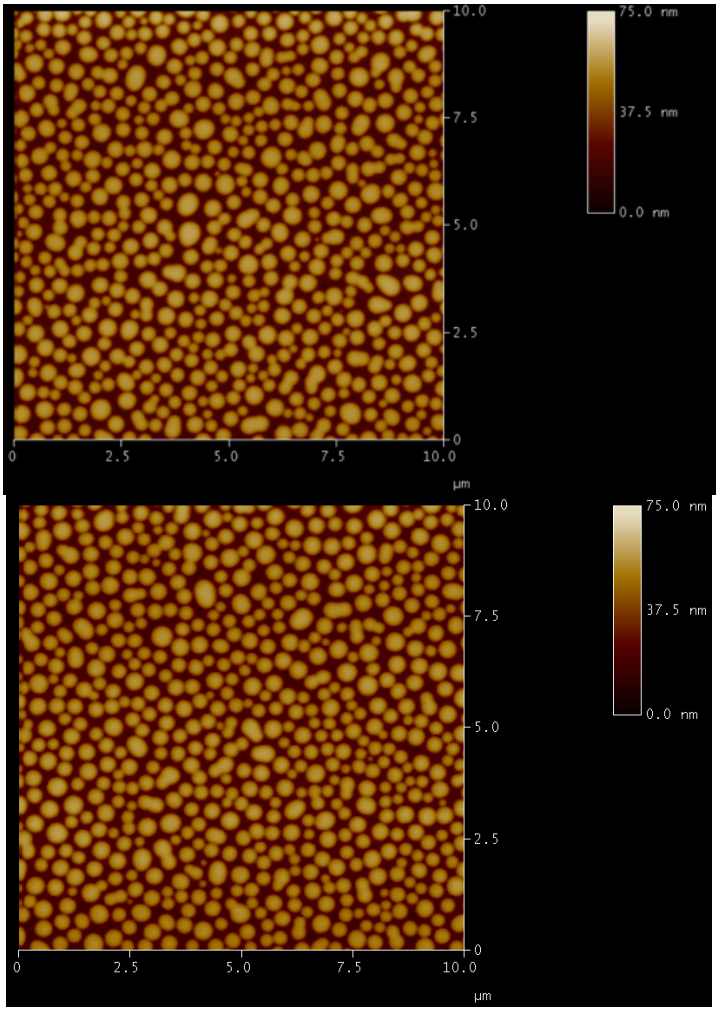

Figure 36. AFM images of BBOBDD active layer films for best performing devices when processed from CB RMS 12.60 (top) and CF RMS 13.47 (bottom).

CONCLUSION

A new "cruciform-like" 2D-conjugated benzobisoxazole based polymer has been synthesized. BBOBDD polymer was synthesized via Stille cross-coupling polymerization in moderate yields. The BBOBDD polymer exhibited good molecular weights with a relatively narrow polydispersity index when compared to other polymer system of similar

structure that have been synthesized under similar polymerization conditions. The overall opto-electronic properties represent a promising outlook for future derivatives of molecular design motif with a HOMO, LUMO, and Eg^{OPT} level of -5.3 eV, -3.5 eV, and 1.8 eV, respectively. In addition, a broad film state absorption profile is observed when compared to other reported BBO based materials which proves to be beneficial towards device performance. Despite the relatively narrow bandgap and good optical properties, poor film thickness led to overall limited device performance of 0.95%. The low Jsc observed warrants further investigation into improving this parameter with evaluating various solvent additives such as 1,8-diiodooctane or diphenyl ether in efforts to improve device performance. Further exploration of other modified BBOBDD polymer structures and device applications will be evaluated in future work to improve upon the photovoltaic performance of BBOBDD based materials.

SECTION FOUR – EXPERIMENTAL METHODS

Materials, Measurements, and Synthesis

4,8-bis(5-(2-ethylhexyl)thiophen-2-yl)-2,6-di(thiophen-2-yl)benzo[1,2-*d*:4,5-*d′*]bis(oxazole) (6)

A solution of 1.51 g of 2-trimethyltinthiophene and 0.969 g of 4,8-dibromo-2,6-di(thiophen-2-yl)benzo[1,2-*d*:4,5-*d′*]bis(oxazole) in toluene was degassed with Argon for 45 min. Then $Pd_2(dba)_3$ (2 mol %) and $P(tol)_3$ was added with gradually heated to reflux and stirring for 24 hours under Argon. The reaction was cooled to room temperature. Reaction mixture was diluted with water and extracted 3x with $HCCl_3$ and brine. Following extraction solution the organic layer was then passed through a short silica column to

remove residual catalyst and salts and then rotovap to concentrate. Solid was further purified via column chromatography gradient 95:5 hexanes: DCM to 80:20 hexanes: DCM gradient. Desired eluents were rotovap to concentrate and dissolved in 2 ml of $HCCl_3$ and precipitated into MeOH at -78°C. Precipitate was filtered to yield a bright yellow solid (0.915 g, 64%). ^{1}HNMR (600 MHz $CDCl_3$) 8.63 (d, 2H), 8.33 (d, 2H), 7.65 (d, 2H), 7.25 (d, 2H), 7.01 (d, 2H) 3.01 (t, 6H), 1.31 (m, 8H) 1.25 (m, 4H), 0.925 (m, 4H) 0.10 (s, 17H) ^{13}CNMR (600 MHz $CDCl_3$) 157.58, 148.38, 147.28, 143.78, 142.96, 137.94, 136.25, 130.78, 130.75, 128.78, 128.24, 107.47

4,8-bis(5-(2-ethylhexyl)thiophen-2-yl)-2,6-bis(5-(trimethylstannyl)thiophen-2-yl)benzo[1,2-*d*:4,5-*d′*]bis(oxazole) (7)

In an oven dried flask, a solution of anhydrous THF containing 0.300 g of (2) was cooled to -10°C. n-Butyl lithium (2.5 M, 0.353 ml) was added dropwise to the reaction mixture. The reaction was allowed to stir at -10°C for 15 minutes then was cooled to -78°C. Reaction was quenched with 1M trimethyltin chloride solution (1.68ml) and warmed to room temperature to stir overnight. The reaction was diluted with distilled H_2O and brine. The organic layer was extracted with dichloromethane and rotovap to concentrate. The resulting oily solid was used without further purification.

2,5-bis(2-ethylhexyl)thiophene (2)

To a solution of 2-ethylhexyl thiophene and TMEDA in dry THF 2.5M solution of n-Buli in hexane was added dropwise under argon at -78 °C. After the solution was warmed to room temperature slowly the solution was cooled to -78 °C and ethylhexyl bromide was added dropwise. Allow reaction to return to root temperature and stir overnight. The

reaction was then quench with H_2O and extracted with diethyl ether x3. The organic layer was then rotovap to concentrated and product was purified via column chromatography hexane eluent to yield desired product as a light yellow oil. 1H NMR (500 MHz, Chloroform-d) δ 6.55 (s, 2H), 3.50 – 3.41 (m, 4H), 2.78 – 2.69 (m, 4H), 1.68 – 1.58 (m, 5H), 1.58 – 1.48 (m, 5H), 1.47 – 1.33 (m, 13H), 1.31 (ddd, J = 6.4, 4.0, 1.1 Hz, 4H), 1.30 – 1.20 (m, 6H), 0.97 – 0.84 (m, 20H). ^{13}C NMR (500 MHz $CDCl_3$) 123.25, 41.04, 39.12, 31.87, 28.81, 25.15, 22.82, 14.03, 10.86 HRMS *m/z*: M^+ calcd for $C_{20}H_{36}S$ 309.0245; found, 308.0269, error 2.79930 ppm

1,3-dibromo-5,7-bis(2-ethylhexyl)-4*H*,8*H*-benzo[1,2-*c*:4,5-*c'*]dithiophene-4,8-dione (4)

To a stirred solution of **2** and **3** in dry toluene anhydrous $AlCl_3$ was added in small portions at 0 ^oC. The mixture was stirred at 0 ^oC for 1 hour and then at room temperature for 8 hours. The reaction mixture was poured into a mixture of ice water and 1M HCl and extracted with DCM. The organic layer was washed with brine and dried over anhydrous $MgSO_4$, and the solvent was removed under vacuum. The crude product was purified via silica gel column with hexanes and DCM as eluent to give compound **4** as a light-yellow solid. ^{13}H NMR (500 MHz $CDCl_3$) δ 3.30 – 3.16 (m, 2H), 1.70 (p, J = 6.3 Hz, 1H), 1.34 – 1.16 (m, 6H), 0.84 (dt, J = 16.0, 7.3 Hz, 5H). ^{13}C NMR (500 MHz $CDCl_3$) 175.04, 154.91, 134.58, 132.63, 119.31, 40.96, 33.87, 33.53, 28.61, 22.98, 14.09, 10.78. HRMS *m/z*: M^+ calcd for $C_{25}H_{34}O_2S_2$ 601.0445; found, 601.0469, error 3.9930 ppm.

BBOBDD

In a dry-argon purged 2N-flask containing **2** and **4** and degassed toluene for 45 min. $Pd_2(dba)_3$ (2 mol %) and $P(tol)_3$ was added and degassed for another 10 min. The reaction was heated to reflux for 3 days. Polymer was endcapped with phenyl and allowed to stir at reflux for another 6 hours. Purification of **BBOBDD** consisted of precipitation in cold methanol with gentle stirring. The polymer precipitate was then filtered into cellulose thimble to undergo Soxhlet extraction in efforts to remove low molecular weight materials. Following Soxhlet extraction, **BBOBDD** were rotavap to concentrated and then dissolved in approximately 5 ml of chloroform and passed through short silica gel column in efforts to remove any residual catalyst and salts. **BBOBDD** were then precipitated again into cold methanol with gentle stirring. **BBOBDD** were dried under high vacuum for at least 48 hours to yield BBOBDD polymer in 40%. ^{1}H NMR (500 MHz, Chloroform-d) δ 8.19 (s, 2H), 7.80 (s, 2H), 7.70 (s, 1H), 6.89 (s, 3H), 3.31 (d, J = 53.4 Hz, 4H), 2.87 (d, J = 22.8 Hz, 7H), 1.69 (d, J = 42.1 Hz, 6H), 1.31 (d, J = 54.8 Hz, 28H), 1.16 – 0.41 (m, 32H).

SUPPLEMENTAL INFORMATION

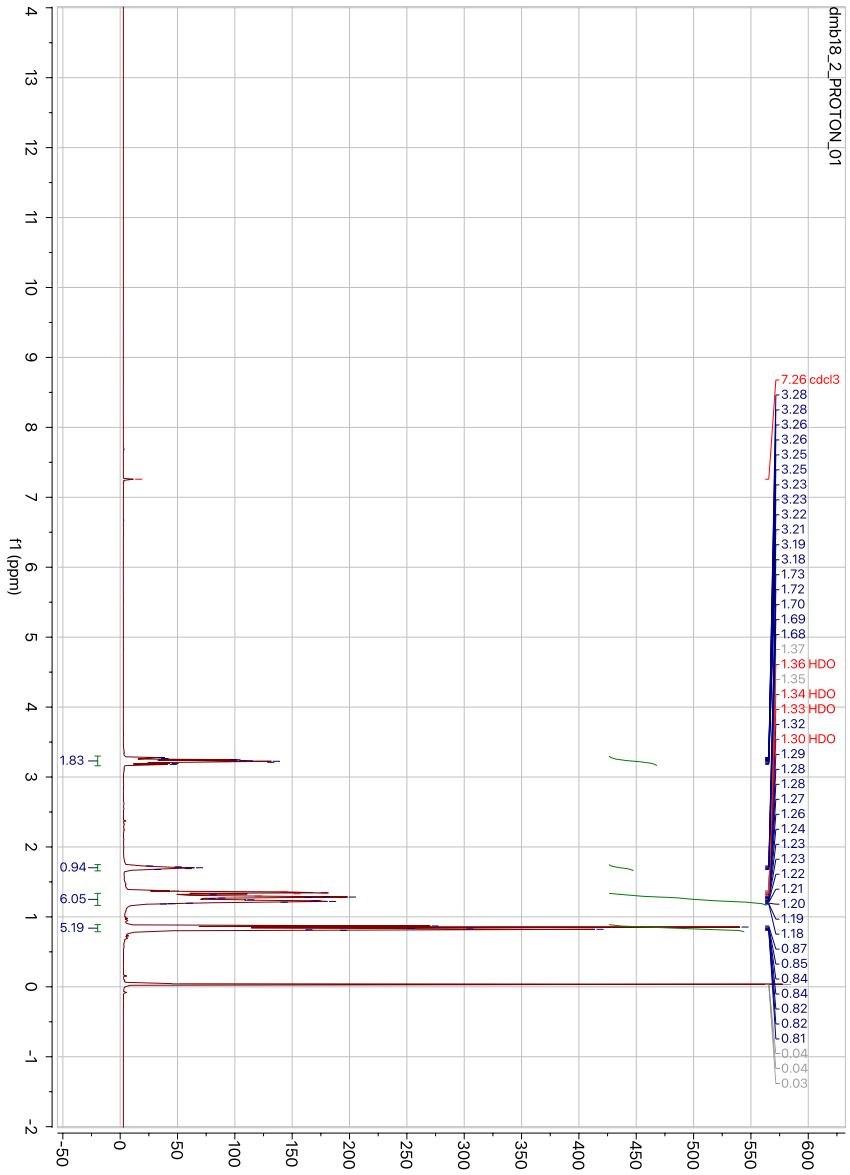

SI Figure 22. H NMR of 1,3-dibromo-5,7-bis(2-ethylhexyl)-4*H*,8*H*-benzo[1,2-*c*:4,5-*c*′]dithiophene-4,8-dione

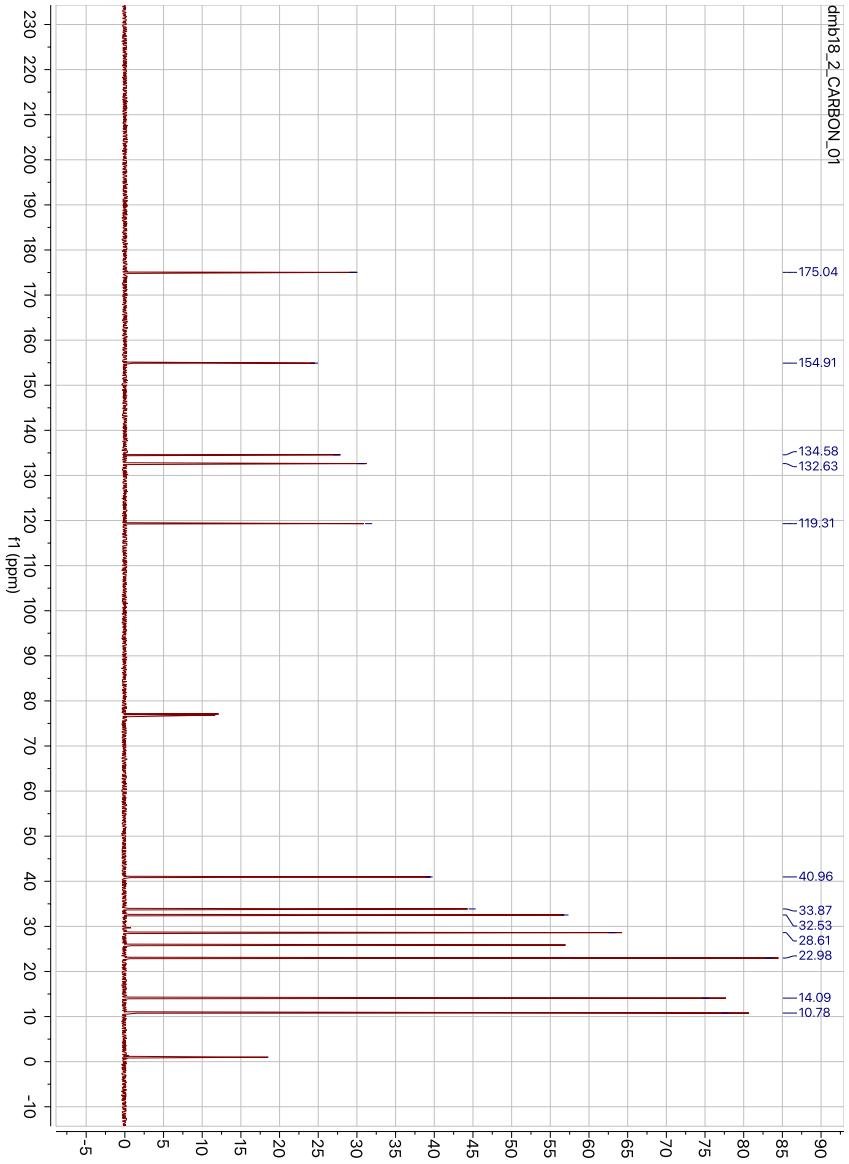

SI Figure 23. C^{13} NMR of 1,3-dibromo-5,7-bis(2-ethylhexyl)-4*H*,8*H*-benzo[1,2-*c*:4,5-*c'*]dithiophene-4,8-dione

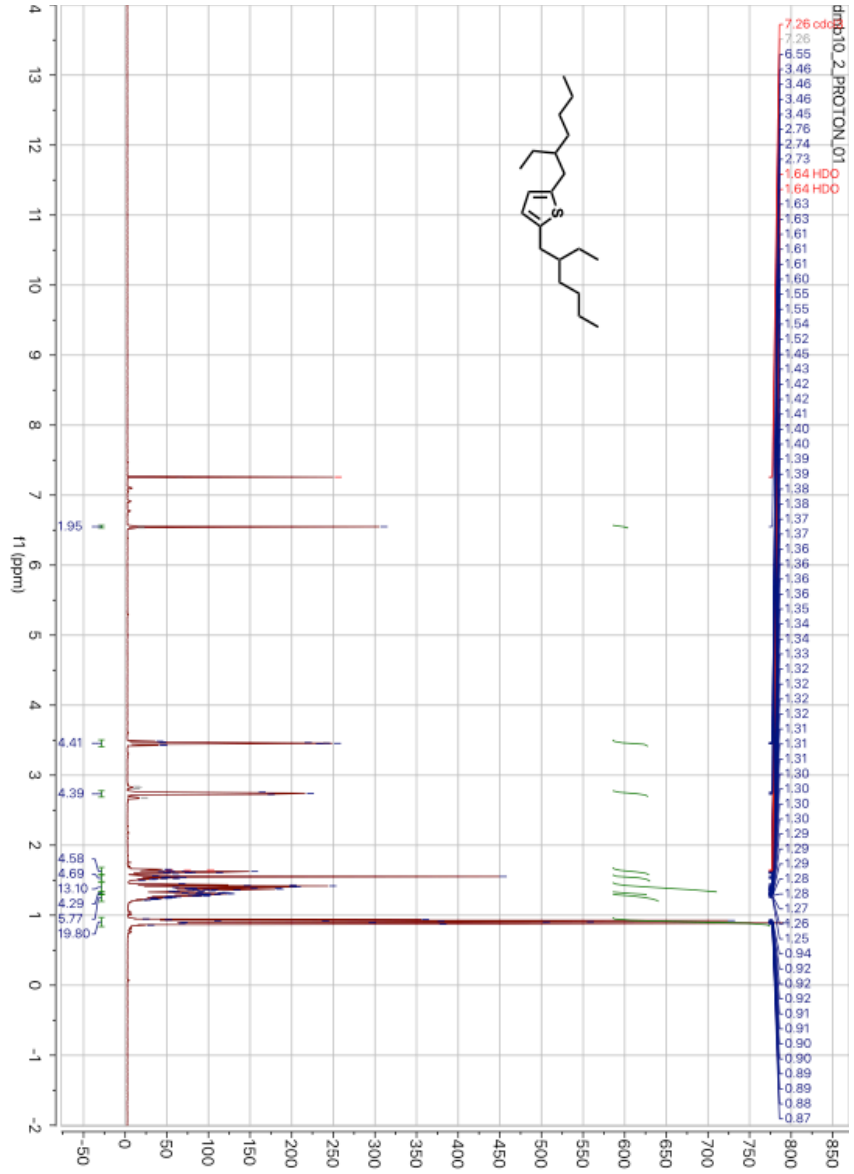

SI Figure 24. H NMR of 2,5-bis(2-ethylhexyl)thiophene.

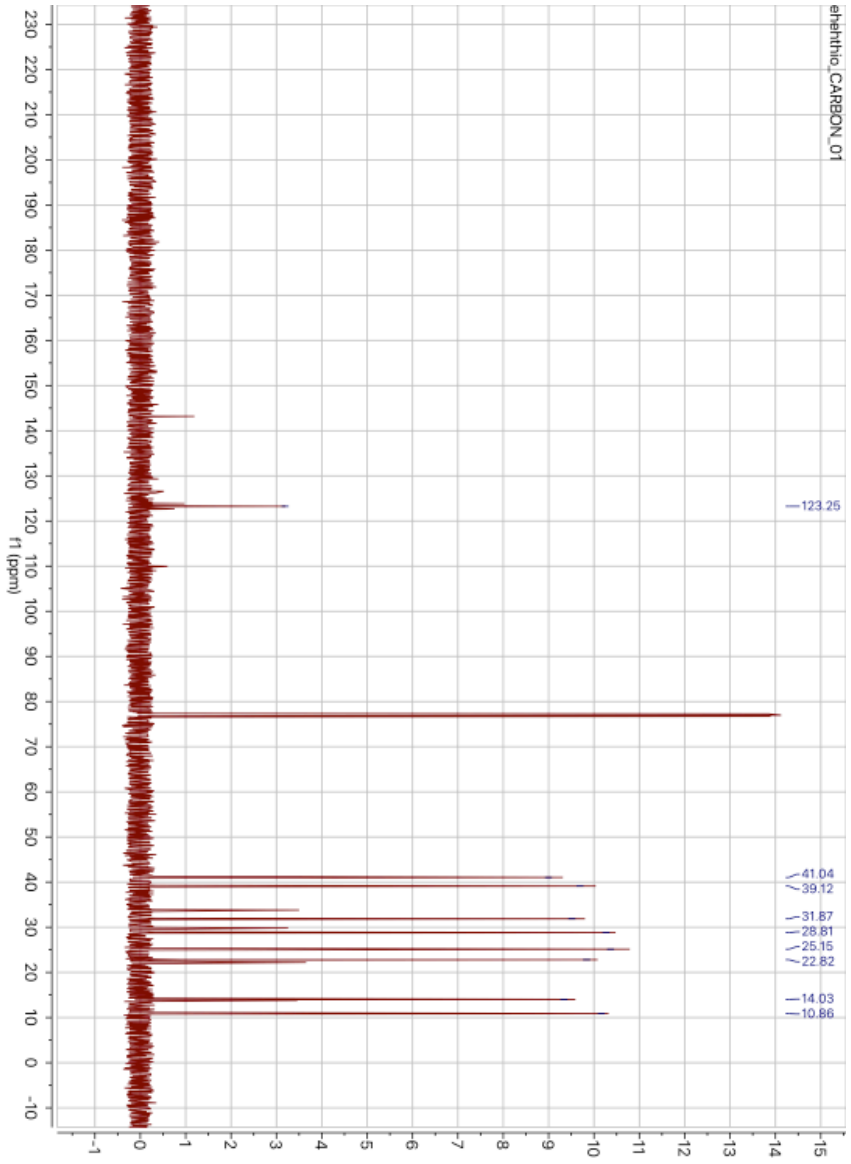

SI Figure 25. H NMR of 2,5-bis(2-ethylhexyl)thiophene.

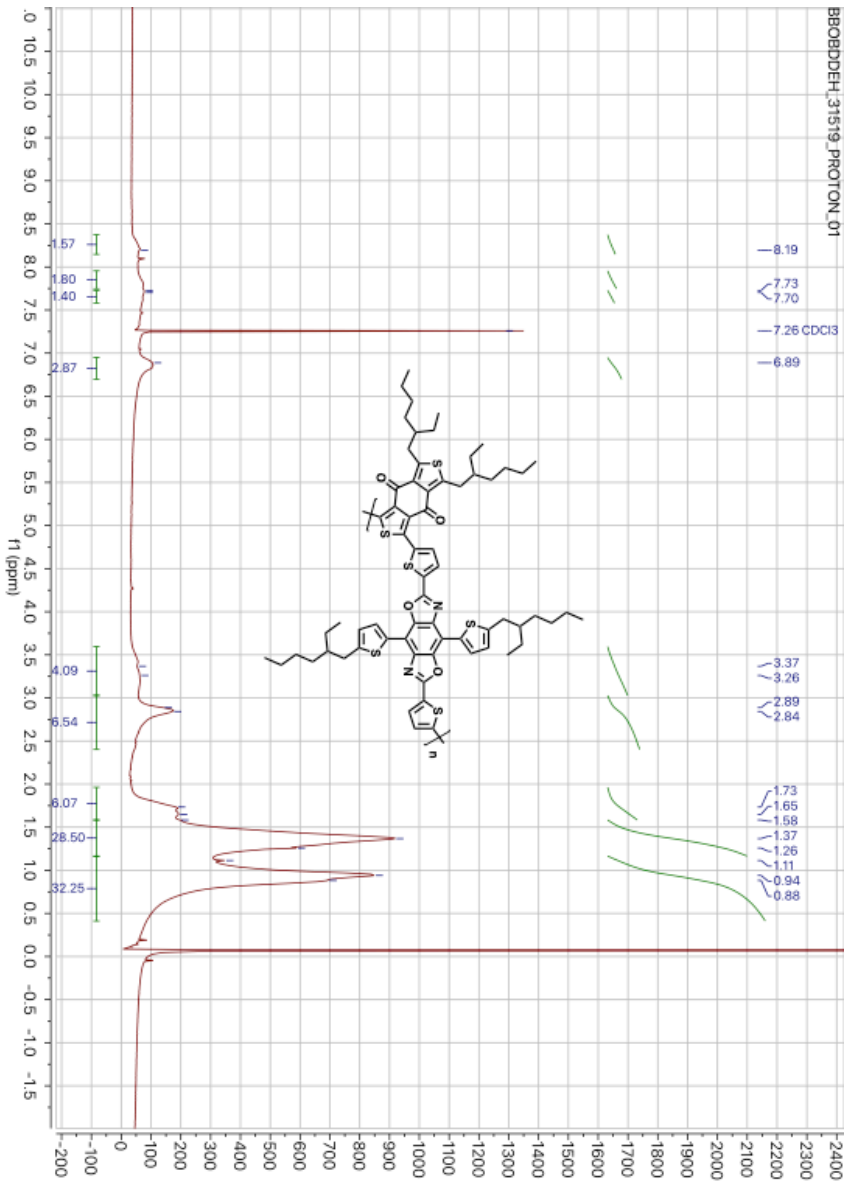

SI Figure 26. H NMR of BBOBDD polymer.

General methods for GPC measurement:

Gel-permeation chromatography (GPC) were collected at a flow rate of 1 mL/min in chloroform at a temperature of 30°C. Molecular weight values were measured using a calibration curve obtained from styrene standards. Molecular weights of purified post Soxhlet polymer was obtained.

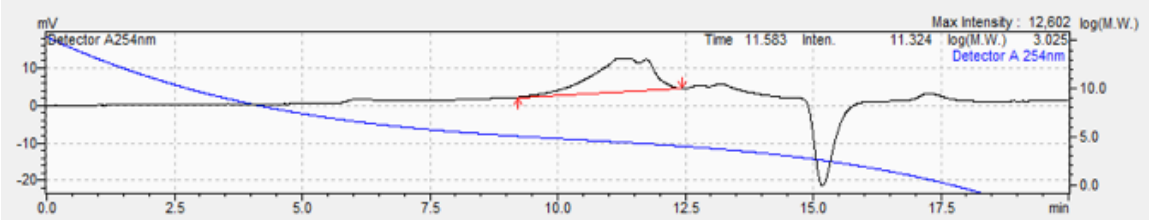

SI Figure 27. GPC measurement of P1 (top) and P2 (bottom).

Thermal Gravimetric Analysis

TGA measurements were obtained using a TA Instruments TGA Q50. All measurements were performed under a flow of nitrogen. 1) Heat to 110 °C at 10 °C/min. 2) Hold at 110 °C for 20 min. 3) Heat to 600 °C at 10 °C/min. 3) Hold at 600 °C for 10 min.

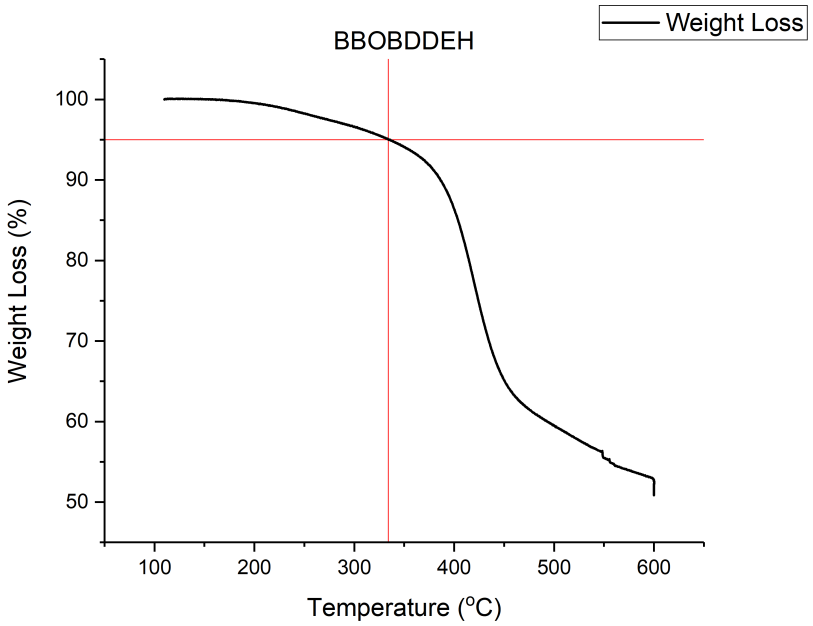

SI Figure 28. BBOBDD 5% Weight loss temperature measured by TGA T_d^a 338 °C.

DIFFERENTIAL SCANNING CALORIMETRY

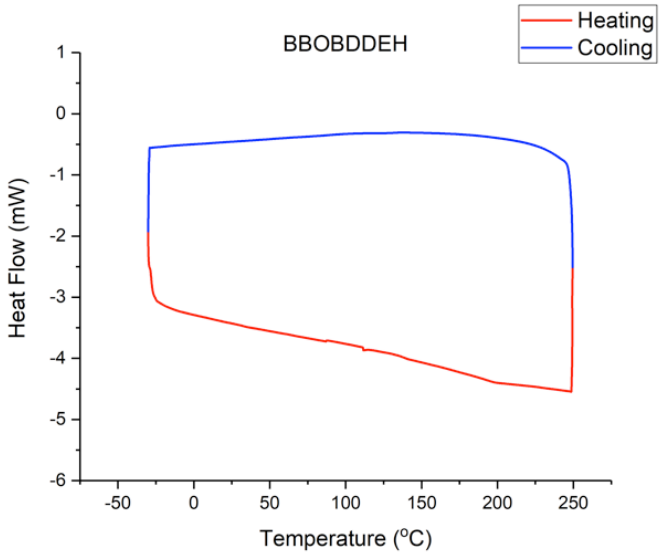

SI Figure 29. Differential Scanning Calorimetry (DSC). Second heating (red) and cooling (blue) scans of BBOBDD. No obvious thermal transitions were observed between -30 and 200°C.

CHAPTER FOUR: BENZOTHIADIAZOLE-BENZOBISOXAZOLE COPOLYMERS: THE EFFECT OF 1,2-DIFLOURINATED VERSUS NON-FLOURINATED BENZOTHIADIAZOLE ACCEPTOR WITH BENZOBIOXZOLE AS A WEAK DONOR FOR ORGANIC SOLAR CELLS

SECTION ONE: ABSTRACT

Many efforts have been put forth towards the design and synthesis of conjugated materials for use in organic photovoltaic applications. Trans benzobisoxazole and benzothiadizole based weak donor - strong acceptor materials were synthesized. The optoelectronic, electrochemical, morphological, and photovolatic properties were investigated. While the

distinction between the two polymers synthesized is the diflourinated acceptor the materials display similar HOMO level values (-5.22 eV to -5.27 eV) and modest difference in LUMO levels (-3.42 eV to -3.57 eV). The BBOBTz based polymers also exhbited good thermal stability well above device operating temperatures. When paired with $PC_{71}BM$ ([6,6]-phenyl C_{71}-butyric acid methyl ester) acceptor they display low power conversion efficiencies and poor surface morphologies.

SECTION TWO: INTRODUCTION

In recent years, immense progress has been accomplished towards developing conjugated polymeric materials with tailored optoelectronic properties for organic electronic applications such as organic light emitting diodes (OLEDs), organic field effect transistors (OFETs), and organic photovoltaics (OPVs).[149–152] Extensive research and development towards the optimization of OPV device parameters has been evaluated towards achieving optimal PCEs.[84,153,154] Simultaneously, a considerable amount of effort has occurred in the design and synthesis of highly conjugated polymers for OPVs. Breakthroughs in push-pull donor acceptor copolymers has led to highly efficient bulk heterojunction solar cells.[84,155] More specifically, the highly accepted approach of combining relatively weak donors and strong acceptors design motif has led towards high performing organic semiconducting materials for OPV applications.[49,156,157] In addition to the weak donor – strong acceptor molecular design motif, the fluorination of highly π-conjugated polymer has been an effective approach towards the development of efficient semiconductor polymers. Currently, semiconductors and small molecules has achieved high PCEs of 8%-10% when fluorine is incorporated into their molecular structures.[83]

Although the impact of fluorination is still not completely understood, it has been shown to influence i) frontier molecular orbitals ii) charge transport characteristics of semiconductors iii) active layer morphology iv) recombination kinetics v) synthetic routes towards desired semiconductors of interest.[158] Attempts to further deepen understanding of the impact of fluorination when incorporated into BBO based weak donor – strong acceptor polymers will be explored and discussed.

Traditionally, polybenzobisazoles commonly known as BBOs, are relatively electron deficient heterocyclic materials. BBOs have been incorporated into polymer light emitting diodes, organic field effect transistors, non-linear optics, and known to form high-performance rigid rod polymers.[24,159–161] In addition, they are thermally and oxidatively stable making them one of the best environmentally suitable materials for OPVs applications.[127,162] Despite these applications and benefits, the inclusion of BBO based materials has been inappreciable due to the relatively harsh reactions conditions needed to synthesize BBO monomers and polymers desired.[160,163] Furthermore, these harsh reaction conditions severly limit functionalization of BBO polymers. In efforts to broaden the scope of application for BBO based materials, the Jeffries-EL group has developed milder reaction conditions via orthoester condensation to afford functionalized BBO materials for organic electronic applications.[32]

Our group has synthesized a series BBO copolymers with qaurterthiophene, 4,8-bis(5-(2-ethylhexyl)-thien-2-yl)-benzo[1,2-*b*:4,5-*b*′]dithiophene (BDT), and dithienylsilole (DTS) achieving modest PCE of 1.14%, 2.78%, and 3.51%, respectively.[145–147] The incorporation of BBO into these copolymers has evaluated BBO as a weak acceptor

when paired with a strong donor. Other design motifs such as the inverse of aforementioned, weak donor- strong acceptor design motif has been an effective design strategy for the current generation of organic semiconductors. Nominal amount of research and development of BBO as a weak donor when coupled with a strong acceptor has been evaluated. Developing an understanding of the structural activity relationship of BBO as a weak donor comonomer in a weak donor-strong acceptor design motif for OPV applications is noteworthy to investigate. Herein, benzo[1,2-*d*;4,5-*d*']bisoxazole (*trans*-BBO) benzo[*c*][1,2,5]thiadiazole (BTz) copolymers were synthesized for OPV applications (**scheme x**).

SECTION THREE: RESULTS AND DISCUSSION

SYNTHESIS AND CHARACTERIZATION

The synthesis and structures for the target polymers are displayed in **scheme x**. Subsequent functionalization of **1** along the 2,6-axis yielded the stannulated BBO monomer and used without further purification. The difficulty of the lithiation of towards compound **2** was performed according to modified literature procedure. Stille cross-coupling reactions were

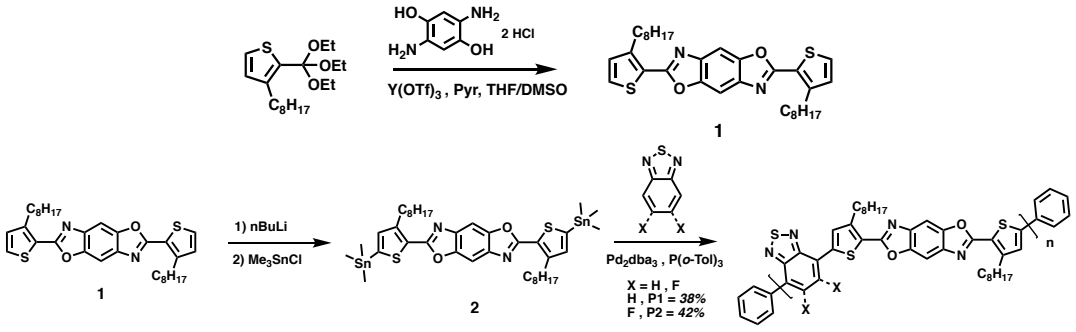

Scheme 5. Synthesis of Benzobisoxazole monomers and polymers.

carried out to yield polymers BBOBTz (**P1**) and BBOBTzF2 (**P2**) in low to moderated yields of 38% and 42%, respectively. Purification of **P1** and **P2** consisted of precipitation in cold methanol with gentle stirring. The polymer precipitate was then filtered into cellulose thimble to undergo Soxhlet extraction in efforts to remove low molecular weight materials. Following Soxhlet extraction, **P1** and **P2** were rotavap to concentrated and then dissolved in approximately 5 ml of chloroform and passed through short silica gel column in efforts to remove any residual catalyst and salts. **P1** and **P2** were then precipitated again into cold methanol with gentle stirring. **P1** and **P2** were dried under high vacuum for at least 48 hours. **P1** and **P2** and exhibit good solubility in chlorinated solvents and were characterized by H^1 NMR spectroscopy and gel permeation chromatography (GPC). The molecular weights are summarized in **table 1**. **P1** displayed higher molecular weights in comparison to **P2**. The absence of fluorine present on the benzothiadizole acceptor unit in the polymer backbone of **P1** has less planarization leading to less aggregation, improved solubility and ultimately higher molecular weights.[164–167] H NMR spectroscopy of was characterized at 50 ^oC and gel permeation chromatography (GPC) in chloroform to identify chemical structure and molecular weights of target polymer. Thermal analysis of **P1** and **P2** was performed utilizing thermal gravimetric analysis (TGA) and differential scanning calorimetry (DSC). TGA displayed excellent thermal stability with 5% thermal decomposition of 353 ^oC and 296 ^oC for **P1** and **P2**, respectively. DSC exhibited no definitive endothermic or exothermic features between -30 ^oC and 200 ^oC.

Polymer	Mw [kDa]	Mn [kDa]	PDI	DPn	Tg
P1	39	30	1.3	45	353
P2	20	20	1.0	23	296

Table 7. Summary of molecular weight characteristics for P1 and P2.

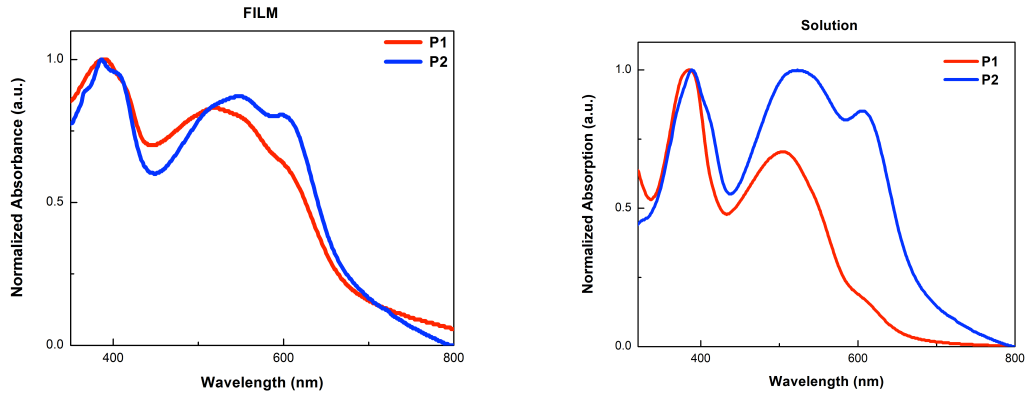

Figure 37. Normalized film (left) and solution (right) state absorption profile of P1 and P2 polymer. Films were spun cast from CF at a concentration of 15 mg/ml.

OPTICAL AND ELECTRONIC PROPERTIES

The opto-electronic properties of **P1** and **P2** were investigated for film and solution state UV-vis spectroscopy summarized in **figure x** and **table 2**. Both **P1** and **P2** exhibit similar absorption profiles with **P1** and **P2** displaying relatively broad absorption coverage and absorption maxima at 522 nm and 548 nm, respectively. In the film state **P2** is more bathochromically shifted in comparison to **P1** likely due to the planarization of the polymer backbone as a result of the fluorinated benzothiadiazole acceptor. In addition, the pronounced shoulder at approximately 575 nm – 625 nm is also indicative of the enhanced

π-π interactions occurring between polymer chains for both polymers. **P2** specifically has a more pronounced shoulder suggesting the incorporation of fluorine into the polymer backbone increases aggregation effects due to aforementioned planarization of the polymer backbone.[158] The electrochemical properties of **P1**-**P2** was evaluated via cyclic voltammetry (cv) and ultraviolet photoelectron spectroscopy (UPS). CV measurements were obtained using a platinum working electrode and an Ag/Ag^+ reference electrode. The onsets were references to Fc/Fc^+ and summarized in **table x**. **P1**-**P2** displayed reproducible redox processes. P1-P2 HOMO and LUMO values obtained were -5.5 eV, -5.6 eV and -3.7 eV and -3.8 eV, respectively. Ultra-photoelectron spectroscopy was performed to investigate the highest occupied molecular orbital (HOMO) of the polymers. **P1** and **P2** had similar HOMO of -5.22 eV and -5.27 eV, respectively (**SI figure x**). Eg^{OPT} was obtained from the absorption onset with **P1** and **P2** having 1.8 eV and 1.7 eV Eg^{OPT}, respectively. Additionally, the lowest unoccupied molecular orbital (LUMO) was obtained from the HOMO + Eg^{OPT} yielding -3.42 eV and -3.57 eV for **P1** and **P2**, respectively. The inclusion of fluorine into the polymer backbone is reportedly known to decrease the frontier molecular orbitals (FMOs, HOMO and LUMO) levels due to its strong electron withdrawing nature (EN = 4, Pauling scale).[158] Slight decrease of the HOMO level (0.05 eV) is observed between **P1** and **P2**. Interestingly for the BBO polymers presented in this study, the largest changes in the FMOs was observed in the estimated LUMO with greater than 0.1 eV change when fluorine was incorporated in the benzobisthiazole acceptor. This potentially suggests there is good separation of the FMOs along the BBO-BTz polymer backbone with fluorination primarily influencing the LUMO levels for this set of polymers.

This warrants further future exploration into tuning of BBO polymer energy levels not performed here in this work. To further gain insight into the optical properties of **P1** and **P2** solution photoluminescence (PL) spectroscopy and PL lifetimes were performed. PL spectroscopy displayed 608 nm and 597 nm emission maxima for **P1** and **P2**, respectively (**table 2, figure x**). The relatively weak shoulder present approximately 700 nm – 750 nm indicates π-π interaction between polymer chains and electronic transition of the lower energy vibrational modes from the ground state and next ground state highest energy vibrational mode. Also, the noticeable blue-shift in emission spectra between **P1** and **P2** is approximately 10 nm. Counterintuitively, this possibly is primarily due to aggregation induced quenching leading to the observed hypochromic shift present observed in the emission spectra. Additionally, several other factors such as lower molecular weight, electron withdrawing effect of fluorine, and steric interactions between fluorine loan pairs and neighboring monomer units can lead to blue shift observed emission for **P2**.[158,168] Time correlated single photon counting (TSCPC) measurement were performed to investigate the PL lifetimes of the exciton formation upon excitation of the BBO polymers. All polymers were excited with a horizontal pulse nanosecond 405 nm laser beam to 10,000 counts. The average PL lifetimes (τ_{avg}) obtained were 2.94 ns and 2.36 ns for **P1** and **P2**, respectively (table 2). **P1** exhibited longer lifetimes relative to that of **P2**. This suggest the incorporation of fluorine on the benzothiadiazole acceptor has an impact on the recombination characteristics of the BBO-BTz polymer. It has been reported that the molecular configuration and fluorination has an impact on the dipole moment of the benzothiadiazole units.[169,170] McCulloch *et al*. investigated fluorinated and non-fluorinated

thiophene flanked benzothiadiazole trimers and illustrated the configuration and fluorination has an impact on dipole moment possibly influencing photovoltaic processes such as charge generation and recombination characteristics. In the case for **P2**, the fluorinated benzothiadiazole unit showed a shorter PL lifetime suggesting the presence of fluorine lowers the dipole moment leading toward more favored recombination relative to that of **P1**. In effort to gain a deeper understanding, further investigation into the influence of fluorine and **P1** and **P2** molecular configuration will be performed in the future within our group via in-depth density functional theory (DFT) and charge generation and recombination dynamic studies.

Polymer	λ_{max}^{film} (nm)	λ_{max}^{soln} (nm)	λ_{emm}^{soln} (nm)	τ_D[a] (ns)	HOMO[b] (eV)	LUMO[b] (eV)	E_g^{opt} [a] (eV)
P1	522	508	608	2.94	-5.22	-3.42	1.8
P2	548	513	597	2.36	-5.27	-3.57	1.7

Table 8. Opto-electronic properties of P1 and P2 in solution and film state. Solution and film absorbance obtained in chloroform and spun cast, respectively. [a] TCSPC used to measure PL lifetimes. Polymers were excited by a horizontal pulse nanosecond 405 nm laser beam to 10,000 counts. The average lifetimes (τ_{avg}) are on the order of nanoseconds (ns). [b]HOMO obtained from UPS. LUMO obtained from LUMO = HOMO + Eg^{OPT}.

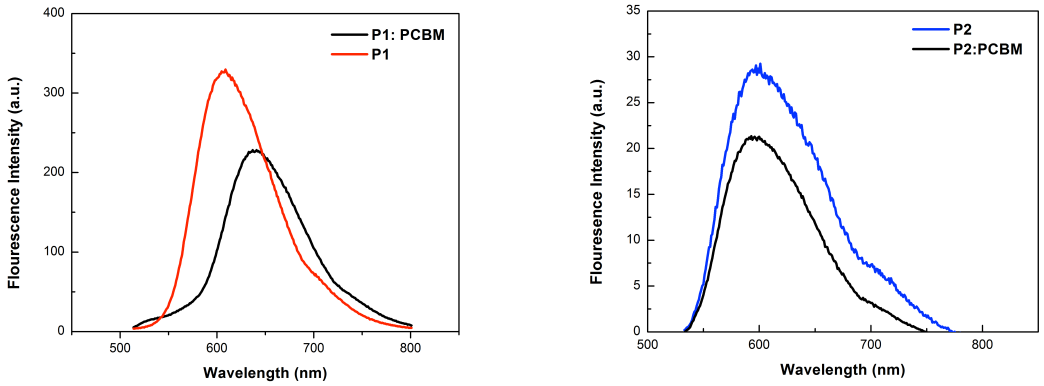

Figure 38. Photoluminescence emission and quenching profiles of P1 and P2 polymer in dichlorobenzene solution. P1: PCBM and P2: PCBM 1:2 donor acceptor ratio.

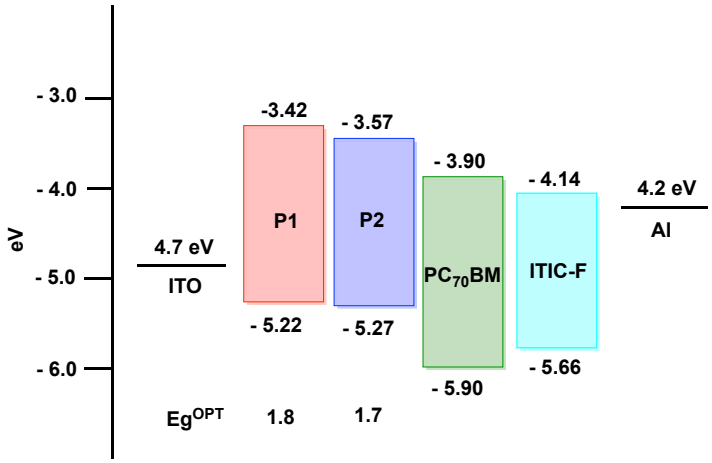

Figure 39. Energy level alignment of P1 and P2 with PC71BM and ITIC-F acceptor.

ORGANIC PHOTOVOLATIAC DEVICES

The preliminary performance of P1 and P2 in OPVs were investigated in a conventional BHJ architecture utilizing PC71BM and ITIC-F as the acceptor with a device configuration of ITO/PEDOT:PSS/**P1**-**P2**:PC71BM/Ca/Al and ITO/PEDOT:PSS/**P1**-**P2**:ITIC-F/Ca/Al.

The use of either acceptor has optimal energy level alignment and solar spectrum overlap (**figure x**). Photovoltaic parameters are summarized in **table 3**. Active layers were spun coated from different solvents (*o*-DCB and CF: *o*-DCB) at optimized spin speeds and summarized in **table 3**. All OPV devices were characterized and prepared in an inert nitrogen atmosphere. **P1**-**P2** exhibited similar performances under the different processing conditions and general exhibited poor solubility. At a 1:1 (**P1**-**P2**: ITIC-F) weight ratio displayed performance of 0.02% and 0.03% when processed from *o*-DCB for **P1** and **P2**, respectively. Attempts to improve photovoltaic parameters through increasing film thickness and spin speed showed no changes in PCE. At a 1:2 (**P1**-**P2**:PC71BM) weight ratio, **P1** and **P2** exhibited the best performance when processed from *o*-DCB. To optimize the photovoltaics parameters the devices, **P1** was subjected to various spin coating speed in efforts to improve film thickness. When processing from *o*-DCB at a spin coating speed of 1000 rpm yielded an active layer thickness of approximately 40 nm and overall PCE of 0.11%. Optimizing D: A ratio from 1:2 to 1:2.5 proved to be detrimental to device performance. Further efforts to improve solution processability and photovoltaic parameters through solvent ratio of 90:10 *o*-DCB: CF led to no improvement in film thickness and PCE for **P1**. Devices using **P2** was also taken through same device optimization. Attempts to improve active layer thicknesses led to no improvement with active layer thicknesses ranging from 31-34 nm and lower PCEs of 0.05% - 0.08% relative to **P1** performance. The use of *o*-DCB: CF for active layer processing led to no change in solution processing and photovoltaic parameters. Specifically, notable trends are observed for **P1** and **P2** photovoltaic parameters. When comparing Voc in polymer: PC71BM

devices, **P2** had significantly higher open circuit voltage in comparison to **P1**. The substitution of fluorine has been known to improve open circuit voltage. The slightly deepened HOMO level of P2 lead to the slightly improved Voc observed. P2 also possessed higher observed fill factors as well. Interestingly, comparing the Jsc in polymer: PC71BM devices, **P1** has a significantly higher short circuit current density relative to that of **P2**. This is plausibly due overall improved absorptivity due better film thickness as a result of the higher molecular weight of **P1** in comparison to **P2**.

Polymer	Solution	Acceptor	Active layer thickness [nm]	D/A	V_{oc} [V]	J_{sc} [mA/cm^2]	FF	PCE [%]
P1	*o*-DCB	ITIC-F	29	1:1	0.29	0.30	24.20	0.02
	o-DCB	C71	40	1:2	0.48	0.88	25.10	0.11
	o-DCB /CF[a]	C71	34	1:2	0.44	0.75	24.06	0.08
	o-DCB	C71	43	1:2.5	0.38	1.00	22.44	0.08
P2	*o*-DCB	ITIC-F	31	1:1	0.32	0.32	28.37	0.03
	o-DCB	C71	32	1:2	0.53	0.36	42.02	0.08
	o-DCB /CF[b]	C71	34	1:2	0.56	0.30	41.21	0.07
	o-DCB	C71	32	1:2.5	0.39	0.35	38.21	0.05

Table 8. Best performing devices. [a]90:10 *o*-DCB: CF ratio, respectivey. [b]80:20 *o*-DCB: CF ratio, respectively.

The active layer surface morphology of the films for the best performing polymer: PC71BM devices for each processing condition was probed via tapping-mode atomic force microscopy (AFM) in efforts to ascertain a correlation between device performance and

surface layer morphologies. Height images of active layer blends are displayed in **figure x and x**. For the best performing devices, active layer surface roughness was found to be 9.23 and 0.55 for **P1** and **P2**, respectively. Depending on device solution processing conditions drastic changes were observed for the surface morphology for both **P1** and **P2**. Attempts to improve solvent processability via mixing of *o*-DCB: CF led to improvement in surface roughness for **P1** (9.23 to 5.05 RMS) while **P2** led to a slight increase in surface roughness (0.55 to 0.99 RMS). Overall surface imaging for P1 and P2 displayed relatively

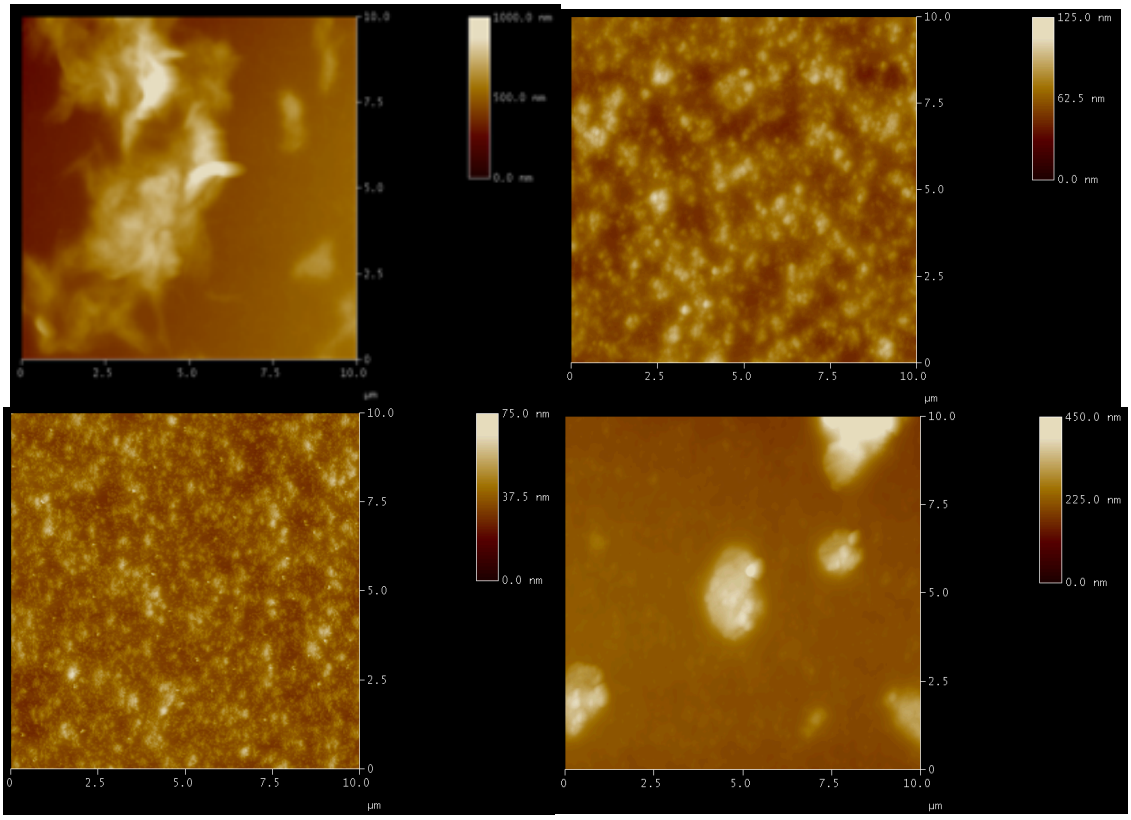

Figure 40. AFM Images of P1:ITIC-F, spun cast from oDCB RMS 111.01 (top left). P1:PCBM, spun cast from CF RMS 9.23 (top right). P1:PCBM spun cast from oDCB:CF (bottom left). P1:PCBM spun cast from oDCB, RMS 5.05 (bottom right).

intermixed domain sizes when processing from *o*-DCB and *o*-DCB: CF. However, this led to no improvement in over PCEs. Optimizing for D:A ratio (1:2 to 1:2.5) led to larger observed domains for both **P1** and **P2** as well as higher surface roughness (43.48 RMS) for **P2** specifically. This relatively high surface roughness can lead to poor ohmic contact between the active layer and electron transport layer. Surface morphology for this condition also indicated potential vertical phase segregation within the active layer as fullerene content increases potentially contributing to lower PCEs. Further investigating morphological characteristics of these polymers via GIWAXS could offer insights into lamellar distances and crystalline coherence lengths impact on film formation and ultimately PCE. Due to experimental limitations GIWAXS data were not obtained.

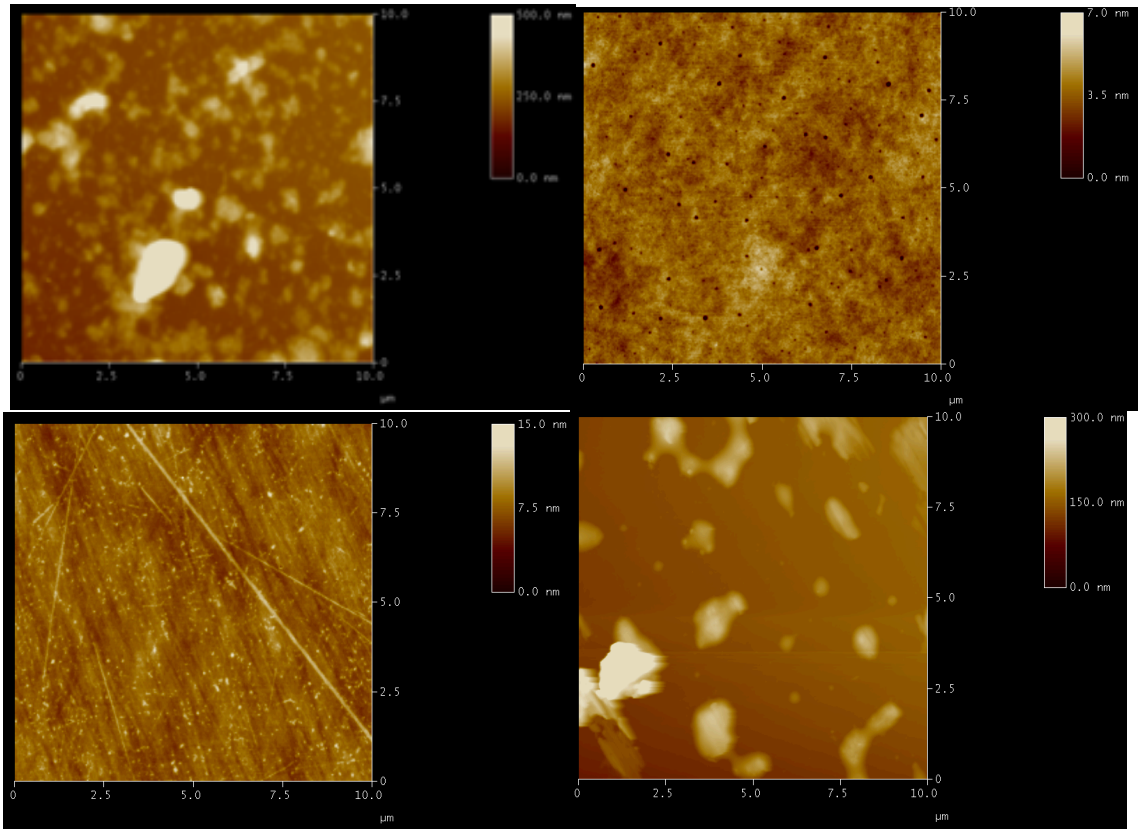

Figure 41. AFM Images of P2:ITIC-F, spun cast from oDCB RMS 111.01 (top left). P2:PCBM, spun cast from CF RMS 9.23 (top right). P2:PCBM spun cast from oDCB:CF (bottom left). P2:PCBM spun cast from oDCB, RMS 5.05 (bottom right).

PHOTOLUMINESCENCE LIFETIME AND QUENCHING

As aforementioned, polymer decay dynamics were analyzed with TCSPC. **P1** has display longer lifetime dynamics suggesting **P1** possibly has a longer-lived exciton in comparison to **P2 (table 2 and figure x)**. **P1** possessing a higher MW in comparison to **P2** could possibly stabilize the formed exciton via chain hopping more readily leading towards longer luminescent lifetimes for **P1**. Further preliminarily exploring exciton and charge transfer dynamics photoluminescent quenching studies were performed. Upon excitation

of polymer: PC71BM active layer solution, both **P1** and **P2** both displayed weak emission profiles with only 30% and 28% quenching occurring, respectively. This indicates P1 and P2 have poor charge transfer characteristics with PC71BM at a 1:2 ratio. Naively, increasing acceptor ratio would improve this charge transfer dynamic. However, as surface morphology depicts, increasing fullerene content led greater phase segregation and higher surface roughness for current devices. This trade-off limits the potential of these materials and require further optimization and reconsideration of molecular design for improved morphology and performance.

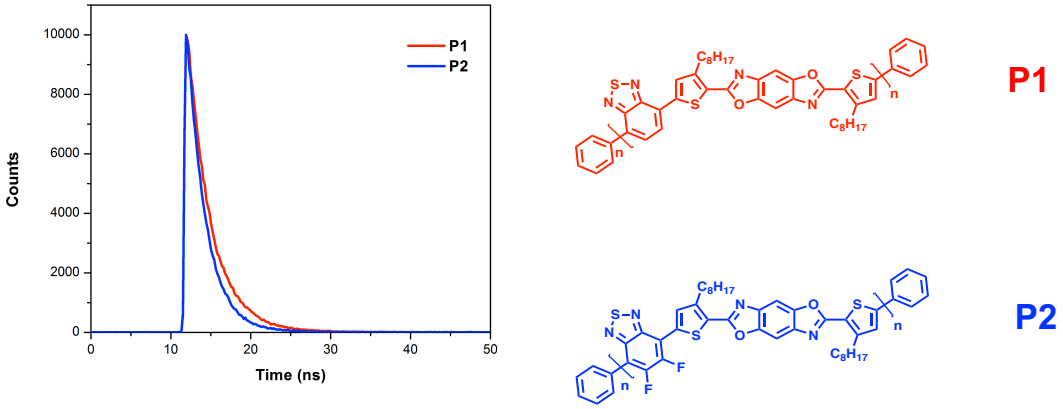

Figure 42. Photoluminescent lifetime of P1 and P2. Time correlated single photon counting techniques with horizontal pulse ns 405 nm laser at 10,000 counts.

SECTION FOUR - CONCLUSIONS

A series of new benzobisoxazole polymers were synthesized based on 2,6-bis(3-octylthiophen-2-yl)benzo[1,2-*d*:4,5-*d′*]bis(oxazole) and benzothiazole. These polymers were synthesized via Stille coupling in moderate yields. Polymers also exhibited good molecular weights and relatively narrow PDIs in comparison to other Benzobisoxazole based polymers. Interestingly, the influence of fluorine had an impact on the opto-electronic properties with slightly broader and red-shifted film state absorption profiles. Photoluminescent lifetimes showed the introduction of fluorine onto the benzobisthiazole acceptor lead to a decrease in photoluminescent lifetimes and plausibly exciton lifetimes. Upon incorporation into OSCs, polymers **P1** and **P2** exhibited low performance. They exhibited poor solubility in processing solvent leading to high surface roughness and large domains. Consequently, this proved to be detrimental to device performance.

EXPERIMENTAL METHODS

Materials, Measurements, and Synthesis

2,6-bis(3-octylthiophen-2-yl)benzo[1,2-*d*:4,5-*d′*]bis(oxazole) (1)

3-octyl-2-(triethoxymethyl)thiophene and $Y(OTf)_3$ in THF was prepared. In a dry round bottom flask DAHQ was placed under Argon. Both flask were deoxygenated under Argon for 30 minutes. After 30 minutes the flask containing 3-octyl-2-(triethoxymethyl)thiophene and $Y(OTf)_3$ in THF was warmed to 55^{o}C. Following, addition of dissolved DAHQ in DMSO and activated with 2 equivalents of pyridine. DAHQ was then added dropwise to the solution containing 3-octyl-2-(triethoxymethyl)thiophene and allowed to stir overnight. The reaction cooled to room temperature and 3:1 mixture of cold methanol and water was

poured into reaction. Cold mixture was then precipitated into 400 ml of -78°C chilled methanol to yield off white powder upon vacuum filtration (63%).

2,6-bis(3-octyl-5-(trimethylstannyl)thiophen-2-yl)benzo[1,2-*d*:4,5-*d'*]bis(oxazole) (2)

In an oven dried flask, containing a solution of anhydrous THF containing 1 was cooled to -10°C. n-Butyl lithium (2.5 M, 0.353 ml) was added dropwise to the reaction mixture. The reaction was allowed to stir at -10°C for 15 minutes then was cooled to -78°C. Reaction was quenched with 1M trimethyltin chloride solution (1.68ml) and warmed to room temperature to stir overnight. The reaction was diluted with distilled H_2O and brine. The organic layer was extracted with dichloromethane and rotovap to concentrate. The resulting oily solid was used without further purification.

Synthesis of P1 and P2

In a dry-argon purged 2N-flask containing **2** and benzothiadiazole acceptor and degassed toluene for 45 min. $Pd_2(dba)_3$ (2 mol %) and $P(tol)_3$ (8 mol %) was added and degassed for another 10 min. The reaction was heated to reflux for 3 days. Polymer was end capped with phenyl and allowed to stir at reflux for another 6 hours. Purification of **P1-P2** consisted of precipitation in cold methanol with gentle stirring. The polymer precipitate was then filtered into cellulose thimble to undergo Soxhlet extraction in efforts to remove low molecular weight materials. Following Soxhlet extraction, **P1-P2** were rotavap to concentrated and then dissolved in approximately 5 ml of chloroform and passed through short silica gel column in efforts to remove any residual catalyst and salts. **P1-P2** were then precipitated again into cold methanol with gentle stirring. **P1-P2** were filtered and dried under high vacuum for at least 48 hours to yield **P1-P2** in 38% and 42% yield, respectively.

SECTION FIVE – SUPPORTING INFORMATION

DEVICE CHRACTERIZATION AND FABRICATION

All organic photovoltaic devices were performed under inert atmosphere and solution based spun cast via spin coater. Conventional architecture were used to fabricated organic photovoltaic devices via (ITO)/ POLY(3,4-ethylenedioxythiophene): poly(styrene sulfonate) (PEDOT:PSS)/polymer:[6,6]-phenyl-C_{71}-butyric acid methyl ester ($PC_{71}BM$)/CA/Al) and (ITO)/ POLY(3,4-ethylenedioxythiophene): poly(styrene sulfonate) (PEDOT:PSS)/ 9-Bis(2-methylene-((3-(1,1-dicyanomethylene)-6,7-difluoro)-indanone))-5,5,11,11-tetrakis(4-hexylphenyl)-dithieno[2,3-d:2',3'-d']-s-indaceno[1,2-b:5,6-b']dithiophene (ITIC-F)/CA/Al). ITO glass substrates were cleaned via (1) sonication (Mucasol), (2) deionized water, (3) acetone, and (4) isopropanol for 10 minutes each respectively. Slides were dried in oven followed by UV-ozone treatment for 15 minutes. PEDOT: PSS layers (Clevios P VP Al 4083) were filtered (0.45 um) and spin-coated onto ITO substrates at 3500 rpm for 2 minutes and annealed for 150^{o}C for 30 min in air. After cooling substrates were transferred into nitrogen filled glove box. All polymer: PC71BM and polymer: ITIC-F solutions were prepared in 1:2 – 2.5 and 1:1 blend ratio (20 mg/ml), respectively, with CF or CB as processing solvent. The prepared solutions were allowed to stir for 24 hrs at 55 ^{o}C (CF) or 80^{o}C (CB) prior to spin coating 1200-2000 rpm for 2 minutes. Following spin coating, Ca (15 nm) and Al (100 nm) electrodes underwent successful deposition via thermal evaporation. Films were also evaluated under post-thermal annealing conditions at 100 ^{o}C for 10 minutes. Current-density (J-V) data were

obtained via Keithley 2400 source meter and simulated AM1.5G illumination (100 mW/cm^2, Newport 91160) calibrated using a KG-5 filter Si reference cell.

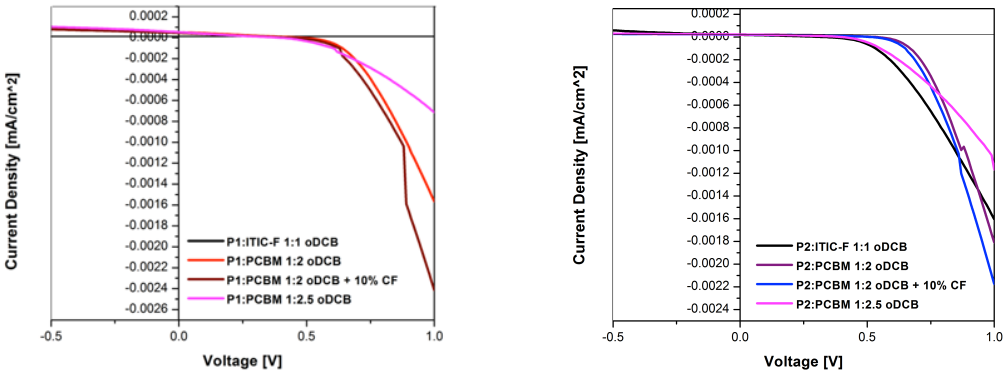

SI Figure 30. J-V curve of P1-P2 series.

UPS MEASUREMENT

Ultraviolet photoelectron spectroscopy (UPS) was used to acquire the ionization potentials and approximate the HOMO values for each material. All substrates (positively doped silicon; 10 × 10 mm^2) had 40 nm of silver deposited via thermal evaporation. Samples were prepared by dissolution in chloroform at a concentration of 5 mg/mL and stirred for a minimum of 4 h. Each solution was filtered to remove potential aggregates and sequentially spin-coated under a nitrogen atmosphere at 4000 RPM. Spectra were then acquired under ultrahigh vacuum. The presented HOMO energies and corresponding standard deviations are determined by using all values obtained at random positions on the formed film.

THERMAL GRAVIMETRIC ANALYSIS

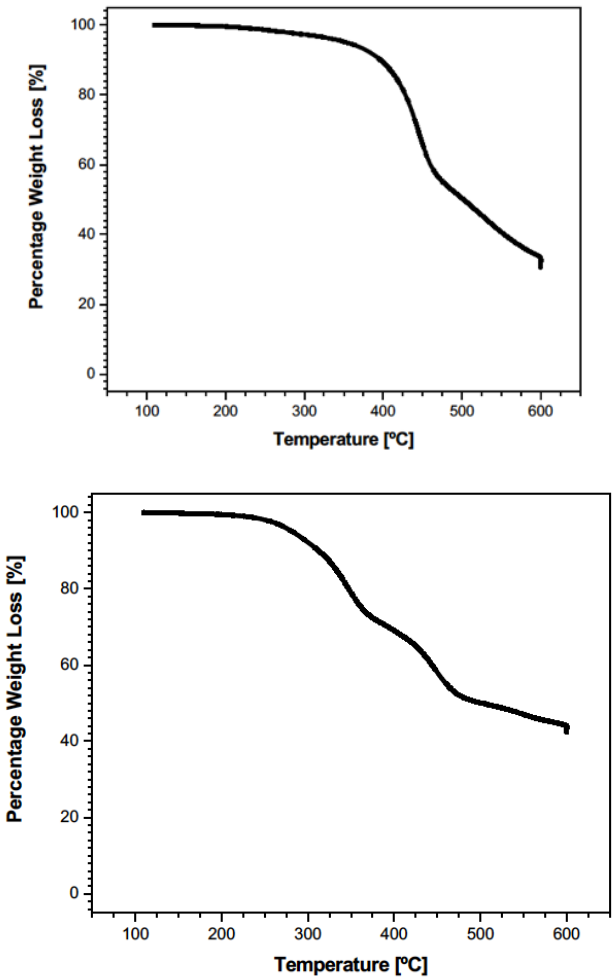

SI Figure 31. TGA thermograms of P1 (left) and P2 (right) heating at a scan rate of 10 °C/min under a N2 atmosphere. T_d^a[°C] 353 and 281 for P1 and P2 respectively.

DIFFERENTIAL SCANNING CALORIMETRY

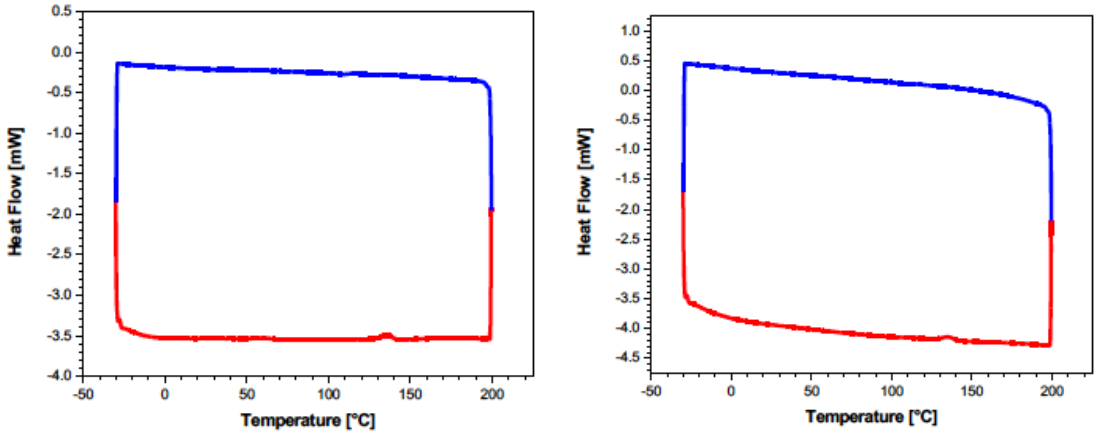

SI Figure 32. Differential Scanning Calorimetry (DSC). Second heating (red) and cooling (blue) scans of P1 (left) and P2 (right). No obvious thermal transitions were observed between -30 and 200°C.

PHOTOLUMINESCENT LIFETIMES

Polymer	τ_1 (ns) [Rel.]	β_1	τ_2 (ns) [Rel.]	β_2	τ_D[a] (ns)
P1	2.89 [97.2%]	10638	10 [2.8%]	88.41	2.94
P2	2.34 [98.8%]	10743	25.15 [1.2%]	12.22	2.36

SI Table 3. [a]Average PL decay lifetime. Time correlated single photon counting techniques with horizontal pulse ns 405 nm laser.

CYCLIC VOLATMETRY

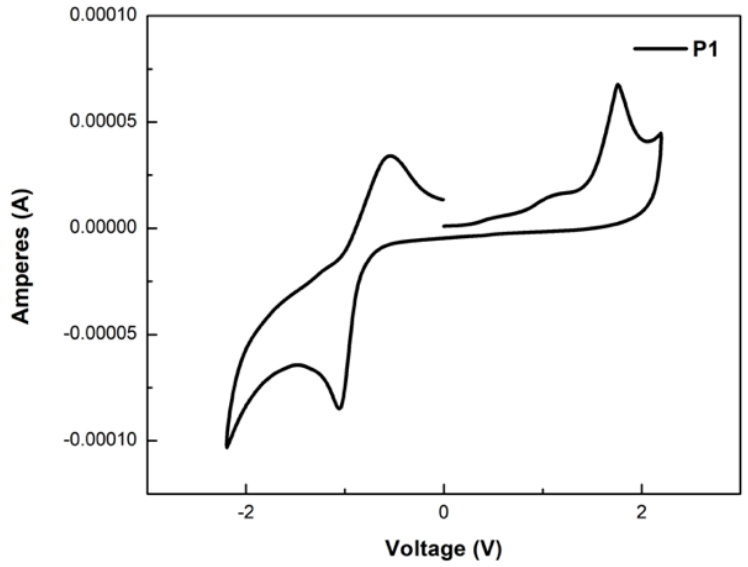

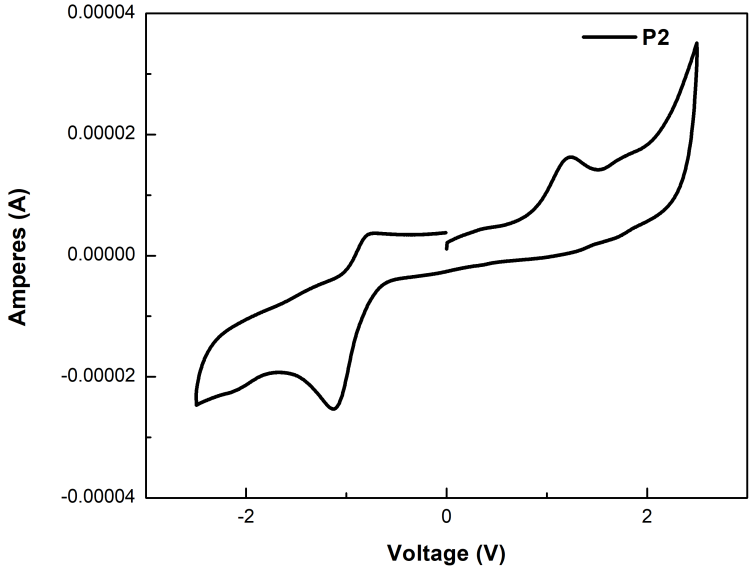

SI Figure 33. CV measurements were obtained using a platinum working electrode and an Ag/Ag^{+} reference electrode. The onsets were references to Fc/Fc^{+}

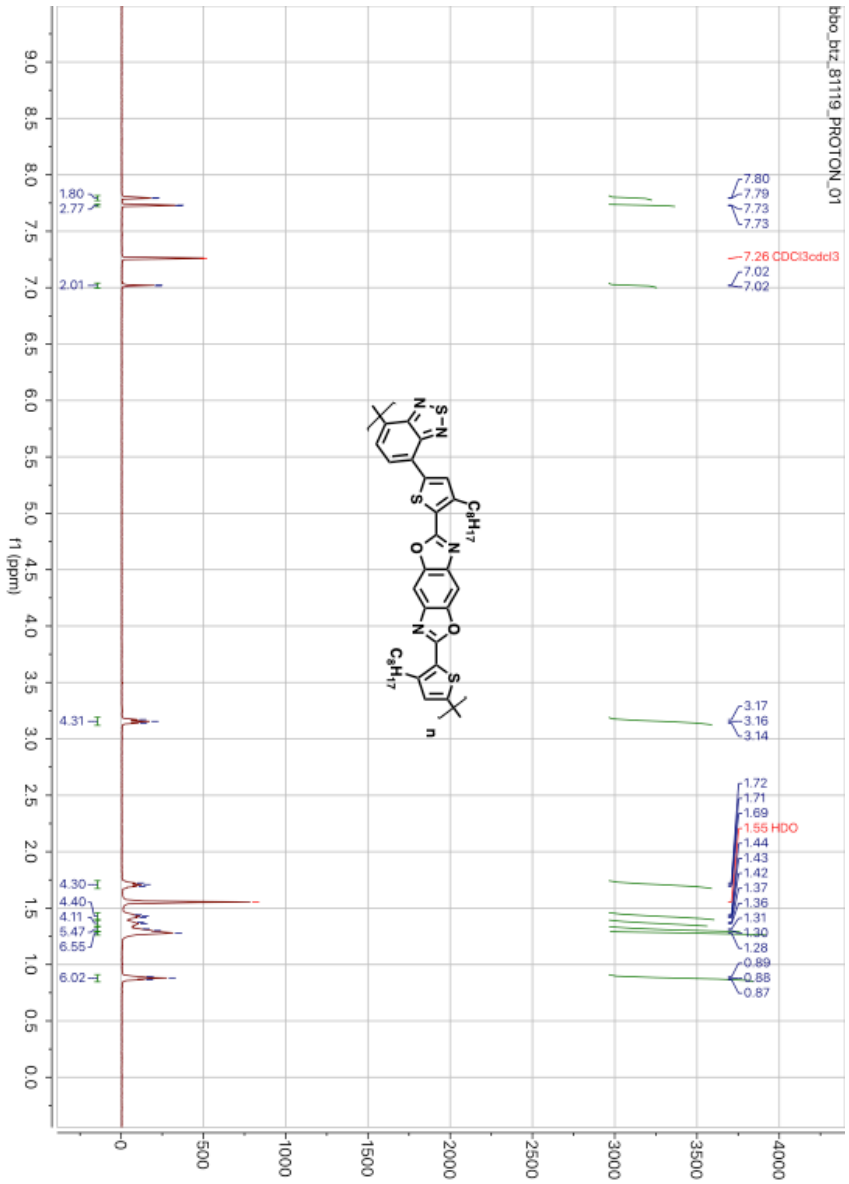

SI Figure 34. H NMR of P1.

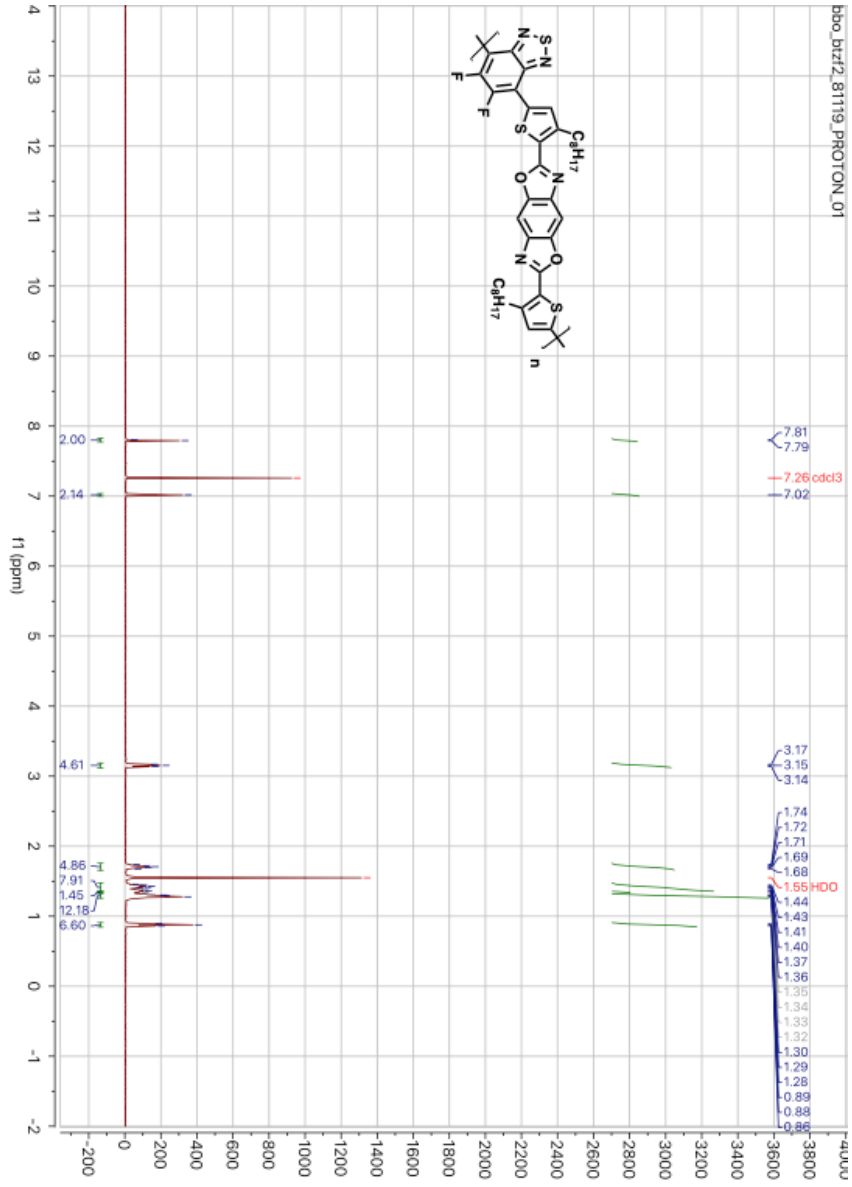

SI Figure 35. H NMR of P2.

General methods for GPC measurement:

Gel-permeation chromatography (GPC) were collected at a flow rate of 1 mL/min in chloroform at a temperature of 30°C. Molecular weight values were measured using a calibration curve obtained from styrene standards. Molecular weights of purified post Soxhlet polymer was obtained.

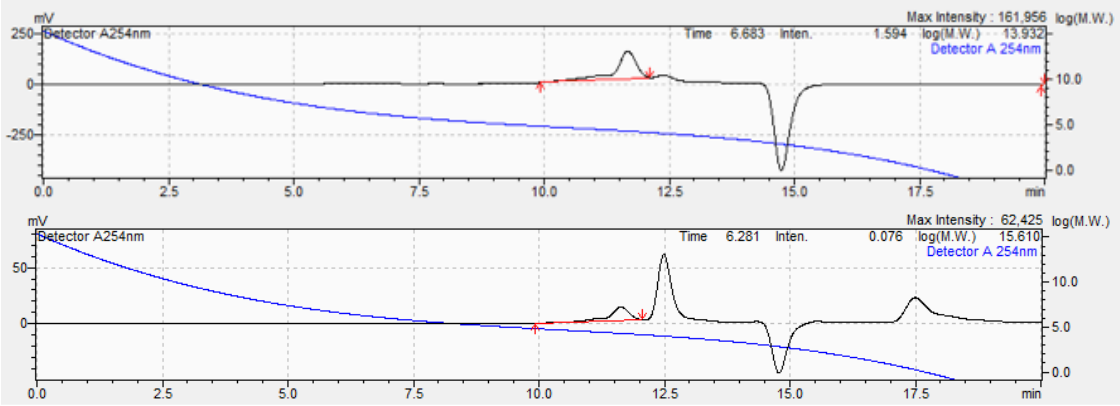

SI Figure 36. GPC measurement of P1 (top) and P2 (bottom).

CHAPTER FIVE: SYNTHESIS AND PHOTOVOLTAIC PROPERTIES OF 1,6-DIDECYLNAPHTHO[1,2-B-:5,6-B']DIFURAN-BASED COPOLYMERS

SECTION ONE: ABSTRACT

The synthesis of four donor–acceptor conjugated co-polymers comprised of the novel donor 1,6-didecylnaphtho[1,2-*b*:5,6-*b'*]difuran and 1,4-diketopyrrolo[3,4-*c*]pyrrole (DPP) acceptor via direct C-H arylation cross-coupling reaction is reported. Thiophene and furan moieties were used to flank the DPP group and the impact of these heterocycles on the polymers' properties was evaluated. The alkyl chains on the diketopyrrolopyrrole

monomers were varied to engineer the solubility and morphology of the materials. All of the polymers have similar optoelectronic properties with narrow optical band-gaps around 1.3 eV, which is ideal for solar energy harvesting. Unfortunately, these polymers also had high-lying HOMO levels of -4.8 to -5.1 eV. As a result, bulk-heterojunction photovoltaic cells fabricated using the soluble fullerene derivative $PC_{71}BM$ as the electron-acceptor and these polymers as donor materials exhibited poor performance due to limited V_{oc} values. An examination of the films from these blends indicates that film-thickness and morphology were also a major hindrance to performance and a potential point of improvement for future materials.

SECTION TWO: INTRODUCTION

As a result of their analogous optical and electronic properties, π-conjugated polymers continue to garner significant interest as alternatives to inorganic semiconductors for use in organic solar cells (OSC)s and organic field-effect transistors (OFET)s. Organic semiconductors offer two key advantages over their inorganic counterparts: the ability to alter the materials' properties through chemical synthesis and the potential to fabricate large-area films using low-cost solution processing techniques.[171–173] Although power conversion efficiencies (PCE)s for polymer OSCs have increased considerably over the years, the materials structures are also becoming more complex. As such, the cost of the materials is now a major part of the expense of OSCs.[171]

To date, the synthesis of numerous materials featuring a range of lowest occupied molecular orbital (LUMO), highest occupied molecular orbital HOMO and band gap values have been reported.[108,174] Often band gap engineering of conjugated polymers is

accomplished via the so called donor-acceptor or push-pull approach in which alternating electron-donating and electron-accepting moieties are combined within the same polymer backbone.[13,117] Such π-conjugated polymers are typically synthesized by metal-catalyzed polycondensation reactions such as Kumada, Stille and Suzuki cross-coupling reactions.[175,176] Although these methods offer tremendous versatility, they also produce stoichiometric amounts of organometallic waste that must be removed to afford the high-purity organic semiconductors required for good device performance.[177] For this reason there has been an increased interest in direct heteroarylation polymerizations (DHAP)s which are based on the cross-coupling of an aryl halide directly with another arene via activation of a C–H bond.[178] The benefits of this method are the reduction in the number of steps for monomer synthesis, and elimination of potentially unstable monomers.[115,178,179] Initially, this methodology was used for the synthesis of small molecules but recently has been used for the synthesis of high molecular weight π-conjugated polymers. One limitation of DHAP reactions is a potential lack of selectivity of C-H bond activation and thus crosslinking may occur if more than one type of C–H bond is reactive within a monomer resulting in side-reactions and defects.[180,181]

Stemming from the early success of poly(3-hexylthiophene) and the ease of synthesis of various functional derivatives, thiophene and its annulated derivatives are ubiquitous in materials for use in organic electronic devices. DHAP has been successfully applied to the synthesis of thiophene containing conjugated polymers including benzodithiophene (BDT) which has been used in the synthesis of some of the best performing OSC materials to date.[180,182] In an effort to improve upon the properties of

BDT-based polymers, several groups have evaluated the impact of substitution with oxygen to produce the analogous benzodifurans.[46,183–185] Although furan is isoelectronic to thiophene, it has a smaller Dewar resonance energy. Thus, replacing thiophene with furan is expected to favor the formation of quinoidal structures. Furthermore, the higher electronegativity of oxygen relative to that of sulfur can result in deeper HOMO and LUMO favorably impacting the open circuit voltage.[48]

These furan type building blocks can be further improved through expansion of the central aromatic ring structures to create the tetracyclic naphthodifuran. The rigid coplanar structure of this type of heterocycle reduces the rotational disorder within the polymer facilitating π-electron delocalization and π-π stacking potentially increasing the charge carrier mobility.[49,50] As a result, mobilities exceeding 5.31 $cm^2\ V^{-1}\ s^{-1}$, and photocurrent efficiencies as high as 6.9 % have been reported.[186] The angular-shaped, or "zigzag", naphtho[1,2-*b*:5,6-*b*']difuran (NDF) is the most promising isomer due to greater degree of delocalization in comparison to the linear analog.[186]

Based on this information we decided to pursue the synthesis of new materials by adding alkyl side chains to the NDF structure to improve solubility. We paired it with diketopyrrolopyrrole (DPP) monomers due to the strong electron-accepting nature which can increase the intramolecular charge transfer within the polymer chain and stabilize the LUMO levels of the resulting materials.[187] The properties of this monomer can also be modified by using either furan or thiophene as the flanking group. The FDPP monomer was chosen to compare with the TDPP due to its potential to enhance solubility. The alkyl side chains were varied to further evaluate the trade-off between improved solubility

afforded by the branched 2-ethylhexyl chains and enhanced film forming properties of the linear dodecyl chains. Due to the common issue of DHAP reaction conditions often being highly substrate specific coupled with our desire to expand the presence of NDF-based materials within the literature, additional polymers were also synthesized using thienopyrrolodieone (TPD) as the electron acceptor to demonstrate the substrate scope of DHAP with NDF as a donor component. The stereoelectronic and reactivity properties of TPD are quite different from those of DPP, and successful synthesis of materials based on both acceptors with similar polymerization conditions is important to establishing a potentially broadly applicable reaction condition for developing new materials based on NDF. Further characterization of these materials in device applications will be explored in future work to evaluate the performance of these materials.

SECTION THREE: RESULTS AND DISCUSSION

The synthesis of the monomers is shown in Scheme 1. The reaction between naphthalene-1,5-diol and 1-bromododecan-2-one produced compound 1 in yields exceeding 95%. The product was cyclized to afford the alkylated NDF **2** with moderate yields between 58% and 67%. Deprotonation of **2** using *n*-butyllithium followed by quenching with the appropriate reagents produced the boronic ester **4** and the stannane **5**. Monomer **4** was isolated in a good yield of 82%; however, purification issues lead to low yields of **5** which prevented meaningful examination of Stille polymerizations of this system. Initial attempts to synthesize the target polymers via Suzuki polymerization produced low molecular weight materials, with low degrees of polymerization (DPn) (~5) and wide poly-dispersity indices (~3). These results, coupled with previously mentioned

issues with isolating the stannane, lead us to investigate the synthesis of the target polymers via DHAP. A major benefit of this approach was the replacement of the organometallic precursors **4** and **5** with the halogenated species **6**, which was synthesized in moderate to good yields (63%). This monomer was readily isolated and purified either via column chromatography or recrystallization.

The general reaction conditions are shown in Scheme 2 and the optimization condition summarized in Table 1. Attempts to form the desired polymers via DHAP from the non-halogenated NDF core and a brominated DPP species did not result in any desired products. This finding is in agreement with previously published evidence that DHAP broadly prefers the more electron-rich species to bear the halogen, although there have been reports of substrates which prefer an inversion of the monomer reactivity in DHAP reactions which further highlights the substrate dependence of particular DHAP reaction conditions and the degree of molecular engineering required in the process.[181] The general reaction conditions are shown in Scheme 2 and the optimization condition summarized in Table 1. Initially, we examined the use of THF as a solvent, but no product was recovered for any reagent combinations investigated. Next, we examined toluene as a solvent and two different catalyst systems: Herrmann-Beller catalyst (di-μ-acetatobis[2-[bis(2-methylphenyl)phosphine]benzyl]dipalladium) / $^{t}Bu_3PHBF_4$ or $Pd(OAc)_2$/ (*o*-OMePh)$_3$P. In either case, only trace amounts of polymer were recovered after heating at 120 °C under high pressure conditions. The catalyst $Pd_2(dba)_3$ was also investigated with toluene as a solvent due to reports of its use in DHAP reactions, however use of this catalyst system were unproductive for the substrates used.[181] Changes to the catalyst system did not

improve the reaction and increasing the reaction temperature also had no benefit, indicating a fundamental incompatibility of NDF-based materials with non-polar DHAP conditions. Changing the solvent system to a blend of toluene and *N,N*-dimethylacetamide (DMAc) in order to reach higher reaction temperatures and increase the solvent polarity also did not yield any improvements. We then moved to using only DMAc as the solvent due to previous examples of success with DHAP reactions in small molecules and conjugated polymers in highly polar solvent systems.[181] Originally, we were concerned that this system would not be adequate for solubilizing high molecular weight polymers due to limited solubility of the monomers, however the catalyst system of Herrmann's catalyst / $^{t}Bu_3PHBF_4$ at 160 °C produced the desired polymers albeit in low yields (~30%). Increasing the reaction temperature did not improve the reaction yield and instead lead to decomposition of the starting materials with no isolable product.

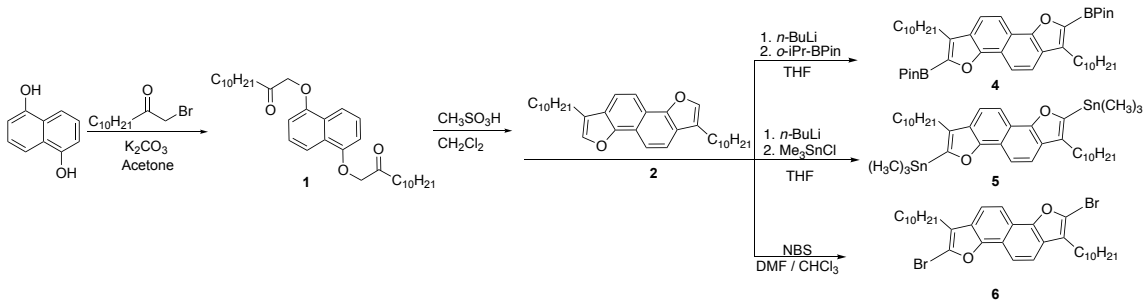

Scheme 6. Synthesis of functional 1,6-didecylnaphtho[1,2-b:5,6-b']difurans.

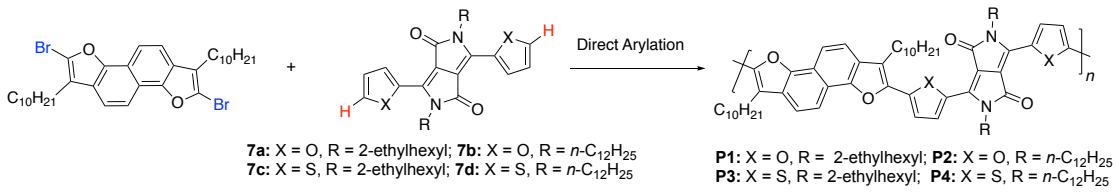

Scheme 7. Synthetic route for polymerization via direct arylation.

Based on other reports of DPP based DHAP reactions we decided to use *N-N'*-dimethylformamide (DMF) as a reaction solvent and $Pd(OAc)_2$ as a catalyst.[188] Under these conditions, we saw comparable results to the previous system consisting of DMAc and Herrmann-Beller catalyst although in even lower yields. In addition to changing the solvent and catalyst system, we investigated changing the nature of the proton-shuttle system involved in the DHAP mechanistic cycle. Switching the base from cesium carbonate to potassium carbonate greatly increased the reaction yields, possibly due to the higher solubility of potassium carbonate in DMF making it more active within the proton-shuttle cycle. This catalyst system was found to not require any external ligand to be present, which is in agreement with reviews of DHAP that have shown such ligands may reduce the activity of palladium catalysts in polar solvents.[178] We note that the DHAP reaction using the non-halogenated NDF **2** and a brominated DPP species did not produce any polymer. This finding highlights the substrate dependence of various DHAP reaction conditions.[180]

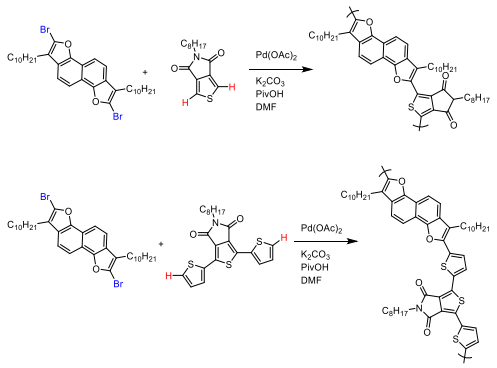

Scheme 8. Synthetic route for polymerization via direct arylation.

The DHAP reaction of **6** and the corresponding DPPs **7a** –**d** using $Pd(OAc)_2$ in DMF afforded polymers **P1** – **P4** in good yields (61 – 66%) after purification by Soxhlet extraction. Additionally, two polymers featuring TPD-based acceptors (**P5-P6**) were obtained using identical reaction conditions to establish a wider substrate scope for the coupling conditions. These polymers were obtained in similar yield and repeat unit lengths, indicating that the catalyst system used may be broadly applicable to a variety of NDF-based materials. The molecular weights were estimated using gel permeation chromatography (GPC) at 35 °C using chloroform as the eluent. The resulting data is summarized in Table 2. All the polymers exhibited narrow PDI value which can be explained by the use of Soxhlett fractioning to remove lower weight polymers, which reduces the overall isolated yield of the polymerization reaction but results in the isolation of higher molecular weight materials with narrow dispersity. Additionally, highly planar conjugated polymers often exhibit limited solubility at higher molecular weights and consequently narrower PDI values compared to highly soluble materials which can reach

higher chain lengths and widen the range of obtainable molecular weight materials. The thermal properties of the polymers were evaluated using thermal gravimetric analysis (TGA) and the results are summarized in Table 2. The 5 % weight loss onsets occurred between 244 – 294 °C which is well above the operational threshold temperature for OSCs. Differential scanning calorimetry (DSC) measurements were performed to observe any potential glass-transition behaviours, and no obvious transitions were seen in the temperature range used indicating that the polymers exhibit largely amorphous behaviour.

Solvent	Monomer	Catalyst	Ligand	Temp (°C)	Time (hr)	Yield
THF	7a	Herrmann's catalyst	$^{t}Bu_3PHBF_4$	80	48	NR
THF*	7c	Herrmann's catalyst	$^{t}Bu_3PHBF_4$	150	1.5	NR
THF	7b, 7c	Herrmann's catalyst	(*o*-OMePh)$_3$P	80	48	NR
THF*	7a, 7b	$Pd(OAc)_2$	(*o*-OMePh)$_3$P	150	1.5	NR
Toluene	7a, 7d	Herrmann's catalyst	$^{t}Bu_3PHBF_4$	120	48	Trace
Toluene	7d	$Pd(OAc)_2$	(*o*-OMePh)$_3$P	120	48	Trace
Toluene	7b, 7d	$Pd(OAc)_2$	None	120	48	NR
Toluene	7d	$Pd(OAc)_2$	$(CyHex)_3PHBF_4$	120	48	NR
Toluene	7d	$Pd_2(dba)_3$	None	120	48	NR
Toluene*	7b, 7c	Herrmann's catalyst	(*o*-OMePh)$_3$P	200	1.5	NR
Toluene*	7d	$Pd(OAc)_2$	$^{t}Bu_3PHBF_4$	200	1.5	NR
Toluene / DMAc	7a, 7b	$Pd(OAc)_2$	$(CyHex)_3PHBF_4$	120	48	NR
DMAc	All	Herrmann's catalyst	$^{t}Bu_3PHBF_4$	160	48	61 – 66%
DMAc	7b	Herrmann's catalyst	(*o*-OMePh)$_3$P	160	48	10%
DMAc	7d	$Pd(OAc)_2$	$(CyHex)_3PHBF_4$	160	48	NR
DMAc*	7a, 7c	$Pd(OAc)_2$	(*o*-OMePh)$_3$P	200	1.5	Trace
DMAc*	7a, 7d	$Pd(OAc)_2$	$^{t}Bu_3PHBF_4$	200	1.5	Trace
DMAc*	7d	Herrmann's catalyst	$^{t}Bu_3PHBF_4$	250	1.5	NR
DMAc*	7b	Herrmann's catalyst	$^{t}Bu_3PHBF_4$	250	4	37%
DMF	All	$Pd(OAc)_2$	None	120	48	60 – 64%

Table 9. Optimization of DHAP for NDF and DPP monomers. Entries bearing an asterisk were conducted under pressure in an Anton-Parr reactor.

Polymer[a]	Yield (%)[b]	T_c[c] [°C]	M_w[d]	M_w/M_n	DPn
P1	62	294	54.9	1.07	46
P2	65	270	37.3	1.14	33
P3	66	244	30.6	1.14	25
P4	61	246	30.8	1.10	30
P5	71	260	22.2	1.05	31
P6	67	277	23.8	1.06	33

Table 10. Reaction conditions and molecular weight data for NDF-DPP polymers. [a] [monomer] = 0.25 M in DMF, and Pd catalyst loading = 4 mol%. [b] Isolated yield after Soxhlett purification. [c] 5% weight loss temperature determined by TGA. Molecular weight data was obtained by GPC (see ESI).

SECTION FOUR: OPTICAL AND ELECTRONIC PROPERTIES

The normalized absorption spectra of $CHCl_3$ solutions of **P1**-**P4** and their thin films are shown in Figures 1 and 2 respectively, and the collected optical data is summarized in Table 3. The materials all feature broad absorption profiles that approach 900 nm for the absorption onset in solution and extending towards 1000 nm in the solid state. The high energy transition observed around 350 nm is attributable to localized π-π* transitions, while the lower energy transitions between 670 nm and 719 nm are attributed to intramolecular charge transfer between the donor and acceptor monomer units. The furyl-flanked DPP polymers **P1** and **P2** exhibit a significant bathochromic shift of 32 - 39 nm in their absorption profiles compared to the thienyl-flanked DPP polymers **P3** and **P4** in solution. We attribute this difference to the enhanced planarity of **P1** and **P2** arising from lessened twisting of the polymer backbone owing to the smaller size of furan compared to thiophene, allowing for greater orbital overlap between the donor and acceptor monomers.

When cast onto glass substrates, the separate absorption profiles observed in the solution spectra converge to yield very similar absorption maxima. The furan-

linked **P1** and **P2** exhibited a hypsochromic shift of 7 to 25 nm compared to their solution maxima, while the thienyl **P3** and **P4** underwent a bathochromic shift of 30 and 28 nm compared to their solution maxima. In addition to the shifts in absorption maxima, **P3** and **P4** demonstrated overall broader absorption profiles than **P1** and **P2**, with absorption onsets beginning around 940 nm compared to approximately 870 nm.

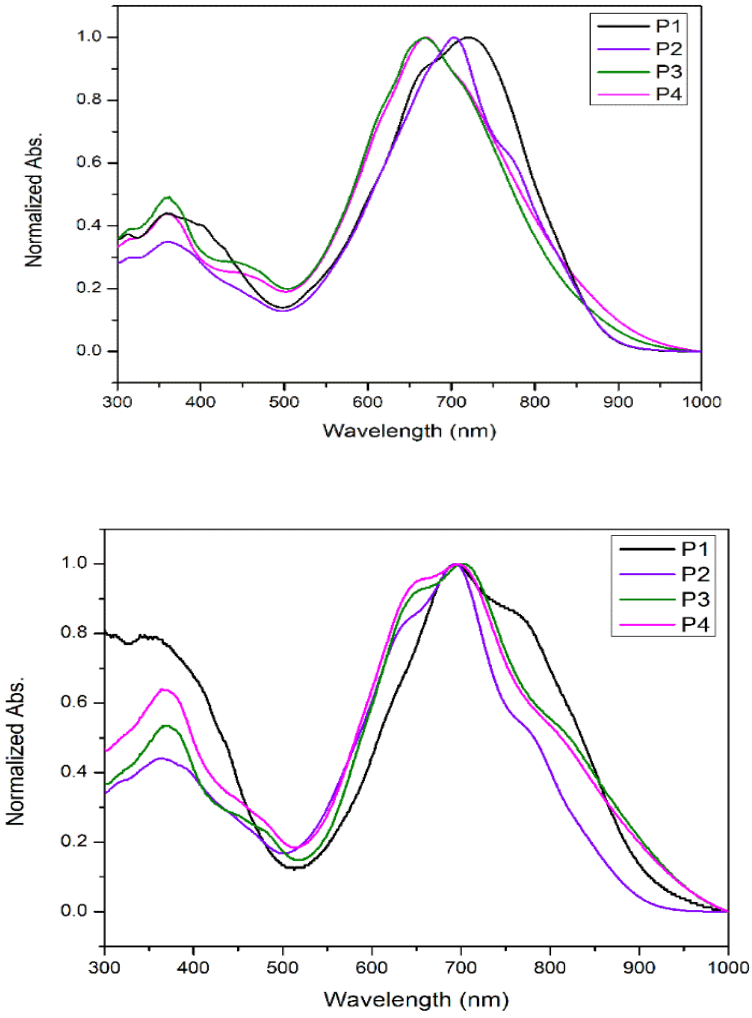

Figure 43. UV-Vis absorption of P1-P4 in solution (top) and film (bottom)

Polymer	λ_{max}^{soln} (nm)	λ_{max}^{film} (nm)	HOMO[b] (eV)	HOMO[d] (eV)	LUMO[c] (eV)	E_g^{opt}[a] (eV)
P1	719	694	-5.1	-4.83	-3.8	1.31
P2	702	695	-5.2	-4.90	-3.9	1.32
P3	670	700	-5.1	-4.77	-3.9	1.25
P4	671	698	-5.1	-5.05	-3.9	1.25

Table 8. Optical and electronic properties for P1-P4. [a] Estimated from the absorption onset of the film. [b] HOMO= -(E_{onset}^{ox} + 4.4) eV. [c] LUMO = HOMO + E_g. [d] HOMO determined via UPS.

The hypsochromic shift of P1 and P2 can potentially be attributed to a disruption of the planarity of the conjugated backbone of the polymers. The presence of a distinct aggregate peak near 800 nm is an indicator of aggregate behavior within the thin-film, which can lead to non-ideal optoelectronic behavior of the material. The bathochromic shift of P3 and P4 can be attributed to enhanced planarity in the solid state and is commonly observed in thiophene-containing materials. The driving force for this enhanced planarity is attributed to more pronounced intramolecular S-O interactions between the adjacent heterocycles of P3 and P4 in the solid state compared to the relatively weak O-O interactions in P1 and P2. In the solid state, P3 and P4 are beneficiaries of increased planarity arising from enhanced intramolecular interactions while P1 and P2 suffer from a decrease in orbital overlap when they transition from solution to solid state. The overall convergence of the four polymers is indicative that all materials exhibit similar optoelectronic properties despite the differences in structural composition.

SECTION FIVE: ELECTROCHEMISTRY

The redox properties of these materials were investigated using cyclic voltammetry (CV) to probe the characteristics of the frontier energy levels. All

materials exhibit reversible oxidation onsets that correspond to HOMO levels of approximately -5.1eV. The materials did not exhibit reduction cycles suitable for determination of the LUMO level. Each of the materials exhibit similar oxidation behavior indicating that the presence of different acceptor monomers did not meaningfully affect the HOMO energy levels. While somewhat shallow compared to other widely reported donor materials, these energy levels are similar to the limited examples of NDF-based materials in the literature.[189] Using these HOMO values along with the optical bandgaps derived from the onset of absorption from the material's UV-Vis absorption spectra in the solid-state, the LUMO values were calculated to range from -3.8 eV and -3.9 eV. These LUMO levels are appropriately offset from those of PCBM to energetically promote the separation of excitons which is necessary for OPV applications.

In order to determine the most accurate HOMO levels for our materials, we employed ultraviolet photoelectron spectroscopy (UPS) to eliminate any uncertainty associated with CV.[190] The values obtained using UPS show that the various polymers have HOMO levels between -4.77eV and -5.05 eV, which are 0.2eV - 0.4eV shallower than those reported by CV. The relatively small difference in the HOMO values between the polymers demonstrates that the energetic influence of the different acceptor monomers is not the driving factor for the difference in characteristics of these materials. One impact of a shallow HOMO level is a lower maximum potential V_{oc} due to the limited energy level offset with the LUMO of the

acceptor component of the active layer and likely accounts for the relatively low V_{oc} observed in the fabricated devices.[191,192]

SECTION SIX: PHOTOVOLTAIC DEVICES

Polymer	Solution	D/A	V_{oc} [V]	J_{sc} [mA/cm^2]	FF	PCE [%]
P1	*o*-DCB	1:2	0.65	1.84	50.66	0.60
	o-DCB[a]	1:2	0.66	2.16	44.74	0.64
	***o*-DCB[d]**	**1:2**	**0.68**	**1.81**	**51.38**	**0.64**
	CF	1:2	0.70	0.95	52.25	0.35
	CF/*o*-DCB[e,d]	1:2	0.68	1.41	44.62	0.43
P2	*o*-DCB	1:2	0.46	1.52	38.26	0.26
	o-DCB[a]	1:2	0.56	2.24	43.82	0.55
	CF	1:2	0.63	2.22	44.15	0.61
	CF/*o*-DCB[b]	**1:2**	**0.64**	**2.44**	**57.12**	**0.90**
P3	***o*-DCB[d]**	**1:2**	**0.52**	**2.18**	**37.62**	**0.43**
	o-DCB[a,d]	1:2	0.50	1.64	42.19	0.35
	CF	1:2	0.84	0.48	45.30	0.19
	CF/*o*-DCB	1:2	0.54	0.34	21.80	0.04
P4	*o*-DCB[d]	1:2	0.57	2.02	44.31	0.51
	***o*-DCB[d,a]**	**1:2**	**0.62**	**1.87**	**44.44**	**0.52**
	CF	1:2	0.52	0.82	41.31	0.18
	CF/*o*-DCB[b]	1:2	0.53	0.20	15.52	0.02

Table 9. Photovoltaic performances for P1-P4. Spin coated at 1200 rpm[a]. 7:3 CF:*o*-DCB solvent ratio respectively[b]. Annealed at 70 °C for 10 minutes[d]. 4:1 CF:*o*-DCB solvent ratio respectively[e].

The performance of **P1-P4** in OSCs were evaluated in BHJ architecture using $PC_{71}BM$ as the electron acceptor with a device configuration of ITO/PEDOT:PSS/**P1** – **P4**:$PC_{71}BM$/Ca/Al. Active layers were spin coated from different solvents (*o*-DCB, CF, CF:*o*-DCB), spin speeds, and are summarized in Table S1. Illustrative examples are listed in Table 4. All devices were prepared and characterized under inert nitrogen atmosphere. The polymers all exhibited unique performances for a given set of processing conditions. At 1:2 (polymer: $PC_{71}BM$) weight ratio, **P1**, **P3**, and **P4** display the best performances when processed from *o*-DCB. The best overall device performance for **P2** was attained when spin coated from a CF/*o*-DCB solvent mixture. To optimize the photovoltaic

parameters of the devices, **P1**, **P3**, and **P4** were subjected to thermal annealing. We also evaluated the introduction of different amounts of diiodooctane (DIO) in *o*-DCB for active layer processing. Spin coating of the **P1: $PC_{71}BM$** active layer from *o*-DCB provided a film thickness of 36 nm and displayed a PCE of 0.60%. To optimize film thickness, **P1: $PC_{71}BM$** *o*-DCB films were spin coated at lower speeds yielding a film thickness of 46nm and a marginally improved PCE of 0.64%. The **P1: $PC_{71}BM$** active layer film processed from CF has a negative influence on device performance despite producing a film thickness of approximately 152 nm. Thermal annealing of both *o*-DCB and CF active layers at 70°C for 10 minutes showed no notable difference in device performance (see table S1). The use of a CF:*o*-DCB (4:1) blend ratio for active layer processing had a detrimental impact on photovoltaic performance yielding a PCE of 0.43%. Devices using **P3** and **P4** processed from *o*-DCB provided a PCE of 0.34% and 0.41%, respectively. Optimized film thickness slightly improved PCE to 0.43% and 0.46%, respectively. Thermal annealing of **P3** and **P4** processed from *o*-DCB at 70°C for 10 minutes had a positive impact on device performance increasing PCE to 0.35% and 0.52%, respectively. In attempts to optimize morphological parameters, the incorporation of different ratios of DIO in *o*-DCB for active layer processing led to no improvement in device performance for **P3** and **P4**, respectively (see Table S1). Evaluating **P2**, active layers spin coated from pure *o*-DCB provided 25 nm thick films ultimately leading to poorer efficiencies and photovoltaic parameters. Decreasing spin coating speeds increased film thickness to 35 nm with approximately a doubling of the PCE from 0.26% to 0.55%. Pure chloroform spin coated films displayed film thickness of approximately 157 nm resulting in a better fill factor of 44.15 and PCE of 0.61%.

Thermally annealing the active layers at 70°C for 10 minutes showed a negative effect on device performance and parameters. When subjecting **P2** to a CF: *o*-DCB solvent blend ratio of 4:1, the devices exhibited a PCE of 0.84% with an enhanced film thickness of approximately 90 nm (see Table S1). In efforts to further optimize **P2**, active layers with different CF:*o*-DCB ratios (9:1, 8:2, 7:3) were also probed to improve photovoltaic properties. With increasing *o*-DCB ratio, there is an increase in OPV parameters leading to the solvent ratio blend ratio of 7:3 exhibiting the best device performance of 0.91%. The improvement in OPV parameters with increasing *o*-DCB content suggest potential changes in the morphology of the active layer are heavily influenced by the processing solvent leading to increase in J_{sc}, V_{oc}, FF, and ultimately the PCE for **P2**. The surface morphology of the films for the best performing devices was examined via tapping-mode atomic force microscopy (AFM) to determine correlations between device efficiencies and active-layer surface morphologies. The height images of these polymer/fullerene blends are shown in Fig 3. The active layer surface roughness was found to be **24.40**, **10.36**, **2.88**, and **2.15** for **P1**, **P2**, **P3**, and **P4,** respectively. Both **P1** and **P3** exhibited potentially more phase segregated domains with fullerene-rich surfaces indicating vertical phase separation within the active layer. Notably, **P2** and **P4** displayed interesting film forming behaviour in comparison to **P1** and **P3**. Attempts to obtain morphological properties via conventional XRD measurements were unsuccessful due to the short interchain distances of the polymers in the solid state, and the limited performance of the materials prohibited the acquisition of GIWAXS data due to lack of ready access. Further probing into the morphological characteristics of the various polymers via GIWAXS could offer insights

into **P2** and **P4** lamellar distances between side chains and ordered networks of aggregation overall impact on film forming ability and PCE, and will be an important characterization technique for future NDF-based materials.[193] Both **P1** and **P2** have notably higher molecular weights contributing to their higher J_{sc} and performance in comparison to **P3** and **P4**. As processing conditions were optimized, domains and intermixing with the fullerene acceptor behaved more beneficially which improved the morphology of the active layer (see Figure S17-S19). In an effort to improve the solution processability for **P2**, increasing the CF ratio had interesting results on film thickness and surface morphological characteristics. Spin casting **P2** from pure *o*-DCB, CF, and 1:4 CF:*o*-DCB yielded film thicknesses of 34 nm, 154 nm, and 64 nm respectively. Efforts to improve the film thickness proved to be detrimental to device performance when film thickness was above 100 nm for **P2**. Tuning the film thickness through solution processing techniques and spin coating speed led to optimal active layer thickness of 64 nm yielding improved photovoltaic parameters. **P1-P4** photovoltaic parameters need further optimizations of the device fabrication and processing conditions to improve active layer morphology and film forming ability to achieve more optimal device performance.

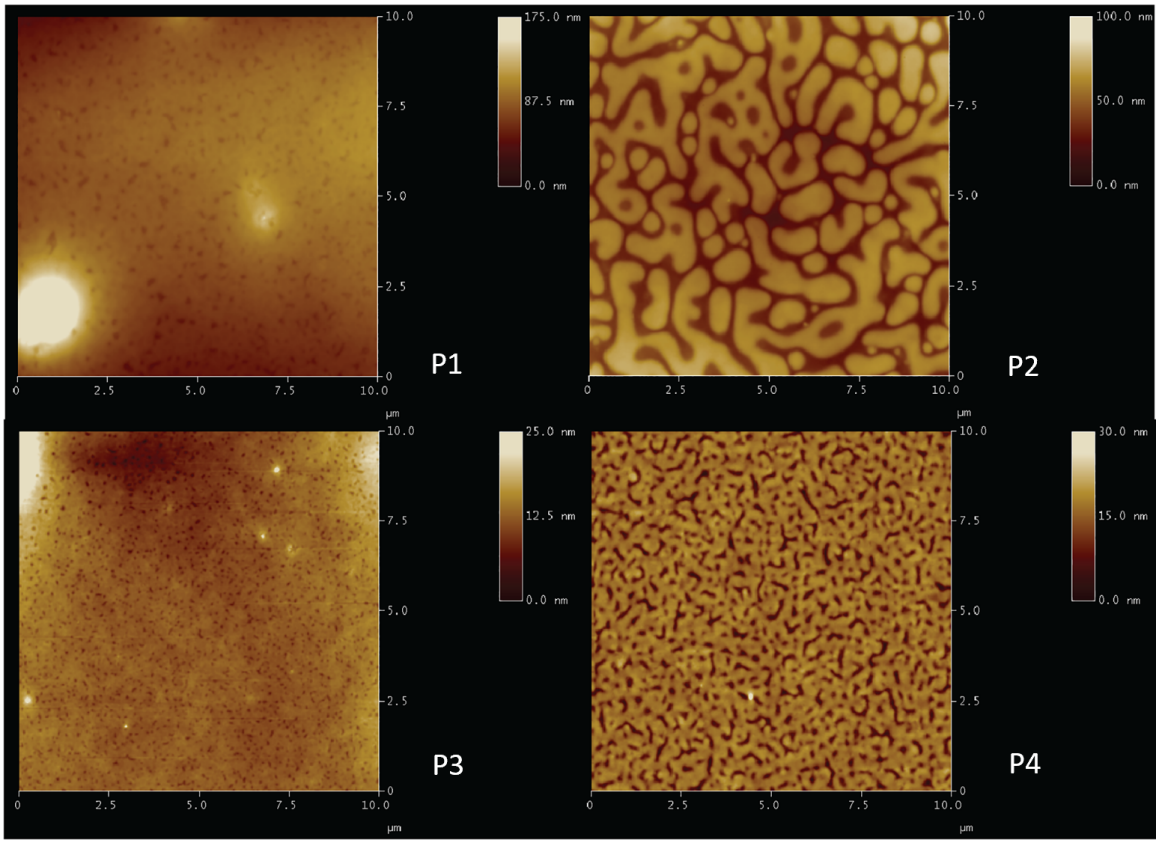

Figure 44. AFM Images (10 um x 10 um) of optimized device conditions for polymers P1-P4.

SECTION SEVEN: CONCLUSIONS

We have demonstrated the synthesis of a series of new polymers based on 1,6-didecylnaphtho[1,2-*b*:5,6-*b'*]difuran and diketopyrrolopyrrole. Each of the polymer systems were synthesized via DHAP in decent yields utilizing a simple and economical catalyst system. The polymers exhibited good molecular weights coupled with narrower PDI values when compared to similar systems made using other cross-coupling conditions, further demonstrating the benefits of replacing traditional polymerization reactions with C-H activation chemistry. The impacts of structural changes to the DPP acceptor unit were

also investigated through variations in the heterocyclic linkage and the alkyl character of the *N*-alkylated DPP core. While the polymers all demonstrated similar optical properties and exhibited similar molecular weights, their film-forming properties varied drastically and lead to significantly different device performances. The polymers exhibited similar optoelectronic characteristics with HOMO values between -4.83 eV and -5.05 eV, LUMO values between -3.8 eV and -3.9 eV, and similar narrow bandgaps between 1.25 and 1.32 eV. The materials also exhibited strong absorption profiles across a wide region of the UV-Vis spectrum which is an important requirement for use in OPV devices.

Despite featuring narrow bandgaps and favorable absorption profiles, a combination of low V_{oc} values arising from shallow HOMO levels of the donor material coupled with low fill-factors due to poor film-forming characteristics led to limited device performances of only 0.9%. Improvements to the solubility of this system may lead to more ideal film-forming behavior and lessened aggregate behavior during device fabrication, which may lead to increased film-thicknesses and better device performance. Additionally, the pairing of NDF with different acceptor moieties may lead to better energetic values of the FMOs and increase the V_{oc} which was a severe limiting factor of the devices. The low cost of synthesis of NDF coupled with its qualities as a highly planar electron-donating building block make it an interesting building block within future organic electronic materials for a variety of applications.

SECTION EIGHT: EXPERIMENTAL

MATERIALS

All reactions were carried out under ambient atmosphere and temperature (18-25 ^{o}C) unless otherwise specified. 2-dodecanone was purchased from Alfa-Aesar. Trans-Bis(acetato)bis[o-(di-*o*-tolylphosphino)benzyl]dipalladium(II) was purchased from Strem Chemicals. All other chemicals were purchased from Sigma-Aldrich and were used without further purification unless otherwise specified. Bromododecan-2-one, 3,6-bisfuryl-2,5-bis(2-ethylhexyl)pyrrolo[3,4-c]pyrrole-1,4(2H,5H)-dione, 3,6-bisfuryl-2,5-bis(dodecyl)pyrrolo[3,4-c]pyrrole-1,4(2H,5H)-dione, 3,6-bisthienyl-2,5-bis(2-ethylhexyl)pyrrolo[3,4-c]pyrrole-1,4(2H,5H)-dione, and 3,6-bisthienyl-2,5-bis(dodecyl)pyrrolo[3,4-c]pyrrole-1,4(2H,5H)-dione, were synthesized according to previously published procedures. Nuclear magnetic resonance (NMR) spectra were carried out in $CDCl_3$ and recorded at 400MHz (^{1}H) using an Agilent 400 MHz VNMRS. ^{1}H NMR were internally referenced to the residual protonated solvent peak, and the ^{13}C NMR were referenced to the central carbon peak of the solvent. In all spectra, chemical shifts are given in δ relative to the solvent. Gel permeation chromatography (GPC) measurements were performed on a Shimadzu LC-20A system with a UV-Vis detector. Analyses were conducted at 35 ^{o}C using chloroform as the eluent at a flow rate of 1.0 mL/min. Calibration was based on polystyrene standards. Cyclic voltammetry was performed using a potentiostat with a scanning rate of 100mV/s. The polymer solutions were drop-cast on a glassy carbon electrode from chloroform and Ag/Ag^{+} was used as the reference electrode. All electrochemistry experiments were performed in degassed CH_3CN under an Ar atmosphere using 0.1M tetrabutylammonium hexafluorophosphate as

the electrolyte. UV-Vis spectroscopy was performed using a Shimadzu UV-1800 with polymer solutions in chloroform and thin-films cast from chloroform onto cleaned glass slides. High resolution mass spectrometry data was obtained on a Waters Qtof (hybrid quadrupolar/time-of-flight) API US system by electrospray (ESI) in the [positive or negative] mode. Mass correction was done by an external reference using a Waters Lockspray accessory. Mobile phases were water and acetonitrile with 0.1% formic acid. The MS settings were: capillary voltage = 3kV, cone voltage = 35, source temperature = 120 °C and dissolvation temperature = 350 °C. Differential scanning calorimetry (DSC) measurements were performed using a TA Instruments DSC Q100 machine, at a scan rate of 10 °C/min under a nitrogen atmosphere. Thermal gravimetric analysis (TGA) was performed using a TA Instruments TGA Q50 machine, at a scan rate of 10 °C/min under a nitrogen atmosphere. Tapping-mode atomic force microscopy were conducted using a Bruker Dimension 3000 instrument.

FABRICATION OF PHOTOVOLTAIC DEVICES

All devices were evaluated under inert atmosphere via solution-based spin-casting fabrication techniques. Organic photovoltaic devices were fabricated in conventional architecture indium tin oxide (ITO)/ Poly(3,4-ethylenedioxythiophene): poly(styrene sulfonate) (PEDOT:PSS)/polymer:[6,6]-phenyl-C_{71}-butyric acid methyl ester ($PC_{71}BM$)/CA/Al). ITO glass substrates were cleaned via (i) sonication (Mucasol), (ii) deionized water, (iii) acetone, and (iv) isopropanol for 10 minutes each respectively. Slides were dried in oven followed by

UV-ozone treatment for 15 minutes. PEDOT: PSS layers (Clevios P VP Al 4083) were filtered (0.45 um) and spin-coated onto ITO substrates at 3500 rpm for 2 minutes then annealed at 150ºC for 30 min in air. After cooling, the substrates were transferred into nitrogen filled glove box. Polymer: $PC_{71}BM$ solution were prepared in a blend ratio of 1:2 (30 mg/ml **P1**, **P3-P.4**, 10 mg/ml **P2**) with different solvents (*o*-DCB or CF) and processing additive ratios (0-4 vol % 1,8-diiodooctane). The prepared solutions were then allowed to stir for 48 hours at 55ºC (CF) or 80 ºC (*o*-DCB) prior to spin coating (1200 – 2000 rpm, for 2 min). Films evaluated under annealing conditions were annealed at 70 ºC for 10 minutes and placed under vacuum. Ca (15 nm) and Al (100 nm) electrodes were successfully deposited via thermal evaporation. Current density (J-V) data were measured utilizing a Keithley 2400 source meter and simulated AM1.5G illumination (100 mW/cm^2, Newport 91160) calibrated using a KG-5 filter Si reference cell.

SYNTHESIS

1,1'-(naphthalene-1,5-diylbis(oxy))bis(dodecan-2-one) (1)

Freshly recrystallized 1,5-dihydroxynaphthalene (3.2g, 20mmol), bromododecan-2-one (13.15g, 50mmol), and potassium carbonate (13.8g, 100 mmol) were combined in acetone (120mL) and were brought to reflux overnight. The solution was cooled to room temperature and the solid product precipitated by pouring into water. The resulting suspension was filtered and dried under vacuum to yield a tan solid (10.3g, 97%). ^{1}H NMR; $CDCl_3$ 0.88 (6H, t, J=6.5Hz), 1.23 – 1.43 (32H, m), 1.67 (4H, m), 2.72 (4H, t, J= 7.3Hz), 4.71 (4H, s), 6.76 (2H, d, J= 7.7Hz), 7.41 (2H, t, J= 8.2Hz), 7.98 (2H, d, J= 8.4Hz); ^{13}C NMR; $CDCl_3$ 13.96, 22.51, 22.98, 29.06, 29.13, 29.24,

29.28, 29.38, 31.72, 39.07, 72.89, 105.66, 115.05, 125.22, 153.21, 207.93, HRMS *m/z*: M^+ calcd for $C_{34}H_{52}O_4$ 525.3844; found, 525.3937, error 1.3ppm.

1,6-didecylnaphtho[1,2-*b*:5,6-*b'*]difuran (2)

To a solution of methylene chloride (50mL) and compound 1 (2.6g, 5mmol) was added methanesulfonic acid (2.62mL, 40mmol) dropwise. The dark-colored solution was brought to reflux for 5 hours, turning dark purple over the period. After conclusion of the reaction, the solution was cooled to room temperature and poured into water. The product was extracted with methylene chloride (3x20mL), washed with brine and saturated $NaHCO_3$, then dried with Na_2SO_4. After removal of the solvent, the resulting dark solid was purified by column chromatography using hexanes as the eluent to yield a yellow solid (1.54g, 63%). ^{1}H NMR; $CDCl_3$ 0.88 (6H, t, J= 6.7 Hz), 1.23 – 1.32 (32H, m), 1.76 (4H, m, J= 7.8Hz), 2.76 (4H, t, J= 7.5Hz), 7.56 (2H, s), 7.72 (2H, d, J= 8.5Hz), 8.12 (2H, d, J= 8.4Hz); ^{13}C NMR; $CDCl_3$ 14.12, 22.68, 23.71, 29.34, 29.46, 29.52, 29.62, 31.90, 109.99, 114.98, 118.71, 119.03, 121.99, 123.32, 140.08, 151.39, HRMS *m/z*: M^+ calcd for $C_{34}H_{48}O_2$ 489.3733; found, 489.3717, error 3.2ppm.

2,7-dibromo-1,6-didecylnaphtho[1,2-b:5,6-b']difuran (6)

A solution of chloroform and DMF (9:1, 40mL) containing compound **2** (2.35g, 4.7mmol) was cooled to 0 ^{o}C, placed under Ar, and protected from light. Recrystallized NBS (1.77g, 10mmol) was added portion-wise followed by continued stirring under the aforementioned conditions for 1.5 hours. The resulting solution was poured into water, extracted with chloroform (3x20mL), washed with brine, and dried using Na_2SO_4. After removal of the

solvent, the resulting yellow-brown solid was purified by column chromatography using an eluent gradient from hexanes to hexanes: ethyl acetate (8:2) to yield a yellow-white solid (1.52g, 53%). Alternatively, the crude product was purified by recrystallization from hexanes by successive heating and cooling to afford the pure product in slightly lower overall yields. ^{1}H NMR; $CDCl_3$ 0.87 (6H, t, J= 6.5 Hz), 1.21 – 1.43 (32H, m), 1.72 (4H, m, J= 7.8Hz), 2.77 (4H, t, J= 7.5 Hz), 7.65 (2H, d, J= 8.4Hz), 8.08 (2H, d, J= 8.4Hz); ^{13}C NMR; $CDCl_3$ 14.12, 22.67, 24.19, 29.04, 29.29, 29.32, 29.40, 29.59, 31.88, 47.43, 115.46, 118.01, 118.27, 120.99, 124.20, 144.20, 151.23. HRMS *m/z*: M^+ calcd for $C_{34}H_{46}Br_2O_2$ 645.1943; found, 645.1929, error 2.1ppm.

General procedure for the synthesis of copolymers under high pressure conditions

To a Parr vial was added solvent (THF, toluene, or DMAC: 2mL) and placed under an atmosphere of Ar. After an appropriate amount of time, **6** (1.0 equiv.), **7a-d** (1.0 equiv.), pivalic acid (1.0 equiv.), cesium carbonate (2.5 equiv.), a palladium source ($Pd(OAc)_2$, or Herrmann-Beller: 0.05 equiv.), and a phosphine ligand ($P(o\text{-}OMePH)_3$, $(CyHex)_3PHBF_4$, or $^{t}Bu_3PHBF_4$: 0.1 equiv.) was added. The flask was heated using an Anton-Parr reactor to an appropriate temperature and pressure for 1.5 hours. The reaction mixture was cooled to room temperature and precipitated into cold methanol followed by filtration through a cellulose thimble. The polymers were purified by Soxhlet extraction by rinsing with acetone, hexanes, and chloroform. The final product was obtained after removal of the solvent and dried under heated vacuum.

General procedure for the synthesis of copolymers under standard pressure conditions

To a 15mL round bottomed flask was added **6** (1.0 equiv.), **7a-d** (1.0 equiv.) and DMF (3mL). To the flask was added pivalic acid (1.0 equiv), potassium carbonate (2.5 equiv.), and $Pd(OAc)_2$ (0.05 equiv.) in one portion and the reaction was heated to 130 ^oC for 3 days. The reaction mixture was cooled to room temperature and precipitated into cold methanol followed by filtration through a cellulose thimble. The polymers were purified via Soxhlet extraction by rinsing with acetone, hexanes, and chloroform. The final product was obtained after removal of the solvent and dried under heated vacuum.

Synthesis of P1

Following the general polymerization conditions using compounds **3** (171 mg, 0.25 mmol) and **7a** (154mg, 0.25mmol) using a reaction time of 3 days yielded a blue-green solid (97mg, 63%).^{1}H NMR; $CDCl_3$ 0.87 (12H, b), 1.25 (72H, b), 3.02 (4H, b), 7.75 (4H, b), 8.20 (4H, b) GPC ($CHCl_3$, 35 ^oC): M_w = 54.9 kDa. M_n = 52.7 kDa. PDI = 1.05.

Synthesis of P2

Following the general polymerization conditions using compounds **3** (160 mg, 0.24 mmol) and **7b** (130mg, 0.26mmol) using a reaction time of 3 days yielded a blue solid (102mg, 65%). ^{1}H NMR; $CDCl_3$ 0.87 (18H, b), 1.25 (50H, b), 2.80 (4H, b), 4.04 (4H, b), 7.39 – 8.28 (8H, b) GPC ($CHCl_3$, 35 ^oC): M_w = 33.3 kDa. M_n = 31.1 kDa. PDI = 1.07.

Synthesis of P3

Following the general polymerization conditions using compounds **3** (171 mg, 0.26 mmol) and **7c** (145mg, 0.26mmol) using a reaction time of 3 days yielded a blue solid (114mg,

68%). ^{1}H NMR; $CDCl_3$ 0.87 (12H, b), 1.25 (68H, b), 3.02 (4H, b), 4.00 (4H, b),7.32 – 7.71 (4H, b), 7.85 (2H, b), 9.01 – 9.21 (4H, b) GPC ($CHCl_3$, 35 ^{o}C): M_w = 24.3 kDa. M_n = 23.7 kDa. PDI = 1.02.

Synthesis of P4

Following the general polymerization conditions using compounds **3** (269 mg, 0.41 mmol) and **7d** (196mg, 0.40mmol) using a reaction time of 3 days yielded a blue solid (172mg, 59%). ^{1}H NMR; $CDCl_3$ 0.87 (18H, b), 1.25 (50H, b), 2.75 (4H, b), 4.08 (4H, b) 6.82 (2H, b) 7.71 (2H, b), 8.14 (2H, b), 8.61 (2H, b) GPC ($CHCl_3$, 35 ^{o}C): M_w = 30.8 kDa. M_n = 28.1 kDa. PDI = 1.10.

SUPPLEMENTAL INFORMATION

Device Fabrication and Characterization

All devices were fabricated and characterized under inert atmosphere via solution-based spin-casting fabrication techniques. Organic photovoltaic devices were fabricated in conventional architecture indium tin oxide (ITO)/ Poly(3,4-ethylenedioxythiophene): poly(styrene sulfonate) (PEDOT:PSS)/polymer:[6,6]-phenyl-C_{71}-butyric acid methyl ester ($PC_{71}BM$)/CA/Al). ITO glass substrates were cleaned via (i) sonication (Mucasol), (ii) deionized water, (iii) acetone, and (iv) isopropanol for 10 minutes each respectively. Slides were oven dried followed by UV-ozone treatment for 15 minutes. PEDOT: PSS layers (Clevios P VP Al 4083) were filtered (0.45 um) and spin-coated onto ITO substrates at 3500 rpm for 2 minutes followed by thermal annealment for 150^{o}C for 30 min in air. After cooling, substrates were transferred into nitrogen filled glove box. Polymer: $PC_{71}BM$ solutions were prepared in a blend ratio of 1:2 (30 mg/ml **P1**, **P3-P.4**, 10 mg/ml **P2**) with

different solvents (*o*-DCB or CF) and processing additive ratios (0-4 vol % 1,8-diiodooctane). The prepared solutions were then allowed to stir for 48 hours at 55°C (CF) or 80 °C (*o*-DCB) prior to spin coating (1200 – 2000 rpm, for 2 min). Films evaluated under annealing conditions were annealed at 70 °C for 10 minutes and placed under vacuum. Ca (15 nm) and Al (100 nm) electrodes were successfully deposited via thermal evaporation. Current density (J-V) data were measured utilizing a Keithley 2400 source meter and simulated AM1.5G illumination (100 mW/cm^2, Newport 91160) calibrated using a KG-5 filter Si reference cell.

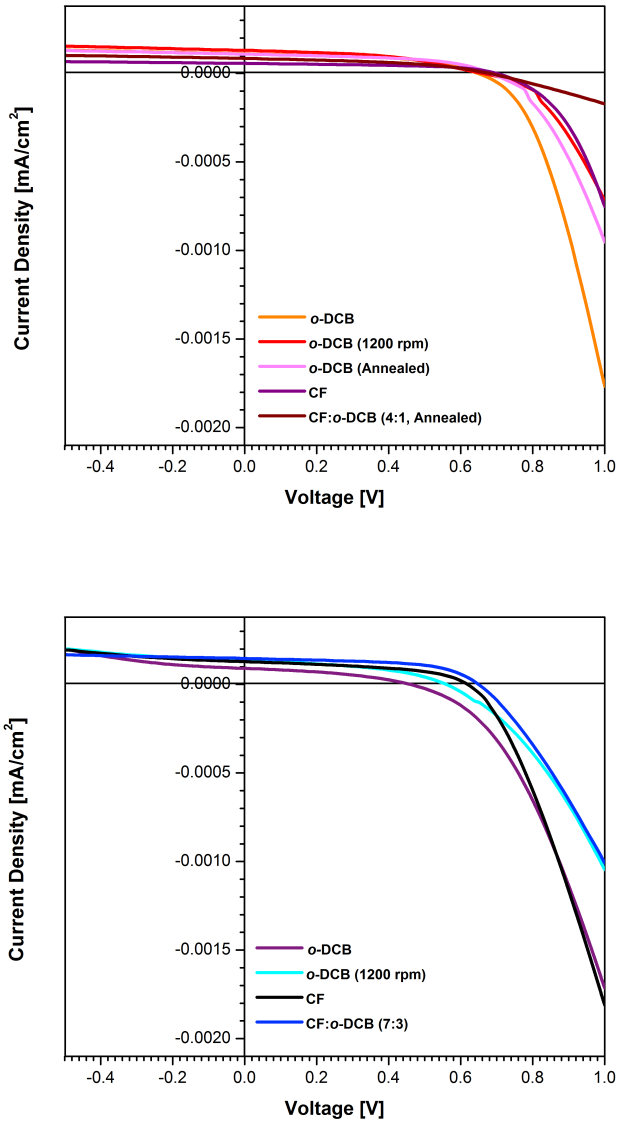

SI Figure 37. Current-voltage characteristics for P1 based OPV (top) and P2 based OPV. (bottom)

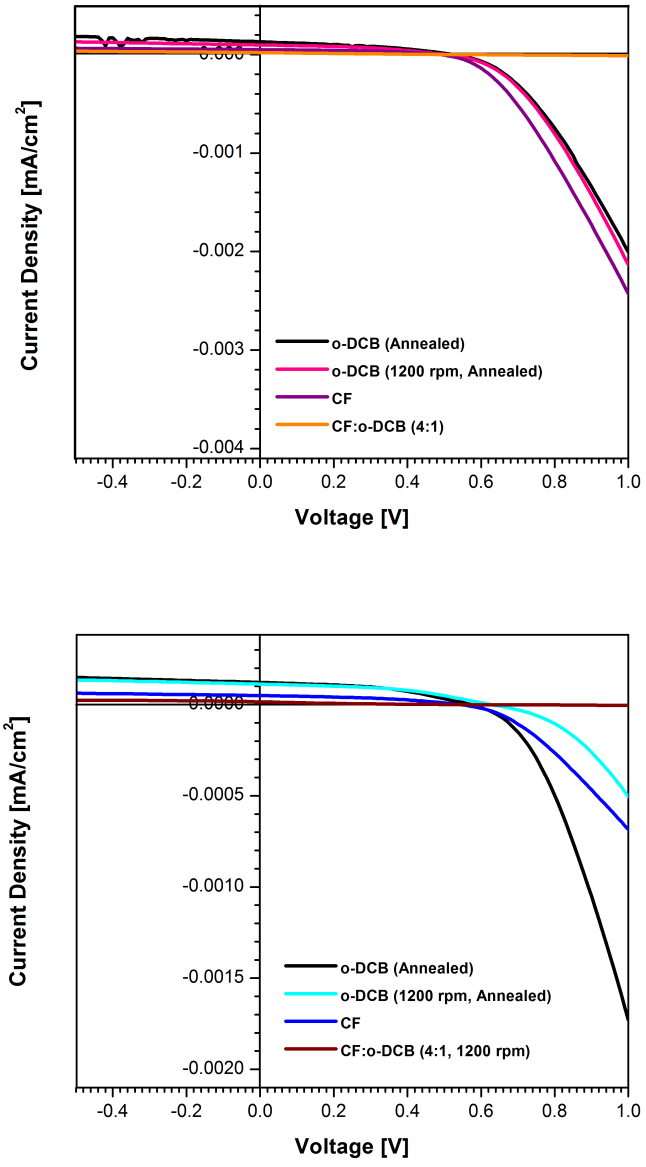

SI Figure 38. Current-voltage characteristics for P3 based OPV (top) and P4 based OPV. (bottom)

Polymer	*Solution*	*D/A*	*Voc [V]*	*Jsc [mA/cm^2]*	*FF*	*PCE [%]*
P1	*o*-DCB	1:2	0.65	1.84	50.66	0.60
	o-DCB[a]	1:2	0.66	2.16	44.74	0.64
	***o*-DCB[d]**	**1:2**	**0.68**	**1.81**	**51.38**	**0.64**
	CF	1:2	0.70	0.95	52.25	0.35
	CF/*o*-DCB[e,d]	1:2	0.68	1.41	44.62	0.43
P2	*o*-DCB	1:2	0.46	1.52	38.26	0.26
	o-DCB[a]	1:2	0.56	2.24	43.82	0.55
	CF	1:2	0.63	2.22	44.15	0.61
	CF/*o*-DCB[b]	**1:2**	**0.64**	**2.44**	**57.12**	**0.90**
P3	***o*-DCB[d]**	**1:2**	**0.52**	**2.18**	**37.62**	**0.43**
	o-DCB[a,d]	1:2	0.50	1.64	42.19	0.35
	o-DCB + 2% DIO[a,d]	1:2	0.45	2.61	30.87	0.36
	o-DCB + 4% DIO[a,d]	1:2	0.38	2.68	35.76	0.37
	o-DCB + 6% DIO[a,d]	1:2	0.45	2.04	38.75	0.36
	CF	1:2	0.84	0.48	45.30	0.19
	CF/*o*-DCB	1:2	0.54	0.34	21.80	0.04
	o-DCB[d]	1:2	0.57	2.02	44.31	0.51
P4	***o*-DCB[d,a]**	**1:2**	**0.62**	**1.87**	**44.44**	**0.52**
	o-DCB + 2% DIO[a,d]	1:2	0.45	2.14	33.29	0.32
	o-DCB + 4% DIO[a,d]	1:2	0.40	3.07	29.04	0.36
	o-DCB + 6% DIO[a,d]	1:2	0.41	1.74	32.09	0.23
	CF	1:2	0.52	0.82	41.31	0.18
	CF/*o*-DCB[b]	1:2	0.53	0.20	15.52	0.02

SI Table 5. Photovoltaic device performance of P1-P4 with PCBM. Spin coated at 1200 rpm[a]. 7:3 CF:*o*-DCB solvent ratio respectively[b]. Annealed at 70 °C for 10 minutes[d]. 4:1 CF:*o*-DCB solvent ratio respectively[e]

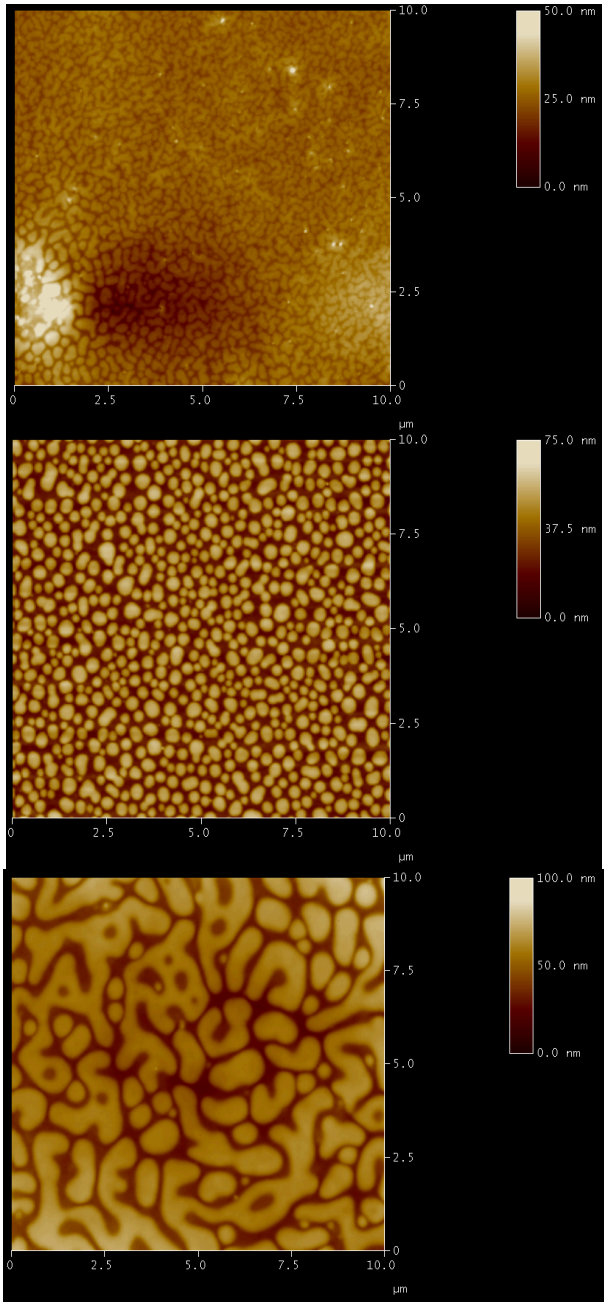

SI Figure 39. AFM image at 10 um x 10 um of devices with P2:PCBM 1:2 spin coated from *o*-DCB with a RMS of 4.80. (top) and AFM image at 10 um x 10 um of devices with P2:PCBM 1:2 spin coated from CF with a RMS of 11.96. (middle) AFM image at 10 um x 10 um of devices with P2:PCBM 1:2 spin coated from CF:*o*-DCB with a RMS of 10.36.

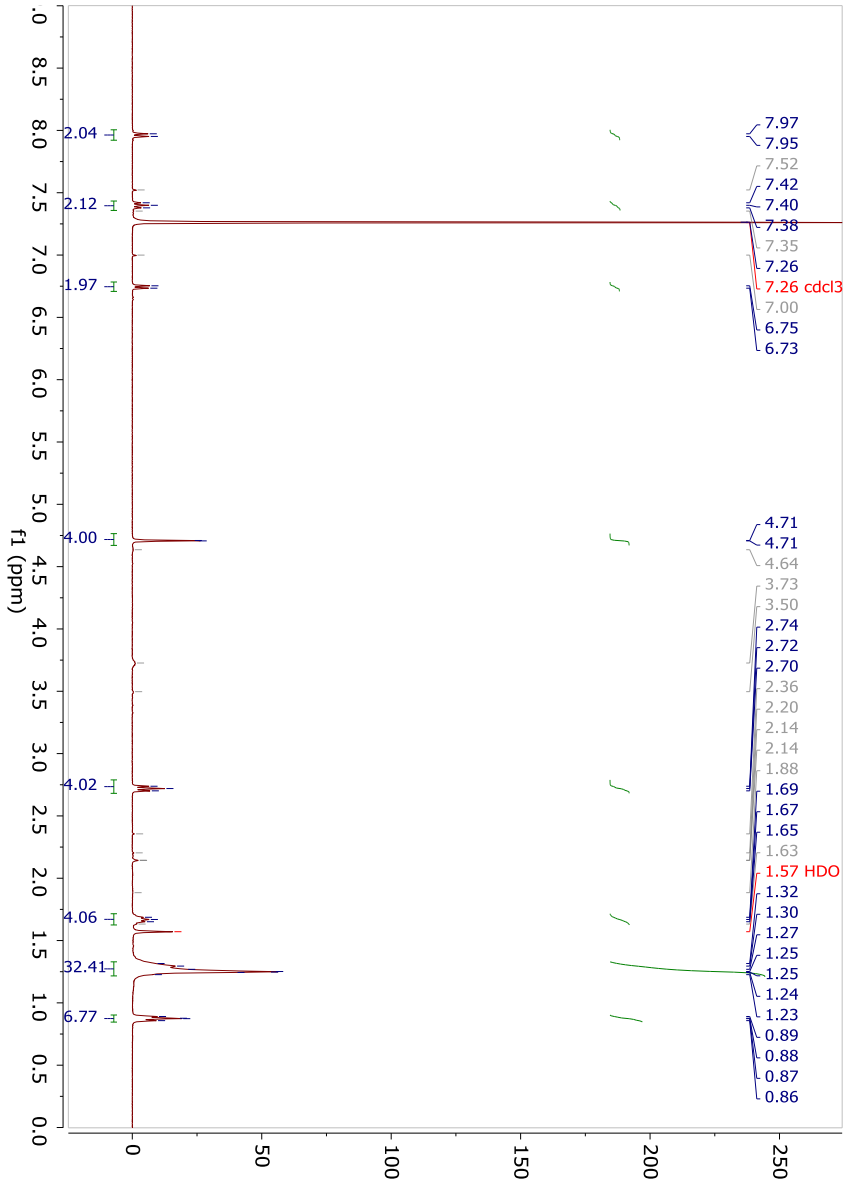

SI Figure 40. H NMR Spectra of 1,1'-(naphthalene-1,5-diylbis(oxy))bis(dodecan-2-one)

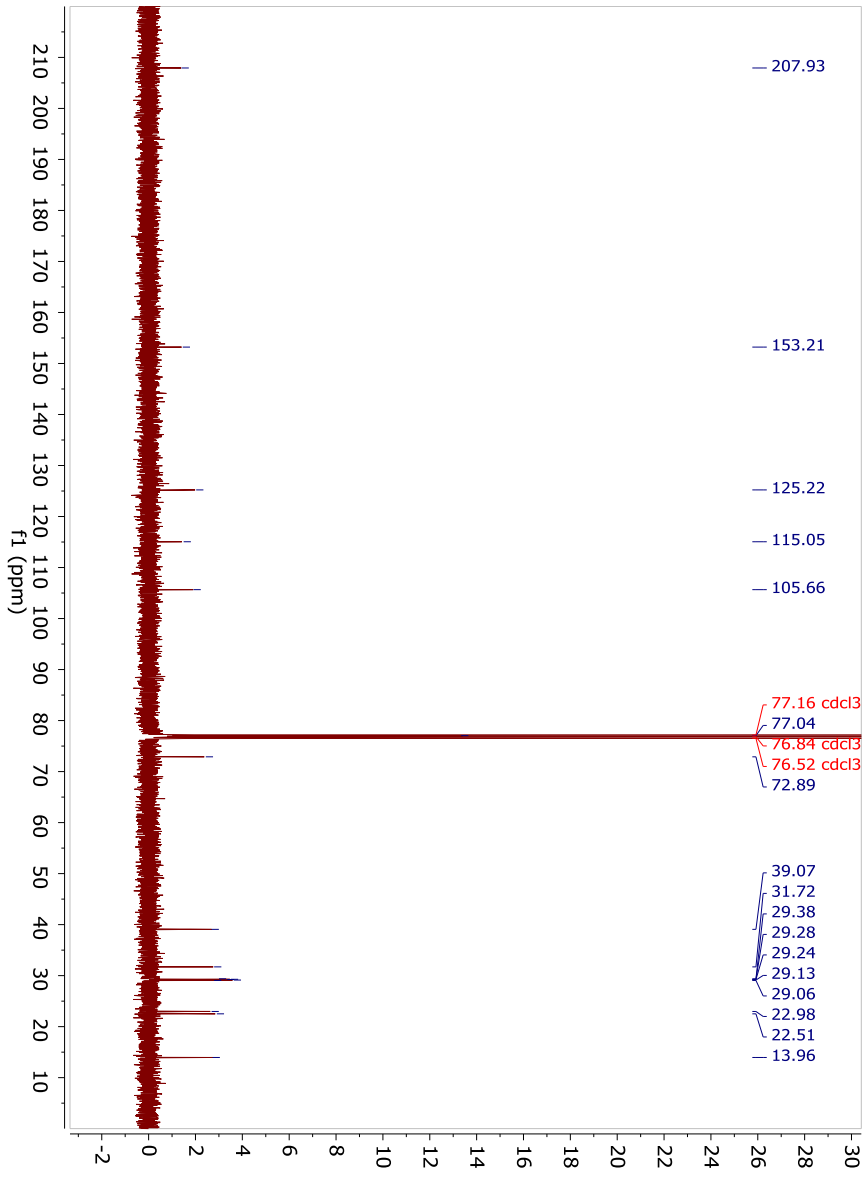

SI Figure 41. C^{13} NMR Spectra of 1,1'-(naphthalene-1,5-diylbis(oxy))bis(dodecan-2-one)

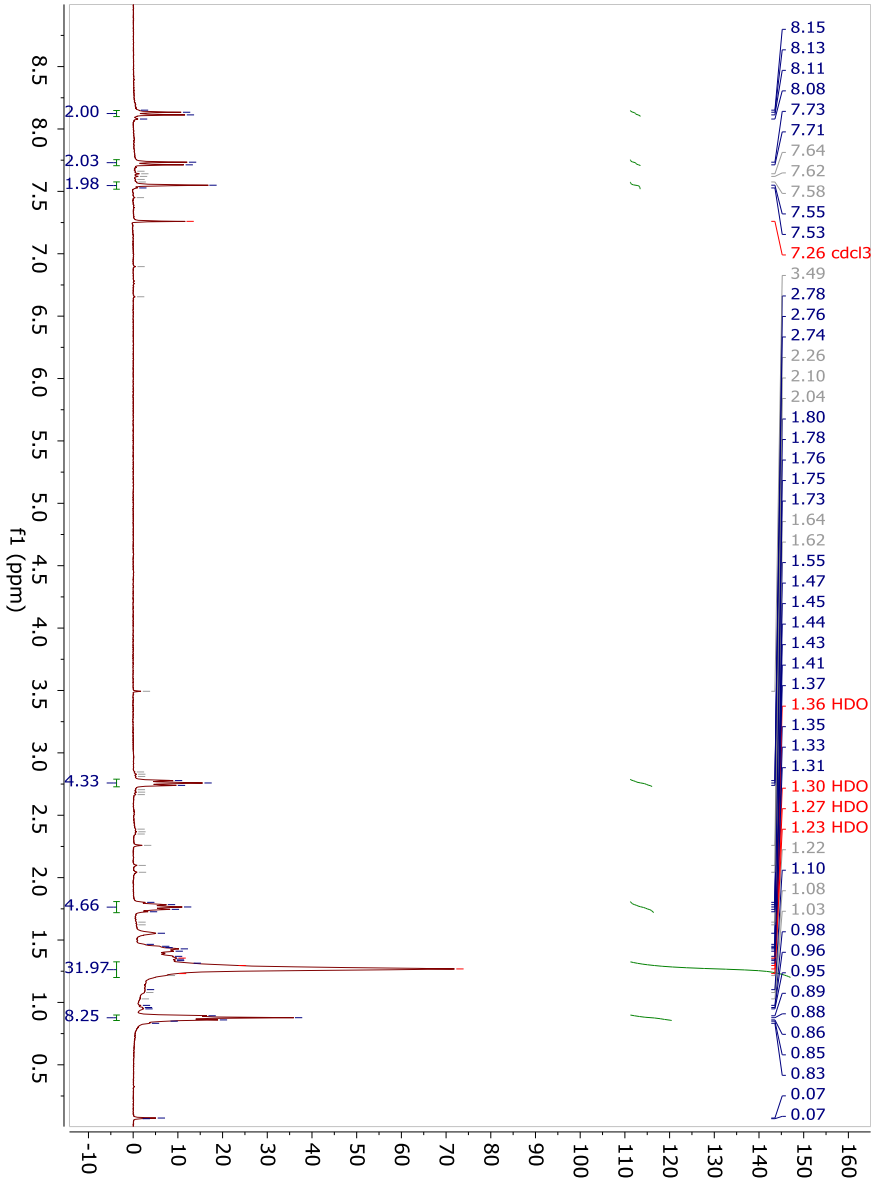

SI Figure 42. H[1] NMR Spectra of 1,6-didecylnaphtho[1,2-b:5,6-b']difuran

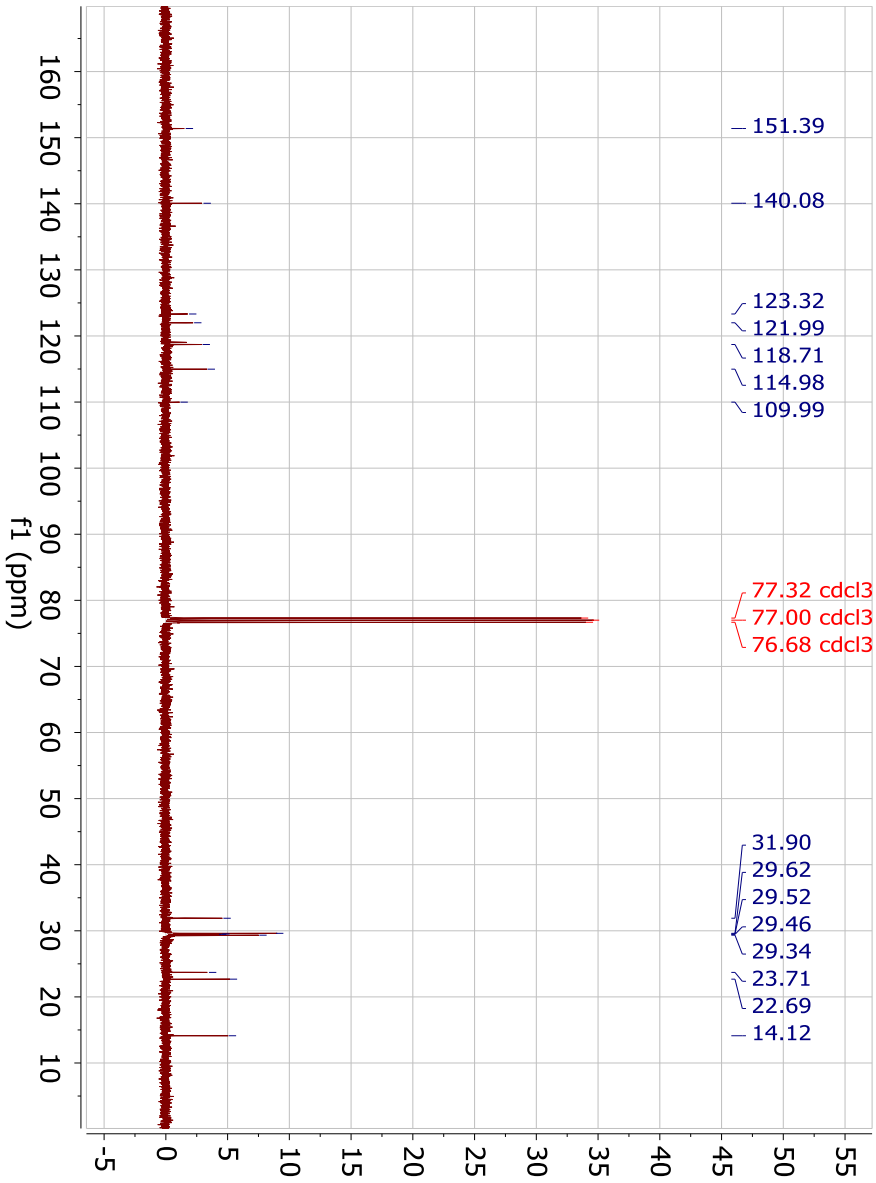

SI Figure 43. C^{13} NMR Spectra of 1,6-didecylnaphtho[1,2-b:5,6-b']difuran

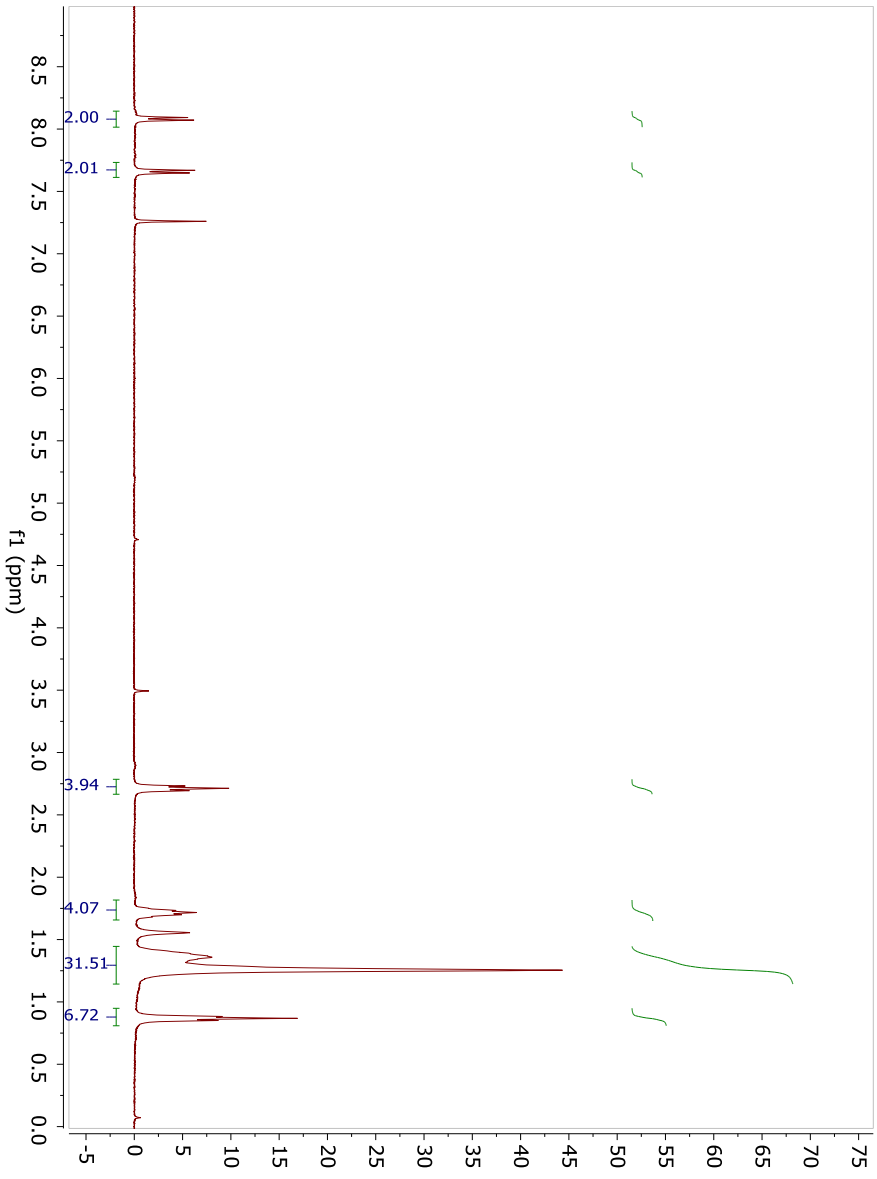

SI Figure 44. H[1] NMR Spectra of 2,7-dibromo-1,6-didecylnaphtho[1,2-b:5,6-b']difuran

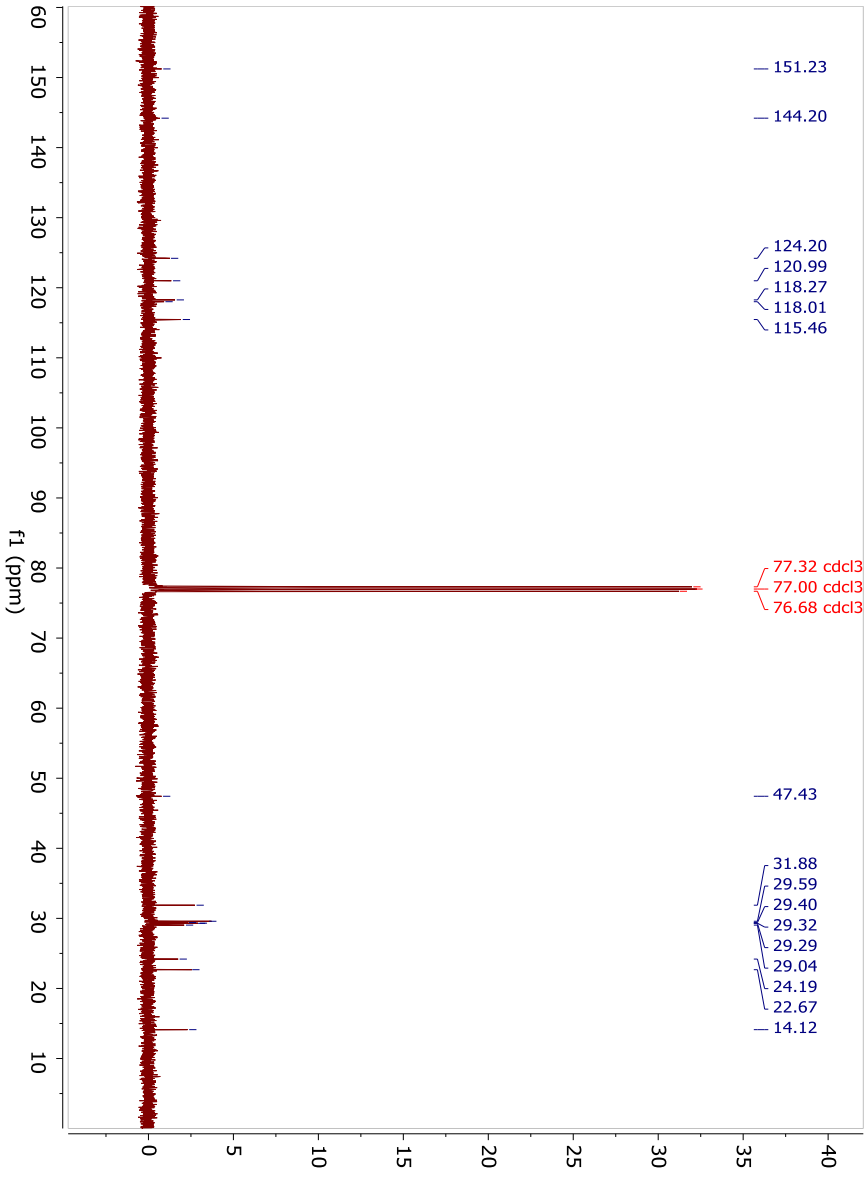

SI Figure 45. C^{13} NMR Spectra of 2,7-dibromo-1,6-didecylnaphtho[1,2-b:5,6-b']difuran

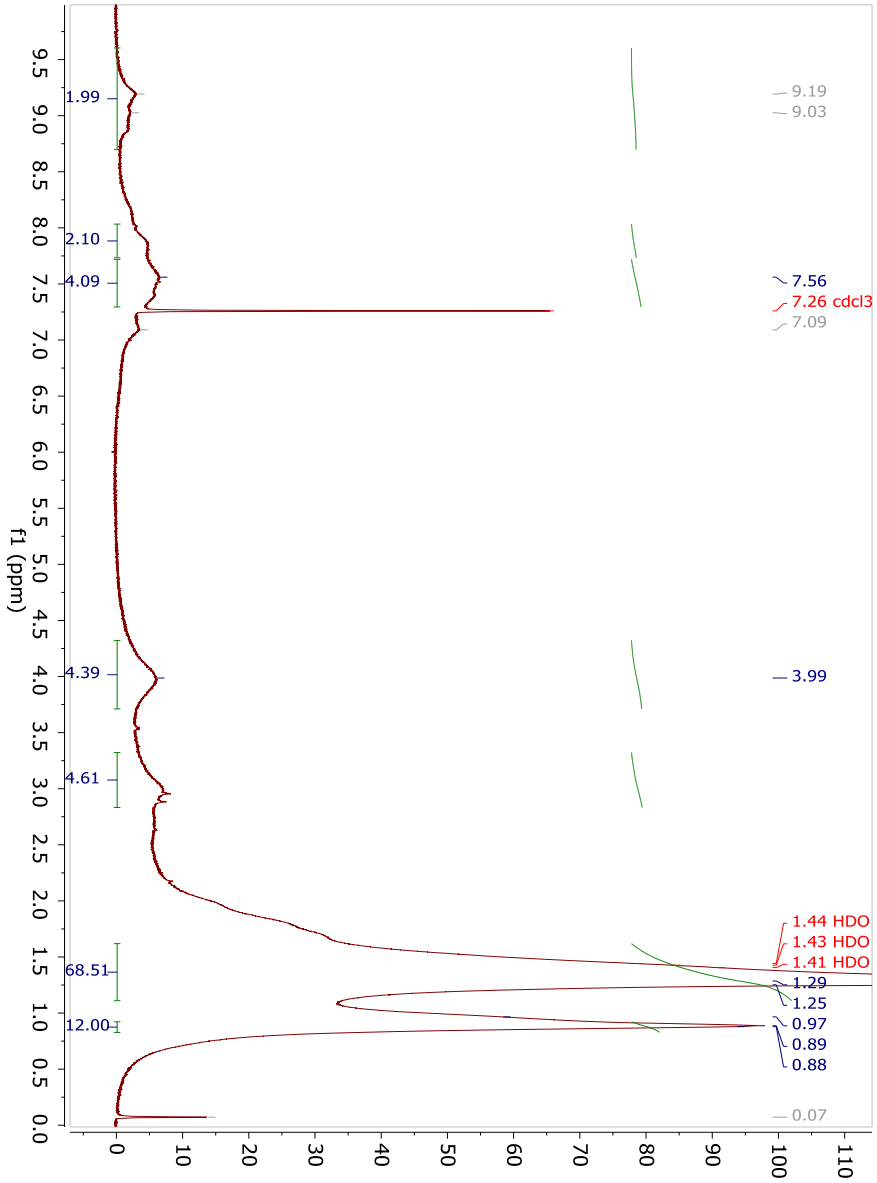

SI Figure 46. H[1] NMR Spectra of P1

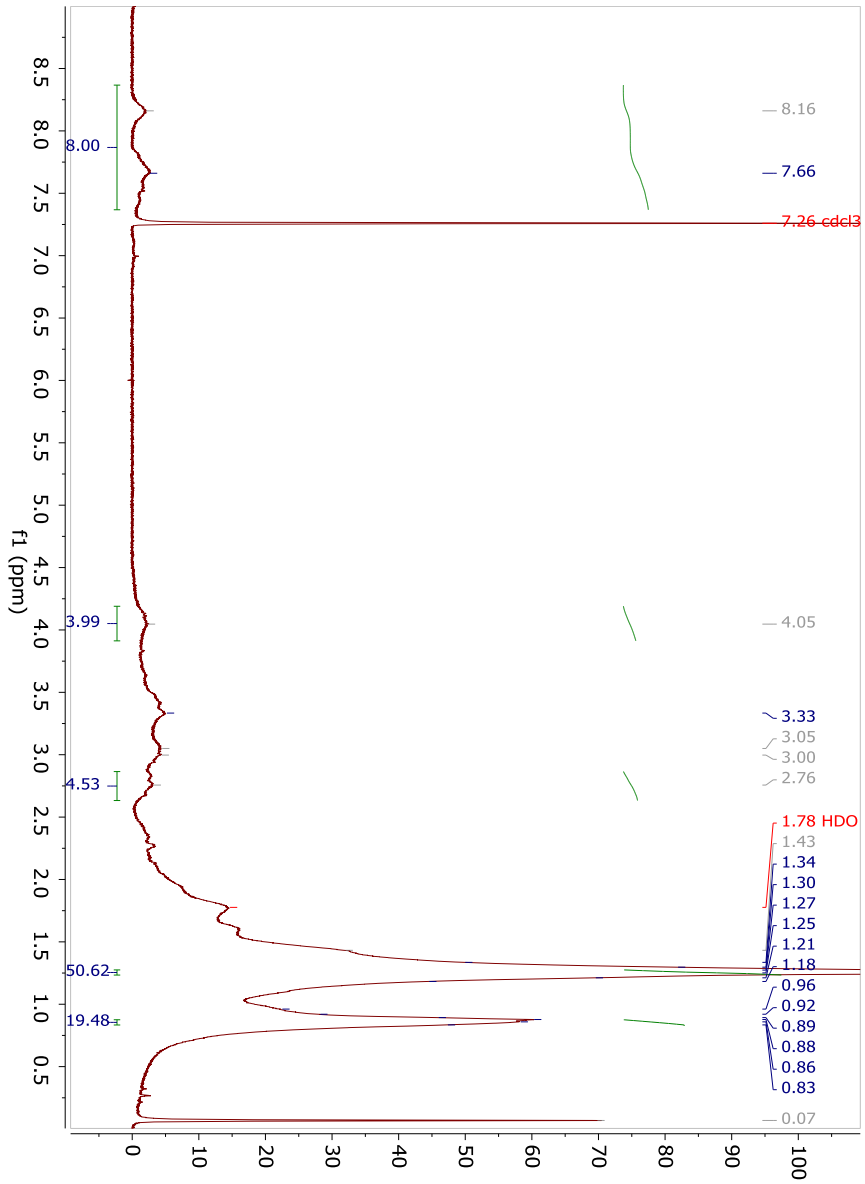

SI Figure 47. H[1] NMR Spectra of P2

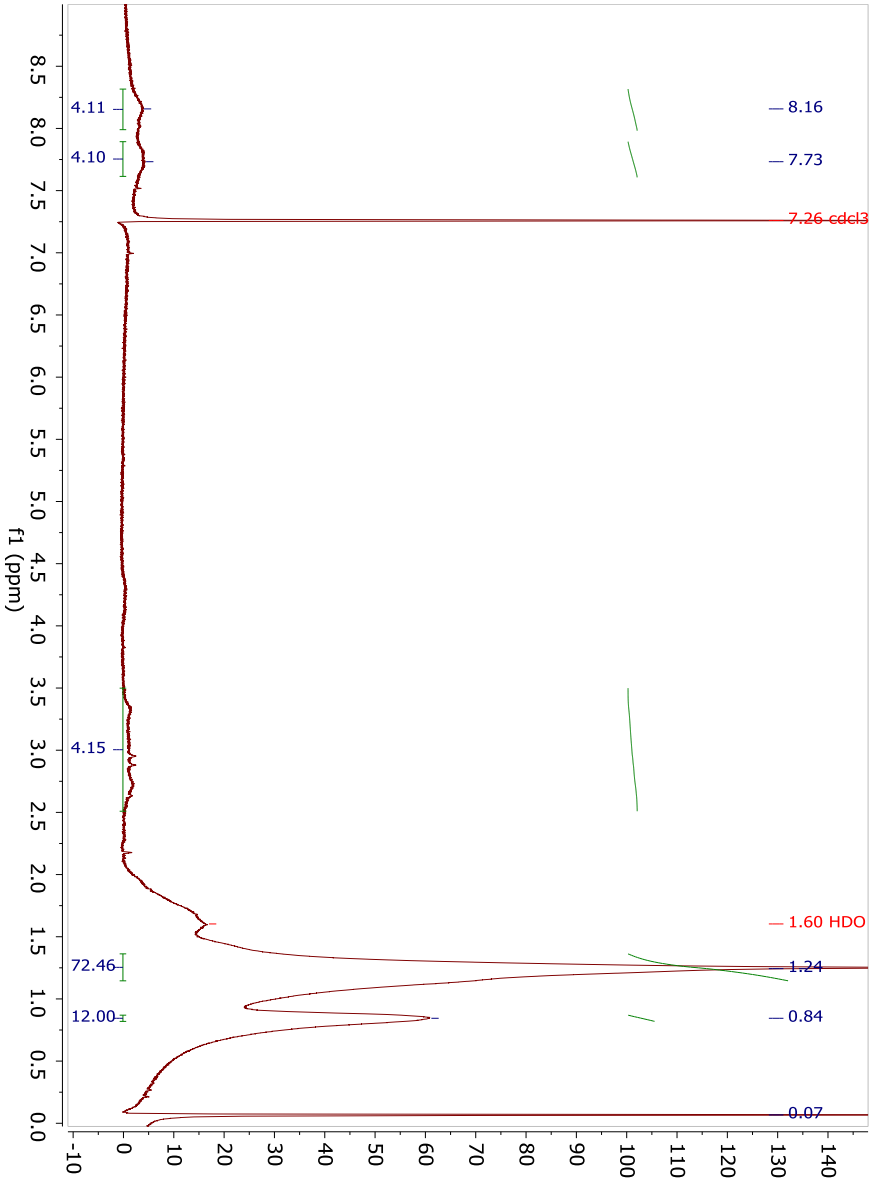

SI Figure 48. H[1] NMR Spectra of P3

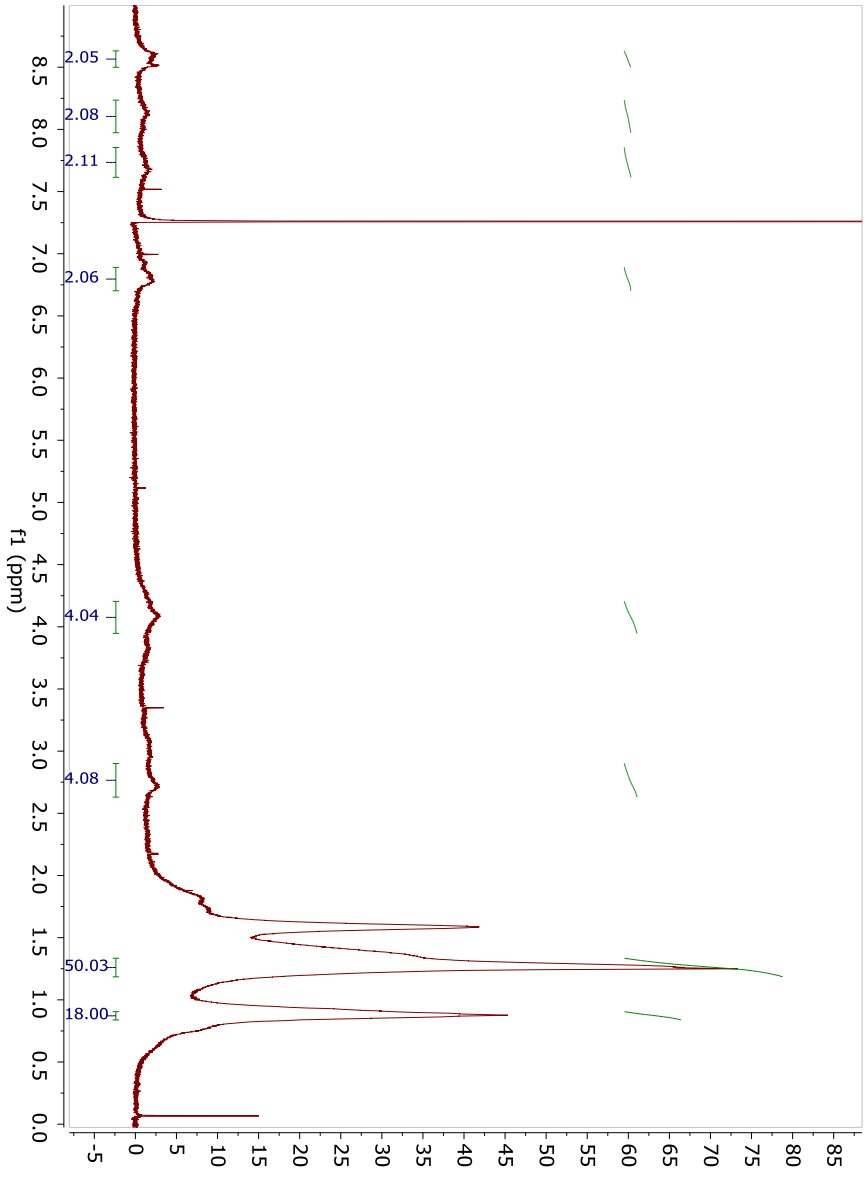

SI Figure 49. H[1] NMR Spectra of P4

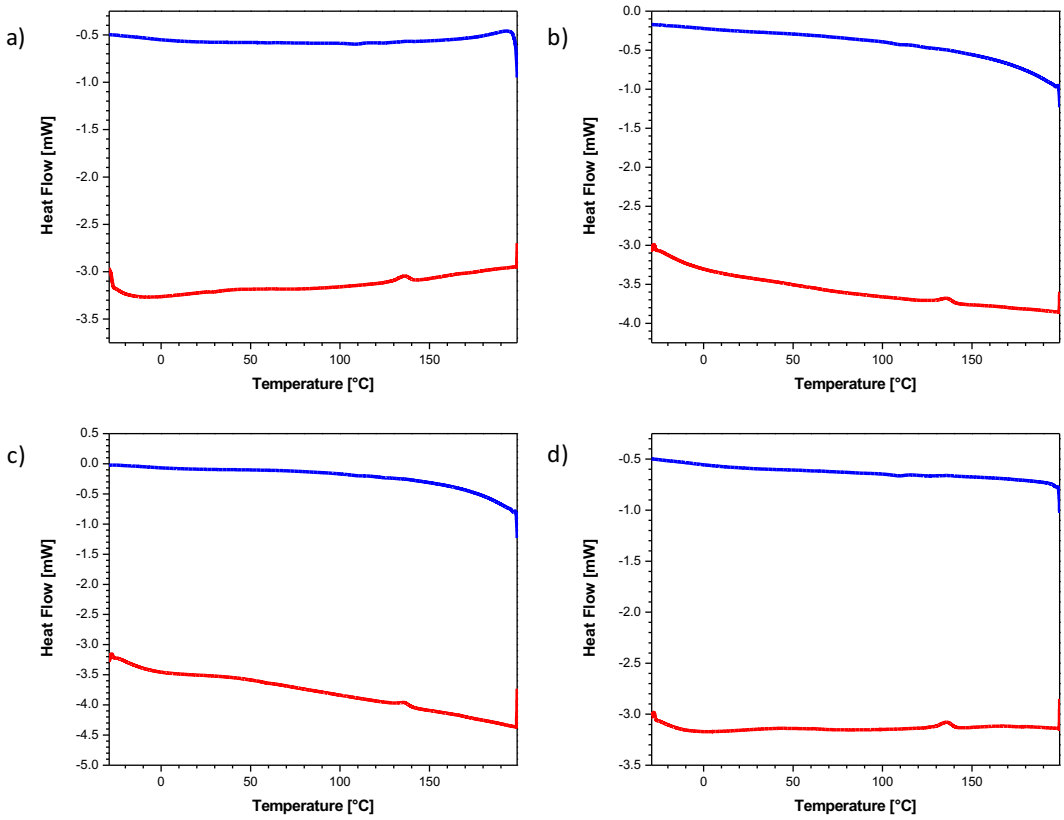

SI Figure 50. Second heating (red) and cooling (blue) scans of a) P1, b) P2, c) P3, and d) P4 measured using DSC between -30 and 200 °C, under a nitrogen atmosphere.

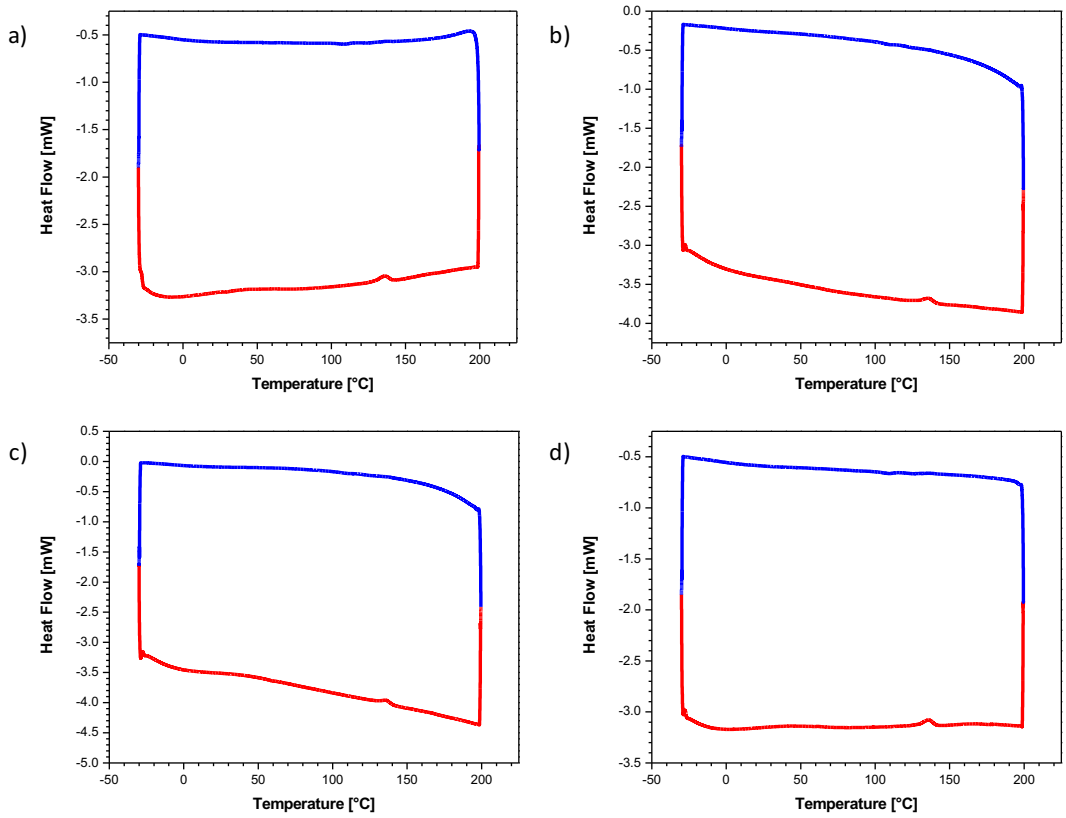

SI figure 51. Second heating (red) and cooling (blue) scans of a) P1, b) P2, c) P3, and d) P4 measured using DSC between -30 and 200 °C, under a nitrogen atmosphere.

General Methods/Experimental

Differential scanning calorimetry (DSC) measurements were performed using a TA Instruments DSC Q100 machine, at a scan rate of 10 °C/min under a nitrogen atmosphere.

Thermal Gravimetric Analysis

No obvious thermal transitions were observed in the temperature range studied.

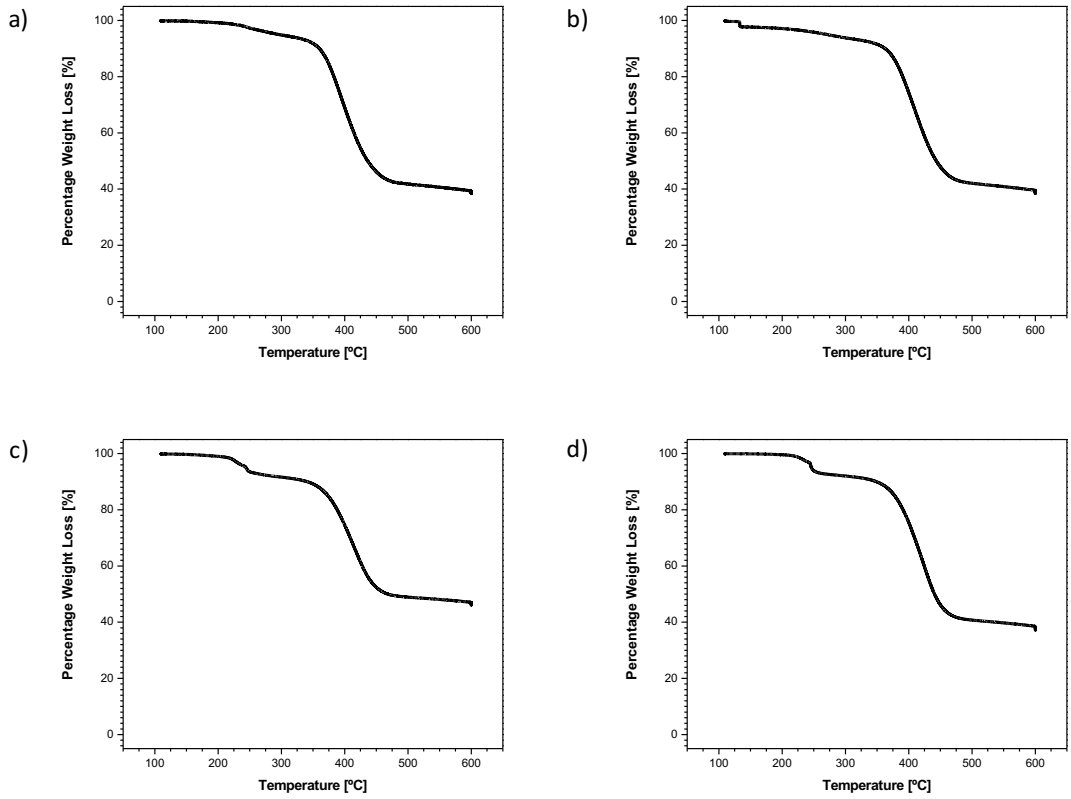

SI Figure 52. TGA thermograms of a) P1, b) P2, c) P3, and d) P4 heating at a scan rate of 10 °C/min under a nitrogen atmosphere.

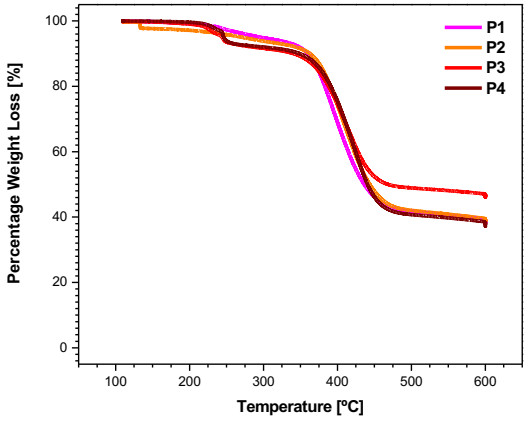

SI Figure 53. TGA thermograms of P1-4 heating at a scan rate of 10 °C/min under a nitrogen atmosphere.

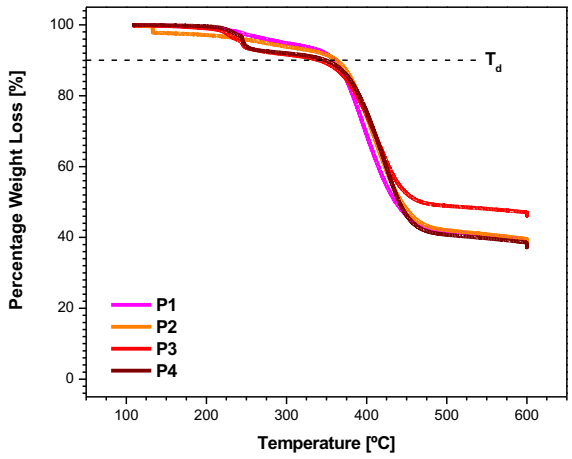

SI Figure 54. TGA thermograms of P1-4 heating at a scan rate of 10 °C/min under a nitrogen atmosphere.

Thermal gravimetric analysis (TGA) was performed using a TA Instruments TGA Q50 machine, at a scan rate of 10 °C/min under a nitrogen atmosphere.

	T_d[a] [°C]
P1	294
P2	270
P3	244
P4	246

[a] 5% weight loss temperature determined by TGA.

The thermal stability of P1-4 was probed using thermal gravimetric analysis with a 5% weight loss observed after 240 °C for all polymers.

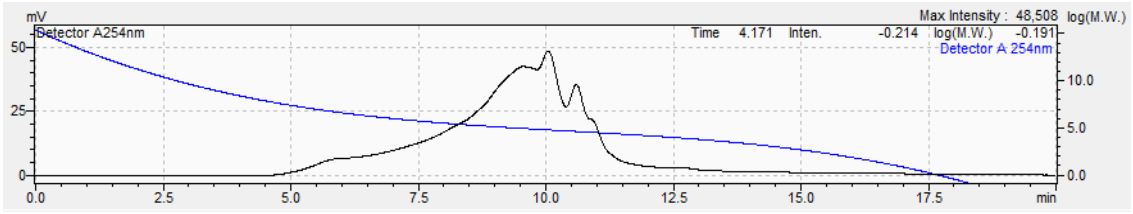

SI Figure 55. GPC trace of P1

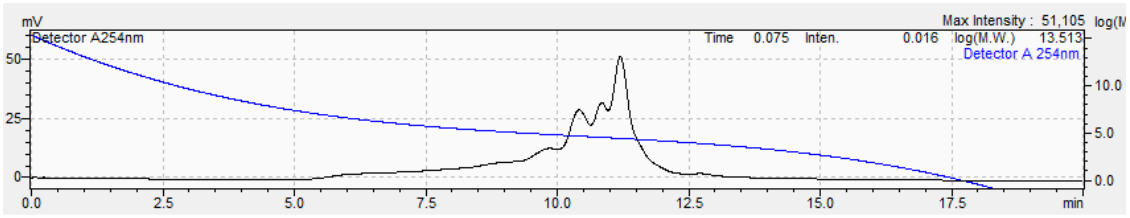

SI Figure 56. GPC trace of P2

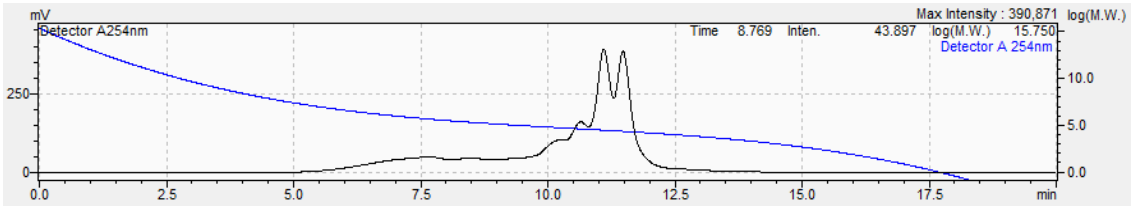

SI Figure 57. GPC trace of P3

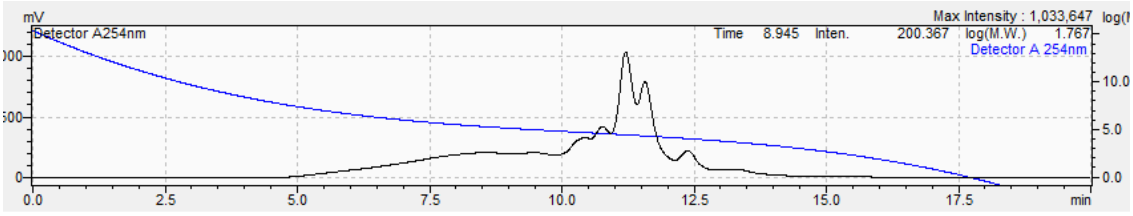

SI Figure 58. GPC trace of P4

General methods for GPC measurement:

Gel-permeation chromatography (GPC) were collected at a flow rate of 1 mL/min at a temperature of 30°C. Molecular weight values were measured using a calibration curve obtained from styrene standards.

BIBLIOGRAPHY

(1) Mazzio, K. A.; Luscombe, C. K. Erratum: The Future of Organic Photovoltaics (Chem. Soc. Rev. (2015) 44 (78-90)). *Chemical Society Reviews.* **2015**, *44* (15), 5744.

(2) Lewis, N. S.; G. Daniel. Powering the Planet: Chemical Challenges in Solar Energy Utilization. **2007**, *104* (42).

(3) Jefferson, M. A Renewable Energy Future? *Handbook. Energy Climate Change.* **2013**, *285* (x), 687–690.

(4) Lu, L.; Zheng, T.; Wu, Q.; Schneider, A. M.; Zhao, D.; Yu, L. Recent Advances in Bulk Heterojunction Polymer Solar Cells. *Chemical Review.* **2015**, *115* (23), 12666–12731.

(5) Allard, S.; Forster, M.; Souharce, B.; Thiem, H.; Scherf, U. Organic Semiconductors for Solution-Processable Field-Effect Transistors (OFETs). *Angewandte. Chemie - International Edition.* **2008**, *47* (22), 4070–4098.

(6) Shaheen, S. E.; Ginley, D. S.; Jabbour, G. E.; Editors, G. O Rganic-Based Photovoltaics : Toward Low-Cost Power Generation. **2005**, *30* (January), 10–19.

(7) Hebner, T. R.; Wu, C. C.; Marcy, D.; Lu, M. H.; Sturm, J. C. Ink-Jet Printing of Doped Polymers for Organic Light Emitting Devices. *Applied Physics Letters.* **1998**, *72* (5), 519–521.

(8) Roncali, J. Synthetic Principles for Bandgap Control in Linear Pi-Conjugated Systems. *Chemial Reviews.* **1997**, *97* (1), 173–206.

(9) Mullekom, H. A. M. van; Vekemans, J. A. J. M.; Havinga, E. E.; Meijer, E. W. *Developments in the Chemistry and Band Gap Engineering of Donor- Acceptor Substituted Conjugated Polymers*; 2001; Vol. 32.

(10) Yannoni, C. S.; Clarke, T. C. Molecular Geometry of Cis- and Trans-Polyacetylene by Nutation NMR Spectroscopy. *Physical Reviews Letters* **1983**, *51* (13), 1191–1193.

(11) Geng, Y.; Liu, W.; Liu, Q.; Wang, F.; Tian, H.; Yao, B.; Xie, Z. Synthesis and Chain-Length Dependent Properties of Monodisperse Oligo(9,9-Di- n -Octylfluorene-2,7-Vinylene)S . *Macromolecules* **2007**, *40* (6), 1851–1857.

(12) Perepichka, I. F.; Perepichka, D. F.; Meng, H. *Thiophene-Based Materials for Electroluminescent Applications*; 2009.

(13) Havinga, E. E.; Rotte, I.; Meijer, E. W.; Box, P. O.; Eindhoven, J. A. Philips Research Laboratories,. **1991**, *43*, 473–478.

(14) Mei, J.; Heston, N. C.; Vasilyeva, S. V.; Reynolds, J. R. A Facile Approach to Defect-Free Vinylene-Linked Benzothiadiazole-Thiophene Low-Bandgap Conjugated Polymers for Organic Electronics. *Macromolecules* **2009**, *42* (5), 1482–1487.

(15) Wudl, F.; Kobayashi, M.; Heeger, A. J. Poly(Isothianaphthene). *Journal of Organic Chemistry.* **1984**, *49* (18), 3382–3384.

(16) Cheng, Y.-J.; Yang, S.-H.; Hsu, C.-S. Synthesis of Conjugated Polymers for Organic Solar Cell Applications. *Chemical Reviews.* **2009**, *109* (11), 5868–5923.

(17) Bhuwalka, A.; Mike, J. F.; He, M.; Intemann, J. J.; Nelson, T.; Ewan, M. D.; Roggers, R. A.; Lin, Z.; Jeffries-El, M. Quaterthiophene-Benzobisazole Copolymers for Photovoltaic Cells: Effect of Heteroatom Placement and Substitution on the Optical and Electronic Properties. *Macromolecules* **2011**, *44* (24), 9611–9617.

(18) Kanimozhi, C.; Yaacobi-Gross, N.; Burnett, E. K.; Briseno, A. L.; Anthopoulos, T. D.; Salzner, U.; Patil, S. Use of Side-Chain for Rational Design of n-Type Diketopyrrolopyrrole-Based Conjugated Polymers: What Did We Find Out? *Physical Chemistry Chemical Physics.* **2014**, *16* (32), 17253–17265.

(19) Szarko, J. M.; Guo, J.; Liang, Y.; Lee, B.; Rolczynski, B. S.; Strzalka, J.; Xu, T.; Loser, S.; Marks, T. J.; Yu, L.; et al. When Function Follows Form: Effects of Donor Copolymer Side Chains on Film Morphology and BHJ Solar Cell Performance. *Advanced Materials.* **2010**, *22* (48), 5468–5472.

(20) Yang, L.; Zhou, H.; You, W. Quantitatively Analyzing the Influence of Side Chains on Photovoltaic Properties of Polymer-Fullerene Solar Cells. *Journal of Physical Chemistry. C* **2010**, *114* (39), 16793–16800.

(21) Boese, R.; Weiss, H.-C.; Blaser, D. Analyses of Propane at 30 K and of n -Butane to n -Nonane at 90 K **. *Angewandte Chemie International Edition.* **1999**, *38*

(5484922), 988.

(22) Lei, T. *Design, Synthesis, and Structure-Property Relationship Study of Polymer Field-Effect Transistors*; 2015.

(23) Szarko, J. M.; Guo, J.; Liang, Y.; Lee, B.; Rolczynski, B. S.; Strzalka, J.; Xu, T.; Loser, S.; Marks, T. J.; Yu, L.; et al. When Function Follows Form: Effects of Donor Copolymer Side Chains on Film Morphology and BHJ Solar Cell Performance. *Advanced Materials.* **2010**, *22* (48), 5468–5472.

(24) Wolfe, J. F.; Arnold, F. E. Rigid-Rod Polymers. 1. Synthesis and Thermal Properties of Para-Aromatic Polymers with 2,6-Benzobisoxazole Units in the Main Chain. *Macromolecules* **1981**, *14* (4), 909–915.

(25) Jenekhe, S. A.; Roberts, M. F. Effects of Intermolecular Forces on the Glass Transition of Polymers. *Macromolecules* **1993**, *26* (18), 4981–4983.

(26) Osaheni, J. A.; Jenekhe, S. A. Efficient Blue Luminescence of a Conjugated Polymer Exciplex. *Macromolecules* **1994**, *27* (3), 739–742.

(27) Kang, C. S.; Paik, M. J.; Park, C. W.; Baik, D. H. Synthesis and Characterization of Polyhydroxyamide Copolymers as Precursors of Polybenzoxazoles. *Fibers Polymer.* **2015**, *16* (2), 239–244.

(28) Kim, Y. J.; Einsla, B. R.; Tchatchoua, C. N.; Mcgrath, J. E. Synthesis of High Molecular Weight Polybenzoxazoles in Polyphosphoric Acid and Investigation of Their Hydrolytic Stability under Acidic Conditions. *High Performance Polymers.* **2005**, *17* (3), 377–401.

(29) Jenekhe, S. A.; Yi, S. Efficient Photovoltaic Cells from Semiconducting Polymer Heterojunctions. *Applied Physics Letters.* **2000**, *77* (17), 2635–2637.

(30) Ahmed, E.; Kim, F. S.; Xin, H.; Jenekhe, S. A. Benzobisthiazole−Thiophene Copolymer Semiconductors: Synthesis, Enhanced Stability, Field-Effect Transistors, and Efficient Solar Cells. *Macromolecules* **2009**, *42* (22), 8615–8618.

(31) Mike, J. F.; Inteman, J. J.; Ellern, A.; Jeffries-EL, M. Facile Synthesis of 2,6-Disubstituted Benzobisthiazoles: Functional Monomers for the Design of Organic Semiconductors. *Journal of Organic Chemistry.* **2010**, *75* (2), 495–497.

(32) Mike, J. F.; Intemann, J. J.; Cai, M.; Xiao, T.; Shinar, R.; Shinar, J.; Jeffries-EL, M. Efficient Synthesis of Benzobisazole Terpolymers Containing Thiophene and Fluorene. *Polymer Chemistry.* **2011**, *2* (10), 2299.

(33) Brian C. Tlach,† Aimée L. Tomlinson,‡ Achala Bhuwalka, † and Malika Jeffries-EL. Tuning the Optical and Electronic Properties of 4,8-Disubstituted Benzobisoxazoles via Alkyne Substitution. 1–103.

(34) Tlach, B. C.; Tomlinson, A. L.; Ryno, A. G.; Knoble, D. D.; Drochner, D. L.; Krager, K. J.; Jeffries-El, M. Influence of Conjugation Axis on the Optical and Electronic Properties of Aryl-Substituted Benzobisoxazoles. *Journal of Organic Chemistry.* **2013**, *78* (13), 6570–6581.

(35) Chavez III, R.; Cai, M.; Tlach, B.; Wheeler, D. L.; Kaudal, R.; Tsyrenova, A.; Tomlinson, A. L.; Shinar, R.; Shinar, J.; Jeffries-EL, M. Benzobisoxazole Cruciforms: A Tunable, Cross-Conjugated Platform for the Generation of Deep Blue OLED Materials. *Journal of Material Chemistry C.* **2016**, *4* (17), 3765–3773.

(36) Lim, J.; Albright, T. A.; Martin, B. R.; Miljanić, O. S. Benzobisoxazole Cruciforms: Heterocyclic Fluorophores with Spatially Separated Frontier Molecular Orbitals. *Journal of Organic Chemistry.* **2011**, *76* (24), 10207–10219.

(37) Lim, J.; Miljanić, O. Š. Benzobisoxazole Fluorophore Vicariously Senses Amines, Ureas, Anions. *Chemical Communication.* **2012**, *48* (83), 10301–10303.

(38) Wilson, J. N.; Bunz, U. H. F. Switching of Intramolecular Charge Transfer in Cruciforms: Metal Ion Sensing. *Journal of American Chemical Society.* **2005**, *127* (12), 4124–4125.

(39) Gard, M. N.; Zucchero, A. J.; Kuzmanich, G.; Oelsner, C.; Guldi, D.; Dreuw, A.; Bunz, U. H. F.; Garcia-Garibay, M. A. Cruciforms' Polarized Emission Confirms Disjoint Molecular Orbitals and Excited States. *Organic Letters.* **2012**, *14* (4), 1000–1003.

(40) Wilson, J. N.; Hardcastle, K. I.; Josowicz, M.; Bunz, U. H. F. Synthesis and Electronic Properties of Bis-Styryl Substituted Trimeric Aryleneethynylenes. Comparison of Cruciforms with Iso-Cruciforms. *Tetrahedron* **2004**, *60* (34), 7157–7167.

(41) Paulus, F.; Engelhart, J. U.; Hopkinson, P. E.; Schimpf, C.; Leineweber, A.; Sirringhaus, H.; Vaynzof, Y.; Bunz, U. H. F. The Effect of Tuning the Microstructure of TIPS-Tetraazapentacene on the Performance of Solution Processed Thin Film Transistors. *Journal of Materials Chemistry C.* **2016**, *4* (6), 1194–1200.

(42) Chen, W.; Xiao, M.; Han, L.; Zhang, J.; Jiang, H.; Gu, C.; Shen, W.; Yang, R. Unsubstituted Benzodithiophene-Based Conjugated Polymers for High-

Performance Organic Field-Effect Transistors and Organic Solar Cells. *ACS Applied Materials Interfaces.* **2016**, *8* (30), 19665–19671.

(43) Yuan, J.; Zhang, Y.; Yuan, J.; Zhang, Y.; Zhou, L.; Zhang, G.; Yip, H.; Lau, T.; Lu, X. Single-Junction Organic Solar Cell with over 15 % Efficiency Using Fused-Ring Acceptor with Electron-Deficient Core Single-Junction Organic Solar Cell with over 15 % Efficiency Using Fused-Ring Acceptor with Electron-Deficient Core. *Joule* 1–12.

(44) Shi, X.; Zuo, L.; Jo, S. B.; Gao, K.; Lin, F.; Liu, F.; Jen, A. K. Y. Design of a Highly Crystalline Low-Band Gap Fused-Ring Electron Acceptor for High-Efficiency Solar Cells with Low Energy Loss. *Chemistry of Materials.* **2017**, *29* (19), 8369–8376.

(45) Du, J.; Fortney, A.; Washington, K. E.; Biewer, M. C.; Kowalewski, T.; Stefan, M. C. Benzo[1,2-: B:4,5- b ′]Difuran and Furan Substituted Diketopyrrolopyrrole Alternating Copolymer for Organic Photovoltaics with High Fill Factor. *Journal of Materials Chemistry A.* **2017**, *5* (30), 15591–15600.

(46) Woo, C. H.; Beaujuge, P. M.; Holcombe, T. W.; Lee, O. P.; Fréchet, J. M. J. Incorporation of Furan into Low Band-Gap Polymers for Efficient Solar Cells. *Journal of American Chemistry Society.* **2010**, *132* (44), 15547–15549.

(47) Huang, P.; Du, J.; Biewer, M. C.; Stefan, M. C. Developments of Furan and Benzodifuran Semiconductors for Organic Photovoltaics. *Journal of Materials Chemistry A.* **2015**, *3* (12), 6244–6257.

(48) Huo, L.; Liu, T.; Fan, B.; Zhao, Z.; Sun, X.; Wei, D.; Yu, M.; Liu, Y.; Sun, Y. Organic Solar Cells Based on a 2D Benzo[1,2-b:4,5-B′]Difuran-Conjugated Polymer with High-Power Conversion Efficiency. *Advanced Materials* **2015**, *27* (43), 6969–6975.

(49) Wu, J. S.; Cheng, S. W.; Cheng, Y. J.; Hsu, C. S. Donor-Acceptor Conjugated Polymers Based on Multifused Ladder-Type Arenes for Organic Solar Cells. *Chemical Society Reviews.* **2015**, *44* (5), 1113–1154.

(50) Peng, H.; Luan, X.; Feng, L.; Yuan, J.; Zhang, Z. G.; Li, Y.; Zou, Y. Naphthodifuran-Based Zigzag-Type Polycyclic Arene with Conjugated Side Chains for Efficient Photovoltaics. *Physical Chemistry Chemical Physics.* **2017**, *19* (22), 14289–14295.

(51) Shi, S.; Shi, K.; Yu, G.; Li, X.; Wang, H. Naphtho[1,2b;5,6b′]Difuran-Based Donor-Acceptor Polymers for High Performance Organic Field-Effect Transistors.

RSC Advances. **2015**, *5* (86), 70319–70322.

(52) Coronel, E.; Hultqvist, A. Wafer Bonded Four-Junction GaInP/GaAs//GaInAsP/GaInAs Concentrator Solar Cells with 44.7% Efficiency. *Progress on Photovolt Research Applications.* **2014**, *13* (January), 277–282.

(53) Zhang, H.; Yao, H.; Hou, J.; Zhu, J.; Zhang, J.; Li, W.; Yu, R. Over 14 % Efficiency in Organic Solar Cells Enabled by Chlorinated Nonfullerene Small-Molecule Acceptors. **2018**, *1800613*, 1–7.

(54) Wen, S.; Li, Y.; Rath, T.; Li, Y.; Wu, Y.; Bao, X.; Han, L.; Ehmann, H.; Trimmel, G.; Zhang, Y.; et al. A Benzobis(Thiazole)-Based Copolymer for Highly Efficient Non-Fullerene Polymer Solar Cells. *Chemistry of Materials.* **2019**, acs.chemmater.8b04265.

(55) Blom, P. W. M.; Mihailetchi, V. D.; Koster, L. J. A.; Markov, D. E. Device Physics of Polymer:Fullerene Bulk Heterojunction Solar Cells. *Advanced Materials.* **2007**, *19* (12), 1551–1566.

(56) Green, M. A. Improved Value for the Silicon Free Exciton Binding Energy. *AIP Advances.* **2013**, *3* (11).

(57) Kietzke, T. Recent Advances in Organic Solar Cells. *Advanced Optoelectronics.* **2007**, *2007*.

(58) Glowacki, E. D.; Sariciftci, N. S.; Tang, C. W. *Organic Solar Cells*; 2013.

(59) Gu, S.; Neugebauer, H.; Sariciftci, N. S. Conjugated Polymer-Based Organic Solar Cells. **2007**, 1324–1338.

(60) Waldrop, J. R.; Cohen, M. J.; Heeger, A. J.; MacDiarmid, A. G. The Mechanism of Schottky-Barrier Formation in Polyacetylene. *Applied Physics Letters.* **1981**, *38* (1), 53–55.

(61) Ishii, H.; Sugiyama, K.; Ito, E.; Seki, K. Energy Level Alignment and Interfacial Electronic Structures at Organic/Metal and Organic/Organic Interfaces. *Advanced Materials.* **2002**, *11* (8), 605–625.

(62) Hwang, J.; Wan, A.; Kahn, A. Energetics of Metal-Organic Interfaces: New Experiments and Assessment of the Field. *Material Science Engineering Reports* **2009**, *64* (1–2), 1–31.

(63) Li, G.; Chu, C. W.; Shrotriya, V.; Huang, J.; Yang, Y. Efficient Inverted Polymer

Solar Cells. *Applied Physical Letter.* **2006**, *88* (25), 1–4.

(64) Snaith, H. J.; Grätzel, M. The Role of a "Schottky Barrier" at an Electron-Collection Electrode in Solid-State Dye-Sensitized Solar Cells. *Advanced Materials.* **2006**, *18* (14), 1910–1914.

(65) Vandewal, K.; Tvingstedt, K.; Gadisa, A.; Inganäs, O.; Manca, J. V. On the Origin of the Open-Circuit Voltage of Polymer-Fullerene Solar Cells. *Nature Materials.* **2009**, *8* (11), 904–909.

(66) Peumans, P.; Forrest, S. R. Erratum: Very-High-Efficiency Double-Heterostructure Copper Phthalocyanine/C60 Photovoltaic Cells (Applied Physics Letters (2001) 79 (126)). *Applied Physical Letters.* **2002**, *80* (2), 338.

(67) Lee, T. W.; Chung, Y. Control of the Surface Composition of a Conducting-Polymer Complex Film to Tune the Work Function. *Advanced Functional Materials.* **2008**, *18* (15), 2246–2252.

(68) Ni, J.; Yan, H.; Wang, A.; Yang, Y.; Stern, C. L.; Metz, A. W.; Jin, S.; Wang, L.; Marks, T. J.; Ireland, J. R.; et al. MOCVD-Derived Highly Transparent, Conductive Zinc- and Tin-Doped Indium Oxide Thin Films: Precursor Synthesis, Metastable Phase Film Growth and Characterization, and Application as Anodes in Polymer Light-Emitting Diodes. *Journal of American Chemical Society.* **2005**, *127* (15), 5613–5624.

(69) Zhang, S.; Kumar, P.; Nouas, A. S.; Fontaine, L.; Tang, H.; Cicoira, F. Solvent-Induced Changes in PEDOT:PSS Films for Organic Electrochemical Transistors. *APL Materials.* **2015**, *3* (1).

(70) Lai, T. H.; Tsang, S. W.; Manders, J. R.; Chen, S.; So, F. Properties of Interlayer for Organic Photovoltaics. *Materials Today.* **2013**, *16* (11), 424–432.

(71) Lee, J.; Kang, H.; Kim, G.; Back, H.; Kim, J.; Hong, S.; Park, B.; Lee, E.; Lee, K. Achieving Large-Area Planar Perovskite Solar Cells by Introducing an Interfacial Compatibilizer. *Advanced Materials.* **2017**, *29* (22), 1–8.

(72) Agnihotri, P.; Sahu, S.; Tiwari, S. Recent Advances & Perspectives in Electron Transport Layer of Organic Solar Cells for Efficient Solar Energy Harvesting. *2017 International Conference Energy, Communication, Data Analytics, Software Computing. ICECDS 2017* **2018**, 1568–1573.

(73) Loewe, R. S.; Ewbank, P. C.; Liu, J.; Zhai, L.; McCullough, R. D. Regioregular, Head-to-Tail Coupled Poly(3-Alkylthiophenes) Made Easy by the GRIM Method:

Investigation of the Reaction and the Origin of Regioselectivity. *Macromolecules* **2001**, *34* (13), 4324–4333.

(74) Ong, S.; Wu, Y.; Liu, P.; Gardner, S. High-Performance Semiconducting Polythiophenes for Organic Thin-Film Transistors. **2004**, No. 100, 3378–3379.

(75) Ong, B. S.; Wu, Y.; Liu, P. Structurally Ordered Polythiophene Nanoparticles for High-Performance Organic Thin-Film Transistors **. **2005**, 1141–1144.

(76) Kline, R. J.; Mcgehee, M. D.; Kadnikova, E. N.; Liu, J.; Fre, J. M. J.; Toney, M. F. Dependence of Regioregular Poly (3-Hexylthiophene) Film Morphology and Field-Effect Mobility on Molecular Weight. **2005**, 3312–3319.

(77) Antwi, B. Y.; Taylor, R. G. D.; Cameron, J.; Owoare, R. B.; Kingsford-Adaboh, R.; Skabara, P. J. Acceptor-Donor-Acceptor Small Molecules Based on Derivatives of 3,4-Ethylenedioxythiophene for Solution Processed Organic Solar Cells. *RSC Advances.* **2016**, *6* (101), 98797–98803.

(78) Zhou, H.; Yang, L.; You, W. Rational Design of High Performance Conjugated Polymers for Organic Solar Cells. *Macromolecules* **2012**, *45*, 607–632.

(79) Zhang, W.; Smith, J.; Watkins, S. E.; Gysel, R.; Mcgehee, M.; Salleo, A.; Kirkpatrick, J.; Ashraf, S.; Anthopoulos, T.; Heeney, M. Indacenodithiophene Semiconducting Polymers for High-Performance , Air-Stable Transistors. **2010**, 11437–11439.

(80) Zhang, X.; Bronstein, H.; Kronemeijer, A. J.; Smith, J.; Kim, Y.; Kline, R. J.; Richter, L. J.; Anthopoulos, T. D.; Sirringhaus, H.; Song, K.; et al. Molecular Origin of High Field-Effect Mobility in an Indacenodithiophene- Benzothiadiazole Copolymer. *Nature Communications.* **2013**, *4*, 1–9.

(81) Koch, A.; Wudl, F. Two Different Fullerenes Have the Same Cyclic Voltammetry. **1991**, *04* (4), 1050–1051.

(82) Chen, H. Y.; Hou, J.; Zhang, S.; Liang, Y.; Yang, G.; Yang, Y.; Yu, L.; Wu, Y.; Li, G. Polymer Solar Cells with Enhanced Open-Circuit Voltage and Efficiency. *Nature Photonics.* **2009**, *3* (11), 649–653.

(83) Liang, Y.; Li, G.; Tsai, S.-T.; Yu, L.; Ray, C.; Feng, D.; Wu, Y. Highly Efficient Solar Cell Polymers Developed via Fine-Tuning of Structural and Electronic Properties. *Journal of American Chemical Society.* **2009**, *131* (22), 7792–7799.

(84) Yu, L.; Liang, Y. A New Class of Semiconducting Polymers for Bulk

Heterojunction Solar Cells with Exceptionally High Performance. *Accounts of Chemical Research.* **2010**, *43* (9), 1227–1236.

(85) Yan, C.; Barlow, S.; Wang, Z.; Yan, H.; Jen, A. K. Y.; Marder, S. R.; Zhan, X. Non-Fullerene Acceptors for Organic Solar Cells. *Nature Reviews Materials.* **2018**, *3*.

(86) Bloking, J. T.; Giovenzana, T.; Higgs, A. T.; Ponec, A. J.; Hoke, E. T.; Vandewal, K.; Ko, S.; Bao, Z.; Sellinger, A.; McGehee, M. D. Comparing the Device Physics and Morphology of Polymer Solar Cells Employing Fullerenes and Non-Fullerene Acceptors. *Advanced Energy Materials.* **2014**, *4* (12), 1–12.

(87) Arbogast, J. W.; Foote, C. S. Photophysical Properties of C70. *Journal of American Chemical Society.* **1991**, *183* (May 1991), 8886–8889.

(88) Tang, C. W. Two-Layer Organic Photovoltaic Cell. **2003**, *183* (1986).

(89) Hoppe, H.; Niggemann, M.; Winder, C.; Kraut, J.; Hiesgen, R.; Hinsch, A.; Meissner, D.; Sariciftci, N. S. Nanoscale Morphology of Conjugated Polymer/Fullerene-Based Bulk-Heterojunction Solar Cells. *Advanced Functional Materials.* **2004**, *14* (10), 1005–1011.

(90) Yu, G.; Gao, J.; Hummelen, J. C.; Wudl, F.; Heeger, A. J. Polymer Photovoltaic Cells- Enhanced Efficiencies via a Network of Internal Donor-Acceptor Heterojunction. *Science* **1995**, *270*, 1789–1791.

(91) Koster, L. J. A.; Smits, E. C. P.; Mihailetchi, V. D.; Blom, P. W. M. Device Model for the Operation of Polymer/Fullerene Bulk Heterojunction Solar Cells. *Physical. Reviews. B - Condensed Matter Material Physics.* **2005**, *72* (8), 1–9.

(92) Heeger, A. J. 25th Anniversary Article: Bulk Heterojunction Solar Cells: Understanding the Mechanism of Operation. *Advanced Materials.* **2014**, *26* (1), 10–28.

(93) Elumalai, N. K.; Uddin, A. Open Circuit Voltage of Organic Solar Cells: An in-Depth Review. *Energy Environmental Science.* **2016**, *9* (2), 391–410.

(94) Zhao, F.; Wang, C.; Zhan, X. Morphology Control in Organic Solar Cells. *Advanced Energy Materials.* **2018**, *8* (28), 1–34.

(95) Zhong, Y.; Tada, A.; Izawa, S.; Hashimoto, K.; Tajima, K. Enhancement of VOCwithout Loss of JSCin Organic Solar Cells by Modification of Donor/Acceptor Interfaces. *Advanced Energy Materials.* **2014**, *4* (5), 1–8.

(96) Thompson, B. C.; Fréchet, J. M. J. Polymer-Fullerene Composite Solar Cells. *Angewandte Chemie - International Edition.* **2008**, *47* (1), 58–77.

(97) Liao, H. C.; Ho, C. C.; Chang, C. Y.; Jao, M. H.; Darling, S. B.; Su, W. F. Additives for Morphology Control in High-Efficiency Organic Solar Cells. *Materials Today.* **2013**, *16* (9), 326–336.

(98) Peet, J.; Kim, J. Y.; Coates, N. E.; Ma, W. L.; Moses, D.; Heeger, A. J.; Bazan, G. C. Efficiency Enhancement in Low-Bandgap Polymer Solar Cells by Processing with Alkane Dithiols. *Nature Materials.* **2007**, *6* (7), 497–500.

(99) Lee, J. K.; Ma, W. L.; Brabec, C. J.; Yuen, J.; Moon, J. S.; Kim, J. Y.; Lee, K.; Bazan, G. C.; Heeger, A. J. Processing Additives for Improved Efficiency from Bulk Heterojunction Solar Cells.-Supporting Information. *Journal of American. Chemical Society.* **2008**, *130* (11), 3619.

(100) Coates, N. E.; Hwang, I. W.; Peet, J.; Bazan, G. C.; Moses, D.; Heeger, A. J. 1,8-Octanedithiol as a Processing Additive for Bulk Heterojunction Materials: Enhanced Photoconductive Response. *Applied Physics Letters.* **2008**, *93* (7), 6–9.

(101) Nam, S.; Jang, J.; Cha, H.; Hwang, J.; An, T. K.; Park, S.; Park, C. E. Effects of Direct Solvent Exposure on the Nanoscale Morphologies and Electrical Characteristics of PCBM-Based Transistors and Photovoltaics. *Journal of Materials Chemistry.* **2012**, *22* (12), 5543.

(102) Guo, X.; Cui, C.; Zhang, M.; Huo, L.; Huang, Y.; Hou, J.; Li, Y. High Efficiency Polymer Solar Cells Based on Poly(3-Hexylthiophene)/Indene- C70 Bisadduct with Solvent Additive. *Energy & Environmental Science.* **2012**, *5* (7), 7943–7949.

(103) Qi, B.; Wang, J. Fill Factor in Organic Solar Cells. *Physical Chemistry Chemical Physics.* **2013**, *15* (23), 8972–8982.

(104) Tumbleston, J. R.; Ko, D. H.; Samulski, E. T.; Lopez, R. Nonideal Parasitic Resistance Effects in Bulk Heterojunction Organic Solar Cells. *Journal of Applied Physics.* **2010**, *108* (8).

(105) Kim, M. S.; Kim, B. G.; Kim, J. Effective Variables to Control the Fill Factor of Organic Photovoltaic Cells. *ACS Applied Materials Interfaces.* **2009**, *1* (6), 1264–1269.

(106) Wang, C.; Dong, H.; Hu, W.; Liu, Y.; Zhu, D. Semiconducting π-Conjugated Systems in Field-Effect Transistors: A Material Odyssey of Organic Electronics. *Chemical Reviews.* **2011**, *112* (4), 2208–2267.

(107) Anthony, J. E.; Facchetti, A.; Heeney, M.; Marder, S. R.; Zhan, X. N-Type Organic Semiconductors in Organic Electronics. *Advanced Materials.* **2010**, *22* (34), 3876–3892.

(108) Facchetti, A. π-Conjugated Polymers for Organic Electronics and Photovoltaic Cell Applications. *Chemistry Materials.* **2010**, *23* (3), 733–758.

(109) Huser, T.; Yan, M.; Rothberg, L. J. Single Chain Spectroscopy of Conformational Dependence of Conjugated Polymer Photophysics. *Proceedings National Academy Science.* **2000**, *97* (21), 11187–11191.

(110) Hu, D.; Yu, J.; Wong, K.; Bagchi, B.; Rossky, P. J.; Barbara, P. F. Collapse of Stiff Conjugated Polymers with Chemical Defects into Ordered, Cylindrical Conformations. *Nature* **2000**, *405* (6790), 1030–1033.

(111) Kan, B.; Li, M.; Zhang, Q.; Liu, F.; Wan, X.; Wang, Y.; Ni, W.; Long, G.; Yang, X.; Feng, H.; et al. A Series of Simple Oligomer-like Small Molecules Based on Oligothiophenes for Solution-Processed Solar Cells with High Efficiency. *Journal of American Chemical Society.* **2015**, *137* (11), 3886–3893.

(112) Zhang, Q.; Kan, B.; Liu, F.; Long, G.; Wan, X.; Chen, X.; Zuo, Y.; Ni, W.; Zhang, H.; Li, M.; et al. Small-Molecule Solar Cells with Efficiency over 9%. *Nature Photonics* **2014**, *9*, 35.

(113) Sun, Y.; Welch, G. C.; Leong, W. L.; Takacs, C. J.; Bazan, G. C.; Heeger, A. J. Solution-Processed Small-Molecule Solar Cells with 6.7% Efficiency. *Nature Materials.* **2011**, *11*, 44.

(114) Duan, C.; Huang, F.; Cao, Y. Recent Development of Push–Pull Conjugated Polymers for Bulk-Heterojunction Photovoltaics: Rational Design and Fine Tailoring of Molecular Structures. *Journal of Materials Chemistry.* **2012**, *22* (21), 10416–10434.

(115) Gendron, D.; Leclerc, M. New Conjugated Polymers for Plastic Solar Cells. *Energy Environmental Science.* **2011**, *4* (4), 1225–1237.

(116) Koster, L. J. A.; Mihailetchi, V. D.; Blom, P. W. M. Ultimate Efficiency of Polymer/Fullerene Bulk Heterojunction Solar Cells. *Appl. Phys. Lett.* **2006**, *88* (9), 86–89.

(117) Havinga, E. E.; ten Hoeve, W.; Wynberg, H. Alternate Donor-Acceptor Small-Band-Gap Semiconducting Polymers; Polysquaraines and Polycroconaines. *Synth. Met.* **1993**, *55* (1), 299–306.

(118) van Mullekom H.A.M.; J.A.J.M., V.; E.E., H.; E.W.[1], M. *Developments in the Chemistry and Band Gap Engineering of Donor-Acceptor Substituted Conjugated Polymers*; 2001; Vol. 32.

(119) E. Coughlin, J.; B. Henson, Z.; C. Welch, G.; C. Bazan, G. Design and Synthesis of Molecular Donors for Solution-Processed High-Efficiency Organic Solar Cells. *Accounts of Chemical Research.* **2013**, *47* (1), 257–270.

(120) Klare, J. E.; Tulevski, G. S.; Nuckolls, C. Chemical Reactions with Upright Monolayers of Cruciform π-Systems. *Langmuir* **2004**, *20* (23), 10068–10072.

(121) Zhu, H.; Liu, B.; Liu, J.; Zhang, W.; Zhu, W.-H. D–A–π–A Featured Sensitizers by Modification of Auxiliary Acceptor for Preventing "Trade-off" Effect. *Journal of Material Chemistry C.* **2015**, *3* (26), 6882–6890.

(122) McGrier, P. L.; Solntsev, K. M.; Miao, S.; Tolbert, L. M.; Miranda, O. R.; Rotello, V. M.; Bunz, U. H. F. Hydroxycruciforms: Amine-Responsive Fluorophores. *Chemistry – A European Journal.* **2008**, *14* (15), 4503–4510.

(123) Marsden, J. A.; Miller, J. J.; Shirtcliff, L. D.; Haley, M. M. Structure − Property Relationships of Fluorinated Donor / Acceptor Tetrakis (Phenylethynyl) Benzenes and Bis (Dehydrobenzoannuleno) Benzenes Structure-Property Relationships of Fluorinated Donor / Acceptor Tetrakis (Phenylethynyl) Benzenes and Bis (. *Journal of American Chemical Society.* **2005**, *127* (11), 2464–2476.

(124) L. Spitler, E.; M. Monson, J.; M. Haley, M. Structure−Property Relationships of Fluorinated Donor/Acceptor Tetrakis(Phenylethynyl)Benzenes and Bis(Dehydrobenzoannuleno)Benzenes. *Journal of Organic Chemistry.* **2008**, *73* (6), 2211–2223.

(125) L. Spitler, E.; D. Shirtcliff, L.; M. Haley, M. Systematic Structure−Property Investigations and Ion-Sensing Studies of Pyridine-Derivatized Donor/Acceptor Tetrakis(Arylethynyl)Benzenes. *Journal of Organic Chemistry.* **2006**, *72* (1), 86–96.

(126) E. Klare, J.; S. Tulevski, G.; Sugo, K.; de Picciotto, A.; A. White, K.; Nuckolls, C. Cruciform π-Systems for Molecular Electronics Applications. *Journal of American Chemical Society.* **2003**, *125* (20), 6030–6031.

(127) Intemann, J. J.; Hellerich, E. S.; Ewan, M. D.; Tlach, B. C.; Speetzen, E. D.; Shinar, R.; Shinar, J.; Jeffries-EL, M. Investigating the Impact of Conjugation Pathway on the Physical and Electronic Properties of Benzobisoxazole-Containing

Polymers. *Journal of Material Chemistry C.* **2017**, No. Scheme 1.

(128) Osowska, K.; Miljanić, O. Š. Supramolecular Organization of Extended Benzobisoxazole Cruciforms. *Chemical Communication.* **2010**, *46* (24), 4276–4278.

(129) A. Saeed, M.; T. M. Le, H.; Š. Miljanić, O. Benzobisoxazole Cruciforms as Fluorescent Sensors. *Accounts of Chemical Research.* **2014**, *47* (7), 2074–2083.

(130) Tlach, B. C.; Tomlinson, A. L.; Morgan, K. D.; Collins, C. R.; Zenner, M. D.; Jeffries-EL, M. Effect of Extended Conjugation on the Optoelectronic Properties of Benzo[1,2-*d*:4,5-*D′*]Bisoxazole Polymers. *Australian Journal of Chemistry.* **2014**, *67* (5), 711–721.

(131) C. Thompson, B.; Kim, Y.-G.; R. Reynolds, J. Spectral Broadening in MEH-PPV:PCBM-Based Photovoltaic Devices via Blending with a Narrow Band Gap Cyanovinylene−Dioxythiophene Polymer. *Macromolecules* **2005**, *38* (13), 5359–5362.

(132) Savikhin, V.; Babics, M.; Neophytou, M.; Liu, S.; Oosterhout, S. D.; Yan, H.; Gu, X.; Beaujuge, P. M.; Toney, M. F. Impact of Polymer Sidechain Modification on OPV Morphology and Performance. *Chemistry of Materials.* **2018**, acs.chemmater.8b03455.

(133) J. Vázquez, R.; Kim, H.; M. Kobilka, B.; J. Hale, B.; Jeffries-EL, M.; Zimmerman, P.; Goodson, T. Evaluating the Effect of Heteroatoms on the Photophysical Properties of Donor–Acceptor Conjugated Polymers Based on 2,6-Di(Thiophen-2-Yl)Benzo[1,2-b:4,5-B′]Difuran: Two-Photon Cross-Section and Ultrafast Time-Resolved Spectroscopy. *Journal of Physical Chemistry C.* **2017**, *121* (27), 14382–14392.

(134) Zhang, X.-F. The Effect of Phenyl Substitution on the Fluorescence Characteristics of Fluorescein Derivatives via Intramolecular Photoinduced Electron Transfer. *Photochemical Photobiological Science.* **2010**, *9* (9), 1261–1268.

(135) Keller, B.; Mclean, A.; Kim, B.; Chung, K.; Kim, J.; Goodson, T. Ultrafast Spectroscopic Study of Donor − Acceptor Benzodithiophene Light Harvesting Organic Conjugated Polymers. **2016**.

(136) Son, H. J.; He, F.; Carsten, B.; Yu, L. Are We There yet? Design of Better Conjugated Polymers for Polymer Solar Cells. *Journal of Materials Chemistry.* **2011**, *21* (47), 18934–18945.

(137) Carter, E. A.; Goddard, W. A. Correlation-consistent Singlet–Triplet Gaps in Substituted Carbenes. *Journal of Chemical Physics.* **1988**, *88* (3), 1752–1763.

(138) Bredas, J.-L. Mind the Gap! *Material Horizons.* **2014**, *1* (1), 17–19.

(139) Cardona, C. M.; Li, W.; Kaifer, A. E.; Stockdale, D.; Bazan, G. C. Electrochemical Considerations for Determining Absolute Frontier Orbital Energy Levels of Conjugated Polymers for Solar Cell Applications. *Advanced Materials.* **2011**, *23* (20), 2367–2371.

(140) Mitschke, U.; Bäuerle, P. The Electroluminescence of Organic Materials. *Journal of Material Chemistry.* **2000**, *10* (7), 1471–1507.

(141) Bronstein, H.; Chen, Z.; Ashraf, R. S.; Zhang, W.; Du, J.; Durrant, J. R.; Tuladhar, P. S.; Song, K.; Watkins, S. E.; Geerts, Y.; et al. Thieno[3,2-b]Thiophene-Diketopyrrolopyrrole-Containing Polymers for High-Performance Organic Field-Effect Transistors and Organic Photovoltaic Devices. *Journal of American Chemical Society.* **2011**, *133* (10), 3272–3275.

(142) Scharber, M. C.; Mühlbacher, D.; Koppe, M.; Denk, P.; Waldauf, C.; Heeger, A. J.; Brabec, C. J. Design Rules for Donors in Bulk-Heterojunction Solar Cells - Towards 10 % Energy-Conversion Efficiency. *Advanced Materials.* **2006**, *18* (6), 789–794.

(143) Mang Ling, M.; Bao, Z. Thin Film Deposition, Patterning, and Printing in Organic Thin Film Transistors. *Chemistry of Materials.* **2004**, *16* (23), 4824–4840.

(144) N. Hoth, C.; Schilinsky, P.; A. Choulis, S.; J. Brabec, C. Printing Highly Efficient Organic Solar Cells. *Nano Letters.* **2008**, *8* (9), 2806–2813.

(145) Bhuwalka, A.; Jeffries-el, M. Design and Synthesis of Novel Heterocycles for Organic Semiconducting Materials. **2014**.

(146) Bhuwalka, A.; Ewan, M. D.; Mike, J. F.; Elshobaki, M.; Kobilka, B.; Chaudhary, S.; Jeffries-El, M. Synthesis, Characterization, and Photovoltaic Properties of Dithienylbenzobisazole-Dithienylsilole Copolymers. *Journal of Polymer Science. Part A Polymer Chemistry.* **2015**, *53* (13), 1533–1540.

(147) Bhuwalka, A.; Ewan, M. D.; Elshobaki, M.; Mike, J. F.; Tlach, B.; Chaudhary, S.; Jeffries-EL, M. Synthesis and Photovoltaic Properties of 2,6-Bis(2-Thienyl) Benzobisazole and 4,8-Bis(Thienyl)-Benzo[1,2-B:4,5-B′]Dithiophene Copolymers. *Journal of Polymer Science Part A Polymer Chemistry.* **2016**, *54* (3), 316–324.

(148) Intemann, J. J.; Hellerich, E. S.; Ewan, M. D.; Tlach, B. C.; Speetzen, E. D.; Shinar, R.; Shinar, J.; Jeffries-El, M. Investigating the Impact of Conjugation Pathway on the Physical and Electronic Properties of Benzobisoxazole-Containing Polymers. *Journal of Materials Chemistry C.* **2017**, *5* (48), 12839–12847.

(149) Bronstein, H.; Chen, Z.; Shahid Ashraf, R.; Zhang, W.; Du, J.; R. Durrant, J.; Shakya Tuladhar, P.; Song, K.; E. Watkins, S.; Geerts, Y.; et al. Thieno[3,2-b]Thiophene−Diketopyrrolopyrrole-Containing Polymers for High-Performance Organic Field-Effect Transistors and Organic Photovoltaic Devices. *Journal of American Chemical Society.* **2011**, *133* (10), 3272–3275.

(150) E. Katz, H.; Bao, Z. The Physical Chemistry of Organic Field-Effect Transistors. *Journal of Physical Chemistry B.* **1999**, *104* (4), 671–678.

(151) Zaumseil, J.; Sirringhaus, H. Electron and Ambipolar Transport in Organic Field-Effect Transistors. *Chemical Reviews.* **2007**, *107* (4), 1296–1323.

(152) Muccini, M.; Nazionale, C. PROGRESS ARTICLE A Bright Future for Organic Fi Eld-Effect Transistors. *Group* **2006**, 605–613.

(153) Park, S. H.; Roy, A.; Beaupré, S.; Cho, S.; Coates, N.; Moon, J. S.; Moses, D.; Leclerc, M.; Lee, K.; Heeger, A. J. Bulk Heterojunction Solar Cells with Internal Quantum Efficiency Approaching 100%. *Nature Photonics.* **2009**, *3*, 297.

(154) Liu, Y.; Zhao, J.; Li, Z.; Mu, C.; Ma, W.; Hu, H.; Jiang, K.; Lin, H.; Ade, H.; Yan, H. Aggregation and Morphology Control Enables Multiple Cases of High-Efficiency Polymer Solar Cells. *Nature Communications.* **2014**, *5*, 5293.

(155) Zhou, H.; Yang, L.; You, W. Rational Design of High Performance Conjugated Polymers for Organic Solar Cells. *Macromolecules* **2012**, *45* (2), 607–632.

(156) Graham, K. R.; Wieruszewski, P. M.; Stalder, R.; Hartel, M. J.; Mei, J.; So, F.; Reynolds, J. R. Improved Performance of Molecular Bulk-Heterojunction Photovoltaic Cells through Predictable Selection of Solvent Additives. *Advanced Functional Materials* **2012**, *22* (22), 4801–4813.

(157) Katsouras, A.; Gasparini, N.; Koulogiannis, C.; Spanos, M.; Ameri, T.; Brabec, C. J.; Chochos, C. L.; Avgeropoulos, A. Systematic Analysis of Polymer Molecular Weight Influence on the Organic Photovoltaic Performance. *Macromolecular Rapid Communication.* **2015**, *36* (20), 1778–1797.

(158) Leclerc, N.; Chávez, P.; Ibraikulov, O. A.; Heiser, T.; Lévêque, P. Impact of Backbone Fluorination on π -Conjugated Polymers in Organic Photovoltaic

Devices : A Review. **2016**.

(159) A. Wolak, M.; Jang, B.-B.; C. Palilis, L.; H. Kafafi, Z. Functionalized Pentacene Derivatives for Use as Red Emitters in Organic Light-Emitting Diodes. *Journal of Physical Chemistry B*. **2004**, *108* (18), 5492–5499.

(160) Loo, J. F. W. and B. H. Rigid-Rod Polymers. 2. Synthesis and Thermal Properties of Para-Aromatic Polymers with 2,6-Benzobisthiazole Units in the Main Chain1. *Macromolecules* **1981**, *920* (19), 915–920.

(161) Wolf, J.; Babics, M.; Wang, K.; Saleem, Q.; Liang, R. Z.; Hansen, M. R.; Beaujuge, P. M. Benzo[1,2-b:4,5-B′]Dithiophene-Pyrido[3,4-b]Pyrazine Small-Molecule Donors for Bulk Heterojunction Solar Cells. *Chemistry of Materials.* **2016**, *28* (7), 2058–2066.

(162) J. Intemann, J.; S. Hellerich, E.; C. Tlach, B.; D. Ewan, M.; A. Barnes, C.; Bhuwalka, A.; Cai, M.; Shinar, J.; Shinar, R.; Jeffries-EL, M. Altering the Conjugation Pathway for Improved Performance of Benzobisoxazole-Based Polymer Guest Emitters in Polymer Light-Emitting Diodes. *Macromolecules* **2012**, *45* (17), 6888–6897.

(163) Wolfe, R. M. W.; Culver, E. W.; Rasmussen, S. C. Synthesis and Characterization of Bis[1]Benzothieno[3,2-b:20,30-d]Pyrroles: Quantitative Effects of Benzannulation on Dithieno[3,2-b:20,30-d]Pyrroles. *Molecules* **2018**, *23* (9), 11–16.

(164) Homyak, P.; Liu, Y.; Liu, F.; P. Russel, T.; Bryan Coughlin, E. Systematic Variation of Fluorinated Diketopyrrolopyrrole Low Bandgap Conjugated Polymers: Synthesis by Direct Arylation Polymerization and Characterization and Performance in Organic Photovoltaics and Organic Field-Effect Transistors. *Macromolecules* **2015**, *48* (19), 6978–6986.

(165) Liu, D.; Zhao, W.; Zhang, S.; Ye, L.; Zheng, Z.; Cui, Y.; Chen, Y.; Hou, J. Highly Efficient Photovoltaic Polymers Based on Benzodithiophene and Quinoxaline with Deeper HOMO Levels. *Macromolecules* **2015**, *48* (15), 5172–5178.

(166) Mueller, C. J.; Gann, E.; McNeill, C. R.; Thelakkat, M. Influence of Fluorination in π-Extended Backbone Polydiketopyrrolopyrroles on Charge Carrier Mobility and Depth-Dependent Molecular Alignment. *Journal of Materials Chemistry C.* **2015**, *3* (34), 8916–8925.

(167) Hao, M.; Li, X.; Shi, K.; Xie, D.; Zeng, X.; Fang, J.; Yu, G.; Yang, C. Highly Efficient Photovoltaics and Field-Effect Transistors Based on Copolymers of

Mono-Fluorinated Benzothiadiazole and Quaterthiophene: Synthesis and Effect of the Molecular Weight on Device Performance. *Polymer Chemistry.* **2015**, *6* (33), 6050–6057.

(168) Farinola, G. M.; Cardone, A.; Babudri, F.; Martinelli, C.; Naso, F.; Bruno, G.; Losurdo, M. Fluorinated Poly(p-Phenylenevinylene)s: Synthesis and Optical Properties of an Intriguing Class of Luminescent Polymers. *Materials (Basel)*. **2010**, *3* (5), 3077–3091.

(169) Nielsen, C. B.; White, A. J. P.; McCulloch, I. Effect of Fluorination of 2,1,3-Benzothiadiazole. *Journal of Organic Chemistry.* **2015**, *80* (10), 5045–5048.

(170) Bronstein, H.; M. Frost, J.; Hadipour, A.; Kim, Y.; B. Nielsen, C.; Shahid Ashraf, R.; P. Rand, B.; Watkins, S.; McCulloch, I. Effect of Fluorination on the Properties of a Donor–Acceptor Copolymer for Use in Photovoltaic Cells and Transistors. *Chemistry of Materials.* **2013**, *25* (3), 277–285.

(171) Burgués-Ceballos, I.; Stella, M.; Lacharmoise, P.; Martínez-Ferrero, E. Towards Industrialization of Polymer Solar Cells: Material Processing for Upscaling. *Journal Materials Chemistry A*. **2014**, *2* (42), 17711–17722.

(172) Li, G.; Zhu, R.; Yang, Y. Polymer Solar Cells. *Nature Photonics.* **2012**, *6*, 153.

(173) Su, Y.-W.; Lan, S.-C.; Wei, K.-H. Organic Photovoltaics. *Materials Today.* **2012**, *15* (12), 554–562.

(174) Chen, J.; Cao, Y. Development of Novel Conjugated Donor Polymers for High-Efficiency Bulk-Heterojunction Photovoltaic Devices. *Accounts of Chemical Research.* **2009**, *42* (11), 1709–1718.

(175) Carsten, B.; He, F.; Jung Son, H.; Xu, T.; Yu, L. Stille Polycondensation for Synthesis of Functional Materials. *Chemical Reviews.* **2011**, *111* (3), 1493–1528.

(176) Marrocchi, A.; Facchetti, A.; Lanari, D.; Petrucci, C.; Vaccaro, L. Current Methodologies for a Sustainable Approach to π-Conjugated Organic Semiconductors. *Energy Environmental Science.* **2016**, *9* (3), 763–786.

(177) Nikiforov, M. P.; Lai, B.; Chen, W.; Chen, S.; Schaller, R. D.; Strzalka, J.; Maser, J.; Darling, S. B. Detection and Role of Trace Impurities in High-Performance Organic Solar Cells. *Energy Environmental Science.* **2013**, *6* (5), 1513–1520.

(178) Pouliot, J.-R.; Grenier, F.; Terence Blaskovits, J.; Beaupré, S.; Leclerc, M. Direct (Hetero)Arylation Polymerization: Simplicity for Conjugated Polymer Synthesis.

Chemical Reviews. **2016**, *116* (22), 14225–14274.

(179) Alberico, D.; E. Scott, M.; Lautens, M. Aryl−Aryl Bond Formation by Transition-Metal-Catalyzed Direct Arylation. *Chemical Reviews.* **2007**, *107* (1), 174–238.

(180) Bura, T.; Beaupré, S.; Légaré, M.-A.; Quinn, J.; Rochette, E.; Blaskovits, J. T.; Fontaine, F.-G.; Pron, A.; Li, Y.; Leclerc, M. Direct Heteroarylation Polymerization: Guidelines for Defect-Free Conjugated Polymers. *Chemical Science.* **2017**, *8* (5), 3913–3925.

(181) Wang, X.; Wang, M. Synthesis of Donor–Acceptor Conjugated Polymers Based on Benzo[1{,}2-b:4{,}5-B′]Dithiophene and 2{,}1{,}3-Benzothiadiazole via Direct Arylation Polycondensation: Towards Efficient C–H Activation in Nonpolar Solvents. *Polymer Chemistry.* **2014**, *5* (19), 5784–5792.

(182) Marzano, G.; Carulli, F.; Babudri, F.; Pellegrino, A.; Po, R.; Luzzati, S.; Farinola, G. M. PBDTTPD for Plastic Solar Cells via Pd(PPh3)4-Catalyzed Direct (Hetero)Arylation Polymerization. *Journal of Material Chemistry A.* **2016**, *4* (43), 17163–17170.

(183) Du, J.; Fortney, A.; Washington, K. E.; Biewer, M. C.; Kowalewski, T.; Stefan, M. C. Benzo[1{,}2-b:4{,}5-B′]Difuran and Furan Substituted Diketopyrrolopyrrole Alternating Copolymer for Organic Photovoltaics with High Fill Factor. *Journal of Materials Chemistry A.* **2017**, *5* (30), 15591–15600.

(184) Li, H.; Tang, P.; Zhao, Y.; Liu, S.-X.; Aeschi, Y.; Deng, L.; Braun, J.; Zhao, B.; Liu, Y.; Tan, S.; et al. Benzodifuran-Containing Well-Defined π-Conjugated Polymers for Photovoltaic Cells. *Journal of Polymer Science Part A Polymer Chemistry.* **2012**, *50* (14), 2935–2943.

(185) Gao, Y.; Wang, Z.; Zhang, J.; Zhang, H.; Lu, K.; Guo, F.; Wei, Z.; Yang, Y.; Zhao, L.; Zhang, Y. Wide-Bandgap Conjugated Polymers Based on Alkylthiofuran-Substituted Benzo[1,2-b:4,5-B′]Difuran for Efficient Fullerene-Free Polymer Solar Cells. *Macromolecules* **2018**, *51* (7), 2498–2505.

(186) Li, S.; Yuan, Z.; Deng, P.; Sun, B.; Zhang, Q. Synthesis and Photovoltaic Performances of a Conjugated Polymer Based on a New Naphthodifuran Monomer. *Polymer Chemistry.* **2014**, *5* (7), 2561–2566.

(187) Li, W.; H. Hendriks, K.; M. Wienk, M.; A. J. Janssen, R. Diketopyrrolopyrrole Polymers for Organic Solar Cells. *Accounts of Chemical Research.* **2015**, *49* (1), 78–85.

(188) Areephong, J.; Hendsbee, A. D.; Welch, G. C. Facile Synthesis of Unsymmetrical and π-Extended Furan-Diketopyrrolopyrrole Derivatives through C–H Direct (Hetero)Arylation Using a Heterogeneous Catalyst System. *New Journal of Chemistry.* **2015**, *39* (9), 6714–6717.

(189) Shi, S.; Xie, X.; Gao, C.; Shi, K.; Chen, S.; Yu, G.; Guo, L.; Li, X.; Wang, H. Synthesis and Characterization of Angular-Shaped Naphtho[1,2-b;5,6-B′]Difuran–Diketopyrrolopyrrole-Containing Copolymers for High-Performance Organic Field-Effect Transistors. *Macromolecules* **2014**, *47* (2), 616–625.

(190) Salaneck, W. R. Classical Ultraviolet Photoelectron Spectroscopy of Polymers. *J. Electron Spectroscopic Related Phenomena* **2009**, *174* (1), 3–9.

(191) Lotz, B.; Miyoshi, T.; Z. D. Cheng, S. 50th Anniversary Perspective: Polymer Crystals and Crystallization: Personal Journeys in a Challenging Research Field. *Macromolecules* **2017**, *50* (16), 5995–6025.

(192) Wong, W.-Y.; Wang, X.-Z.; He, Z.; Chan, K.-K.; B. Djurišić, A.; Cheung, K.-Y.; Yip, C.-T.; Man-Ching Ng, A.; Yan Xi, Y.; S. K. Mak, C.; et al. Tuning the Absorption, Charge Transport Properties, and Solar Cell Efficiency with the Number of Thienyl Rings in Platinum-Containing Poly(Aryleneethynylene)S. *Journal of American Chemical Society.* **2007**, *129* (46), 14372–14380.

(193) O'Hara, K.; Takacs, C. J.; Liu, S.; Cruciani, F.; Beaujuge, P.; Hawker, C. J.; Chabinyc, M. L. Effect of Alkyl Side Chains on Intercrystallite Ordering in Semiconducting Polymers. *Macromolecules* **2019**, *52* (7), 2853–2862.

CURRICULUM VITAE